

PROBING THE STATISTICAL STRUCTURE OF
TURBULENCE WITH MEASUREMENTS OF TRACER
PARTICLE TRACKS

A Dissertation
Presented to the Faculty of the Graduate School
of Cornell University
in Partial Fulfillment of the Requirements for the Degree of
Doctor of Philosophy

by

Nicholas Testroet Ouellette

May 2006

© 2006 Nicholas Testroet Ouellette

ALL RIGHTS RESERVED

PROBING THE STATISTICAL STRUCTURE OF TURBULENCE WITH
MEASUREMENTS OF TRACER PARTICLE TRACKS

Nicholas Testroet Ouellette, Ph.D.

Cornell University 2006

This thesis reports measurements of the statistics of passive Lagrangian tracer particles in an intensely turbulent laboratory water flow. The tracers are imaged with three high-speed CMOS cameras and their trajectories are reconstructed using specialized particle tracking algorithms. Various tracking algorithms were studied quantitatively to determine the algorithm used in this work.

The scaling behavior of the Lagrangian structure functions is investigated as a function of structure function order, and is found to deviate strongly from the Kolmogorov (1941a) prediction. The second order Lagrangian structure function is considered in detail, and its scaling constant C_0 , an essential parameter in turbulence models, is measured independently from the structure function and the Lagrangian velocity spectrum. These measurements of C_0 show strong anisotropy. These results are confirmed by measurements of the spatial dispersion of single tracer particles. In addition, the first measurement of the multifractal dimension spectrum of Lagrangian turbulence is reported.

The relative motion of multiple tracer particles is also measured. Turbulent relative dispersion, the growth of the separation of a pair of tracers, is measured and found to be in excellent agreement with the results of Batchelor (1950), with no observed Richardson-Obukhov scaling. Other proposed models of turbulent

relative dispersion are also investigated in detail. A coarse-grained model of the velocity gradient tensor based on clusters of four tracers, known as tetrads, is also investigated, as well as the statistics of the tetrad shape changes.

BIOGRAPHICAL SKETCH

Nicholas Testroet Ouellette was born on April 5, 1980 in Albany, New York, the only child of Michael and Helen. After moving from nearby Schenectady to Chicago and then to Amherst, Massachusetts, Nick and his family settled in Cambridge, Massachusetts in 1990. There, Nick attended Buckingham Browne & Nichols School, graduating in 1998. He attended Swarthmore College for his undergraduate degree and graduated in 2002 with high honors in both Physics and Computer Science. At Swarthmore, he wrote his honors thesis under the guidance of Professor John Boccio, studying quantum computation. In 2002, he began his graduate work at Cornell, where he has worked with Professor Eberhard Bodenschatz. Nick has wholeheartedly enjoyed his time in Ithaca, which was highlighted by his marriage to Lisa Larrimore on August 21, 2004. In his spare time, Nick enjoys rock climbing, Mahler symphonies, gourmet food, and wine tasting, and he spends altogether too much time obsessing over the Boston Red Sox.

To my grandparents,
Mike and Jean Ouellette and Frank and Dorothy Testroet.

ACKNOWLEDGEMENTS

Science is never done in a vacuum, and the work presented here is no exception.

I am incredibly grateful for the support of my advisor, Eberhard Bodenschatz, whose sheer excitement for science is contagious. He has always helped me understand how our work fits in with that of the broader scientific community. By challenging me to think for myself and allowing me to design my own experiments, he has helped me to become a more self-reliant scientist. I have very much appreciated the opportunity to attend many conferences and meetings; discussing my work with other scientists has been an important part of my graduate career. I will always remember Eberhard's mantra of being proud of my work.

I also owe a huge debt of gratitude to Haitao Xu, without whom my thesis work would never have been finished. Haitao always seemed to know a way to fix whatever problems cropped up in the lab, and he taught me everything I know about error analysis. His independent analysis of our data was invaluable for much of the work in this thesis. Haitao has also graciously taught me diplomacy with his patient comments on seemingly endless paper drafts.

I have been lucky to be a part of a dynamic and supportive group of collaborators here at Cornell. Many thanks to the rest of the Cornell Lagrangian turbulence group: Nicolas Mordant and Alice Crawford, for passing on a (more or less) reliable experiment and their experience in dealing with the kind of mishaps that are inevitable in a lab with large quantities of water; Mickaël Bourgoin, for the excellent control systems on the new experiment and for being my translator in Nice; Jacob Berg, for being a source of constant amusement; Sathya Ayyalaso-mayajula and Armann Gylfason, for putting up with all our noisy computers when we moved into their lab this past year; Andrea Lamorgese, for patiently listening

to our experimental woes throughout endless meetings; Lance Collins and Zellman Warhaft, for sharing their wisdom and experience; and, more recently, Kelken Chang, Matthias Kinzel, Laurent Mydlarski, Holger Nobach, and Dario Vincenzi. Thanks also to the rest of the Bodenschatz group, who have helped create a great working environment: Albert Bae, Carsten Beta, Will Brunner, Stefan and Gisa Luther, Angela Meister, Jon McCoy, Katharina Schneider, Amgad Squires, and Danica Wyatt. Thanks especially to Jon for reading all my paper drafts without complaining and for patiently explaining things to me whenever I had a math question.

I have also benefited a great deal from the kindness of other scientists in the field who have shared their insight and time with me. Many thanks to Guido Boffetta, Antonio Celani, Laurent Chevillard, Bob Ecke, Grisha Falkovich, Julian Hunt, Jakob Mann, Søren Ott, Alain Pumir, Brian Sawford, Jörg Schumacher, Raymond Shaw, Willem van de Water, Richard Wiener, P. K. Yeung, and former Bodenschatz group members Karen Daniels and Greg Voth.

I would never had made it this far without the love and support of my family. Many thanks to my parents, Michael and Helen, for believing in me and always being willing to listen to long-winded descriptions of whatever I'm working on. And, of course, thanks and love to Lisa, my partner in everything.

Finally, none of this research would have been possible without generous funding from both the National Science Foundation and the Max Planck Society.

TABLE OF CONTENTS

Biographical Sketch	iii
Dedication	iv
Acknowledgements	v
Table of Contents	vii
List of Tables	ix
List of Figures	x
1 Introduction	1
2 Theory and Phenomenology	5
2.1 The Governing Equations of Fluid Dynamics	5
2.2 Homogeneous, Isotropic Turbulence and Kolmogorov's Hypotheses .	11
2.3 Beyond K41	15
3 Experimental Techniques	20
3.1 Lagrangian Particle Tracking	20
3.1.1 Particle Finding Problem	24
3.1.2 Stereoscopic Reconstruction	43
3.1.3 Particle Tracking	44
3.2 Time Derivatives	52
3.2.1 Calculation	52
3.2.2 Error Analysis	55
3.3 Apparatus	58
3.3.1 Flow Chamber	59
3.3.2 Illumination	62
3.3.3 Tracer Particles	63
3.3.4 Data Acquisition and Processing	64
3.4 Camera Calibration	66
3.5 Experimental Parameters	71
4 Single Particle Statistics	74
4.1 Velocity and Acceleration	74
4.1.1 Small Measurement Volume	75
4.1.2 Large Measurement Volume	78
4.1.3 Biases	79
4.2 Eulerian Structure Functions	84
4.3 Lagrangian Structure Functions	89
4.3.1 Second Order Structure Functions	91
4.3.2 Higher-Order Structure Functions	104
4.4 Single Particle Dispersion	116
4.5 Multifractals	120

5	Multiparticle Statistics	131
5.1	Turbulent Relative Dispersion	131
5.1.1	The Richardson-Obukhov Law	132
5.1.2	Batchelor's Extension	133
5.1.3	Experimental Results	135
5.1.4	Higher-Order Statistics	147
5.1.5	Distance Neighbor Function	153
5.1.6	Fixed Scale Statistics	161
5.2	Coarse-Grained Models	167
5.2.1	Tetrad Dynamics	168
5.2.2	The Geometry of Turbulence	175
6	Conclusions and Outlook	179

LIST OF TABLES

3.1	Sensor resolution and corresponding maximum framerates for the Phantom v7.1 CMOS camera.	23
3.2	Experimental parameters for the $2 \times 2 \times 2$ cm 3 data runs.	72
3.3	Experimental parameters for the $5 \times 5 \times 5$ cm 3 data runs.	73
4.1	Values of the relative scaling exponents measured in our experiment using ESS.	111
4.2	Values of the absolute scaling exponents measured in our experiment.	112
4.3	Values of C_0 extrapolated to infinite Reynolds number from each of the four independent measurements.	120

LIST OF FIGURES

2.1	The Richardson Cascade	13
3.1	Sample portions of images generated with different intensity profiles.	34
3.2	The effects of particle seeding density.	37
3.3	The effects of particle image size.	39
3.4	The effects of changing the standard deviation of additive white Gaussian noise.	40
3.5	The effects of changing the mean noise level.	42
3.6	Illustration of the four tracking heuristics.	48
3.7	Tracking errors for the eight algorithms tested.	51
3.8	Relative error due to the velocity kernel with no position noise, calculated from DNS data.	57
3.9	Sketch of the turbulence generator, lasers, and cameras.	59
3.10	Decomposition of the large-scale flow into a pumping mode (top) and a shearing mode (bottom).	60
3.11	Sketch of the total mean flow pattern in the flow chamber.	61
3.12	Raw images taken with each of the three cameras at one instant in the flow.	69
3.13	Images of the calibration mask from each of the three cameras. .	70
4.1	Radial velocity PDFs in the $2 \times 2 \times 2 \text{ cm}^3$ measurement volume. .	76
4.2	Axial velocity PDFs in the $2 \times 2 \times 2 \text{ cm}^3$ measurement volume. .	77
4.3	Acceleration PDFs in the $2 \times 2 \times 2 \text{ cm}^3$ measurement volume. .	78
4.4	Radial velocity PDFs in the $5 \times 5 \times 5 \text{ cm}^3$ measurement volume. .	80
4.5	Axial velocity PDFs in the $5 \times 5 \times 5 \text{ cm}^3$ measurement volume. .	81
4.6	Acceleration PDFs in the $5 \times 5 \times 5 \text{ cm}^3$ measurement volume. .	82
4.7	Distribution of track lengths	83
4.8	Second-order Eulerian velocity structure function at $R_\lambda = 815$ measured in the small measurement volume.	87
4.9	Compensated Eulerian structure function at $R_\lambda = 815$	88
4.10	Third-order Eulerian velocity structure function at $R_\lambda = 815$ in the small measurement volume.	89
4.11	Compensated third-order Eulerian velocity structure function at $R_\lambda = 815$	90
4.12	Second-order Lagrangian velocity structure function at $R_\lambda = 815$. .	92
4.13	The xx (■), yy (●), and zz (▼) components of the compensated Lagrangian structure functions at $R_\lambda = 815$	94
4.14	Measurements of C_0 from the Lagrangian structure function tensor for the xx component (■), yy component (●), and zz component (▼) as a function of Reynolds number.	96
4.15	Compensated Lagrangian velocity spectra at $R_\lambda = 690$ in the x direction (■), y direction (●), and z direction (▼).	98

4.16	Measurements from the Lagrangian spectra for the x direction (\blacksquare), y direction (\bullet), and z direction (\blacktriangledown).	100
4.17	Ratio of the C_0 values measured in the radial direction and the C_0 values measured in the axial direction for both the structure function and the spectrum.	103
4.18	Extended self-similarity plot of the high-order Lagrangian structure functions at $R_\lambda = 815$	105
4.19	Anomalous scaling of the structure function relative scaling exponents ζ_p^L/ζ_2^L measured using ESS as a function of order.	107
4.20	PDFs of the Lagrangian velocity increments $\delta u(\tau)$ at $R_\lambda = 690$	109
4.21	PDFs of the moments of the Lagrangian differences at $\tau = 4\tau_\eta$	110
4.22	High order Lagrangian structure functions at $R_\lambda = 690$ compensated by the K41 predictions.	114
4.23	Shift of the effective inertial range as a function of structure function order p	115
4.24	Compensated position correlations at $R_\lambda = 815$	118
4.25	C_0 measured from the position correlations as a function of Reynolds number.	119
4.26	Probabilities $\bar{P}_h(\tau)$ plotted as a function of τ/T_L for seven values of h in logarithmic coordinates.	121
4.27	Direct measurement of the Lagrangian multifractal dimension spectrum.	123
4.28	Scaling exponents ζ_p^L of the Lagrangian structure functions as a function of order.	126
4.29	Comparison of the direct and indirect measurements of the multifractal dimension spectrum.	129
5.1	A pair of measured particle trajectories at $R_\lambda = 690$	136
5.2	Evolution of the mean-square particle separation at $R_\lambda = 815$	137
5.3	Scale collapse of the mean-square particle separation.	138
5.4	Compensated mean-square particle separation.	139
5.5	Compensated mean-square particle separation with time scaled by t_0	139
5.6	Deviation from Batchelor's prediction.	140
5.7	Batchelor's original measure of relative dispersion at $R_\lambda = 815$	141
5.8	Alternative measure of relative dispersion at $R_\lambda = 815$	143
5.9	Applying the time shift of Mann <i>et al.</i> (1999) to our relative dispersion data at $R_\lambda = 815$	144
5.10	Variations of the time shifting procedure of Mann <i>et al.</i> (1999) that show a t^4 power law (top) and a t^5 power law (bottom) when applied to our data.	146
5.11	The Eulerian mixed velocity-acceleration structure function at $R_\lambda = 815$	149

5.12	Longitudinal (\bullet) and transverse (∇) scaling constants for the Eulerian mixed velocity-acceleration structure function as a function of Reynolds number.	150
5.13	Trace of the Eulerian mixed velocity-acceleration structure function as a function of Reynolds number.	151
5.14	The same data from Fig. 5.5 shown with the Batchelor prediction augmented with the third-order correction (solid line).	152
5.15	Plots of the distance neighbor function for different initial separations at $R_\lambda = 815$	157
5.16	Plots of the distance neighbor function for different initial separations at $R_\lambda = 200$	159
5.17	Plots of the distance neighbor function at $R_\lambda = 815$ calculated without subtracting the initial separation.	160
5.18	Average exit times at $R_\lambda = 815$	163
5.19	Average exit times with the initial separation subtracted at $R_\lambda = 815$	163
5.20	The Richardson constant computed from the exit times with the initial separation subtracted at $R_\lambda = 815$	164
5.21	The Richardson constant computed from the exit times without subtracting the initial separation at $R_\lambda = 815$	165
5.22	Average exit times at $R_\lambda = 200$	166
5.23	The Richardson constant computed from the exit times at $R_\lambda = 200$	167
5.24	PDF of all tetrads in the phase space spanned by Q and R at $R_\lambda = 815$	172
5.25	PDF of initially nearly isotropic tetrads at $R_\lambda = 815$	174
5.26	The shape evolution of the nearly isotropic tetrads at $R_\lambda = 815$, as characterized by the eigenvalues of \mathbf{g}	176
5.27	The shape evolution of the full ensemble of tetrads at $R_\lambda = 815$, as characterized by the eigenvalues of \mathbf{g}	178

Chapter 1

Introduction

Turbulence is the normal state of fluid flow in the world around us. It is manifest in simple flows like a stirred cup of coffee or the flow of water through a pipe as well as in more complex flows like hurricanes or ocean currents. Due to its prevalence, it is perhaps surprising that a full understanding of turbulence still eludes us. In 1963, Feynman *et al.* wrote

... There is a physical problem that is common to many fields, that is very old, and that has not been solved. It is not the problem of finding new fundamental particles, but something left over from a long time ago—over a hundred years. Nobody in physics has really been able to analyze it mathematically satisfactorily in spite of its importance to the sister sciences. It is the analysis of circulating or turbulent fluids... We cannot analyze the weather. We do not know the patterns of motions that there should be inside the earth. The simplest form of the problem is to take a pipe that is very long and push water through it at high speed. We ask: to push a given amount of water through that pipe, how much pressure is needed? No one can analyze it from first principles and the properties of water. If the water flows very slowly, or if we use a thick goo like honey, then we can do it nicely. You will find that in your textbook. What we really cannot do is deal with actual, wet water running through a pipe. That is the central problem which we ought to solve some day, and we have not.

Feynman's words remain true today: despite the fact that turbulence is commonplace in a host of scientific fields, we still lack a complete understanding of the subject. This is not to say that no progress has been made in the past forty years; on the contrary, our understanding of the phenomenology of turbulence has grown considerably. New experimental techniques have been developed that allow us to

measure aspects of turbulence that were thought impossible to observe a mere fifteen years ago. Experimental facilities themselves have taken great leaps forward, allowing us to probe more and more intense turbulence in the laboratory. The advent of fast, inexpensive computers has opened up a huge array of possibilities for simulation and modeling. New turbulence models based on fractal and multifractal geometry seem to capture something fundamental. Yet even with these advances, we still lack a truly complete theoretical understanding of the subject.

For many years, turbulence and fluid dynamics in general have been overlooked by the physics community and have been considered to be purely engineering topics. Over the past decade or so, though, physicists have again become interested in the problem. Perhaps the most intriguing aspect of turbulence to a physicist is its putative universality. Turbulence is incredibly complex and highly chaotic, involving a huge range of length and time scales. We instinctively recognize the complexity of turbulence, as is evident from, for example, our appreciation of artistic representations of clouds and other turbulent flows (Warhaft, 2002). And yet even with all this complexity, ever since the pioneering work of Kolmogorov a significant body of evidence has accumulated that suggests that the small-scale structure of turbulence is independent of how the turbulence is generated. We are therefore hopeful that the dynamics of turbulent flows can be described in a unified framework that may be simpler than the governing equations, which, as Feynman points out, we cannot solve except in very special circumstances.

Despite these advances, several fundamental questions remain open and unanswered. Many of these questions deal with understanding the connection between different descriptions of turbulence that should be complementary but that currently seem disparate. For example, it is most common in turbulence research to

consider a statistical description of the subject where the scaling behavior of averaged quantities are studied. We also know, however, that turbulent flows abound with coherent structures, such as vortex tubes that mix the small and large scales of the flow, the ramp and cliff structures in the concentration of a passive scalar advected with the flow (Shraiman and Siggia, 2000), or the horseshoe vortices that appear in turbulent boundary layers. We do not currently know how to connect the statistical description of turbulence with a description in terms of these coherent structures, but it seems likely that both will be needed to give us a complete understanding of turbulence. Perhaps new statistical geometry models, like those we discuss in Chapter 5, may someday be able to bridge this gap.

Also fundamental to turbulence, as well as to fluid dynamics in general, is an understanding of the connection between the Eulerian and Lagrangian frameworks. In the Eulerian framework, fluid-dynamical quantities are defined relative to a fixed, external coordinate system. In the Lagrangian framework, however, quantities are defined relative to the trajectories of individual parcels of fluid that deform and move throughout the entire flow field. Eulerian measurements have traditionally been far easier to perform in the laboratory, and so much of what we know about turbulence is Eulerian. For many theoretical approaches to fluid dynamics, however, the Lagrangian framework is far more natural, and so corresponding Lagrangian measurements are needed. Only when we have a complete picture of Lagrangian turbulence comparable to the wealth of knowledge we have of the Eulerian description can we fully understand the mapping between the two frameworks.

Lagrangian measurements have only recently become possible in the the laboratory, due to advances both in imaging technology and machine vision. In this

thesis, we present a series of experimental Lagrangian measurements of the turbulent velocity as well as the simultaneous multipoint statistics of several fluid elements using a Lagrangian particle tracking technique.

The organization of this thesis is straightforward. In Chapter 2, we present a brief overview of the theory of turbulence as it is known today. We begin by deriving the governing equations, and then discuss why they are difficult to solve in turbulence. We then present an overview of Kolmogorov's seminal scaling theory that has dominated turbulence modeling for the past sixty years, as well as some of the fractal ideas that are currently being used to extend this scaling theory.

In Chapter 3, we present the techniques we have used to measure Lagrangian statistics, including an overview of the various particle tracking algorithms in use today in fluid dynamics. Chapter 4 then discusses the statistics of single fluid elements in our experiment. After a brief discussion of the probability density functions of the turbulent velocity and acceleration, we move on to the two-point Eulerian and Lagrangian structure functions and the related problem of the dispersion of a single fluid element. Finally, we discuss our measurements of the multifractal dimension spectrum of Lagrangian turbulence.

In Chapter 5, we move on to the simultaneous statistics of multiple fluid elements. We focus primarily on the relative dispersion of pairs of fluid elements, but also present some measurements of the dynamics of clusters of four particles known as tetrads.

Finally, in Chapter 6, we summarize the results presented in this thesis, and discuss future measurements that can complement and extend the conclusions of this work.

Chapter 2

Theory and Phenomenology

2.1 The Governing Equations of Fluid Dynamics

The equations of motion for a fluid are inherently more complex than those of a rigid body. Since each individual element of fluid is deformable, the internal motion must be accounted for in determining bulk properties of the flow. This leads to two complementary frameworks for describing a fluid. In the Eulerian framework, the fluid is described relative to a set of coordinates fixed with respect to a laboratory reference frame. In contrast, the Lagrangian description of fluid flow considers the motion of individual fluid elements and computes quantities in local coordinate systems pinned to the fluid elements. As an example, consider a scalar field ϕ . In the Eulerian framework, we can represent this field as $\phi^E(\mathbf{x}, t)$ where \mathbf{x} is a coordinate relative to the laboratory frame. The same field can be represented in the Lagrangian framework as $\phi^L(\mathbf{y}, t)$ where \mathbf{y} labels the position of a fluid element at $t = 0$ with respect to the laboratory frame. At $t = 0$, $\phi^E(\mathbf{a}, 0) = \phi^L(\mathbf{a}, 0)$ for some position \mathbf{a} . At $t' \neq 0$, however, $\phi^L(\mathbf{a}, t')$ refers to the field value not at the laboratory coordinate \mathbf{a} but instead at the position in space where the fluid element that was at \mathbf{a} at $t = 0$ is located at $t = t'$. The two representations of the field refer to the same point in space if

$$\phi^L(\mathbf{y}, t) = \phi^E(\mathbf{x}(\mathbf{y}, t), t), \quad (2.1)$$

where $\mathbf{x}(\mathbf{y}, t)$ is the position of the fluid element at time t that was at \mathbf{y} at $t = 0$.

This equivalence has consequences for time derivatives of fluid dynamical quanti-

ties. Taking the time derivative of eq. (2.1), we have

$$\frac{d\phi^L}{dt} = \frac{\partial\phi^E}{\partial t} + \frac{\partial\mathbf{x}}{\partial t} \cdot \nabla\phi^E, \quad (2.2)$$

where we have used the chain rule. Since, from eq. (2.1), $\phi^E = \phi^L$ and is arbitrary, the differential operators in eq. (2.2) must be equivalent. This operator is known as the material or substantive derivative, and measures the rate of change of a quantity following a fluid element. The material derivative is represented as D/Dt , and is given by

$$\frac{D}{Dt} = \frac{\partial}{\partial t} + \mathbf{u} \cdot \nabla \quad (2.3)$$

since $\partial\mathbf{x}/\partial t = \mathbf{u}$, the fluid velocity.

Similar arguments must also be used when deriving conservation laws for fluids. Such laws can usually be expressed in terms of the flux through a control surface or volume. In a fluid system, however, control surfaces and volumes are not fixed but can move and deform. These effects are captured by the Reynolds Transport Theorem, which states in three dimensions that

$$\frac{d}{dt} \int_{\mathcal{V}(t)} \psi d\mathcal{V} = \int_{\mathcal{V}(t)} \left[\frac{\partial\psi}{\partial t} + \nabla \cdot (\mathbf{u}\psi) \right] d\mathcal{V}, \quad (2.4)$$

where the integrals run over a time dependent control volume $\mathcal{V}(t)$ and ψ is an arbitrary (tensor) field. Let us now apply this theorem to the conservation of mass. We take $\psi = \rho$, the mass density. The left hand side of the Transport Theorem then gives the rate of change of the total mass present in the control volume, which must be zero if mass is conserved. We therefore have

$$\frac{\partial\rho}{\partial t} + \nabla \cdot (\rho\mathbf{u}) = 0. \quad (2.5)$$

If the density of the fluid is constant in time and uniform in space, this equation reduces to

$$\nabla \cdot \mathbf{u} = 0, \quad (2.6)$$

defining an incompressible fluid.

The Reynolds Transport Theorem may also be used to derive the equation of motion for the velocity field of an incompressible fluid. Letting ψ in eq. (2.4) be $\rho\mathbf{u}$, the momentum density in the fluid, we have that

$$\begin{aligned}\frac{d}{dt} \int_{\mathcal{V}(t)} \rho u_j d\mathcal{V} &= \int_{\mathcal{V}(t)} \left[\frac{\partial \rho u_j}{\partial t} + \frac{\partial u_i \rho u_j}{\partial x_i} \right] d\mathcal{V} \\ &= \int_{\mathcal{V}(t)} \rho \frac{Du_j}{Dt} d\mathcal{V},\end{aligned}\quad (2.7)$$

where we have used the continuity equation (2.5) and summation is implied over repeated indices. The left hand side of this equation is simply the rate of change of the momentum of the fluid. Using Newton's second law, this must be equal to the force on the fluid. Neglecting forces external to the fluid, we therefore have

$$\frac{d}{dt} \int_{\mathcal{V}(t)} \rho u_j d\mathcal{V} = \int_{\mathcal{S}(t)} n_i \tau_{ij} d\mathcal{S} = \int_{\mathcal{V}(t)} \frac{\partial \tau_{ij}}{\partial x_i} d\mathcal{V}, \quad (2.8)$$

where $\mathcal{S}(t)$ is a control surface, n_i is a unit vector normal to that surface, and τ_{ij} is the stress tensor for the fluid. The last equality follows from the tensor form of Gauss's Theorem. For an incompressible Newtonian fluid, the stress tensor is given by

$$\tau_{ij} = -p\delta_{ij} + \mu \left[\frac{\partial u_i}{\partial x_j} + \frac{\partial u_j}{\partial x_i} \right], \quad (2.9)$$

where p is the pressure and μ is the dynamic viscosity. Putting these equations together, using the fact that the control volume \mathcal{V} is arbitrary, and again using continuity, we arrive at

$$\frac{Du_j}{Dt} = \frac{\partial u_j}{\partial t} + u_i \frac{\partial u_j}{\partial x_i} = -\frac{1}{\rho} \frac{\partial p}{\partial x_j} + \nu \frac{\partial^2 u_j}{\partial x_i \partial x_i}, \quad (2.10)$$

where $\nu = \mu/\rho$ is the kinematic viscosity and is assumed to be constant and uniform. Together, eq. (2.10) and eq. (2.6) are the celebrated Navier-Stokes equations that govern the flow of incompressible Newtonian fluids.

There are several notable aspects of eq. (2.10). First and foremost, due to the presence of the convective term in the material derivative, the Navier-Stokes equations are nonlinear. Because of this, analytical solutions of the Navier-Stokes equations exist only for a handful of special cases. In addition to the nonlinearity, the highest order derivative in the equations is in the viscous term. Because the kinematic viscosity of a typical Newtonian fluid is so small, however, the magnitude of this term, which necessitates an additional boundary condition, can be orders of magnitude smaller than the inertial terms in the equations.

As written in eq. (2.10), both the viscosity and the density of the fluid appear in the equations. By rewriting the equations in a nondimensional form, however, the first hints of possible universality emerge. By picking suitable length and velocity scales \mathcal{L} and \mathcal{U} and denoting dimensionless variables with tildes, we can rewrite the Navier-Stokes equations in nondimensional form as

$$\frac{\partial \tilde{u}_j}{\partial \tilde{x}_j} = 0 \quad (2.11)$$

$$\frac{\partial \tilde{u}_j}{\partial \tilde{t}} + \tilde{u}_i \frac{\partial \tilde{u}_j}{\partial \tilde{x}_i} = -\frac{\partial \tilde{p}}{\partial \tilde{x}_j} + \left(\frac{\nu}{\mathcal{U}\mathcal{L}} \right) \frac{\partial^2 \tilde{u}_j}{\partial \tilde{x}_i \partial \tilde{x}_i}. \quad (2.12)$$

It is now clear that there is only a single parameter in the equations. This nondimensional ratio, known as the Reynolds number and defined as

$$\text{Re} = \frac{\mathcal{U}\mathcal{L}}{\nu}, \quad (2.13)$$

is of central importance in fluid dynamics and especially in turbulence. The Reynolds number represents the ratio of the inertial and viscous forces in the Navier-Stokes equations (Batchelor, 1967). When the Reynolds number is smaller than unity, viscous forces dominate the dynamics, and the flow is laminar and smooth. When the Reynolds number is larger than unity, however, the nonlinear inertial forces dominate the dynamics and the flow becomes turbulent and chaotic.

For flows with an externally imposed geometry, relevant velocity and length scales used to define the Reynolds number are readily apparent. In a pipe flow, for example, the length scale is usually taken to be the pipe diameter and the velocity scale to be the mean velocity. Boundaries, however, impose additional complexity for studying turbulence. For this reason, research in turbulence has focussed on the case of statistically homogeneous, isotropic flows. In homogeneous turbulence, flow statistics do not depend on the absolute location in space: only relative spatial coordinates are relevant. Likewise, in isotropic turbulence statistics are independent of global rotations. It follows, then, that a homogeneous, isotropic flow can have no boundaries. There are therefore no externally imposed scales with which to define the Reynolds number. Instead, intrinsic scales are used. The velocity scale is taken to be the standard deviation of the velocity field, u' . A length scale L , known as the integral length scale, is determined by integrating the velocity autocorrelation function. The resulting Reynolds number $\text{Re}_L = u'L/\nu$ is therefore based purely on the statistics of the turbulence. For historical reasons, an additional Reynolds number based on the Taylor microscale λ is often used, and is given by

$$R_\lambda = \frac{u'\lambda}{\nu} = \sqrt{15\text{Re}_L}. \quad (2.14)$$

As mentioned above, high Reynolds number flows are turbulent, and the motion of individual fluid elements is chaotic. The hallmark of chaos is an extreme sensitivity to initial conditions, and turbulence is no exception. Even if there were a general solution to the Navier-Stokes equations, then, any prediction of the subsequent fluid evolution would require the specification of the initial and boundary conditions to a precision unfeasible for any practical application. Just as in many other branches of physics and engineering, we are therefore forced into a statistical

description of turbulence.

The statistical approach, however, brings its own new difficulties to the problem. As an example, let us consider the equation of motion for the mean velocity field, the simplest statistical description of a flow. In order to arrive at this equation, we simply take the mean of eqs. (2.6) and (2.10), where the symbol $\langle \cdot \rangle$ denotes an ensemble average. The continuity equation is unchanged, since differentiation commutes with the averaging:

$$\nabla \cdot \langle \mathbf{u} \rangle = 0. \quad (2.15)$$

The momentum equations, however, are not as simple. We have

$$\frac{\partial \langle u_j \rangle}{\partial t} + \frac{\partial \langle u_i u_j \rangle}{\partial x_i} = -\frac{1}{\rho} \frac{\partial \langle p \rangle}{\partial x_j} + \nu \frac{\partial^2 \langle u_j \rangle}{\partial x_i \partial x_i}, \quad (2.16)$$

where we have used the continuity equation to rewrite the nonlinear term. This equation contains the quantity $\langle u_i u_j \rangle$, which is not trivially related to the mean velocity field. Since any quantity can be decomposed into the sum of its mean value and the fluctuations about the mean, we can write

$$u_i = \langle u_i \rangle + u'_i, \quad (2.17)$$

where we have used a prime to indicate the fluctuation. In turbulence, this is known as the Reynolds decomposition (Pope, 2000). The nonlinear term may then be rewritten as

$$\begin{aligned} \langle u_i u_j \rangle &= \langle [\langle u_i \rangle + u'_i][\langle u_j \rangle + u'_j] \rangle \\ &= \langle u_i \rangle \langle u_j \rangle + \langle u'_i u'_j \rangle, \end{aligned} \quad (2.18)$$

since the mean of a fluctuation is zero. Inserting this result into eq. (2.16), we arrive at

$$\frac{\partial \langle u_j \rangle}{\partial t} + \frac{\partial \langle u_i \rangle \langle u_j \rangle}{\partial x_i} = -\frac{1}{\rho} \frac{\partial \langle p \rangle}{\partial x_j} + \nu \frac{\partial^2 \langle u_j \rangle}{\partial x_i \partial x_i} - \frac{\partial \langle u'_i u'_j \rangle}{\partial x_i}. \quad (2.19)$$

These equations are known as the Reynolds Averaged Navier-Stokes (RANS) equations, and are a basic tool in computational fluid dynamics. The most important feature of the RANS equations is the appearance of the final term on the right hand side that involves the correlation of the velocity fluctuations, known as the Reynolds stress. In the RANS formulation, we have four equations (the continuity equation and the equations of motion of the three components of the mean velocity), just as in the total Navier-Stokes equations. Unlike the Navier-Stokes equations, however, which had four unknowns (the pressure and the three components of velocity), the RANS equations are underdetermined. The Reynolds stress adds an extra six unknowns to the system with no corresponding new equations. This type of difficulty is referred to as a closure problem, and is ubiquitous in the statistical description of fluid flow. Modeling of the extra unknowns is required to close the equations of motion, and is therefore of central importance in constructing a practical, useful description of turbulence.

2.2 Homogeneous, Isotropic Turbulence and Kolmogorov's Hypotheses

By far the most important and influential model of turbulence is that of A. N. Kolmogorov. Usually referred to simply as K41 theory, Kolmogorov's 1941 phenomenological model is based on a handful of physically-motivated hypotheses with surprisingly far-reaching consequences. We note that due to the difficulties inherent in dealing with boundaries, K41 theory applies only to homogeneous, isotropic turbulence. In addition, we consider only the fluctuations about the mean velocity, since these fluctuations are the signature of turbulence.

The dynamics of a turbulent flow at scales larger than the integral length scale L are flow-specific. For smaller scales, however, the flow is thought to become statistically universal, and the details of how the turbulence was generated are washed away. Classically, the small scale flow is modeled as a cascade process, an idea first put forward by Richardson (1922). Consider a coherent structure in the flow of a size comparable to L , which we loosely term an eddy. In the cascade model, energy is fed to this structure by the non-universal large scales of the flow at a rate ϵ , where ϵ is typically taken to be a power per unit mass. This eddy is, however, short-lived: due to turbulent fluctuations, it breaks up into smaller eddies. In the cascade model, this process is presumed to occur with no loss of energy. These smaller eddies in turn break up into yet smaller eddies, until finally they are small enough that molecular viscosity can play a role in their dynamics and dissipate the turbulent energy into heat, again at the same rate ϵ . At scales where energy is dissipated, the flow relaminarizes. The Richardson cascade is illustrated schematically in Fig. 2.1, and is expressed well in Richardson's (1922) famous rhyme:

“Big whirls have little whirls,
That feed on their velocity;
Little whirls have lesser whirls,
And so on to viscosity.”

Underlying the cascade model are assumptions of locality of scale and perfect self-similarity (Frisch, 1995). Each eddy is assumed to have contact only with those directly larger and smaller than it. Small eddies are merely swept along by large eddies without being influenced by the large scale motion. In addition, eddies are assumed to break up into essentially identically smaller copies of themselves.

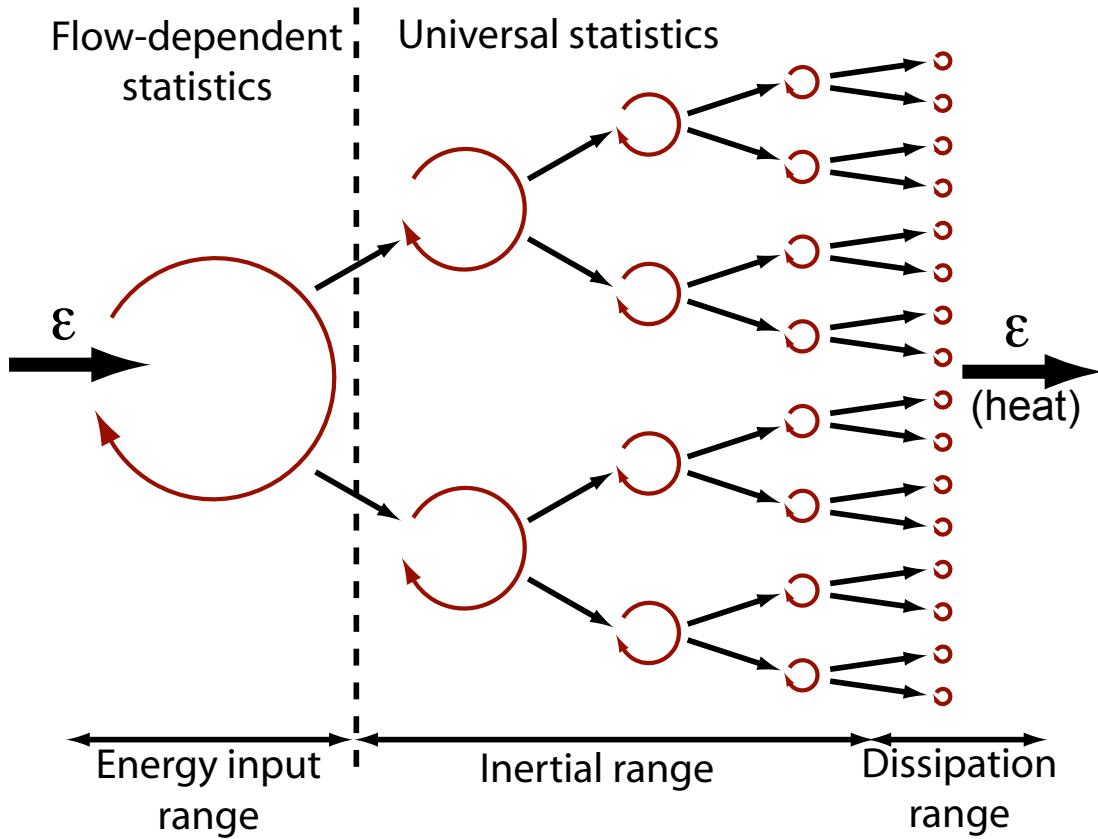


Figure 2.1: The Richardson cascade. Energy from the large scale flow is injected into eddies at the integral scale L at a rate ϵ . These large eddies break up into smaller eddies, which break up further until they are small enough that molecular viscosity can dissipate the turbulent energy into heat. Above the integral scale, statistics are flow dependent. In the inertial and dissipation ranges, however, statistics are universal regardless of how the turbulence is generated.

Kolmogorov (1941a) incorporated these ideas into his similarity hypotheses and was able to make the cascade model predictive.

Strictly applicable only in the limit of infinite Reynolds number, the Kolmogorov (1941a) similarity hypotheses are

1. **Hypothesis of Local Isotropy.** At scales small compared to the integral length scale L and far away from any boundaries, turbulence is statistically homogeneous and isotropic.
2. **First Similarity Hypothesis.** At scales very small compared to L , turbulence statistics have a universal form determined *only* by the viscosity ν and the energy dissipation rate ϵ . The regime is termed the “dissipation range.”
3. **Second Similarity Hypothesis.** At scales small compared to L but large compared to the dissipation scale, turbulence statistics have a universal form determined *only* by the dissipation rate ϵ . This regime is known as the “inertial range.”

When coupled with dimensional analysis and the theory of isotropic tensors, the Kolmogorov hypotheses allow the prediction of scaling laws for many of the quantities of interest in turbulence. K41 theory can also be used to define the smallest scales of turbulent motion. In the cascade model, the smallest turbulent scales are those where energy is dissipated by viscous forces. According to the first similarity hypothesis, such scales can only depend on the viscosity and the dissipation rate. Using dimensional analysis, then, we define the Kolmogorov length scale η , time scale τ_η , and velocity scale u_η as

$$\eta \equiv \left(\frac{\nu^3}{\epsilon} \right)^{1/4} \quad \tau_\eta \equiv \left(\frac{\nu}{\epsilon} \right)^{1/2} \quad u_\eta \equiv \frac{\eta}{\tau_\eta} = (\epsilon \nu)^{1/4}. \quad (2.20)$$

We then expect that, statistically, the flow at scales smaller than the Kolmogorov scales is laminar. This is borne out by the fact that the Reynolds number based on the Kolmogorov scales, $R_\eta = u_\eta \eta / \nu$, is unity.

As discussed above, the cascade model, and therefore K41 theory, is local in scale. Therefore, the similarity hypotheses can only be applied to statistics that are similarly local (Batchelor, 1950). It is difficult to determine *a priori* whether a given quantity is local in scale. A general rule of thumb, however, is that differences are local in scale while products are not. As an example, consider the Eulerian velocity correlation function $R_{ij}(r) = \langle u_i(x+r)u_j(x) \rangle$. This tensor mixes velocities of all scales, and therefore K41 cannot be applied to it. Indeed, measurements of $R_{ij}(r)$ show that it decays approximately exponentially with r , while K41 theory always predicts power laws. Let us consider instead the correlation function of the velocity differences, $D_{ij}(r) = \langle [u_i(x+r)-u_i(x)][u_j(x+r)-u_j(x)] \rangle = \langle \delta u_i(r)\delta u_j(r) \rangle$, better known as the Eulerian structure function. Since it involves only velocity differences, this tensor is local in scale. As will be discussed in detail in Chapter 4.2, K41 predicts that, in the inertial range, this tensor should be only a function of r and the dissipation rate ϵ . Therefore,

$$D_{ij}(r) \sim (\epsilon r)^{2/3}, \quad (2.21)$$

since $D_{ij}(r)$ has units of velocity squared. This power law scaling is well-confirmed experimentally (Sreenivasan, 1995).

2.3 Beyond K41

Classical K41 theory, as described above, is elegant in its simplicity and its great utility in generating scaling laws for turbulence statistics. Over the past several

decades, however, experiments have made it clear that some of the basic tenets of the K41 model are violated in real turbulence. A hallmark of turbulent flow is its “bursty” nature: turbulence is characterized by short-lived but extremely intense fluctuations of its dynamical quantities. In particular, consider the rate of energy dissipation rate ϵ . The classical K41 model assumes in the Second Similarity Hypothesis that $\langle \epsilon \rangle$, the mean value of the dissipation rate, is sufficient to characterize the statistics of inertial range turbulence. As pointed out by Landau (Frisch, 1995), however, unless ϵ is constant, $\langle \epsilon^p \rangle \neq \langle \epsilon \rangle^p$ and therefore the mean rate of energy dissipation is insufficient to characterize turbulence. This phenomenon is termed intermittency. Intermittency is a general feature in nonlinear dynamical systems, though in turbulence the term has come to refer purely to the large fluctuations of the dissipation rate.

In response to Landau’s comment, Kolmogorov (1962) introduced the Refined Similarity Hypothesis, where, based on physical reasoning, he assumed that the probability density function (PDF) of ϵ was log-normal. Using this form for the PDF, he was able to calculate the difference between $\langle \epsilon^p \rangle$ and $\langle \epsilon \rangle^p$ explicitly, finding that

$$\frac{\langle \epsilon^p \rangle_r}{\epsilon^p} \sim r^{-\frac{1}{2} \mu p(p-1)}, \quad (2.22)$$

where the average is taken over a volume of linear scale r . In analogy with his K41 model, Kolmogorov’s intermittency model is known simply as K62. Subsequent experiments, however, showed that the predictions of the Refined Similarity Hypothesis are also not correct (Anselmet *et al.*, 1984), suggesting that ϵ is not log-normally distributed. The true PDF of the dissipation rate has proved very difficult to measure experimentally. Researchers have therefore turned to a reinterpretation of the Richardson cascade using fractal ideas (Mandelbrot, 1974; Parisi

and Frisch, 1985).

Classical K41 theory assumes that when an eddy in the cascade breaks up, the smaller eddies it forms occupy the same amount of space as the parent eddy. Furthermore, it is assumed that the turbulent eddies participating in the cascade occupy the full volume of turbulent fluid. The dimension of the space occupied by the eddies is therefore three. But now suppose that when a parent eddy breaks up, its child eddies do not occupy the same amount of space. In this case, the eddies will fill only a subspace of the volume of turbulent fluid. Let us suppose that the space filled by the cascade is characterized by a non-integer fractal dimension D . This line of reasoning leads to straightforward corrections to K41 scaling laws: if we consider turbulence statistics at scale r , we must simply weight the corresponding K41 scaling law by a factor expressing the probability that the point of interest in the fluid lies in a turbulent eddy of scale r . This probability factor is given by

$$P_r = \left(\frac{r}{L}\right)^{3-D}, \quad (2.23)$$

where L is the integral length scale, a measure of the size of the maximal volume of fluid the cascade can occupy (Frisch, 1995). More generally, for turbulence in a d -dimensional space, we have

$$P_r = \left(\frac{r}{L}\right)^{d-D}, \quad (2.24)$$

where $d - D$ is known as the codimension. This monofractal model of turbulence is known as the β -model.

To illustrate the use of the β -model, we again turn to the Eulerian structure function, following Frisch (1995). Consider the energy at scale r , which we denote by E_r . Using dimensional analysis and the probability factor P_r , we have

$$E_r \sim u_r^2 P_r = u_r^2 \left(\frac{r}{L}\right)^{3-D}, \quad (2.25)$$

where u_r is the velocity at scale r . The flux of energy to smaller scales is given by $E_r/t_r \sim u_r^3 P_r/r$, but is also given by $\epsilon \sim u'^3/L$, where u' is the large scale root-mean-square (RMS) velocity. Therefore, equating these two relations, we have

$$u_r \sim u' \left(\frac{r}{L} \right)^{\frac{1}{3} - \frac{3-D}{3}} \equiv u' \left(\frac{r}{L} \right)^h, \quad (2.26)$$

where h controls the scaling of u_r with r/L . We can now write down the the β -model scaling law for the Eulerian structure function of order p as

$$\langle \delta u(r)^p \rangle \sim u_r^p P_r \sim u'^p \left(\frac{r}{L} \right)^{hp+3-D}. \quad (2.27)$$

The β -model does not capture the behavior of real turbulence (Anselmet *et al.*, 1984), but is the basis for the multifractal model that captures the phenomenology of turbulence better than any other current model. As a first step, let us consider a bifractal model. In this case, the turbulent eddies are described not by a single fractal dimension but by two, and therefore by two different values for h . A given eddy breaking up will choose to follow the scaling law given by one of the fractal dimensions with probability μ . The bifractal scaling law for the Eulerian structure function is then given by

$$\frac{\langle \delta u(r)^p \rangle}{u^p} \sim \mu_1 \left(\frac{r}{L} \right)^{h_1 p + 3 - D_1} + \mu_2 \left(\frac{r}{L} \right)^{h_2 p + 3 - D_2}. \quad (2.28)$$

The jump to a multifractal model is straightforward. We now assume that the cascade chooses its dynamics from a continuous set of fractal dimensions $D(h)$ indexed by a scaling exponent h that lies in the set $I = (h_{min}, h_{max})$. Extrapolating from the bifractal case, the scaling law for the Eulerian structure function becomes an integral over all values of h :

$$\frac{\langle \delta u(r)^p \rangle}{u^p} \sim \int_{h \in I} d[\mu(h)] \left(\frac{r}{L} \right)^{hp+3-D(h)}. \quad (2.29)$$

As in K41 theory, we suppose that $\langle \delta u_r^p \rangle \sim r^{\zeta_p^E}$. In the inertial range, where this model should be valid, $r \ll L$, and so the smallest exponent in the integral will dominate. Therefore, we have

$$\zeta_p^E = \inf_h [hp + 3 - D(h)]. \quad (2.30)$$

This expression is a Legendre transform between the parameters p and h , and in principle may be inverted to give

$$D(h) = \inf_p [ph + 3 - \zeta_p^E], \quad (2.31)$$

although this is difficult to apply experimentally due to the, in general, poor determination of the ζ_p^E for a wide range of p (Frisch, 1995). We note that in the multifractal model, both I and $D(h)$ are *a priori* unknown, but are presumed to be universal for all turbulent flows, regardless of the large-scale flow structure.

Chapter 3

Experimental Techniques

3.1 Lagrangian Particle Tracking

Almost everything that is known about turbulence is derived from Eulerian measurements, where probes are fixed with respect to a laboratory reference frame. Eulerian measurement techniques have become very robust, and standard techniques are well-known. The workhorse of Eulerian measurement devices is the hot wire anemometer, introduced as early as 1909 (King, 1914). In its most basic form, the hot wire anemometer consists of a small metal wire heated by the application of a voltage. As the fluid sweeps past the wire it advects away heat, requiring the adjustment of the applied voltage in order to regulate the wire temperature. King (1914) worked out the relation between the applied voltage and the fluid velocity. Hot wire anemometry is well suited to measurements in gas flows, and is the standard tool for wind tunnel measurements. Hot wires do not work well, however, in liquid flows.

A whole host of new Eulerian measurement techniques is opened up by the addition of neutrally buoyant passive tracer particles to the flow. This is, in general, easier to accomplish in liquid flows rather than gas flows, but some techniques do exist for creating passive tracers for gas flows as well (Poulain *et al.*, 2004). One elegant technique for making Eulerian measurements in a flow seeded with tracers is Laser Doppler Anemometry (LDA), also referred to as Laser Doppler Velocimetry (LDV). LDA uses the coherence of laser light to make direct measurements of the fluid velocity. By focussing two laser beams on a small spot in the flow, they will interfere and produce a fringe pattern. When a tracer particle (and ideally

only one at a time) passes through the measurement volume, it produces a burst of flickering reflected light. The frequency of the flickering of this reflected light depends only on the wavelength of the laser light and the crossing angle of the beams, both known quantities, as well as the velocity of the particle normal to the fringes. Measuring the flicker frequency therefore directly gives a single component of the particle velocity. By using multiple pairs of beams, all three components of the Eulerian velocity can be measured simultaneously.

Seeding a flow with passive tracers is also the basis for the Eulerian technique Particle Image Velocimetry (PIV). PIV has become a very popular tool in industry and in the engineering community, and is well suited to characterizing complex mean flow patterns or microfluidic flows, where the effects of turbulence are minimal. The tracer particles are illuminated by a laser sheet and a camera is used to take two images of the flow spaced very closely in time. By assuming that nearby particles move similarly, average velocity vectors for groups of particles are estimated, usually from the cross-correlation of the two images (Adrian, 1991). PIV usually measures only two components of the velocity, though stereoscopic and holographic PIV systems have been developed to measure all three velocity components (Hinsch and Hinrichs, 1996).

Eulerian measurements have been very important in the development of the theory of turbulence, but a complete understanding of turbulence is not possible without corresponding Lagrangian information. Lagrangian measurements require identifying individual fluid elements and measuring flow statistics along their trajectories. Although some progress has been made in tagging and following true fluid elements (Pashtrapanshka and van de Water, 2005), passive tracer particles similar to those used in LDA and PIV are commonly employed as approximations

of true fluid elements. The motion of these tracers may then be followed to extract Lagrangian trajectories, a technique known as Lagrangian Particle Tracking (LPT). It is common to use several detectors in LPT system, in order to resolve all three components of the motion of the particles.

LPT systems have been designed using many different types of detectors. In the present work, we image the tracer particles optically. Acoustic LPT methods have also been used (Mordant *et al.*, 2001), though they measure the particle velocity directly and must integrate the velocity tracks to find the particle positions. For geophysical flows, Lagrangian tracers may be tracked by radio beacons, radar (Hanna, 1981), or the Global Positioning System.

In general, there are three algorithmic components of an optical LPT system. First, individual particles must be identified in the image space of each detector. Next, the two-dimensional information from each detector must be combined to generate 3D information for each particle coordinate. Finally, the motion of the particles must be tracked in time. The last two steps may be logically interchanged; there are, however, good reasons for presenting them in this order, as will be discussed below.

Optical LPT systems have been used for many years. The first such systems consisted of photographs of tracer particles that were analyzed by hand (Chiu and Rib, 1956). Modern optical LPT systems use digital cameras and process the images using computer algorithms to accomplish the LPT tasks outlined above. Most such digital cameras, however, are not fast enough to resolve the fastest time scales of the turbulent motion at high Reynolds numbers. Previously, the Bodenschatz research group has adapted the silicon strip detectors used in the vertex detectors in high energy particle accelerators to the LPT problem, with

Table 3.1: Sensor resolution and corresponding maximum framerates for the Phantom v7.1 CMOS camera.

Sensor Resolution (pixels)	Maximum Framerate (Hz)
800×600	4800
512×512	8300
512×384	10900
320×384	13500
240×320	24400
256×256	27000
256×128	47600
128×128	68500
64×64	121000
32×32	160000

excellent results (La Porta *et al.*, 2001; Voth *et al.*, 2001, 2002). Unfortunately, these detectors are only one-dimensional and can measure only a single particle at a time. Therefore, despite the strip detectors' data rate of up to 70 kHz, in the present work we have used the Phantom v7.1 high-speed CMOS digital cameras manufactured by Vision Research, Inc. These cameras also have very fast data rates, as shown in Table 3.1, and using the algorithms described below can be used to track hundreds of tracers simultaneously.

There is no agreement in the LPT community as to the optimal algorithms to use for accurate, efficient data processing. We have undertaken a quantitative study of many existing LPT algorithms, and have introduced new methods as well, as described in Ouellette, Xu, and Bodenschatz (2006a). Below, we describe the

tests of the various algorithms in detail. We begin with algorithms to determine the positions of the tracers on the detector, continue with a description of the algorithm we use for stereomatching of the images from multiple cameras, and finally present algorithms for particle tracking itself.

3.1.1 Particle Finding Problem

The accuracy of an LPT system depends crucially on the precision with which the tracer particles can be identified in the camera images. In general, it is sufficient to determine the coordinates of the particle centers. An ideal particle finding algorithm must meet several criteria:

1. *Sub-pixel accuracy.* When the particle images cover several pixels, the center of the particle may be found to within a fraction of a pixel.
2. *Speed.* Due to the extremely high data rate from the detectors necessary for the measurement of an intensely turbulent flow, a particle finding algorithm must be efficient and fast.
3. *Overlap handling.* When the images of multiple particles overlap on a single detector plane, it becomes more difficult to determine the particle centers. A good particle finding algorithm must remain effective for locating the centers of clusters of overlapping particle images.
4. *Robustness to noise.* Even the best cameras have some background noise in the images. A particle finding algorithm must locate the particle centers accurately even for moderate noise levels.

It is common to assume that every local maximum in image intensity above some threshold corresponds to a particle, and we make this assumption in this

analysis. The simplest method, then, for determining a particle center is simply to pick the center of this local maximum pixel. This method is certainly fast, can handle overlap, and is moderately robust to noise. The accuracy of this method, however, is very poor: no sub-pixel resolution is possible. Many classes of more intelligent algorithms have been proposed, including weighted averaging schemes (Maas *et al.*, 1993; Maas, 1996; Doh *et al.*, 2000), function fitting (Cowen and Monismith, 1997; Mann *et al.*, 1999), and template matching (Guezennec *et al.*, 1994), as well as the standard PIV technique of image cross-correlation (Adrian, 1991; Westerweel, 1993). Template matching suffers if all particle images are not the same size, and is suitable only for experiments using laser sheets to illuminate their tracers. Since we illuminate three-dimensional volumes of the flow, we shall not consider template matching algorithms. Cross-correlation techniques are more suited to very densely seeded flows, and so we shall also not consider them. Below, we shall compare a weighted averaging algorithm with both one- and two-dimensional Gaussian fitting and a neural network-based technique. We shall first discuss the algorithms being tested in more detail.

Description of Algorithms

Weighted averaging is a very simple technique, and is therefore widely employed in LPT systems. Camera images must first be segmented into contiguous groups of bright pixels, representing ideally single particles. The coordinates (x_c, y_c) of the center of the pixel group are then determined by averaging the positions of all the pixels in the group weighted by their intensity grey values. More precisely, if we let $I(x, y)$ be the intensity of the pixel at (x, y) , x_c is given by

$$x_c = \frac{\sum_p x_p I(x_p, y_p)}{\sum_p I(x_p, y_p)}, \quad (3.1)$$

similar to the determination of the center of mass of a cluster of point masses. y_c is defined similarly.

In the analysis presented here, we use a variant of the weighted averaging procedure due to Maas and co-workers (Maas *et al.*, 1993; Maas, 1996) that includes improved handling of overlapping particle images. As mentioned above, we assume that every local intensity maximum above a threshold represents a particle. Therefore, when segmenting the camera image into groups of contiguous active pixels for averaging, we assume that a group of pixels with N intensity maxima contains N particles. Maas's algorithm includes a preprocessing step that further segments such pixels groups into N subgroups, each containing only a single intensity maximum. The subgroups are divided by assuming that the intensity of the pixels in a particle image should fall off monotonically as the distance from the particle center increases. Local intensity minima are arbitrarily assigned to the contiguous subgroup containing the brightest local maximum.

This weighted averaging scheme is very efficient and simple to implement, and has some capability for handling overlapping particle images. As we will show below, however, both the accuracy of this algorithm and its robustness to noise are poor compared to the other algorithms tested.

If we know the functional form of the intensity profile of the particle images on the detector, a fit of this function to the image would produce a very accurate determination of the particle center. *A priori*, however, the functional form is not known. Instead, it is common to approximate it as a Gaussian (Mann *et al.*, 1999). We begin by segmenting the image into pixel groups as above for the weighted averaging scheme, and then use the Levenberg-Marquardt algorithm (Press *et al.*,

1992) to fit the function

$$I(x, y) = \frac{I_0}{2\pi\sigma_x\sigma_y} \exp \left\{ -\frac{1}{2} \left[\left(\frac{x - x_c}{\sigma_x} \right)^2 + \left(\frac{y - y_c}{\sigma_y} \right)^2 \right] \right\}, \quad (3.2)$$

where σ_x and σ_y are the Gaussian widths in the horizontal and vertical directions.

If a pixel group contains N local maxima, we simply fit the sum of N Gaussians to the group.

This method is very accurate and handles overlap well. It is, however, significantly more computationally intensive than the other methods studied, taking approximately a factor of four more time in our tests. Additionally, this 2D Gaussian fit requires large particle images. Inspection of eq. (3.2) shows that each Gaussian requires the determination of five parameters, namely the overall intensity I_0 , the widths σ_x and σ_y , and the centers x_c and y_c . At minimum, then, the pixel group must contain at least $5N$ pixels for a fit to be possible, and more for the fit to be accurate. Small particle images must then either be ignored or processed with a different method.

A more efficient and less demanding approximation of a full 2D Gaussian fit can be accomplished by using instead two 1D Gaussians (Cowen and Monismith, 1997). We fit single 1D Gaussians to the horizontal pixel coordinates and the vertical coordinates in turn. Each Gaussian has only three fit parameters, as opposed to the five needed by the 2D Gaussian, and so smaller particle image sizes are sufficient. In addition, unlike in the 2D case, we can find an analytical solution for the particle center based on only the local maximum pixel and its closest horizontal and vertical neighbors. Labeling the horizontal pixel coordinates x_1 , x_2 , and x_3 , where x_2 is the coordinate of the local maximum, we can solve the system

of equations

$$I_i = \frac{I_0}{\sqrt{2\pi}\sigma} \exp \left[-\frac{1}{2} \left(\frac{x_i - x_c}{\sigma_x} \right)^2 \right] \quad (3.3)$$

for $i = 1, 2, 3$ to give

$$x_c = \frac{1}{2} \frac{(x_1^2 - x_2^2) \ln(I_2/I_3) - (x_2^2 - x_3^2) \ln(I_1/I_2)}{(x_1 - x_2) \ln(I_2/I_3) - (x_2 - x_3) \ln(I_1/I_2)}. \quad (3.4)$$

The vertical coordinate of the particle center is defined analogously. This 1D Gaussian Estimator retains much of the accuracy of the 2D Gaussian fit but at only a fraction of the computational cost. The image segmentation step required for the 2D fit can be omitted, and only the particle center needs to be computed, with the fit parameters I_0 , σ_x , and σ_y left undetermined. Additionally, inspection of eq. (3.4) shows that the coordinates of the particle centers depend only on the coordinates of the three pixels used in the fit and the natural logarithms of the pixel intensities. Since the cameras are digital, however, the pixel intensities are quantized, and therefore all necessary logarithms may be precomputed once and used for the determination of all the particle centers. Use of the 1D Gaussian Estimator therefore requires only a few multiplications, and is therefore very efficient.

In addition to the algorithms described above, we have also developed a neural network-based approach to the particle finding problem. Neural networks are a class of machine learning algorithms based on a crude model of the human brain, and hope to exploit some of the same properties that make the brain such a powerful computer. The brain can be viewed as a massively parallel computational network consisting of roughly 10^{11} interconnected neurons that is capable of, among other things, learning and generalization. A neural network is constructed similarly, consisting of many interconnected nodes arranged in layers. In the machine learning and artificial intelligence community, neural networks are known to be

very effective in pattern matching and classification applications. In general, a neural network can be applied to a problem when the function to be evaluated (or “learned” by the network) has a fixed number of inputs and outputs that can be normalized to fall in a known range, when valid input/output pairs may be generated for training, when a slow one-time learning period is acceptable, and when fast evaluation of the function may be necessary. Within these general criteria, neural networks are very flexible. The function to be learned may be discrete-, real-, or vector-valued, or some combination. The input/output pairs used for training the network may contain errors, and the resulting networks are usually very robust to noise in the input data. It is important to note, however, that due to the complexity of a fully trained neural network, the programmer will in general not understand what function the network is evaluating. When such understanding is not required, and when the criteria above are fulfilled, neural networks can be very powerful tools.

Formally, a neural network is a directed, acyclic graph. The nodes of the graph, termed “neurons” in analogy with the brain, may have input connections only (output neurons), output connections only (input nodes), or both (hidden neurons). Every edge in the graph has an associated weight w represented by a real number with $-1 \leq w \leq 1$. “Training” the network refers to adjusting the weights in order to produce the desired output.

A neural network is specified by three pieces of information: the graph topology, the neuron activation function, and the training algorithm used. Neurons are arranged in layers. Every network will contain both an input layer and an output layer, and may contain one or more hidden layers. Input information is fed into the input layer, and the evaluated function values are read from the output layer.

Hidden layers allow the network to perform complex tasks.

The neuron activation function maps the input value of a given neuron to its output value. The simplest activation function is a step function. Let us consider a neuron with N input connections labeled x_1 to x_N . Each input connection also carries an edge weight w_i , where i ranges from 1 to N . Then the step function activation is given by

$$o(x_1, \dots, x_N) = \begin{cases} 1, & \sum_{i=1}^N w_i x_i \geq 0 \\ -1, & \sum_{i=1}^N w_i x_i < 0 \end{cases}. \quad (3.5)$$

Training such a neuron is simple. For each training cycle, the weights of all the input edges are updated as

$$w_i \leftarrow w_i + \Delta w_i, \quad (3.6)$$

where Δw_i is given by

$$\Delta w_i = \eta(t - o)x_i. \quad (3.7)$$

Here t denotes the target output and o the neuron output. η is a constant known as the learning rate that controls how much the network can change over one training iteration. Such a simple neuron is known as a perceptron, and can exactly represent, for example, any Boolean function (Mitchell, 1997).

For more complex functions, however, more complex networks are required. In particular, networks where the activation function is linear in the input values, such as that described above for perceptrons, can only represent linear function. For nonlinear problems, we must use nonlinear activation functions. A common choice is a sigmoid function,

$$o(x_1, \dots, x_N) = \frac{1}{1 + \exp\left(-\sum_{i=1}^N w_i x_i\right)}. \quad (3.8)$$

In addition, we can introduce one more hidden layers, that further enhance the nonlinear capabilities of the network. In general, continuous functions may be approximated arbitrarily well by networks with a single hidden layer, while arbitrary function may be represented with only two hidden layers (Mitchell, 1997), a result that follows from work of Kolmogorov (1957).

With complex networks, we must specify more complex training procedures. The standard training algorithm for such multilayer networks is the backpropagation algorithm. Let us define the total network error as the sum of the errors of each individual output neuron for all the training examples, given by

$$E(w_1, \dots, w_N) = \frac{1}{2} \sum_{d \in D} \sum_{k \in \text{outputs}} (t_{kd} - o_{kd})^2, \quad (3.9)$$

where N is the number of output neurons, D is the set of all training examples, and k runs over the set of output neurons. The backpropagation algorithm then proceeds as follows, for each training example (x_i, t_i) . First, the input values x_i are fed into the network, and an output value o_u is computed for each neuron u . Next, an error δ_k is calculated for each output neuron k , given by

$$\delta_k = o_k(1 - o_k)(t_k - o_k). \quad (3.10)$$

This error is then propagated back through the network and an error is calculated for each hidden neuron h , given by

$$\delta_h = o_h(1 - o_h) \sum_k w_{kh}\delta_k. \quad (3.11)$$

Finally, the edge weights are updated as

$$w_{ji} \leftarrow w_{ji} + \Delta w_{ji}, \quad (3.12)$$

where Δw_{ji} is given by

$$\Delta w_{ji} = \eta \delta_j x_{ji}, \quad (3.13)$$

which amounts to a gradient descent method for finding a local minimum in the error surface, a method justified by Bayes' Theorem. Since gradient descents are susceptible to becoming stuck on flat surfaces or local minimum, a "momentum" term is often added to the standard backpropagation algorithm. Equation (3.13) then becomes

$$\Delta w_{ji}(n) = \eta \delta_j x_{ji} + \alpha \Delta w_{ji}(n - 1), \quad (3.14)$$

where α is the momentum and n indexes the training iteration. For more information on neural networks, the reader is referred to Mitchell's (1997) book.

Neural networks have been applied to both the particle tracking problem (Grant and Pan, 1997; Chen and Chwang, 2003; Labonté, 1999, 2001) and the stereo-matching problem (Grant *et al.*, 1998) before. Carosone *et al.* (1995) applied the Kohonen neural network to the problem of distinguishing images of isolated particles from those of overlapping particles. In the present work, we solve the particle finding problem completely using a neural network.

The network used sigmoid neurons arranged in an input layer of 81 neurons, a single hidden layer of 60 neurons, and an output layer of two neurons. The input to the network was a 9×9 pixel subwindow of the camera image centered on a local intensity maximum. The two output neurons report the horizontal and vertical coordinates of the particle center. By asking the network to find only single particles at a time, the problem of fixing the number of inputs and outputs was solved. If the network had been fed the entire camera image, the number of outputs would not be known. In addition, the network was trained to find particles near the center of the window, so that overlap could be handled simply by centering the window on each local maximum in turn. The 9×9 pixel window was chosen so that full particle images would definitely be contained in the window;

small changes to the size of this window should not affect the performance of the network. The network was trained using the backpropagation algorithm described above augmented with a momentum term.

Training the network is a slow operation, but subsequent computation of the particle centers is fast. The network handles cases of overlap well. As will be shown below, the network is also very robust to noise, as is generally the case with neural networks.

Tests of the Algorithms

A quantitative test of the four particle finding algorithms presented above is not possible without images where the true positions of the particle centers are known. This requirement precludes the use of real experimental images for testing purposes. Instead, we have generated synthetic images computationally. This approach also allows us to study the effects of changing different aspects of the images rigorously and independently.

Images were generated assuming one of two intensity profiles for the particle images. The assumed intensity profile was discretized by integrating over each pixel, just as the true intensity profile would be.

The two intensity profiles used in these tests were a Gaussian and an Airy pattern. Gaussian profiles are often used in tests of particle finding algorithms, introducing a bias towards Gaussian fitting routines. The true intensity profile is, however, most likely well approximated by a Gaussian (Westerweel, 1993; Cowen and Monismith, 1997). To mitigate the effects of any bias we have also used Airy patterns. Generated by diffraction from a circular aperture, the Airy pattern is given by $(J_1(r)/r)^2$, where $J_1(r)$ is the cylindrical Bessel function of order 1 and r

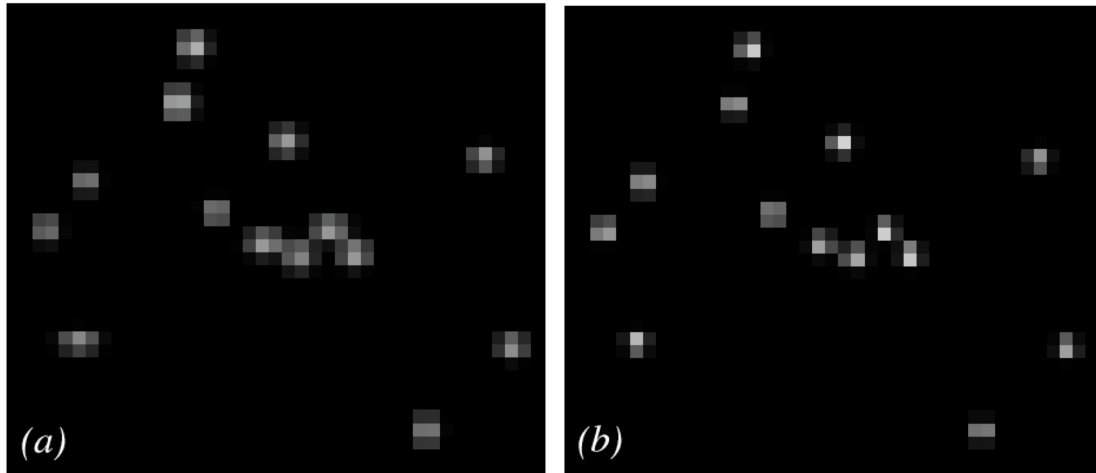


Figure 3.1: Sample portions of images generated with different intensity profiles. Image (a) used Gaussian intensity profiles, while image (b) used Airy pattern profiles.

is the distance from the particle center. The ratio of the Gaussian width and the radius of the first peak of the Airy pattern was fixed at 0.524 to equalize the energy in the 2D Gaussian and the first peak of the 2D Airy pattern. By equalizing the energy rather than the width of the two intensity profiles, we ensure that they are very different, and thus better for testing the performance of the various algorithms under very different conditions.

Images were generated on a 256×256 pixel grid, the same size images as were used in our actual experiment. Each pixel intensity was stored as an 8 bit greyscale value, for a total of 256 possible intensity grey values. In every case, the particle intensity maxima were sampled from a Gaussian distribution centered at 180. Portions of an image generated with Gaussian intensity profiles and Airy patterns are shown in Fig. 3.1. For some sets of images, additive white Gaussian noise was introduced into the images. The central limit theorem suggests that Gaussian noise should be a good approximation for the noise in real images, after

all the many possible sources of image noise are compounded.

The neural network described above was trained only on images with Gaussian intensity profiles, in an attempt to make their baseline performance comparable to the Gaussian fitting routines. Other characteristics of the training images, including particle seeding density, particle image size, and noise levels, were varied.

In order to quantify the performance of the four algorithms, errors were calculated by finding the difference between the true particle centers and the calculated centers for the horizontal and vertical components independently. The distributions of these errors were symmetric with mean zero in all cases, and the distributions for the horizontal and vertical components were identical, showing no bias. For the purpose of comparing the algorithms as a function of the image parameters, we define a parameter Δ given by

$$\int_{-\Delta/2}^{\Delta/2} P(x)dx = 0.8, \quad (3.15)$$

where $P(x)$ is the PDF of the error as a function of the distance x from the true particle center. Δ measures the radius of the circle around the true particle center containing 80% of the measured errors. In addition to measuring the errors of the algorithms, we have also measured the yield of the algorithms, defined as the ratio of identified particles to the total number of particles in the image.

Four aspects of the particle images were tested independently. The results of varying the particle seeding density from 150 particles per image to 600 particles per image are shown in Fig. 3.2. For this test, the particle image half-width was fixed at 0.8 pixels. No noise was added to these images.

Increasing the seeding density increases the likelihood of particle overlap, making the particle finding problem more difficult. Since overlapping particle images are significantly more difficult to handle than isolated particles, the accuracy should

decrease as the seeding density increases. As seen in Fig. 3.2, this is indeed the case, although the error increase is only moderate. The two Gaussian fitting algorithms performed almost equally well while the weighted averaging algorithm performed by far the poorest. The neural network method fell in between the other three in terms of accuracy. In addition, we note that the accuracy of the two Gaussian fitting methods and the neural network method decreased when Airy pattern intensity profiles were used. The accuracy of the weighted averaging method, however, was actually improved when applied to the Airy pattern images. This may because the strong central peak of the Airy pattern weighted the central pixel more heavily than the Gaussian intensity profile.

Focusing on the error only suggests that a seeding density of 600 particles per 256×256 pixel image is acceptable for LPT. The yield, however, drops very quickly as the seeding density increases, as shown in Fig. 3.2, dropping as low as 68% for the weighed averaging method. For this reason, for the rest of the simulated images used we considered a seeding density of only 300 particles per image, given that all four algorithms maintained a yield of over 90% at this seeding density.

As with increasing the seeding density, larger particle images lead to more overlap and therefore a more difficult problem. On the other hand, larger particle images provide more information to the center finding algorithm, and can therefore lead to increased accuracy. A balance must be struck between these two effects.

In Fig. 3.3 we show the performance of the four algorithms as a function of particle image size. As mentioned above, the number of particles per image was fixed at 300, and no noise was added to any of these images.

For the data sets using Gaussian intensity profiles, the error showed a minimum at a half-width between 0.7 and 0.9 pixels for both of the Gaussian fitting methods

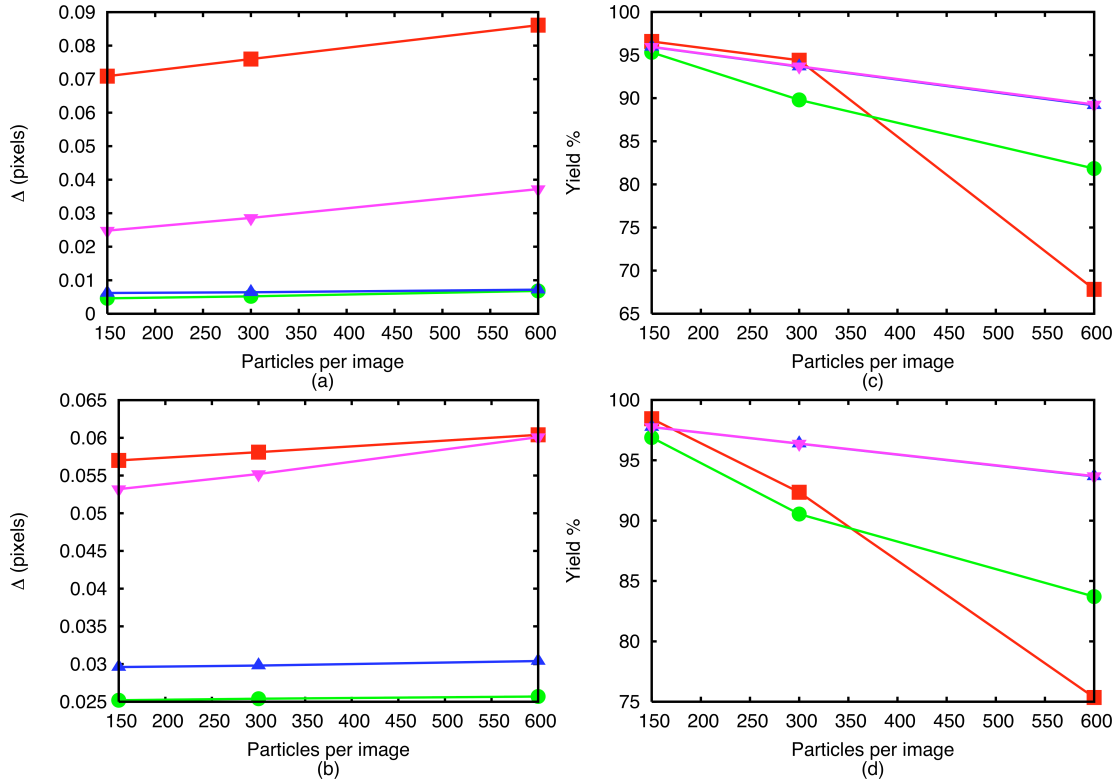


Figure 3.2: The effects of particle seeding density. The error of the four algorithms increases with the number of particles in each 256×256 pixel image for both Gaussian intensity profiles (a, c) and Airy pattern profiles (b,d). The yield of the algorithms shows a stronger dependence on particle seeding density. Symbols: ■ Weighted Averaging; ● 2D Gaussian Fit; ▲ 1D Gaussian Estimator; ▼ Neural Network.

and for the neural network. The behavior of the weighted averaging algorithm is more varied. The peak in error at a particle image half-width of 0.7 pixels may perhaps be explained by the introduction of significant levels of overlap while at the same time maintaining very small clusters of pixels in each particle image.

Different behavior is seen for the images generated with Airy pattern intensity profiles. For the two Gaussian fitting methods, the error peaked at about 0.8 pixels, and decreased for larger particle images. This may perhaps be explained by considering that larger Airy patterns appear more Gaussian around their peaks. The neural network and weighted averaging methods have a similar peak in error, though at larger particle sizes. In addition, both algorithms performed significantly worse on very small particle images. We also note that the weighted averaging method gave better results when applied to the particle images generated with Airy patterns, as found above as a function of particle seeding density.

After testing the performance of the four algorithms on noiseless images, we fixed the particle image half-width at 0.8 pixels and the seeding density at 300 particles per image and added noise to the simulated camera images. In a real LPT system, noise will be introduced into the images in the form of errors from the camera sensor, thermal noise in the electronics, shot noise in the detection of the photons scattered from the tracer particles, and many other sources. The central limit theorem states that as all the various noise sources are compounded, the distribution of the noise will approach a Gaussian. For that reason, we have chosen to apply additive white Gaussian noise to our simulated images.

By fixing the mean of the added noise at zero and varying the standard deviation of the noise, we have tested the sensitivity of the four algorithms to fluctuations in the noise level, shown in Fig. 3.4. As expected, as the standard deviation

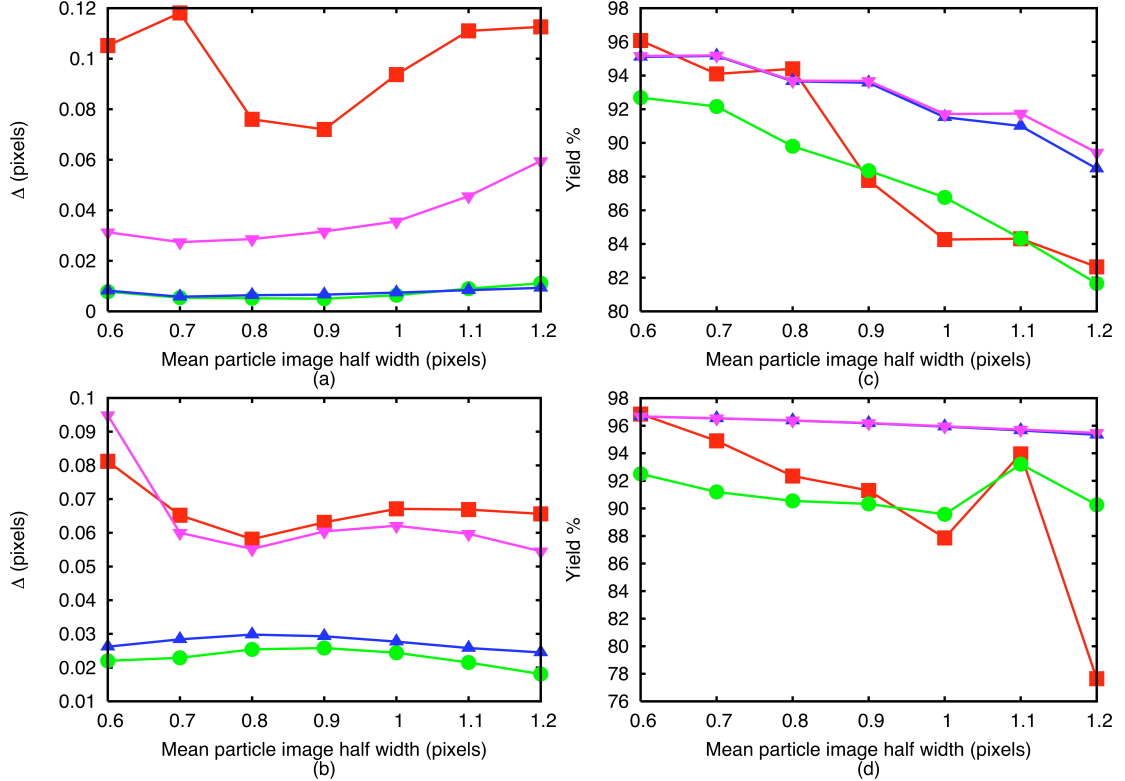


Figure 3.3: The effects of particle image size on the four algorithms. Plots (a) and (c) were generated with Gaussian intensity profiles, while plots (b) and (d) were generated with Airy pattern profiles. Symbols: ■ Weighted Averaging; ● 2D Gaussian Fit; ▲ 1D Gaussian Estimator; ▼ Neural Network.

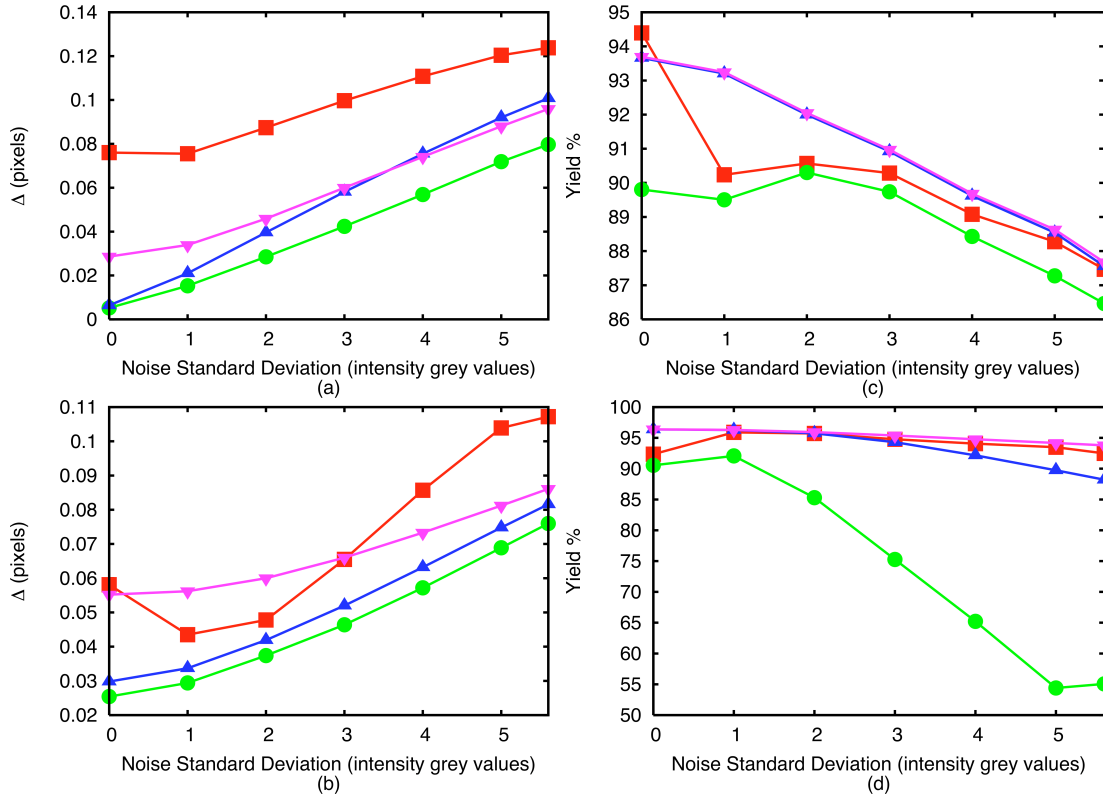


Figure 3.4: The effects of changing the standard deviation of additive white Gaussian noise. For Gaussian intensity profiles, the Neural Network performs nearly as well as the 2G Gaussian Fit algorithm for both Gaussian intensity profiles (a, c) and Airy pattern profiles (b, d) while maintaining high yields as the standard deviation of the noise increases. Symbols: ■ Weighted Averaging; ● 2D Gaussian Fit; ▲ 1D Gaussian Estimator; ▼ Neural Network.

of the noise was increased, both the accuracy and the yield of all the algorithms decreased. The yield of the 2D Gaussian fit algorithm dropped very quickly with noise level when Airy pattern intensity profiles were used. We note, however, that the performance of the neural network degraded slower than that of the other algorithms, beating the 1D Gaussian estimator for high noise levels and Gaussian intensity profiles and nearly matching both Gaussian methods for Airy pattern intensity profiles.

In addition to varying the standard deviation of the noise, we have also fixed the noise fluctuations and varied the mean noise level, corresponding to changing the level of background noise. We have fixed the noise standard deviation at 5.6, corresponding to 2.5 bits of noise, a typical value in our cameras. The performance of the four algorithms as a function of mean noise is shown in Fig. 3.5.

The weighted averaging method and both Gaussian fitting methods showed sensitivity to the mean noise level, though less than they had to the noise standard deviation. The neural network, however, showed almost no changes as the mean noise was increased when Gaussian intensity profiles were used, and only a slow degradation when Airy pattern intensity profiles were used. Coupled with its slow degradation as a function of noise standard deviation, the neural network is significantly more robust to noise than the other algorithms tested.

We may draw several conclusions from the analysis presented above. In all cases, the weighted averaging algorithm is significantly less accurate than the other three algorithms tested. Given that it is also no faster or easier to implement than the 1D Gaussian Estimator, it should not be used in LPT systems. The 1D Gaussian Estimator is also preferable to the 2D Gaussian fit. The two algorithms have comparable accuracy, but the 1D Gaussian Estimator runs at least a factor of four faster and has a higher yield of correctly found particles in all cases.

While the 1D Gaussian Estimator also outperformed the neural network in the absence of noise, the network was far more robust to both changes in mean background noise and to noise fluctuations. We also note that the performance of the neural network was roughly the same when applied to images generated with Gaussian intensity profiles, which the network had been trained on, and images generated with Airy pattern intensity profiles. It is therefore reasonable to assume

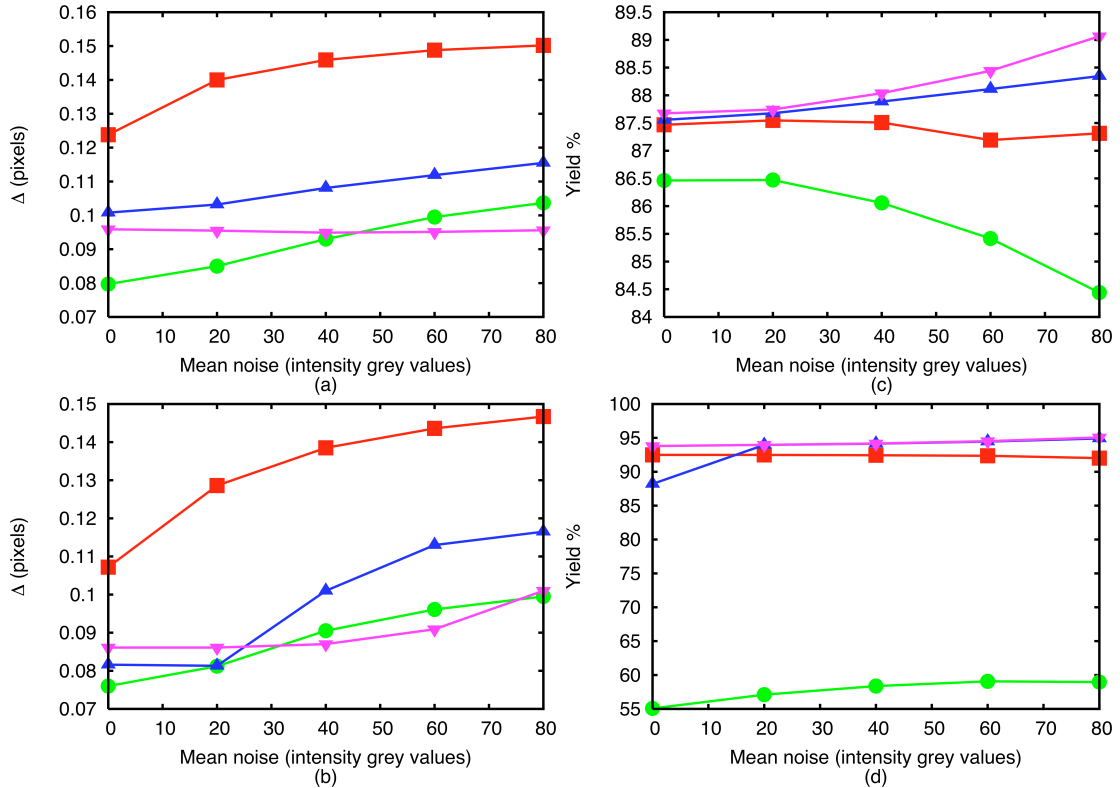


Figure 3.5: The effects of changing the mean noise level. While the Weighted Averaging and both Gaussian algorithms lose accuracy as the mean background noise increases, the Neural Network is almost unaffected for both Gaussian intensity profiles (a, c) and Airy pattern profiles (b, d). Symbols: ■ Weighted Averaging; ● 2D Gaussian Fit; ▲ 1D Gaussian Estimator; ▼ Neural Network.

that the network can properly generalize to finding particles in real images when trained on synthetic images.

Since the noise levels in our cameras are very low, we have chosen to use the 1D Gaussian Estimator to locate the particle centers in the camera images, and we conservatively estimate that the algorithm can find the true particle centers to within 0.1 pixels. In LPT systems with higher noise levels, however, the neural network scheme would be preferable.

3.1.2 Stereoscopic Reconstruction

After determining the 2D coordinates of the particles on each of the camera image planes, a stereomatching process must be used to reconstruct the 3D coordinates of the particles in the laboratory reference frame. In an LPT experiment, the tracer particles have no distinguishing features that can be used to aid in this reconstruction. Instead, the only information that can be used is the photogrammetric condition that, for each camera, the camera projective center, the particle coordinates on the image plane, and the particle coordinates in the laboratory frame must be collinear (Maas *et al.*, 1993). Furthermore, these lines of sight from all the cameras will intersect at the true location of the particle.

Ambiguities can arise in this stereomatching process if multiple particles lie on the same line of sight. This case will arise more frequently when the density of particles in the measurement volume is high. Employing more cameras will help alleviate this problem. Dracos (1996) has shown that for a reasonable particle seeding density, at least three cameras are needed in order to resolve these ambiguities.

The stereomatching algorithm we use is based on those of Dracos (1996) and

Mann *et al.* (1999). Consider a particle image p_i on one detector. As described above, we can project a line of sight from the perspective center of the camera through the particle image. We then in turn project this line of sight onto the image planes of the other cameras. Particle images on these images planes that fall within some tolerance ϵ are considered possible matches to p_i . In this fashion, a list of possible matches for p_i is constructed for every other camera in the system. This process is then repeated for every particle image on every detector. The lists are then checked for consistency, and the 3D coordinates are found.

3.1.3 Particle Tracking

After both finding the 2D positions of the tracer particles and stereomatching them to find the full 3D positions, the particles must be tracked in time. In its most general form, the problem of tracking many particles over many frames is a multidimensional assignment problem. Such multidimensional assignment problems are known to be NP-hard for more than two dimensions (Veenman *et al.*, 2003). There is therefore no known tractable algorithm for solving the full problem. Particle tracking algorithms are instead forced to approximate the optimal solution of the full assignment problem by restricting the temporal scope of the tracking, considering only a few frames at a time.

Let \mathbf{x}_i^n denote the i^{th} particle position in the n^{th} frame. A tracking algorithm attempts to find an \mathbf{x}_j^{n+1} for each \mathbf{x}_i^n such that \mathbf{x}_j is the position of the particle in frame $n + 1$ that was at the position \mathbf{x}_i in frame n . In order to make this match correctly, we define a cost ϕ_{ij}^n for each pair of \mathbf{x}_j^{n+1} and \mathbf{x}_i^n . This cost is one of the quantities that differentiates tracking algorithms. In general, the optimal solution to the tracking problem will be given by creating links between the \mathbf{x}_j^{n+1} and \mathbf{x}_i^n

so that the total cost

$$\Phi = \sum_n \sum_i \sum_j \phi_{ij}^n \quad (3.16)$$

is minimized. As discussed above, however, the full solution is intractable, and so we restrict range of n , minimizing the cost for only a few frames at a time. This type of approximation is generally known as a greedy matching approximation (Veenman *et al.*, 2001). A different class of algorithms employs iterative schemes, attempting to minimize the total cost Φ by making an initial guess at the proper links and then swapping pairs of links in an attempt to find a better solution (Sethi and Jain, 1987; Ohmi and Li, 2000). These iterative schemes work well for some simpler machine vision problems, but are unsuitable for LPT due to the desired long particle tracks.

In addition to restricting the number of frames considered at a time, most tracking algorithms also restrict the \mathbf{x}_j^{n+1} considered for each \mathbf{x}_i^n by imposing a limit on the distance a particle can travel from one frame to the next.

Within these approximations, a tracking algorithm is specified by the number of frames considered at a time, the heuristic used to calculate the cost ϕ_{ij}^n and the method used to break tracking conflicts. A conflict occurs whenever the same particle in frame $n + 1$ is the best match for multiple particles in frame n . These conflicts do not, in general, stem from overlapping particle images, since we track in 3D: overlapping images will have been resolved by the stereomatching algorithm.

In the present work, we consider four different tracking heuristics and two types of conflict breaking. In general, particle tracking heuristics depend on particular properties of the tracer particles, such as velocity and acceleration, changing smoothly and slowly. We describe the individual tracking heuristics tested below, and illustrate them in Fig. 3.6. We note that many of these tracking heuristics

rely on sections of partially completed track; in all cases, the first two frames were matched together using the Nearest Neighbor algorithm.

1. *Nearest Neighbor (NN)*. The tracking cost is given by the distance between the point in frame n and the point in frame $n + 1$, namely

$$\phi_{ij}^n = \|\mathbf{x}_j^{n+1} - \mathbf{x}_i^n\|. \quad (3.17)$$

2. *3 Frame: Minimum Acceleration (3MA)*. The position of the particle in frame $n - 1$ is used along with the position in frame n to estimate a local velocity for the particle, which is then used to extrapolate an estimated position $\tilde{\mathbf{x}}_i^{n+1}$ for the particle in frame $n + 1$, given by

$$\tilde{\mathbf{x}}_i^{n+1} = \mathbf{x}_i^n + \tilde{\mathbf{v}}_i^n \Delta t, \quad (3.18)$$

where $\tilde{\mathbf{v}}_i^n$ is the estimated velocity and Δt is the time elapsed between frames.

The tracking cost,

$$\phi_{ij}^n = \frac{\|\mathbf{x}_j^{n+1} - 2\mathbf{x}_i^n + \mathbf{x}_i^{n-1}\|}{2\Delta t^2}, \quad (3.19)$$

is calculated for all the possible matches falling in some search volume surrounding the estimate, and is given by the estimated particle acceleration (Malik *et al.*, 1993; Dracos, 1996).

3. *4 Frame: Minimum Change in Acceleration (4MA)* The expected position of the particle in frame $n + 1$ is estimated in the same fashion as in the 3MA algorithm. For each particle in the search volume in frame $n + 1$, a position $\tilde{\mathbf{x}}_i^{n+2}$ in frame $n + 2$ is estimated kinematically as

$$\tilde{\mathbf{x}}_i^{n+2} = \mathbf{x}_i^n + \tilde{\mathbf{v}}_i^n(2\Delta t) + \tilde{\mathbf{a}}_i^n(2\Delta t)^2. \quad (3.20)$$

A new search volume around this position is created, and particles in this volume are investigated. The tracking cost is given by the change in acceleration from frame $n + 1$ to frame $n + 2$ (Malik *et al.*, 1993; Dracos, 1996), namely

$$\phi_{ij}^n = \frac{1}{2\Delta t^2} \left\{ \|\mathbf{x}_j^{n+2} - 2\mathbf{x}_j^{n+1} + \mathbf{x}_i^n\| - \|\mathbf{x}_j^{n+1} - 2\mathbf{x}_i^n + \mathbf{x}_i^{n-1}\| \right\}. \quad (3.21)$$

4. 4 Frame: Best Estimate (4BE) This new algorithm is similar to the 4MA algorithm in structure, but with a different cost function. Instead of attempting to estimate the change in acceleration, a third derivative, we simply use the distance between the real particles in frame $n + 2$ and the estimated position, so that

$$\phi_{ij}^n = \|\mathbf{x}_j^{n+2} - \tilde{\mathbf{x}}_i^{n+2}\|. \quad (3.22)$$

Conflicts were handled in two different ways. The simplest method for resolving tracking conflicts is simply to give up: when a conflict occurs, the involved tracks are simply halted at frame n , and a new track is created starting in frame $n + 1$. This solution guarantees that a tracking conflict will not lead to an incorrect match. Conflicts may also be handled, however, by choosing the set of links from frame n to $n + 1$ that minimizes the total frame-to-frame cost $\sum_{ij} \phi_{ij}^n$ (Veenman *et al.*, 2001). This task, a two-dimensional assignment problem, may be solved efficiently using the Munkres Algorithm for non-square matrices, given by Bourgeois and Lasalle (1971).

In order to measure the relative performance of the tracking algorithms quantitatively, we define the tracking error as

$$E_{track} = \frac{T_{imperfect}}{T_{total}}, \quad (3.23)$$

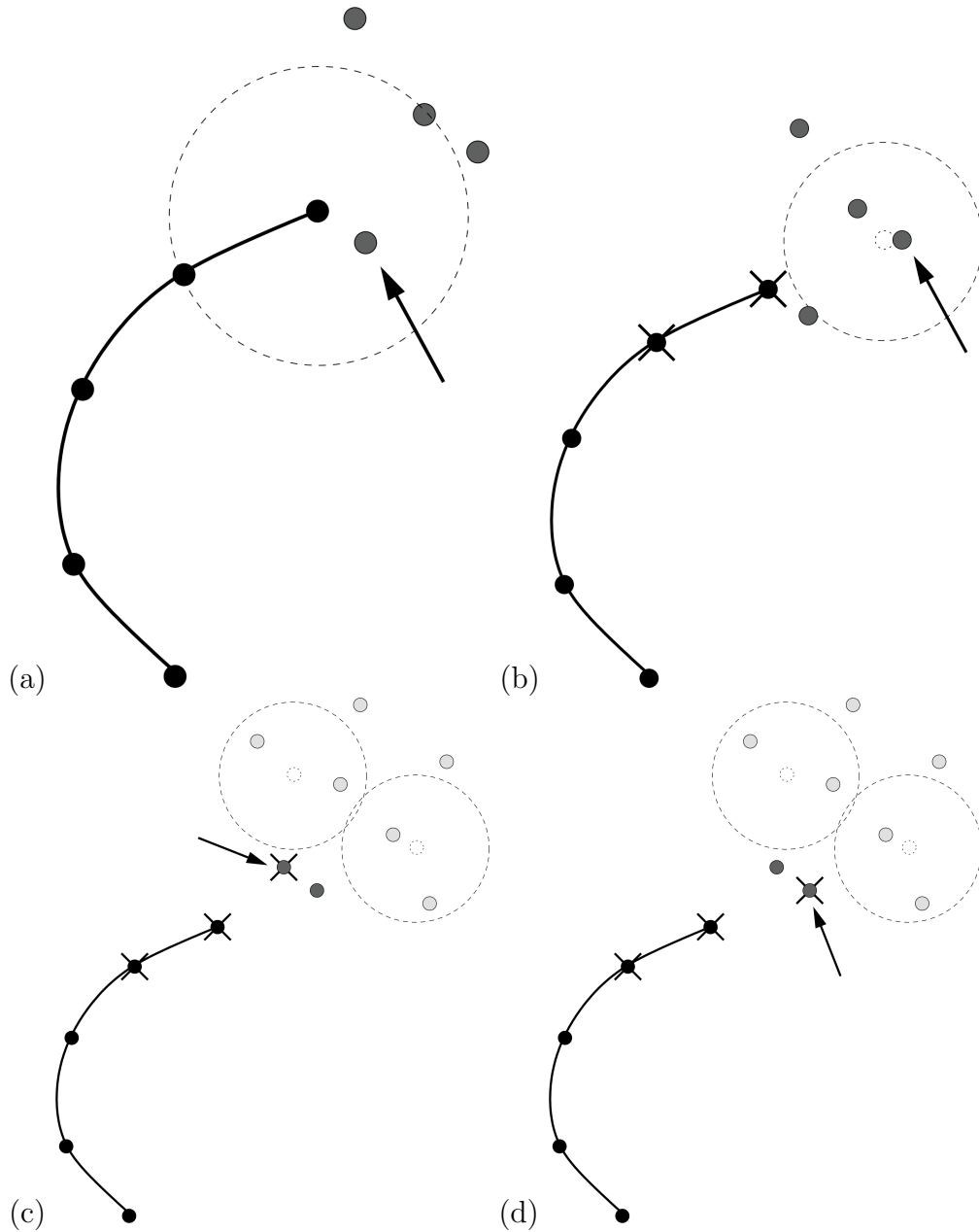


Figure 3.6: Illustration of the four tracking heuristics. The black circles and line indicate positions already joined into a track. Dark grey circles indicate positions a single frame into the future, while light grey circles signify positions two frames into the future. Open circles indicate estimated positions, and the crossed circles indicate the positions used to generate the estimates. (a) shows the Nearest Neighbor heuristic, (b) the 3 Frame: Minimum Acceleration, (c) the 4 Frame: Minimum Change in Acceleration, and (d) the 4 Frame: Best Estimate. In each case, the arrow points out which position will be chosen as the next point on the track.

where $T_{imperfect}$ is the number of tracks the algorithm failed to produce perfectly when compared to known tracks and T_{total} is the total number of tracks in the data set (Chetverikov and Verest  y, 1999). In this analysis, a perfectly constructed track may contain no spurious points and must begin at the same time as the actual data track, although it may not have the same total length. In this way, a track that is broken into many segments by the algorithm but contains no incorrect matches will only count as a single correct track in the error analysis.

We have studied E_{track} as a function of the parameter

$$\xi = \frac{\Delta r}{\Delta_0}, \quad (3.24)$$

where Δr is the mean distance travelled by a particle from one frame to the next and Δ_0 is the mean separation between a particle and its closest neighbor in a single frame. This parameter is the inverse of the parameter p defined by Malik *et al.* (1993). When $\xi \ll 1$, the particle seeding density is low and/or the particles move slowly from frame to frame. In this limit, tracking is not difficult, and most algorithms are expected to perform well. As ξ approaches unity, however, the particle density is high and/or particles move large distance between frames, and tracking becomes very difficult. Experiments, however, will tend to lie in this limit, since a higher particle density increases the data rate of the LPT system and low camera framerates, corresponding usually to lower-priced cameras or those with higher spatial resolution, produce larger frame-to-frame motion.

The algorithms were tested using tracks generated by fully 3D direct numerical simulation (DNS) of the Navier-Stokes equations provided by Lance Collins at Cornell (Collins, 2003). The DNS was carried out at a Reynolds number of $R_\lambda = 52$ in a $2\pi \times 2\pi \times 2\pi$ box with periodic boundary conditions. Despite this low Reynolds number, the individual particles undergo chaotic motion and are not

trivial to track.

Δr was fixed in the DNS, and so to vary ξ we varied Δ_0 . To accomplish this, we simply changed the size of the periodic box. When a track left the box, it was cut and the remaining portion of the track was wrapped back into the box as a new track. All of these sub-tracks were considered to begin at time zero, increasing the initial particle density and therefore ξ . This technique also simulates the effect of particles leaving the measurement volume, though no new particles enter the volume. Because of this, ξ changes over time. Since E_{track} measures the number of tracks generated with no mistakes starting at time zero, the initial, largest value of ξ defines the difficulty of the problem.

For the test of the tracking algorithms, simulated images were not created; instead, the exact fluid particle positions calculated in the DNS were fed to the algorithms. The results of our tests of tracking algorithms are therefore independent of the particle center finding method chosen.

The results of testing the eight tracking algorithms are shown in Fig. 3.7. The 4BE algorithm with no conflict breaking clearly performed better than all other algorithms tested, making no mistakes at all for $\xi < 0.04$. Interestingly, when the Munkres algorithm was used in conjunction with the 4BE algorithm, its performance was the worst of the eight algorithms.

Figure 3.7 also shows a dramatic difference between the 4BE and 4MA algorithms, despite their similarity. This difference in accuracy may be attributed to the 4MA algorithm's estimation of the third derivative in order to select the proper next particle position. With the limited time resolution in these simulations and in any real LPT experiment, the third derivative is very difficult to distinguish from noise, especially with no averaging. Because of the this, the 4MA tracking

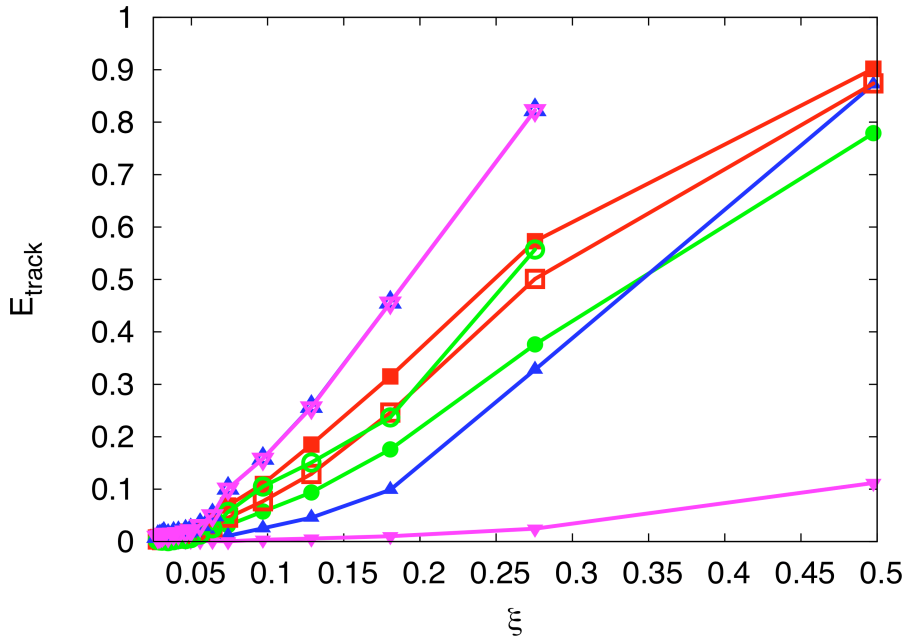


Figure 3.7: Tracking errors for the eight algorithms tested. The tracking error E_{track} is plotted as a function of ξ for each algorithm. The ■ represent the NN algorithm, the ● the 3MA algorithm, the ▲ the 4MA algorithm, and the ▼ the 4BE algorithm. Solid symbols denote algorithms with no conflict breaking, while open symbols denote the use of the Munkres algorithm for resolving tracking conflicts. The 4BE algorithm with no conflict breaking clearly outperforms the other seven algorithms, making no tracking mistakes for $\xi < 0.04$. Interestingly, in all cases except for the NN algorithm, use of the Munkres algorithm degrades the tracking performance.

heuristic is unreliable, especially for high values of ξ .

It is also apparent from Fig. 3.7 that the use of the Munkres algorithm does not, in general, enhance the performance of a tracking algorithm. Except for the NN algorithm, conflict breaking with the Munkres algorithm degrades the performance of each algorithm. This suggests that when a tracking conflict occurs, it is highly unlikely that a resolution algorithm will pick the correct position, and it is wisest simply to halt the conflicting tracks.

On the basis of this analysis, we have chosen to use the 4BE algorithm with no conflict breaking in our experiments. In addition, we have implemented a system to handle the possible loss of a particle for a few frames. This loss may occur due to occlusion of the particle, or possibly a tracking conflict. To handle this situation, we simply extrapolate tracks when they terminate for a few frames with estimated positions, hoping to find a continuation of the track. If such a continuation is not found within a set number of frames, the track is fully terminated and the estimate points are dropped.

3.2 Time Derivatives

3.2.1 Calculation

After processing the raw movies, our data is in the form of particle tracks. These tracks can then be used to calculate many different turbulence statistics. The statistics of interest often involve velocity or acceleration. We must, therefore, calculate time derivatives from our track data. Simple finite differences, however, are not sufficient for differentiating the tracks, even though our temporal resolution is high. Such simple methods are easily contaminated by errors in the determination

of the track positions. Instead, we use a more robust method for numerical differentiation. We convolve the measured particle tracks with a Gaussian smoothing and differentiating filter, as described by Mordant *et al.* (2004a). This filter uses a weighted average of many points to calculate time derivatives, reducing the effect of noise.

The Gaussian kernel is given by

$$k_n(\tau) = \frac{d^n}{d\tau^n} \left[\frac{1}{\sqrt{\pi}w} \exp\left(\frac{-\tau^2}{w^2}\right) \right], \quad (3.25)$$

where n is the order of the derivative we wish to calculate. The derivative of the position is then given by

$$\frac{d^n}{dt^n} x(t) = \int_{-\infty}^{\infty} \tilde{x}(t - \tau) k_n(\tau) d\tau, \quad (3.26)$$

where \tilde{x} denotes the noisy measured data. Integrating by parts n times, the derivative in eq. (3.25) can be passed from the Gaussian to the noisy position. The surface term from each integration by parts vanishes since the Gaussian goes to zero at infinity. Our measured tracks, however, are not infinitely long. If we apply eq. (3.26) blindly, then, we would pick up a nonzero surface term since we cannot integrate out to infinity. Instead, we truncate and renormalize the kernel before convolution with the measured positions. This truncation process also allows us to set the number of points we wish to include in the calculation of the derivative.

To illustrate this process, let us consider the velocity kernel. After truncation and renormalization, we have

$$k_v(\tau) = A_v \tau \exp\left(\frac{-\tau^2}{w^2}\right) + B_v, \quad (3.27)$$

where we have absorbed the $1/(\sqrt{\pi}w)$ in eq. (3.25) into A_v . We now restrict the convolution to lie between T and $-T$, where generally $(2T+1) \approx \tau_\eta$. For simplicity,

we fix $w = T/1.5$ (Mordant *et al.*, 2004a). We can now fix the constants A_v and B_v by requiring that

$$\int_{-T}^T k_v(\tau) d\tau = 0 \quad (3.28)$$

and

$$\int_{-T}^T (t - \tau) k_v(\tau) d\tau = 1. \quad (3.29)$$

These conditions express the requirements that the derivative of a constant be zero and the derivative of t be unity. Solving these equations simultaneously, we have

$$A_v = \left[\frac{1}{2} w^2 \left(w\sqrt{\pi} \operatorname{erf} \left(\frac{T}{2} \right) - 2Te^{-T^2/w^2} \right) \right]^{-1} \quad (3.30)$$

and

$$B_v = 0. \quad (3.31)$$

Similar arguments are sufficient to define the acceleration kernel. Differentiating eq. (3.27), we have

$$k_a(\tau) = A_a \left(\frac{2\tau^2}{w^2} - 1 \right) \exp \left(\frac{-\tau^2}{w^2} \right) + B_a. \quad (3.32)$$

To fix A_a and B_a , we require that

$$\int_{-T}^T k_a(\tau) d\tau = 0 \quad (3.33)$$

and

$$\int_{-T}^T (t - \tau)^2 k_a(\tau) d\tau = 2, \quad (3.34)$$

where the first condition again requires that the second derivative of a constant be zero and the second that the second derivative of t^2 be 2. We note that

$$\int_{-T}^T (t - \tau) k_a(\tau) d\tau = 0 \quad (3.35)$$

is guaranteed since t is an odd function and $k_a(\tau)$ is even. Unlike the case for the velocity kernel, A_a and B_a cannot be specified analytically and must be left

as integrals, which are calculated numerically. Solving the two integral conditions, we have

$$A_a = \left[\int_{-T}^T \left(\frac{1}{2}\tau^2 - \frac{T^2}{6} \right) \left(\frac{2\tau^2}{w^2} - 1 \right) \exp\left(\frac{-\tau^2}{w^2}\right) d\tau \right]^{-1} \quad (3.36)$$

and

$$B_a = -\frac{1}{2T} A_a \int_{-T}^T \left(\frac{2\tau^2}{w^2} - 1 \right) \exp\left(\frac{-\tau^2}{w^2}\right) d\tau. \quad (3.37)$$

Since convolution with the Gaussian kernel described by eq. (3.25) performs smoothing as well as differentiation, it is also useful to define the truncated, renormalized kernel for $n = 0$. In this case, the experimental data is not differentiated but is only filtered. This position kernel is given by

$$k_p(\tau) = A_p \exp\left(\frac{-\tau^2}{w^2}\right) + B_p. \quad (3.38)$$

In order to set A_p and B_p , we must use slightly different conditions from those we used to set the constants in the differentiating kernels above. We require that

$$\int_{-T}^T k_p(\tau) d\tau = 1, \quad (3.39)$$

since a constant should be unchanged by the convolution. The second condition is specified by requiring that the kernel vanish at T and $-T$. The constants A_p and B_p are then given by

$$A_p = \frac{1 - 2TB_p}{w\sqrt{\pi} \operatorname{erf}(T/w)} \quad (3.40)$$

and

$$B_p = \frac{\exp(-T^2/w^2)}{2T \exp(-T^2/w^2) - w\sqrt{\pi} \operatorname{erf}(T/w)}. \quad (3.41)$$

3.2.2 Error Analysis

In this section, we discuss the error associated with the smoothing and differentiation process described above. Since many of the measurements described in the

present work are concerned with the turbulent velocity, we will present an analysis of the error associated with the velocity kernel; errors associated with the other kernels are similarly defined. We note that in this section we shall consider all times to be measured in frames and therefore to be dimensionless.

Let us continue to denote measured values that may contain noise with tildes.

As discussed above, the velocity is defined by

$$\tilde{u}(t) = \int_{-T}^T k_v(\tau) \tilde{x}(t + \tau) d\tau, \quad (3.42)$$

where

$$\tilde{x}(t) = x(t) + \epsilon_x(t). \quad (3.43)$$

Here, $x(t)$ is the true position of the particle and ϵ_x is the error in this measurement.

We can then rewrite the measured velocity as

$$\tilde{u}(t) = \int_{-T}^T k_v(\tau) x(t + \tau) d\tau + \int_{-T}^T k_v(\tau) \epsilon_x(t + \tau) d\tau. \quad (3.44)$$

The first term in this expression can be written as the sum of the true velocity $u(t)$ and an error associated with the filtering process, $\xi_f(T, w)$. The second term is the propagation of the error in the position measurement through the velocity kernel, $\xi_x(T, w)$. By fixing $w = T/1.5$, ξ_f and ξ_x are functions only of the filter length T .

Let us first consider the case of $\xi_x(T) = 0$. The variance of the measured velocity is then given by

$$\langle \tilde{u}(t)^2 \rangle = \left\langle \int_{-T}^T d\tau k_v(\tau) x(t + \tau) \int_{-T}^T d\tau' k_v(\tau') x(t + \tau') \right\rangle. \quad (3.45)$$

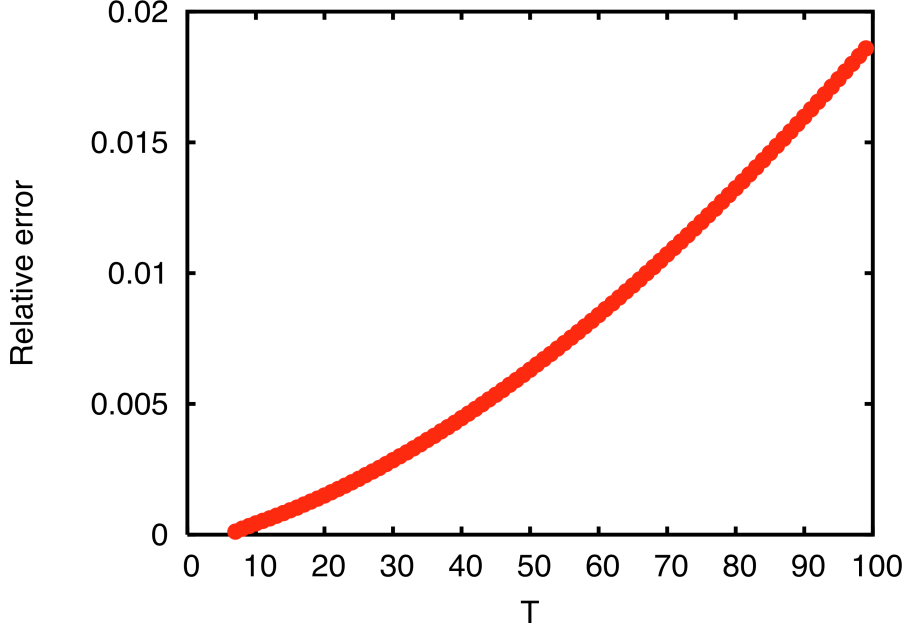


Figure 3.8: Relative error due to the velocity kernel with no position noise, calculated from DNS data.

We can write

$$\begin{aligned}
 \tilde{u}(t) &= \int_{-T}^T d\tau k_v(\tau) x(t + \tau) \\
 &= \int_{-T}^T d\tau k_v(\tau) \left[x(t) + \int_t^{t+\tau} dt' u(t') \right] \\
 &= \int_{-T}^T d\tau k_v(\tau) \int_t^{t+\tau} dt' u(t'),
 \end{aligned} \tag{3.46}$$

since $x(t)$ is a constant and, by definition, the convolution of the velocity kernel with a constant vanishes. Therefore, we have

$$\langle \tilde{u}(t)^2 \rangle = \int_{-T}^T d\tau \int_{-T}^T d\tau' k_v(\tau) k_v(\tau') \int_t^{t+\tau} dt' \int_t^{t+\tau'} dt'' \langle u(t') u(t'') \rangle. \tag{3.47}$$

The only unknown quantity in this expression is the two-time velocity correlation function $R(t' - t'') = \langle u(t') u(t'') \rangle$. The exact form of this function, however, is not known.

To investigate the magnitude of this effect, we have turned again to the DNS

data provided by Lance Collins (Collins, 2003) with no added noise. In Fig. 3.8, we plot the relative error $(\langle u^2 \rangle^{1/2} - \langle \tilde{u}^2 \rangle^{1/2})/\langle u^2 \rangle^{1/2}$ as a function of T . Since this error is less than 1% for $T < 70$, we consider the error purely associated with the convolution process to be negligible.

Let us consider now the variance of $\xi_x(T)$, given by

$$\langle \xi_x(T)^2 \rangle = \int_{-T}^T d\tau \int_{-T}^T d\tau' k_v(\tau) k_v(\tau') \langle \epsilon_x(t + \tau) \epsilon_x(t + \tau') \rangle. \quad (3.48)$$

We cannot calculate this error without some assumptions. Let us assume that the position error is δ -correlated in time and stationary, so that

$$\langle \epsilon_x(t + \tau) \epsilon_x(t + \tau') \rangle = \langle \epsilon_x^2 \rangle \delta(\tau - \tau'). \quad (3.49)$$

This assumption is not truly realistic, since the position error will be correlated while the particle center moves within a single camera pixel. In order to compensate for this under-estimation of the error, we take $\langle \epsilon_x^2 \rangle^{1/2} = 0.1$ pixels, which is probably an overestimate of the position uncertainty. With the assumption of δ -correlation, eq. (3.48) is tractable, and we have that

$$\langle \xi_x(T)^2 \rangle = \langle \epsilon_x^2 \rangle \frac{2 \exp(T^2/w^2)}{w^2 (-2T + w\sqrt{\pi} \exp(T^2/w^2) \operatorname{erf}(T/w))}. \quad (3.50)$$

With $w = T/1.5$, this expression reduces to

$$\langle \xi_x(T)^2 \rangle = \frac{1.95 \langle \epsilon_x^2 \rangle}{T^3}. \quad (3.51)$$

This error is, in general, not negligible, and is reflected by error bars on our velocity statistics.

3.3 Apparatus

Figure 3.9 shows a sketch of the experimental system used to generate and measure turbulence. In general, a Lagrangian particle tracking system consists of a flow

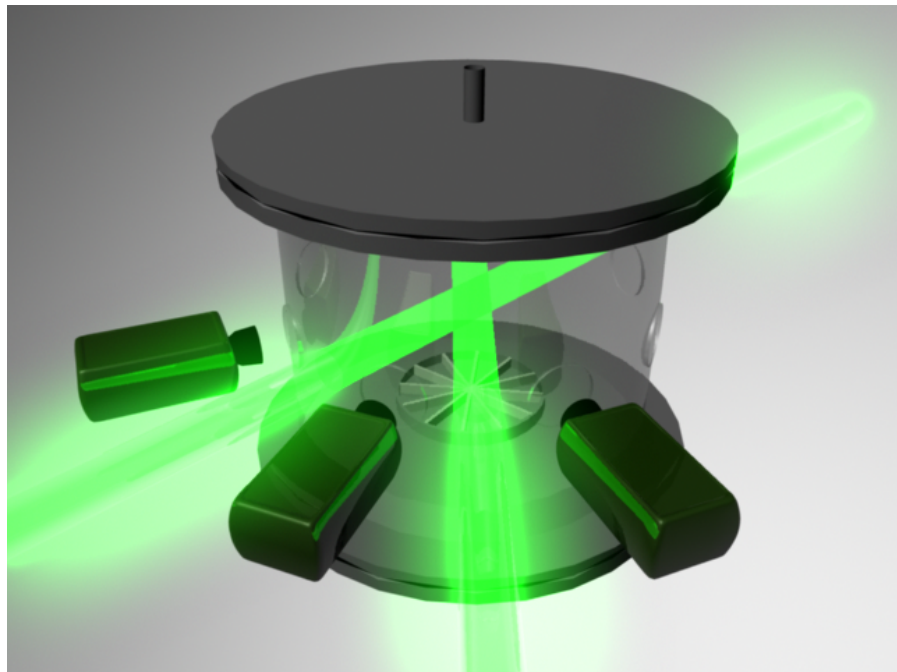


Figure 3.9: Sketch of the turbulence generator, lasers, and cameras.

apparatus, an illumination source, and cameras. We have already discussed the cameras used in our experiments above; the additional components are described below.

3.3.1 Flow Chamber

The flow consists of a closed cylindrical chamber containing roughly 120 L of water. The apparatus has previously been discussed in detail (Voth, 2000; Crawford, 2004), so we will only describe it briefly here. The chamber consists of a cylindrical plexiglass tank 60.5 cm high and with a diameter of 48.3 cm. Glued around the center of the tank are eight round glass windows 12.7 cm in diameter that allow optical access to the flow chamber through flat rather than curved surfaces to avoid lensing effects. The top and bottom of the chamber are plates of hard-anodized aluminum.

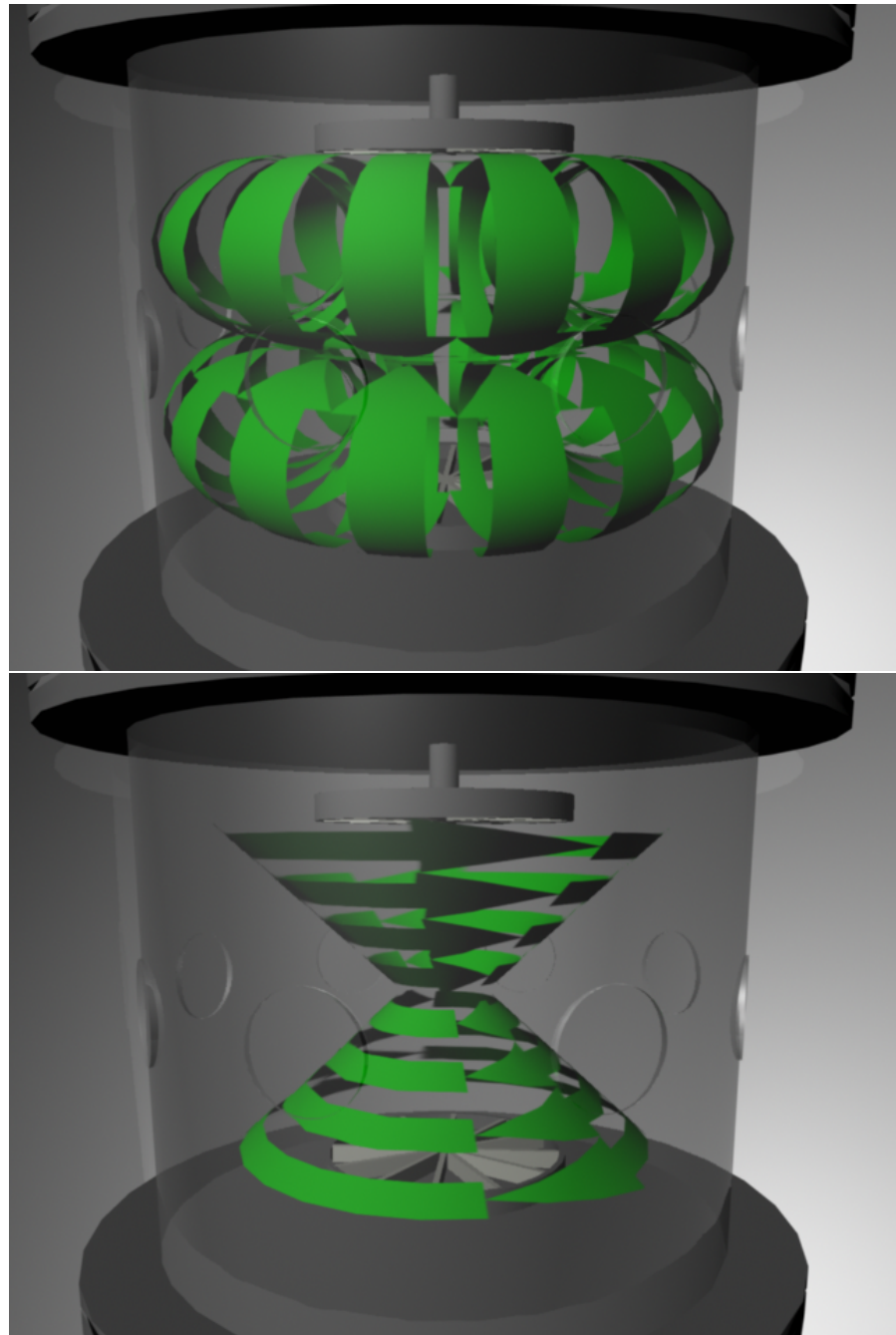


Figure 3.10: Decomposition of the large-scale flow into a pumping mode (top) and a shearing mode (bottom).

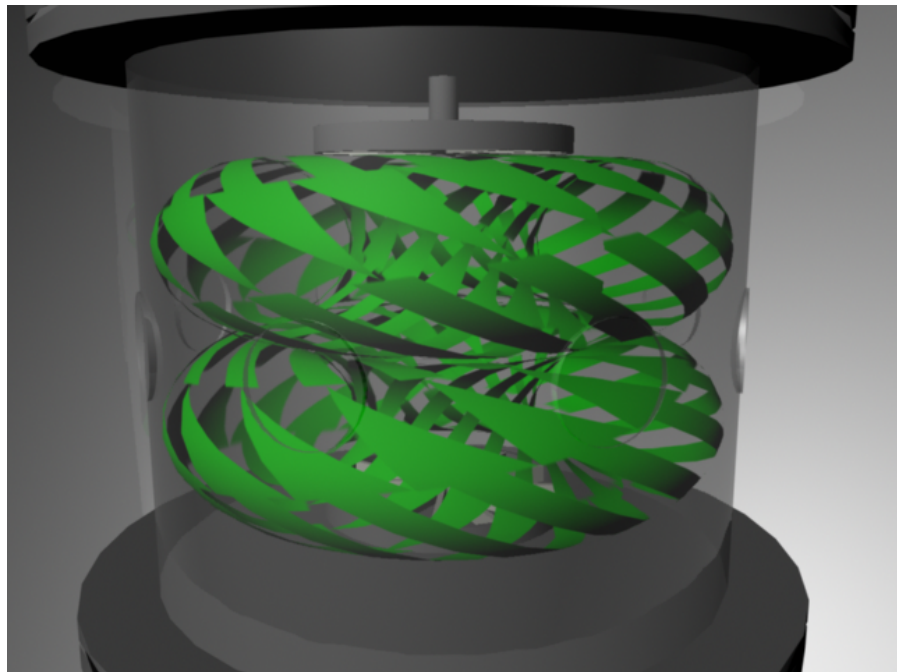


Figure 3.11: Sketch of the total mean flow pattern in the flow chamber.

Turbulence is generated by the counter-rotation of two baffled disks. This type of flow, known as a von Kármán swirling flow (Zandbergen and Dijkstra, 1987), has become increasingly popular in turbulence research in the past few decades despite its nontrivial large-scale mean flow because it can generate high Reynolds numbers in a small laboratory space. The large-scale flow is axisymmetric, and can be decomposed into a pumping mode and a shearing mode, as shown in Figs. 3.10 and 3.11. The disks themselves are 20.3 cm in diameter and have a depth of 4.3 cm. Each contains twelve straight vanes so that the flow is forced inertially. Each disk is surrounded by a plexiglass shield (not shown; see Voth (2000) or Crawford (2004)) that breaks up any large-scale circulation and confines the bulk of the turbulence to the center of the tank. The disks are driven by 0.9 kW DC motors with rotation frequencies controlled through a feedback loop. A channel is cut inside the top and bottom aluminum plates and cooling water is pumped through

in order to control the temperature of the water in the apparatus. The water in the apparatus may be cleaned by pumping it through a filtering loop. A second recirculation loop may be used to pump out bubbles and air from the apparatus or to introduce the tracer particles.

3.3.2 Illumination

As noted above, the Phantom v7.1 cameras used in the experiments presented here record images at a maximum rate of 27,000 frames per second at a resolution of 256×256 pixels. The exposure time of each frame is therefore very short, with a minimum of $37 \mu\text{s}$. In order to illuminate the tracer particles, therefore, a very intense light source must be used. When using multiple cameras, it is also advantageous to use a pulsed light source, since pulsing obviates the need for exact camera synchronization: the cameras will only record particle images when the light source is on, and therefore all the cameras will record images at exactly the same instant.

To these ends, we use Q-switched Nd:YAG solid state lasers for illumination, frequency-doubled with a KTP crystal to provide green light at 532 nm. These lasers are designed for both high power and high pulse rates. Three such lasers were used in these experiments, one pumped with flashlamps and two pumped by diode arrays. To increase the output power, each laser used two Nd:YAG rods in series in the laser cavity.

The flashlamp laser can be run from 30 kHz to 70 kHz, with typical pulse widths of ~ 300 ns and peak power of ~ 60 W. The diode pumped lasers can be operated from 10 kHz to 120 kHz with pulse widths of ~ 120 ns and peak power of ~ 90 W.

Care is taken in each experiment to put the cameras in the forward scattering direction in order to maximize the amount of scattered light collected.

3.3.3 Tracer Particles

In an ideal Lagrangian particle tracking experiment, the particles used would be true passive tracers and would behave exactly as fluid elements. Real particles, however, have finite size and may also have a density different from that of the carrier fluid. Because of these factors, the inertia of the particles will impair their ability to follow the fluid flow exactly.

The importance of the particle inertia is measured by the Stokes number St , defined as the ratio of the particle response time τ_p to the Kolmogorov time of the flow τ_η . The Stokes number is, unfortunately, difficult to define, in great part because it is difficult to write the equation of motion of a spherical particle in a fluid, even at low Reynolds number. One such form is given by Shaw (2003) as

$$\begin{aligned} \rho_p V_p \dot{\mathbf{v}} = & 6\pi\mu a(\mathbf{u} - \mathbf{v}) + \frac{1}{2}\rho_f V_p(\dot{\mathbf{u}} - \dot{\mathbf{v}}) + 6a^2\sqrt{\pi\rho_f\mu} \int_0^t \frac{\dot{\mathbf{u}}(t') - \dot{\mathbf{v}}(t')}{\sqrt{t-t'}} dt' \\ & + \rho_p V_p \mathbf{g} + \rho_f V_p \dot{\mathbf{u}} - \rho_f V_p \mathbf{g}, \end{aligned} \quad (3.52)$$

where ρ_p and ρ_f are the particle and fluid densities, respectively, V_p is the volume of the particle, a is the particle diameter, \mathbf{v} and \mathbf{u} are the particle and fluid velocities, respectively, and \mathbf{g} is the acceleration due to gravity. The terms on the right-hand side of this expression are, in order, Stokes drag, the “added mass” due to the acceleration of the fluid, the Basset “history” force, gravity, the fluid shear stress, and buoyancy. We note that there is no general agreement on this form of the equation of motion, and a different form is given by Voth (2000).

In eq. (3.52), we can neglect the gravitational effects, since they are small

compared with the turbulent accelerations. In the frame of reference of the particle where $\mathbf{v} = 0$, we further assume that $\dot{\mathbf{v}} \sim \dot{\mathbf{u}} \sim u/\tau_p$. We also neglect the Basset history force. We therefore have that

$$\tau_p = \frac{1}{18} \frac{\rho_p - \rho_f}{\rho_f} \frac{d^2}{\nu}. \quad (3.53)$$

The Stokes number can then be written as

$$St = \frac{1}{\tau_\eta} \left(\frac{1}{18} \frac{\rho_p - \rho_f}{\rho_f} \frac{d^2}{\nu} \right) = \frac{1}{18} \frac{\rho_p - \rho_f}{\rho_f} \left(\frac{d}{\eta} \right)^2. \quad (3.54)$$

In our experiments, we have primarily used transparent polystyrene microspheres with a diameter of $25 \mu\text{m}$, manufactured by Duke Scientific Corporation. These microspheres have a density 1.06 times that of water, and their Stokes numbers are shown as a function of Reynolds number in Tabs. 3.2 and 3.3. We have also experimented with $33 \mu\text{m}$ polystyrene microspheres containing a fluorescent dye that absorbs light at the frequency produced by our Nd:YAG lasers and emits in the red. These fluorescent particles have the advantage that the laser light may be optically filtered removing any stray reflections from the camera images. In addition, the scattering angle between the lasers and the cameras becomes unimportant since the fluorescent particles emit light isotropically.

3.3.4 Data Acquisition and Processing

As shown above in Table 3.1, the Phantom v7.1 cameras can take images at a rate of up to 27,000 pictures per second at a resolution of 256×256 pixels. Each pixel stores eight bits of information. With these parameters, then, each camera produces approximately 1.65 gigabytes of information every second. Since we use three cameras in order to avoid problems of tracer particle overlap, as shown in

Fig. 3.9, our experimental system records just under 5 GB of information every second.

These data rates are too high for the cameras to stream the images to disk using current technology. Each camera, therefore, has an internal 4 GB buffer, of which approximately 2.6 GB is available for storing pixel values, the rest being used for overhead. The cameras can then transfer the contents of their internal buffer over gigabit ethernet.

In order to manage and process the large amounts of data produced by this experiment, we use a 16 node, 32-processor Pentium 4 Xeon-based computer cluster with approximately 6 TB of disk space. During a data run, the cameras record movies with typical lengths of one to two eddy turnover times and then transfer the data to the cluster for processing. Since the tracking algorithms discussed above do not lend themselves well to parallelization, the movies are transferred to multiple nodes in sequence. Once the cameras finish transferring one set of three movies, which typically takes about five minutes, they record the next image sequence.

By transferring the movies to the local drives of the individual nodes of the cluster, we eliminate the potential bottleneck that could occur should multiple nodes attempt to access the central data storage at the same time. Once a node has finished processing a set of movies, it transfers a binary file of the calculated particle tracks to the central data storage. The raw movies themselves are not stored, due to space limitations. This entire data acquisition process is completely automated, with no human control needed during the actual data run.

Once the tracks have been calculated, they are processed using specialized software written in C++ and turbulence statistics are computed.

3.4 Camera Calibration

Figure 3.12 shows a single frame from each of the three cameras used in our experiments. These images are fed to the computers, and the 1D Gaussian Estimator described above is used to find the centers of the particle images in image space. For the stereomatching and subsequent particle tracking, however, we must know the coordinates of the particle centers in real space. We construct this mapping using a camera calibration method developed by Tsai (1987).

Let us define the laboratory coordinates of a particle as \mathbf{x}_w , commonly called world coordinates in machine vision. These coordinates can be mapped into the reference frame of the camera with a rotation and a translation, given by

$$\begin{pmatrix} x_c \\ y_c \\ z_c \end{pmatrix} = \begin{pmatrix} R_{11} & R_{12} & R_{13} \\ R_{21} & R_{22} & R_{23} \\ R_{31} & R_{32} & R_{33} \end{pmatrix} \begin{pmatrix} x_w \\ y_w \\ z_w \end{pmatrix} + \begin{pmatrix} T_x \\ T_y \\ T_z \end{pmatrix}, \quad (3.55)$$

where \mathbf{x}_c are the particle coordinates in camera space. We note that in our implementation of this model we combine the rotation and the translation using homogeneous coordinates (see, *e.g.*, Rogers and Adams (1990) for a discussion of the properties of homogeneous coordinates). Here, however, we present the calibration model in standard three-dimensional coordinates.

Assuming a pinhole camera with an effective focal length of f_{eff} , we can write the perspective projection of the camera-space coordinates \mathbf{x}_c onto the ideal detector coordinates \mathbf{x}_u as

$$\begin{pmatrix} x_u \\ y_u \end{pmatrix} = \frac{f_{eff}}{z_c} \begin{pmatrix} x_c \\ y_c \end{pmatrix}. \quad (3.56)$$

Any real camera and lens system, however, will introduce some distortion, and so

the measured coordinates \mathbf{x}_d on the detector will be

$$\begin{pmatrix} x_d \\ y_d \end{pmatrix} = (1 + k_1 r^2 + k_2 r^4 + \dots) \begin{pmatrix} x_u \\ y_u \end{pmatrix}, \quad (3.57)$$

where $r^2 = x_d^2 + y_d^2$. We follow Tsai (1987) in assuming that the distortion is purely radial and that keeping only k_1 is sufficient. Assuming no tangential distortion also allows a significant simplification of the model, which Tsai (1987) refers to as the Radial Alignment Constraint (RAC). If there is no tangential distortion, then the distorted and ideal positions of a particle image on the detector must lie on a line that passes through the center of the image. This condition requires that $\mathbf{x}_u \times \mathbf{x}_d = 0$. The final coordinate system we introduce allows a slight difference between the horizontal and vertical spacing of the physical pixels on the detector.

We define

$$\begin{pmatrix} x_p \\ y_p \end{pmatrix} = \begin{pmatrix} s_x x_d \\ y_d \end{pmatrix}, \quad (3.58)$$

where s_x is a scale factor that should, ideally, be unity if the physical detector is ideal. Calibrating s_x is then a good check on the quality of the calibration.

The calibration model as described above requires the specification of nine parameters: three from the rotation matrix (since it is orthogonal and can be parametrized by the Euler angles), three from the translation vector, the effective focal length f_{eff} , the distortion coefficient k_1 , and s_x . To gather data to set these parameters, we have constructed a calibration mask by printing dots of a known size onto a transparent mylar sheet with a laser printer. The dot pattern was then sealed between two panes of glass and mounted inside the flow chamber on a micrometer stage. Concurrent images of the calibration mask from each of the three cameras are shown in Fig. 3.13. Since the spacing between the dots was known and the position of the mask in the flow chamber could be measured with

the micrometer, imaging the mask at different positions provided a set of known 3D world coordinates paired with their corresponding detector coordinates.

Tsai (1987) presented a method for determining most of the calibration model parameters using only linear least-squares fits. The RAC can be written as

$$\frac{1}{s_x} x_p (R_{21}x_w + R_{22}y_w + R_{23}z_w + T_y) = y_p (R_{11}x_w + R_{12}y_w + R_{13}z_w + T_x). \quad (3.59)$$

This relation can in turn be expressed as a set of seven linear equations, namely

$$\left(\begin{array}{ccccccc} & & & & & & \\ -x_p x_w & -x_p y_w & -x_p z_w & y_p x_w & y_p y_w & y_p z_w & y_p \end{array} \right) \left(\begin{array}{c} T_y^{-1} R_{21} \\ T_y^{-1} R_{22} \\ T_y^{-1} R_{23} \\ T_y^{-1} s_x R_{11} \\ T_y^{-1} s_x R_{12} \\ T_y^{-1} s_x R_{13} \\ T_y^{-1} s_x T_x \end{array} \right) = x_p. \quad (3.60)$$

By fitting these equations to the measured data from the calibration mask, the total rotation matrix, T_x , T_y , and s_x may be determined. Equation (3.57) may then be solved iteratively for the remaining three parameters, after obtaining an initial approximation of f_{eff} and T_z by setting k_1 to zero and again performing a least-squares fit.

Once the calibration parameters have been determined, the model can be used to translate the measured coordinates of the tracer particle centers on the detectors to real, laboratory-space coordinates.

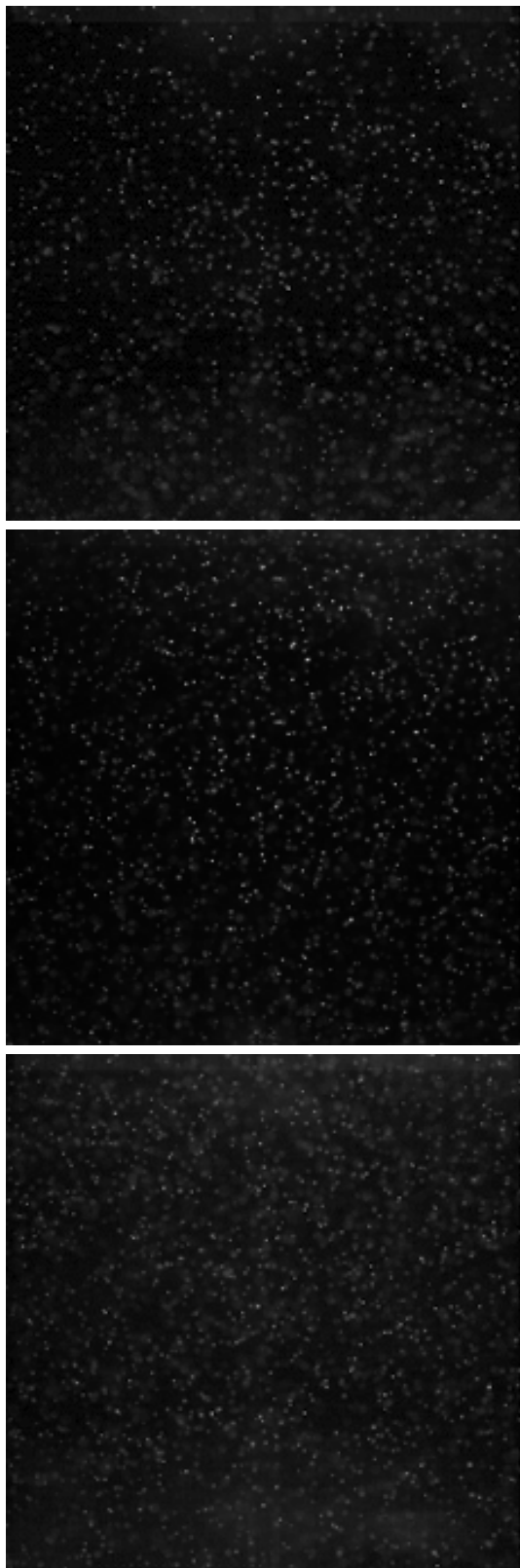


Figure 3.12: Raw images taken with each of the three cameras at one instant in the flow.

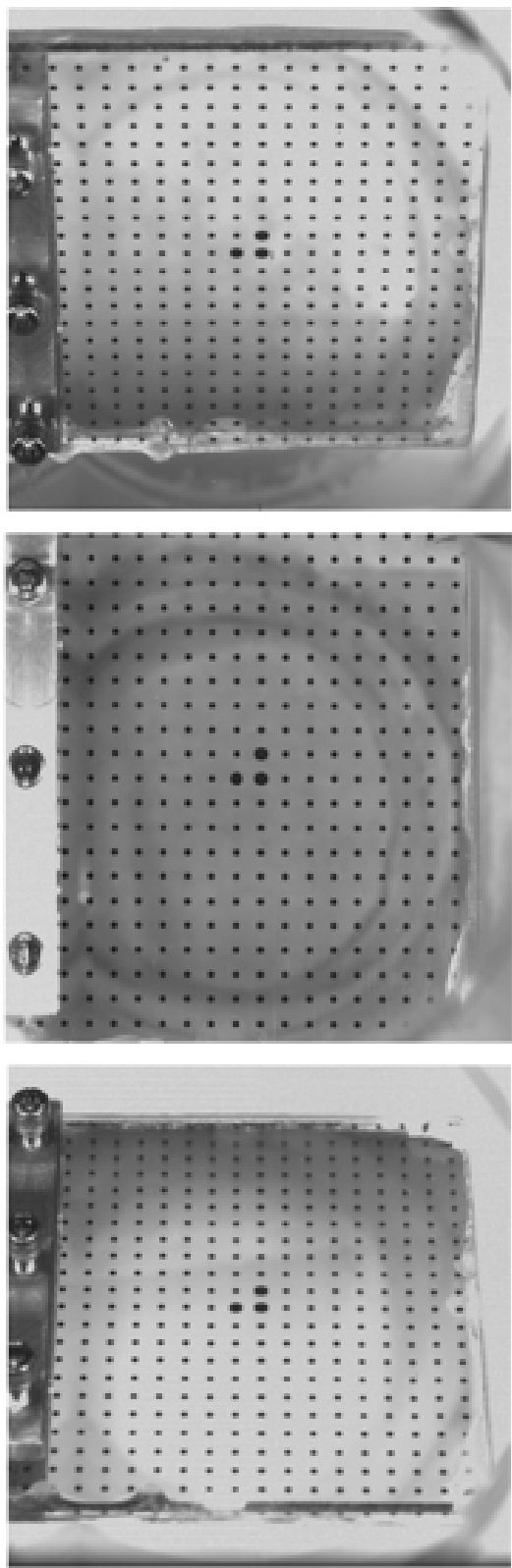


Figure 3.13: Images of the calibration mask from each of the three cameras.

3.5 Experimental Parameters

The analysis in the following chapters is based on a number of large data sets taken with various experimental parameters. In this section, we present the parameters associated with each experimental run.

The integral length scale is fixed in the apparatus, and has previously been found to be 7.1 cm (Voth *et al.*, 2002). The first set of experiments was conducted in a measurement volume of approximately $2 \times 2 \times 2$ cm³. Table 3.2 shows the values of various parameters for these experiments. Likewise, Table 3.3 shows the values of the experimental parameters for data taken in a volume of approximately $5 \times 5 \times 5$ cm³. In each table, the values of the dissipation rate ϵ are measured, as described in the following chapter, while the Kolmogorov scales are estimated from simple scaling arguments.

Table 3.2: Experimental parameters for the $2 \times 2 \times 2 \text{ cm}^3$ data runs. f denotes the rotation rate of the disks, u'_r is the RMS radial velocity, u'_z is the RMS axial velocity, FPS is the number of frames per second, and δt is the time between frames. These data were taken with transparent $25 \mu\text{m}$ polystyrene microspheres.

Data Set	f (Hz)	R_λ	u'_r (ms $^{-1}$)	u'_z (ms $^{-1}$)	ϵ (m 2 s $^{-3}$)	η (μm)	L/η	τ_η (ms)	T_L/τ_η	FPS	δt (ms)	$\tau_\eta/\delta t$	St
050222	0.30	200	0.039	0.025	6.53×10^{-4}	192	365	36.8	51	1000	1.00	37	5.7×10^{-5}
050216	3.50	690	0.473	0.306	1.19	30	2337	0.897	176	27000	0.037	24	2.3×10^{-3}
050221	5.00	815	0.664	0.430	3.24	23	3000	0.544	208	27000	0.037	15	3.9×10^{-3}

Table 3.3: Experimental parameters for the $5 \times 5 \times 5 \text{ cm}^3$ data runs. f denotes the rotation rate of the disks, u'_r is the RMS radial velocity, u'_z is the RMS axial velocity, FPS is the number of frames per second, and δt is the time between frames. These data were taken with transparent $25 \mu\text{m}$ polystyrene microspheres.

Data Set	f	R_λ	u'_r	u'_z	ϵ	η	L/η	τ_η	T_L/τ_η	FPS	δt	$\tau_\eta/\delta t$	St
	(Hz)		(ms $^{-1}$)	(ms $^{-1}$)	(m 2 s $^{-3}$)	(μm)		(ms)		(ms)			
050425	0.30	200	0.039	0.026	7.09×10^{-4}	192	365	36.8	51	1000	1.00	37	5.7×10^{-5}
050424	0.43	240	0.056	0.038	2.03×10^{-3}	146	479	21.3	61	1600	0.625	34	9.8×10^{-5}
050509	0.62	290	0.083	0.054	6.26×10^{-3}	111	630	12.3	74	3000	0.333	37	1.7×10^{-4}
050421	0.90	350	0.121	0.080	2.01×10^{-2}	84	830	7.11	88	5000	0.200	36	2.9×10^{-4}
050414	1.29	415	0.181	0.116	6.17×10^{-2}	64	1090	4.12	106	9000	0.111	37	5.1×10^{-4}
050413	1.86	500	0.262	0.169	0.196	49	1433	2.39	127	27000	0.037	65	8.7×10^{-4}
050408	3.50	690	0.487	0.315	1.24	30	2337	0.897	176	27000	0.037	24	2.3×10^{-3}
050410	5.00	815	0.669	0.440	3.39	23	3000	0.544	208	27000	0.037	15	3.9×10^{-3}

Chapter 4

Single Particle Statistics

4.1 Velocity and Acceleration

The simplest quantities to consider in turbulence are the pointwise velocity and acceleration. In this section, we discuss the measurement of these quantities through their probability density functions (PDFs) before moving on to more complex, multipoint measurements.

The PDF of the turbulent velocity fluctuations is generally expected to be close to Gaussian. As has become apparent in recent years, however, the PDF of the turbulent acceleration is highly non-Gaussian, and instead has a stretched exponential form (La Porta *et al.*, 2001; Voth *et al.*, 2002; Mordant *et al.*, 2004a). This extreme deviation from Guassianity suggests that the acceleration is a far more intermittent variable than the velocity. Extreme, violent acceleration events are far more likely in turbulence than extreme velocities, and so the acceleration is correspondingly more difficult to measure, requiring very high spatial and temporal resolution. In the present work, we have focused on the statistics of the velocity and position; as will be seen below, the acceleration is under-resolved by our measurement system.

Since, as shown in Section 3.2.2, spatial resolution plays a role in the accuracy of the measured velocity and acceleration, we discuss the small and large measurement volume data separately, since the two experiments have different spatial resolution.

4.1.1 Small Measurement Volume

As shown in Section 3.3.1, our apparatus has a complex mean flow. To attempt to account for this, when we calculate the velocity and acceleration, we first average for long times to estimate the mean flow. This mean field is then subtracted away from the measured Lagrangian velocity and accelerations, leaving us with the fluctuating quantities of interest in turbulence. We note that the measured mean accelerations are exceedingly small and are due only to noise rather than to any true mean acceleration field.

The resulting fluctuating velocities and accelerations are not isotropic, however. We consistently find differences in many quantities calculated in the two radial directions (x and y) and in the axial direction (z), as has been seen before in this apparatus (Crawford, 2004). Figure 4.1 shows the standardized PDFs of the turbulent velocity measured in the two radial directions in the $2 \times 2 \times 2 \text{ cm}^3$ measurement volume at the three different Reynolds numbers measured. The solid lines in Fig. 4.1 are standardized Gaussians. The data for all Reynolds numbers and for both radial components is almost perfectly Gaussian.

In contrast, we show the PDFs of the axial velocity component for the same three Reynolds numbers in Fig. 4.2. The PDF of the axial velocity clearly has super-Gaussian tails. This behavior is most likely due to the large-scale forcing of our flow.

All three components of the acceleration are shown in Fig. 4.3 for all three Reynolds numbers. The solid line shows the acceleration PDF measured by Mor-dant *et al.* (2004a) in the same flow using silicon strip detectors at $R_\lambda = 690$. All three components of the current data behave similarly and agree well with the previously measured PDF up to roughly $15\langle a^2 \rangle^{1/2}$, with the tails being somewhat

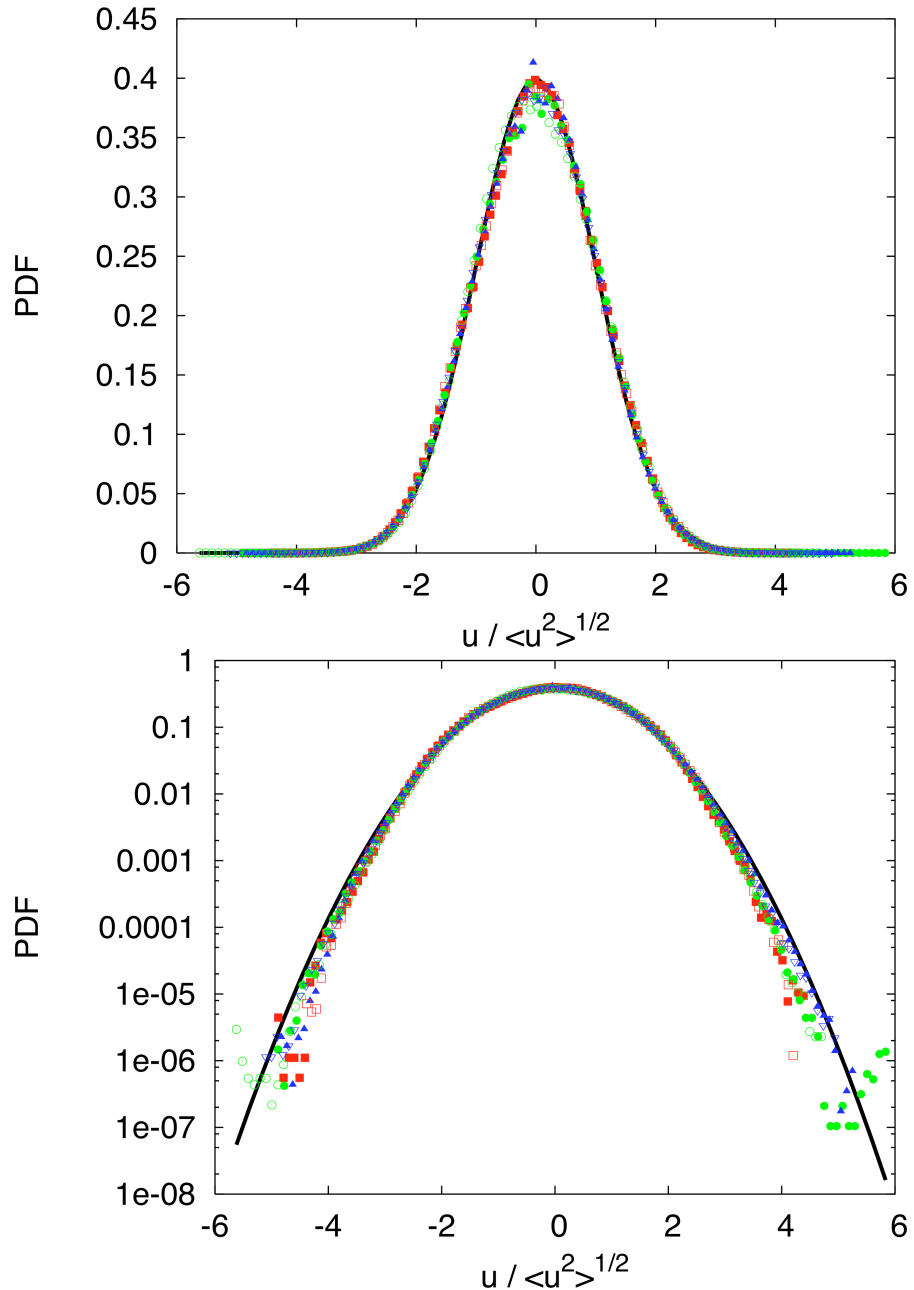


Figure 4.1: Radial velocity PDFs in the $2 \times 2 \times 2 \text{ cm}^3$ measurement volume, normalized by the velocity variance. The solid line is a standardized Gaussian. Data is shown for $R_\lambda = 200$ (■), $R_\lambda = 690$ (●), and $R_\lambda = 815$ (▲). Closed symbols show the PDF of the x component of the velocity, while open symbols show the y component. The upper plot shows the PDFs plotted on a linear scale, while the lower plot shows the same data plotted on semilogarithmic axes.

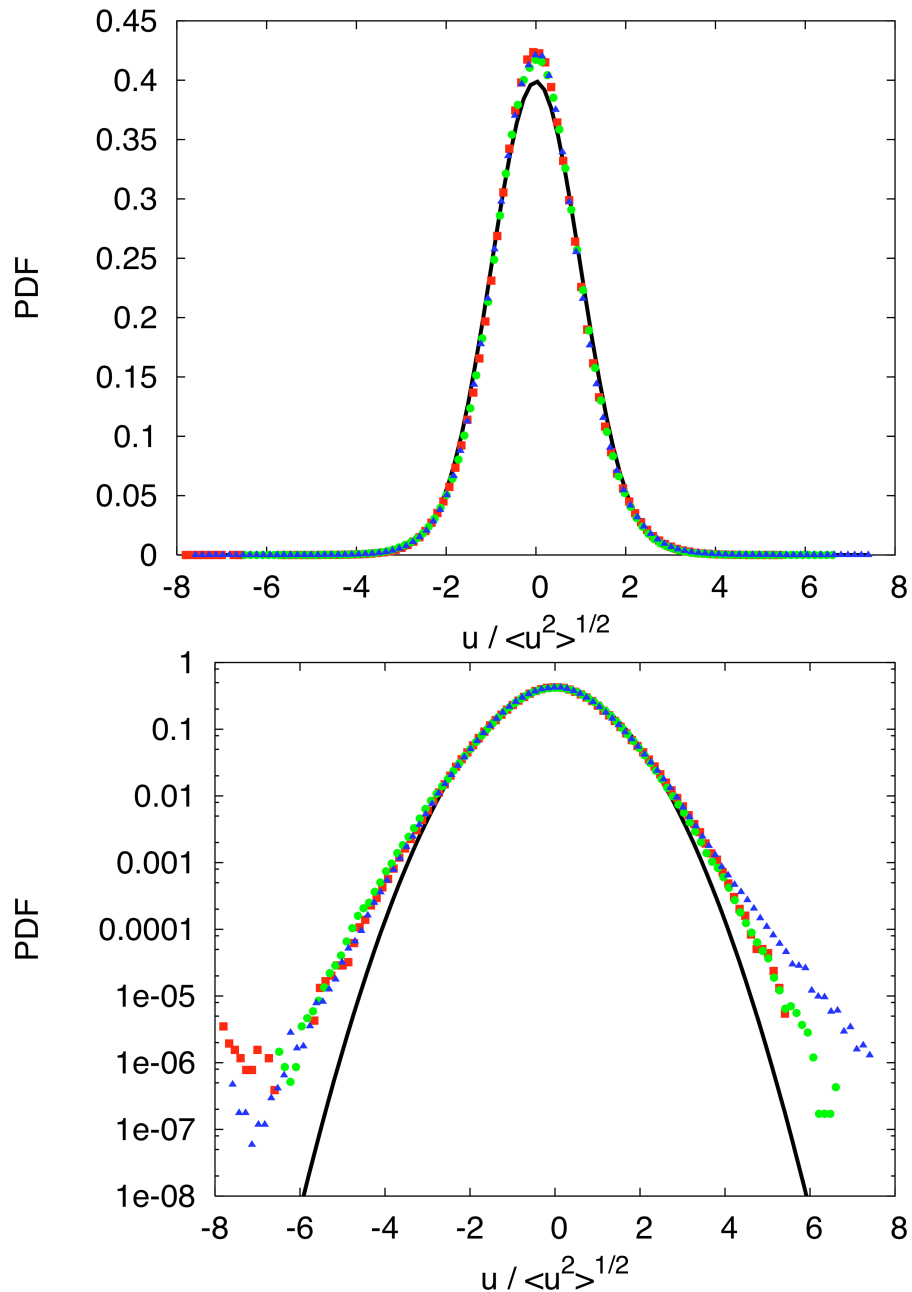


Figure 4.2: Axial velocity PDFs in the $2 \times 2 \times 2 \text{ cm}^3$ measurement volume, normalized by the velocity variance. The solid line is a standardized Gaussian. Data is shown for $R_\lambda = 200$ (■), $R_\lambda = 690$ (●), and $R_\lambda = 815$ (▲). The upper plot shows the PDFs plotted on a linear scale, while the lower plot shows the same data plotted on semilogarithmic axes. Unlike the radial velocity PDFs, which are very Gaussian, the axial velocity PDF has wider tails.

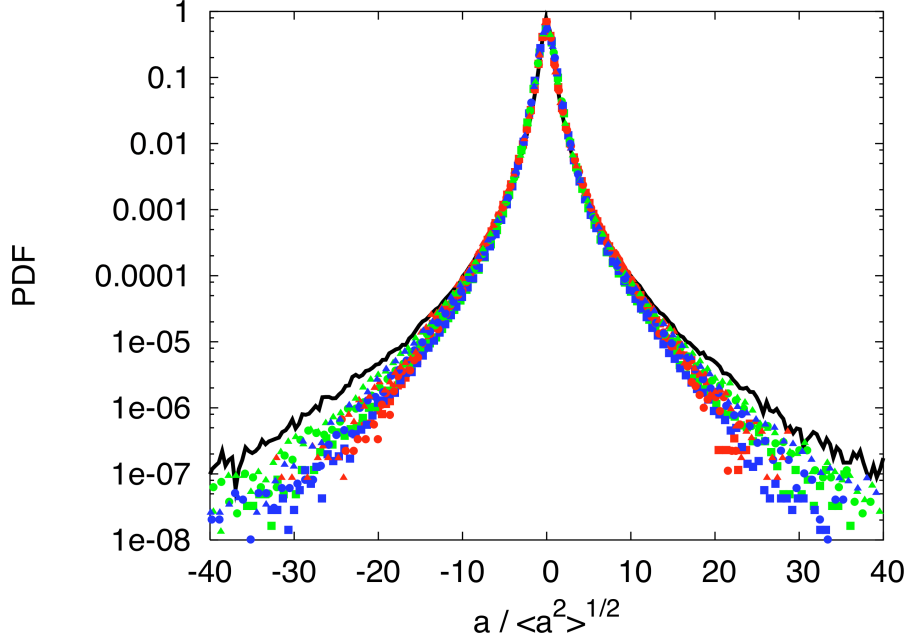


Figure 4.3: Acceleration PDFs in the $2 \times 2 \times 2 \text{ cm}^3$ measurement volume, normalized by the acceleration variance. The solid line is the acceleration PDF measured by Mordant *et al.* (2004a) in the same apparatus using silicon strip detectors at $R_\lambda = 690$. Red symbols denote data taken at $R_\lambda = 200$, green symbols data at $R_\lambda = 690$, and blue symbols data at $R_\lambda = 815$. The ■ denote the x component of the acceleration, the ● the y component, and the ▲ the z component. Unlike the velocity, the acceleration shows no difference between the radial and axial components. The tails of the PDFs measured in the current experiment are narrower than those measured by Mordant *et al.* (2004a), an effect caused by the poorer temporal and spatial resolution of our cameras.

depressed for higher acceleration events. While the highly non-Gaussian shape of the PDF is evident, the spatial and temporal resolution of the current experimental setup are clearly not sufficient to resolve the turbulent acceleration fully.

4.1.2 Large Measurement Volume

Just as with the small measurement volume, we see a difference between the radial and axial velocity PDFs in the larger $5 \times 5 \times 5 \text{ cm}^3$ measurement volume where the

spatial resolution is poorer. The standardized PDFs of one of the radial velocity components are shown in Fig. 4.4 for Reynolds number ranging from $R_\lambda = 200$ to $R_\lambda = 815$. The agreement with the normalized Gaussian is good, though not quite as good as for the smaller measurement volume data set, since the spatial resolution is poorer.

The PDF of the axial velocity component is shown in Fig. 4.5 for the same Reynolds numbers. Just as for the small measurement volume data, the axial component is significantly less Gaussian than the radial component.

Unlike in the small measurement volume case, we see a difference between the radial and axial acceleration PDFs, shown in Fig. 4.6. While both PDFs are seriously under-resolved when compared with the data of Mordant *et al.* (2004a), the tails of the axial PDF are systematically higher than those of the radial PDFs, just as they were in the velocity PDF. Regardless, is it clear that only low moments of the acceleration can be meaningfully measured with the large measurement volume data.

4.1.3 Biases

In any particle tracking experiment, there are a number of factors that can affect the measured turbulence statistics. Some of these factors are purely statistical in nature, and can be corrected by collecting more data. Some, however, are inherent biases that cannot, in general, be corrected for.

Each particle will stay in the field of view of the cameras for a different amount of time, and so therefore each particle track will be a different length. There are far more short tracks than long tracks measured by our experiment, as shown in Fig. 4.7. Statistical convergence can therefore become a problem at long times.

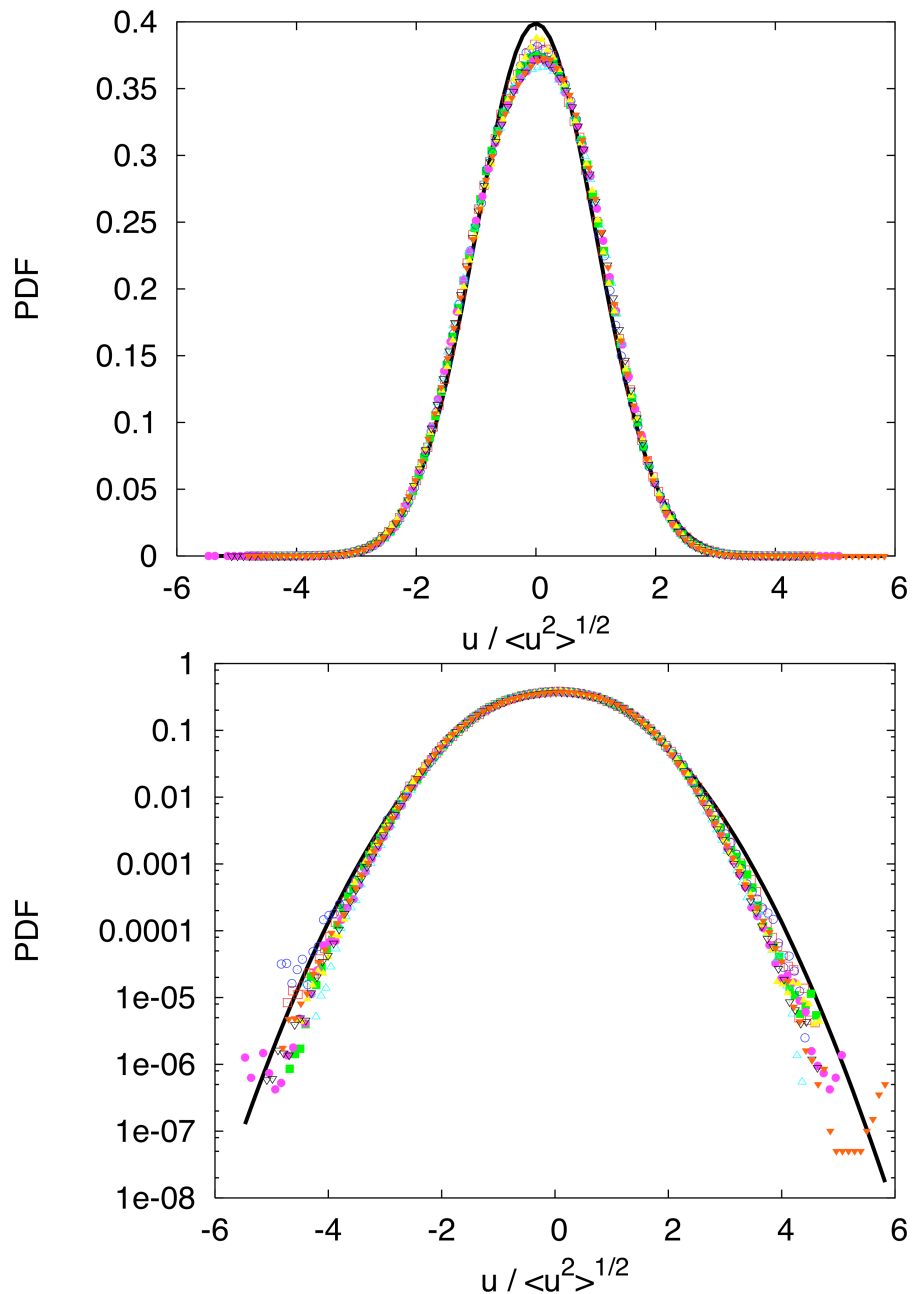


Figure 4.4: Radial velocity PDFs in the $(5 \text{ cm})^3$ measurement volume, normalized by the velocity variance. The solid line is a standardized Gaussian. Data is shown for $R_\lambda = 200$ (\square), $R_\lambda = 240$ (\blacksquare), $R_\lambda = 290$ (\circ), $R_\lambda = 350$ (\bullet), $R_\lambda = 415$ (\triangle), $R_\lambda = 500$ (\blacktriangle), $R_\lambda = 690$ (\triangledown), and $R_\lambda = 815$ (\blacktriangledown). Only the x component of the velocity is shown; the y component is similar.

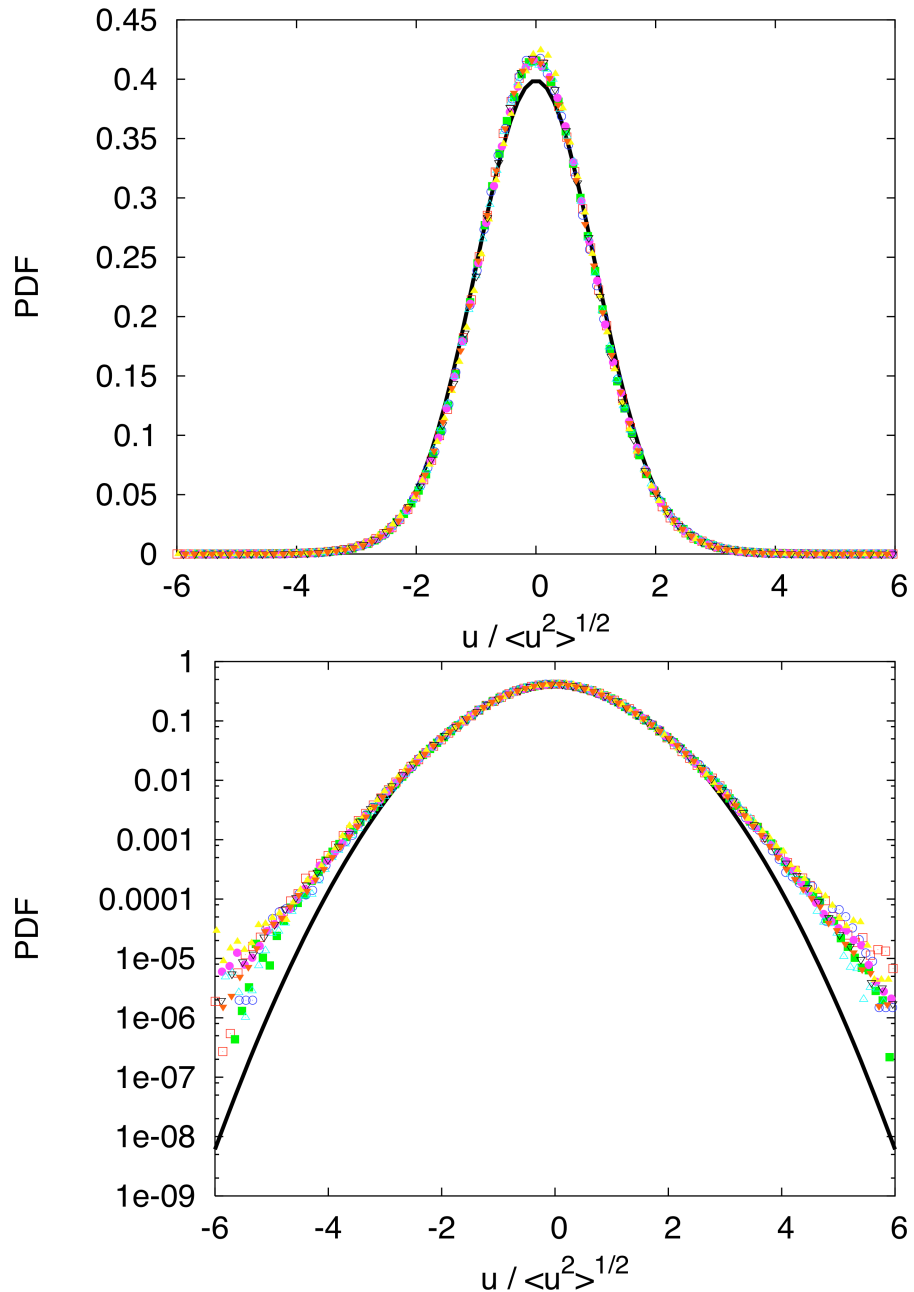


Figure 4.5: Axial velocity PDFs in the $(5 \text{ cm})^3$ measurement volume, normalized by the velocity variance. The solid line is a standardized Gaussian. Data is shown for $R_\lambda = 200$ (\square), $R_\lambda = 240$ (\blacksquare), $R_\lambda = 290$ (\circ), $R_\lambda = 350$ (\bullet), $R_\lambda = 415$ (\triangle), $R_\lambda = 500$ (\blacktriangledown), $R_\lambda = 690$ (\triangledown), and $R_\lambda = 815$ (\blacktriangledown). Just as in the smaller measurement volume, the tails of the axial velocity PDF are super-Gaussian.

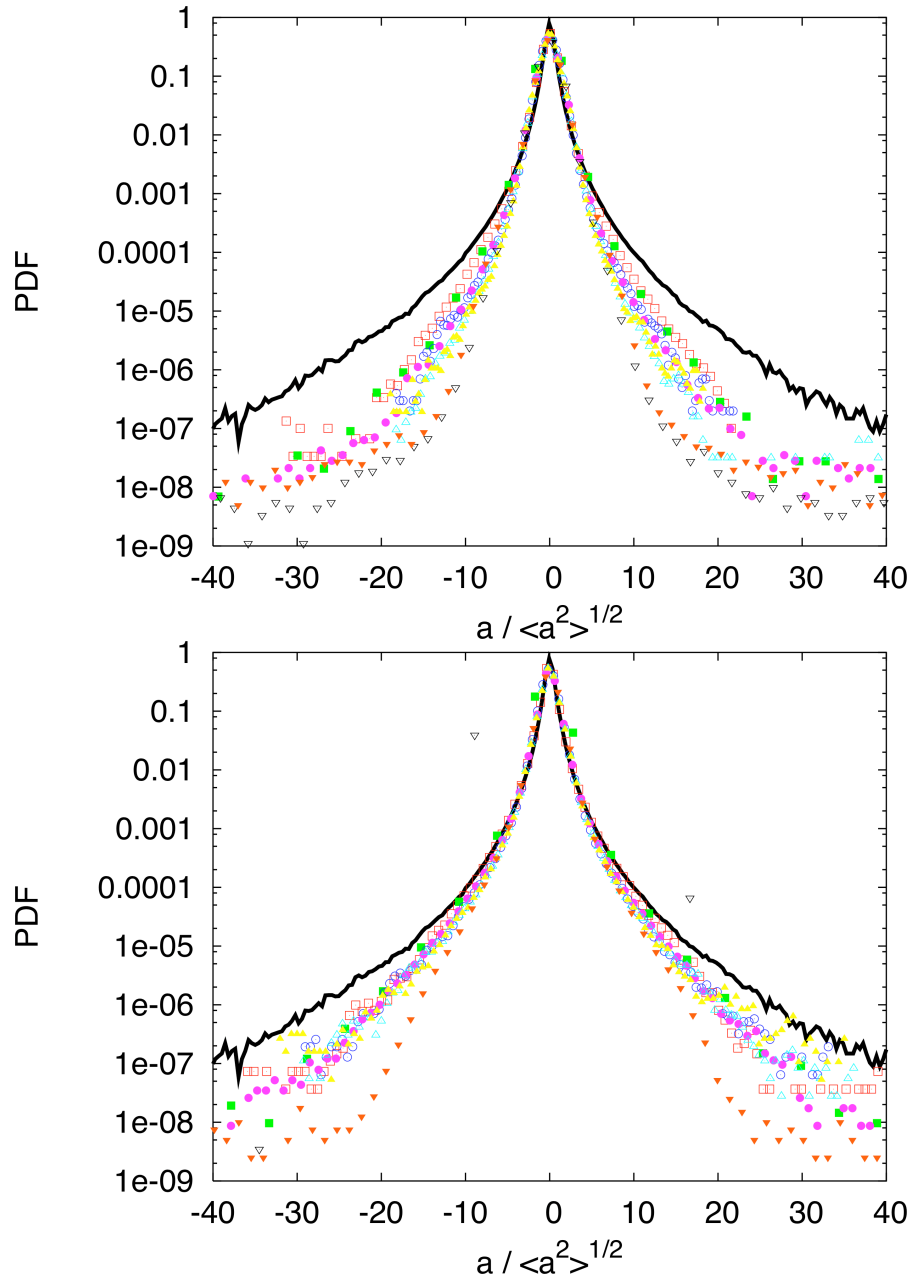


Figure 4.6: Acceleration PDFs in the $(5 \text{ cm})^3$ measurement volume, normalized by the acceleration variance. The solid line is the data measured by Mordant *et al.* (2004a). Data is shown for $R_\lambda = 200$ (\square), $R_\lambda = 240$ (\blacksquare), $R_\lambda = 290$ (\circ), $R_\lambda = 350$ (\bullet), $R_\lambda = 415$ (\triangle), $R_\lambda = 500$ (\blacktriangle), $R_\lambda = 690$ (∇), and $R_\lambda = 815$ (\blacktriangledown). The upper plot shows the radial (x) component, while the lower plot shows the axial component. For all components, the intense acceleration events are significantly under-resolved.

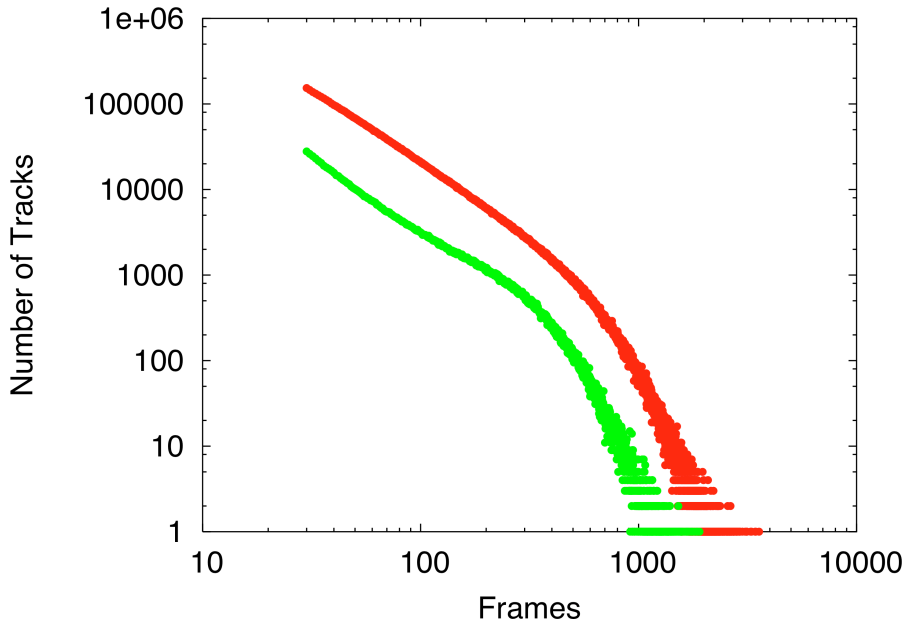


Figure 4.7: Distribution of track lengths at $R_\lambda = 690$ in both the large measurement volume (red symbols) and small measurement volume (green symbols). Tracks shorter than 30 frames were not saved.

Bias errors are more subtle, and cannot be corrected simply by gathering larger data sets. In a particle tracking experiment, biases arise due to the finite measurement volume that is only a subvolume of the entire flow.

As mentioned above, few tracks remain in the measurement volume for long times. In addition to poor statistics at long times, however, bias errors become an issue. The particles that remain in the volume for a long time are more likely either to be moving very slowly or to have trajectories that fold back on themselves. These particles are therefore not representative of the full ensemble of particles in the turbulence, and averages over these particles cannot be considered to be true ensemble averages. More discussion of this type of bias error is given by Mordant (2001), Crawford (2004), and Mordant *et al.* (2004b) in the context of the velocity autocorrelation function. This is the primary source of bias in our experiments.

To avoid this error, we do not measure quantities that mix scales, such as the autocorrelation, but instead focus on quantities that are local in scale, such as the structure functions.

4.2 Eulerian Structure Functions

Some of the most well-studied quantities in turbulence are the moments of the Eulerian velocity increments, known as the structure functions. Defining the velocity increment as $\delta\mathbf{u}(\mathbf{r}) \equiv \mathbf{u}(\mathbf{x} + \mathbf{r}) - \mathbf{u}(\mathbf{x})$, the structure function tensors are formally defined as

$$\mathbf{D}_p^E(\mathbf{r}) = \langle \delta\mathbf{u}(\mathbf{r})^p \rangle. \quad (4.1)$$

In homogeneous turbulence, the structure functions depend only on the separation \mathbf{r} and not the absolute positions of the two velocities.

The most important of the Eulerian structure functions are those of second and third order with $p = 2$ and 3 , respectively. Let us consider the second-order structure function. Assuming isotropy and using the theory of isotropic tensors, we can write

$$D_{ij}^E(\mathbf{r}) = A(r)r_i r_j + B(r)\delta_{ij}, \quad (4.2)$$

where A and B are functions only of the magnitude of \mathbf{r} . Therefore, two scalar functions are sufficient to characterize this second rank tensor fully. It is common to choose these two functions to be the longitudinal structure function $D_{LL}(r)$ where $\delta\mathbf{u}$ is parallel to the separation vector \mathbf{r} and the transverse structure function $D_{NN}(r)$ where it is orthogonal to \mathbf{r} . Defining $\hat{\mathbf{r}}$ as a unit vector in the direction of

\mathbf{r} and $\hat{\boldsymbol{\xi}}$ as a unit vector orthogonal to \mathbf{r} , we have that

$$\begin{aligned} D_{LL}(r) &= D_{ij}^E \hat{r}_i \hat{r}_j = A(r)r^2 + B(r) \\ D_{NN}(r) &= D_{ij}^E \hat{\xi}_i \hat{\xi}_j = B(r), \end{aligned} \quad (4.3)$$

so that

$$D_{ij}^E(\mathbf{r}) = [D_{LL}(r) - D_{NN}(r)] \frac{r_i r_j}{r^2} + D_{NN}\delta_{ij}. \quad (4.4)$$

These two scalar functions are not independent. Using the incompressibility condition, $\partial D_{ij}(\mathbf{r})/\partial r_j = 0$, and so

$$D_{NN}(r) = D_{LL}(r) + \frac{1}{2}r \frac{dD_{LL}(r)}{dr}. \quad (4.5)$$

In the inertial range, K41 gives

$$D_{LL} = C_2(\epsilon r)^{2/3}, \quad (4.6)$$

so that

$$D_{NN} = \frac{4}{3}C_2(\epsilon r)^{2/3}. \quad (4.7)$$

These results for the scaling of the structure functions in the inertial range are of prime importance for experimental studies of turbulence due to the presence of the dissipation rate ϵ . The dissipation rate plays a central role both in the original K41 theory and in modern studies of turbulent intermittency, and so determining ϵ is of the utmost importance in any turbulence experiment. In general, the dissipation rate is defined as

$$\epsilon = 2\nu \langle s_{ij} s_{ij} \rangle, \quad (4.8)$$

where

$$s_{ij} = \frac{1}{2} \left(\frac{\partial u_i}{\partial x_j} + \frac{\partial u_j}{\partial x_i} \right) \quad (4.9)$$

is the symmetric part of the velocity gradient tensor and is known as the rate of strain. Direct measurement of ϵ requires a full determination of the velocity gradient tensor. Such measurements are, in general, exceedingly difficult to perform experimentally, although they have been shown to be possible in Lagrangian particle tracking systems at low Reynolds number (Lüthi, 2002). As shown in eqs. (4.6) and (4.7), however, measurements of the Eulerian structure functions in the inertial range can provide an indirect measurement of the dissipation rate, provided that the scaling constant C_2 is known. The importance of the dissipation rate coupled with the difficulty of its direct measurement have made C_2 one of the best-determined constants in turbulence, with a value of 2.13 ± 0.22 (Sreenivasan, 1995). Our measurements of the dissipation rate ϵ shown in Tables 3.2 and 3.3 are made in this way.

Figure 4.8 shows a typical measurement of the longitudinal and transverse Eulerian structure functions in our experiment in the small measurement volume. The transverse structure functions have been multiplied by $3/4$ in order to make the inertial range values of the structure functions the same. In Fig. 4.9, we show D_{LL} and D_{NN} compensated by $C_2 r^{2/3}$ in order to determine the energy dissipation rate from the plateau value.

The third-order Eulerian structure function is perhaps even more important than the second order. By extending the results of von Kármán and Howarth (1938), Kolmogorov (1941*b*) was able to show directly from the Navier-Stokes equations that in stationary, homogeneous, isotropic turbulence

$$D_{LLL}(r) = -\frac{4}{5}\epsilon r + 6\nu \frac{\partial D_{LL}(r)}{\partial r}, \quad (4.10)$$

where $D_{LLL}(r)$ is the third-order longitudinal structure function, defined analogously to $D_{LL}(r)$ above. In the inertial range, the viscous term is negligible,

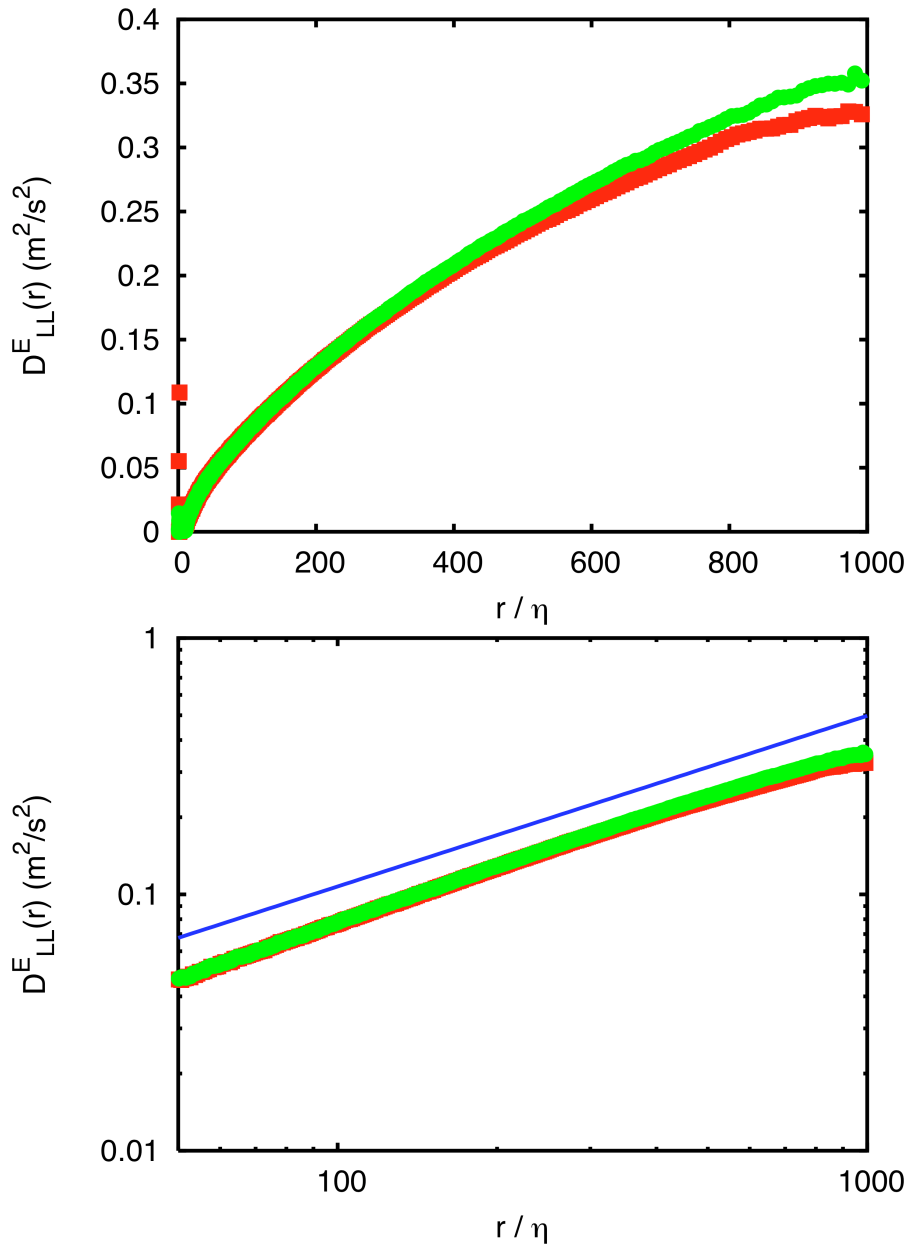


Figure 4.8: Second-order Eulerian velocity structure function at $R_\lambda = 815$ measured in the small measurement volume. The top plot shows $D_{LL}(r)$ (■) and $(3/4)D_{NN}$ (●) with the horizontal coordinate scaled by the Kolmogorov length. The bottom plot shows the same data plotted in logarithmic coordinates to show the power law scaling. The solid line is an $r^{2/3}$ power law for comparison.

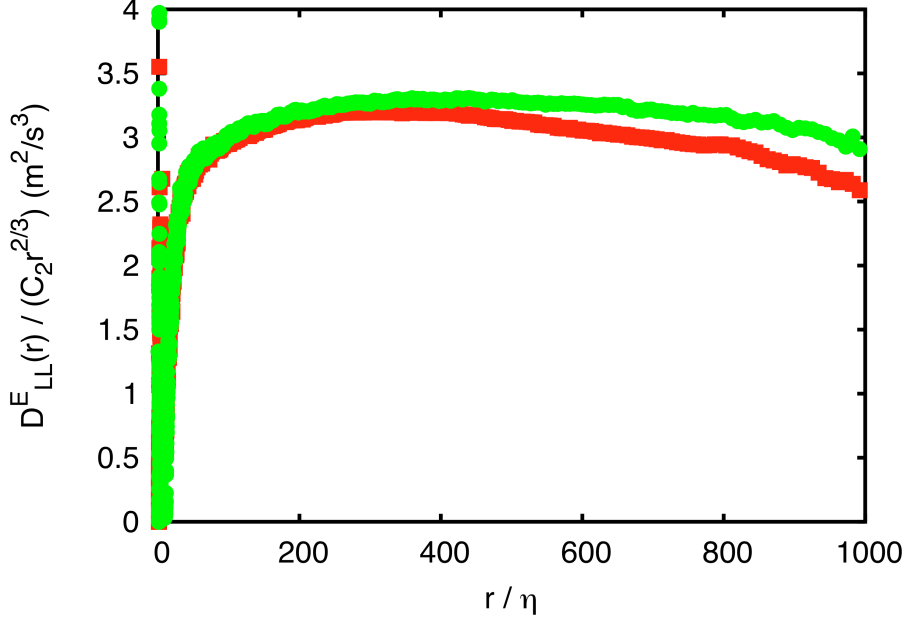


Figure 4.9: Compensated Eulerian structure function at $R_\lambda = 815$. The longitudinal (■) and transverse (●) structure functions have been scaled so that they should show a plateau with a value of ϵ in the inertial range.

according to the K41 hypotheses, and so

$$D_{LLL}(r) = -\frac{4}{5}\epsilon r. \quad (4.11)$$

This result is known as the Kolmogorov 4/5 law. Unlike the second-order structure function, where C_2 must be determined experimentally by comparison with an alternate measurement of the dissipation rate, the determination of ϵ from the third-order structure function is exact.

$D_{LLL}(r)$ as measured at $R_\lambda = 815$ in the small measurement volume is shown in Fig. 4.10. It is clear that the scaling range is smaller for the third-order structure function than it is for the second-order structure functions. The compensated third-order structure function is shown in Fig. 4.11. While the scaling range is very short, the value of ϵ measured from D_{LLL} is consistent with the values measured from the second-order structure functions.

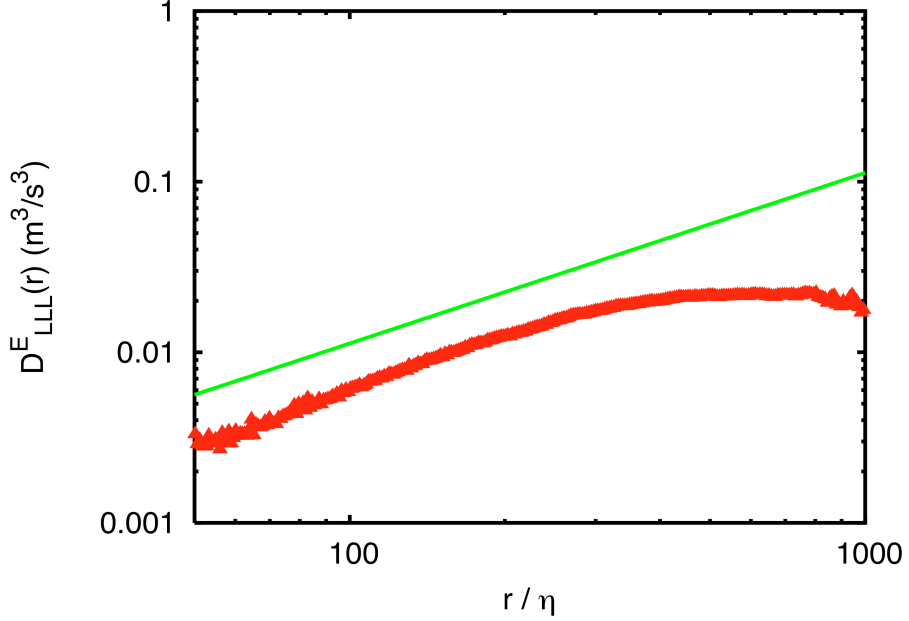


Figure 4.10: Third-order Eulerian velocity structure function at $R_\lambda = 815$ in the small measurement volume. The solid line is a linear power law for comparison. The scaling range for $D_{LLL}(r)$ is shorter than for $D_{LL}(r)$ and $D_{NN}(r)$.

4.3 Lagrangian Structure Functions

Just as the Eulerian structure functions have been instrumental in understanding turbulence, the similarly-defined Lagrangian structure functions are a basic tool in describing turbulence in the Lagrangian framework. To define them, let us consider a Lagrangian velocity increment, $\delta\mathbf{u}(\tau) = \mathbf{u}(t + \tau) - \mathbf{u}(t)$. These increments are taken along the trajectory of an individual fluid element, and are a function of time rather than of space. Since time is not a vector, the Lagrangian structure functions are in some sense easier to work with, since there is no separation vector to project onto. K41 therefore says that, in the inertial range,

$$\mathbf{D}_p^L(\tau) \equiv \langle \delta\mathbf{u}(\tau)^p \rangle \sim \tau^{p/2}, \quad (4.12)$$

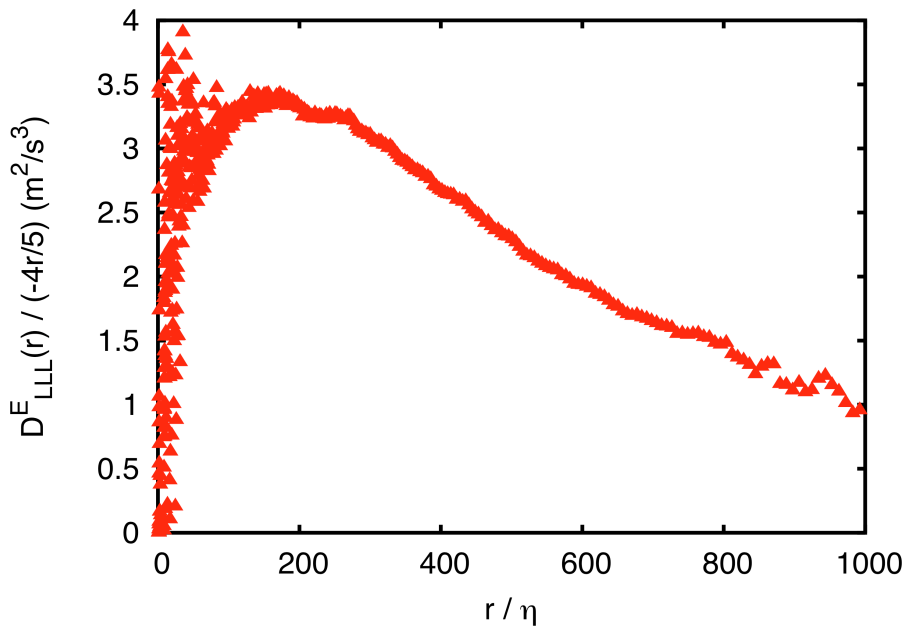


Figure 4.11: Compensated third-order Eulerian velocity structure function at $R_\lambda = 815$. While the scaling range for $D_{LLL}(r)$ is short, the value of ϵ measured from the plateau region is consistent with that measured from the second-order structure functions.

and that furthermore, these tensors should be isotropic. In the following sections, we discuss both the second-order Lagrangian structure function in detail as well as the scaling behavior of the high-order structure functions.

4.3.1 Second Order Structure Functions

In the inertial range, K41 states that the second-order Lagrangian structure function should scale as

$$D_{ij}^L(\tau) = \langle \delta u_i(\tau) \delta u_j(\tau) \rangle = C_0 \epsilon \tau \delta_{ij}, \quad (4.13)$$

where δ_{ij} is the Kronecker delta and C_0 is presumed to be a universal scaling constant for all turbulent flows, similar to C_2 defined above for the second-order Eulerian structure function. Unlike C_2 , however, the value of C_0 is very poorly determined. Lien and D'Asaro (2002) have given a review of the values of C_0 reported in the literature. These previously measured values range from 2.1 to 7.0, spanning nearly an order of magnitude. In particular, there have only been three previous experimental measurements of C_0 (Hanna, 1981; Lien *et al.*, 1998; Mordant *et al.*, 2001). All suffered from large uncertainties, and none resolved the Kolmogorov scales. Given that C_0 is an important parameter in stochastic models of turbulent transport and dispersion (Rodean, 1991; Sawford, 1991; Weinman and Klimenko, 2000), as well as remarkably being connected both to the Richardson constant governing the separation of fluid element pairs and to the structure functions of the fluctuations of a scalar field passively advected by the turbulence (Sawford, 2001), a more precise determination of C_0 is needed. The work presented here has previously been reported by Ouellette, Xu, Bourgoin, and Bodenschatz (2006c).

The second-order Lagrangian structure function measured at $R_\lambda = 815$ in the large measurement volume is shown in Fig. 4.12. As expected, the long-time be-

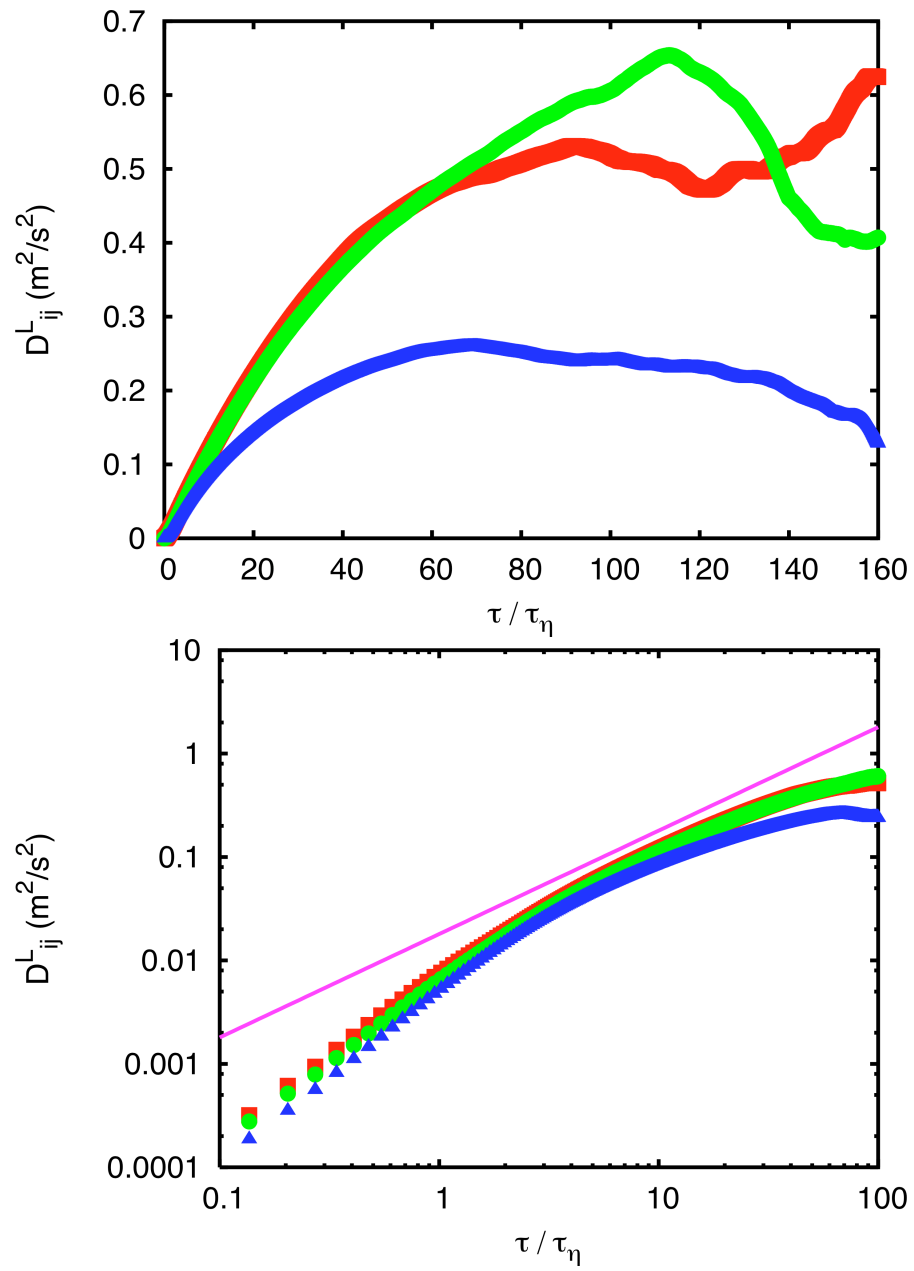


Figure 4.12: Second-order Lagrangian velocity structure function at $R_\lambda = 815$. The bottom plot shows the same data plotted in logarithmic coordinates. The solid line is linear in τ , corresponding to the K41 prediction for the scaling of the structure function in the inertial range. In both plots, the \blacksquare correspond to the xx component, the \bullet to the yy component, and the \blacktriangle to the axial zz component.

havior of the structure function reflects the large-scale anisotropy in our flow, reproducing the difference in the RMS velocity measured in the two radial directions and in the axial direction.

In comparison with the second-order Eulerian structure function shown in Fig. 4.8, the inertial range seen in the Lagrangian structure function occurs at very short times, of the order of a few τ_η compared with several hundred η in the Eulerian case, and for short durations. In analogy with the typical Eulerian definition (Anselmet *et al.*, 1984; Frisch, 1995), we define the Lagrangian inertial range to be the region where the second-order structure function scales linearly with time, as predicted by K41. We note that since the K41 prediction for the second-order Lagrangian structure function is linear in ϵ we expect no intermittency correction, and therefore this working definition of the Lagrangian inertial range should be valid.

The shortness of the Lagrangian inertial range is shown very clearly when we plot the second-order structure function compensated by $\tau\epsilon$, shown in Fig. 4.13. The most striking feature of Fig. 4.13, however, is the reflection of the large-scale anisotropy of our flow in the small-scale behavior of the structure function. Recall the K41 hypothesis of local isotropy: turbulence statistics are presumed to “forget” the large-scale flow structure as energy follows the Richardson cascade down to small scales. In many ways, the celebrated universality of turbulence statistics rests on this assumption of local isotropy, for if small-scale statistics depend on the detailed flow geometry at large scales, they cannot be universal for different flows. Observation of persistent anisotropy at small scales therefore calls many of the most basic assumptions of turbulence theory into question.

The large-scale flow in our cylindrical tank is approximately axisymmetric. Ax-

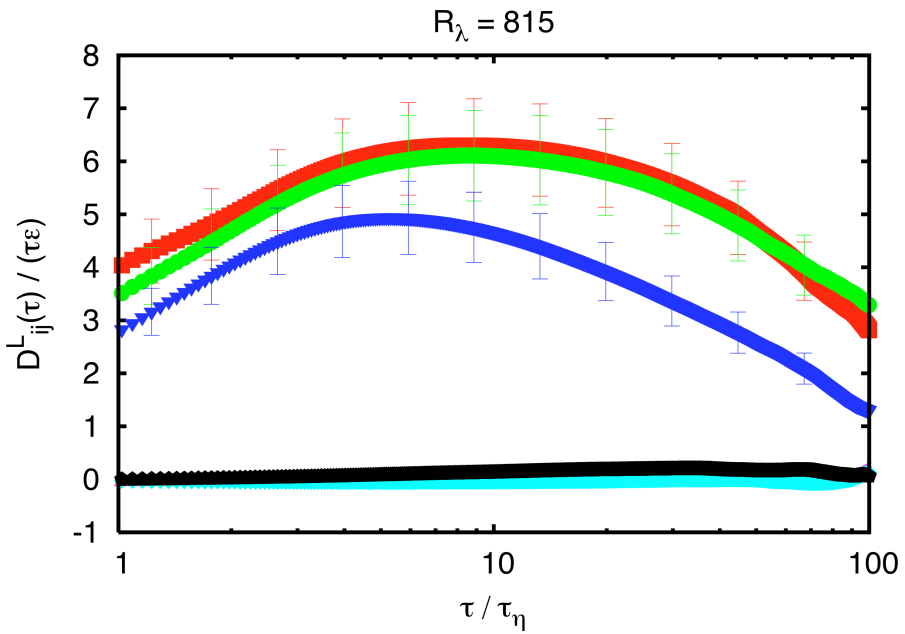


Figure 4.13: The xx (■), yy (●), and zz (▼) components of the compensated Lagrangian structure functions at $R_\lambda = 815$. The other symbols show the off-diagonal components. The structure functions have been scaled by $\tau\epsilon$ so that they should show a plateau in the inertial range. The time axis has been normalized by the Kolmogorov time. The relative magnitude of the radial and axial components reflects the anisotropy of our large-scale flow.

isymmetric turbulence has been the subject of prior theoretical work (Batchelor, 1946; Chandrasekhar, 1950; Ould-Rouiss, 2001) as the simplest relaxation of the local isotropy condition, but has unfortunately not yielded experimentally verifiable predictions similar to those made by K41. The data shown in Fig. 4.13 reflects the large-scale axisymmetry very well: the off-diagonal terms of the structure function tensor are zero to within the experimental precision, and the two radial components are equal and larger than the axial component. It is important to note, however, that we see anisotropy only in the magnitude of the structure function, measured by the value of C_0 , and not in the scaling exponent, which is unity for both the radial and the axial components.

The lack of a long scaling region at moderate Reynolds numbers has made prior measurements of the scaling constant C_0 difficult, accounting for the dearth of such data in the literature. Even at $R_\lambda = 815$, we do not see a very long scaling range. We can nevertheless estimate values for C_0 based on the peaks of the compensated structure functions measured for various Reynolds numbers. As has been seen previously (Sawford, 1991), we find a Reynolds number dependence of C_0 . Our measurements of C_0 are shown as a function of Reynolds number in Fig. 4.14. The data appear to be reaching a plateau at the highest Reynolds numbers measured, suggesting that Yeung's (2002) estimate that true inertial range scaling of Lagrangian quantities could be seen at Reynolds numbers of $R_\lambda = 600 - 700$ is accurate.

The solid lines in Fig. 4.14 are fits of a model due to Sawford (1991) to capture the Reynolds number dependence of C_0 . By fitting his second-order Lagrangian stochastic model to low-Reynolds number DNS, Sawford (1991) proposed that

$$C_0 = \frac{C_0^\infty}{1 + AR_\lambda^{-1.64}}, \quad (4.14)$$

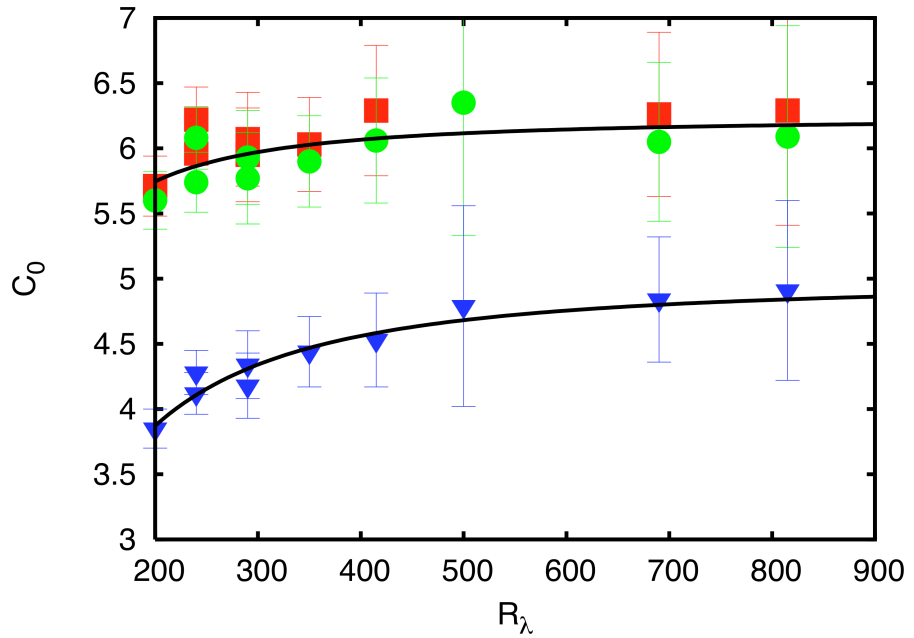


Figure 4.14: Measurements of C_0 from the Lagrangian structure function tensor for the xx component (■), yy component (●), and zz component (▼) as a function of Reynolds number. The zz component C_0 values are smaller than those measured for the two radial components, presumably due to the large scale axisymmetry of our flow. C_0 is observed to increase weakly with Reynolds number. The solid lines are fits of Sawford's model (eq. (4.14)) for the Reynolds number dependence of C_0 (Sawford, 1991). We note that due to the time resolution in the $R_\lambda = 500$ data run, we encountered large uncertainties and were not able to measure a C_0 value from the xx component. We have therefore not included the $R_\lambda = 500$ data points in the fits of eq. (4.14).

where C_0^∞ is the asymptotic value of C_0 at infinite Reynolds number. From his fits, Sawford found that $A \approx 365$, and we find A values of the same order. By fitting this form to our C_0 data, as shown in Fig. 4.14, we find that $C_0^\infty = 6.2 \pm 0.3$ for the radial structure functions and $C_0^\infty = 5.0 \pm 0.4$ for the axial structure functions. Sawford's (1991) scaling form for C_0 appears to fit our measured data very well, but does not predict a return to isotropy at infinite Reynolds number. Instead, the model suggests that the anisotropy persists even as the Reynolds number increases without bound. Further tests of this prediction must wait until a new generation of turbulence generators is developed that can reach much higher Reynolds numbers while retaining measurable length time scales, such as the new high-pressure SF₆ wind tunnel under construction at the Max Planck Institute for Dynamics and Self-Organization.

We have also investigated the scaling behavior of the Lagrangian velocity spectrum $\mathbf{E}^L(\omega)$, defined as the Fourier transform of the Lagrangian velocity autocorrelation tensor. Since the second-order structure function is also related to the velocity autocorrelation, an equivalence can be made between the structure function and the spectrum. From Monin and Yaglom (1975),

$$\begin{aligned} D_{ij}^L(\tau) &= 2 \int_0^\infty (1 - \cos \omega \tau) E_{ij}^L(\omega) d\omega \\ &= C_0 \epsilon \tau \delta_{ij} \end{aligned} \quad (4.15)$$

in the inertial range. K41 tells us that

$$E_{ij}^L(\omega) = B_0 \epsilon \omega^{-2} \delta_{ij} \quad (4.16)$$

in the inertial range, and so

$$C_0 \epsilon \tau = 2 B_0 \epsilon \int_0^\infty \frac{1 - \cos \omega \tau}{\omega^2} d\omega = \pi B_0 \epsilon \tau, \quad (4.17)$$

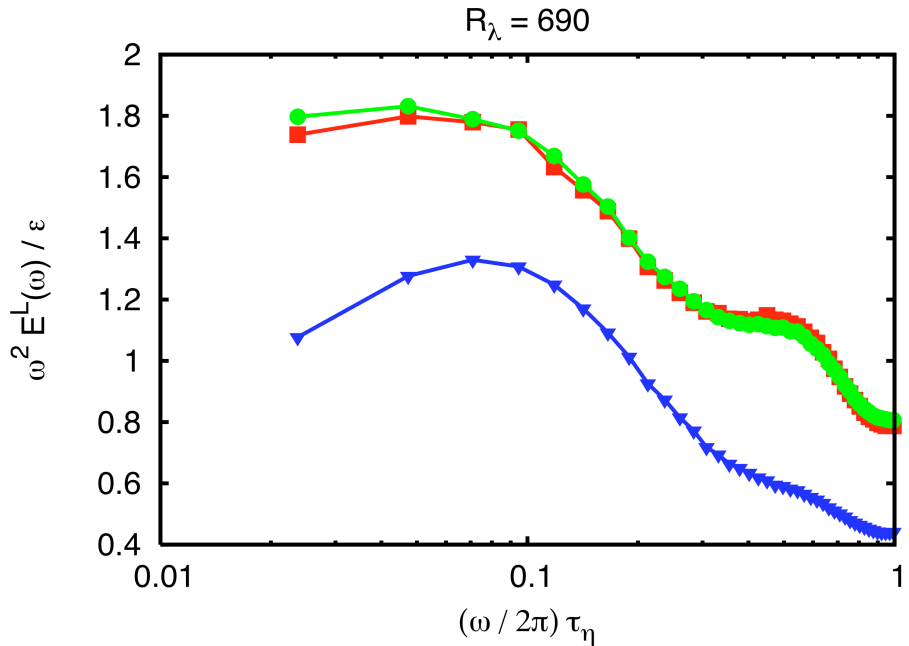


Figure 4.15: Compensated Lagrangian velocity spectra at $R_\lambda = 690$ in the x direction (■), y direction (●), and z direction (▼). By scaling the spectra by $\epsilon\omega^{-2}$, we expect to see a plateau in the inertial range with value B_0 . The frequency axis has been scaled by the Kolmogorov frequency. As above, we note that the difference in magnitude between the radial spectra and the axial spectrum reflects the large scale structure of our flow.

so that

$$C_0 = \pi B_0. \quad (4.18)$$

In addition to giving an independent way to measure the constant C_0 , it has also been suggested that the spectrum may show better inertial range scaling behavior than the structure function at low Reynolds numbers (Lien and D'Asaro, 2002).

Our measurement of the diagonal components of the Lagrangian spectrum at $R_\lambda = 690$ is shown in Fig. 4.15, compensated by $\epsilon\omega^{-2}$. The frequency axis has been scaled by the Kolmogorov frequency; note that in the frequency domain the inertial range corresponds to low frequencies and therefore long tracks. Such long particle tracks are rare in our experiment, as seen in Fig. 4.7, and therefore the inertial range in the frequency domain is under-resolved. Nevertheless, we can estimate values of the scaling constant B_0 from the peaks of the compensated spectra in the inertial range. It is also clear from Fig. 4.15 that the anisotropy observed in our measurements of the structure function is also present in the spectrum.

Just as we measured the scaling constant C_0 as a function of Reynolds number, we have also investigated the dependence of B_0 on R_λ , shown in Fig. 4.16. Contrary to the predictions of Lien and D'Asaro (2002), we find a slightly stronger Reynolds number dependence for the spectral scaling constant. We have again used Sawford's (1991) model to extrapolate asymptotic values for B_0 , finding that $\pi B_0^\infty = 6.3 \pm 0.4$ for the radial components and $\pi B_0^\infty = 4.7 \pm 0.4$ for the axial component. These values are in excellent agreement with the asymptotic values estimated for C_0 from the structure functions. In particular, the anisotropy again persists for all Reynolds numbers.

Persistent anisotropy has been studied previously in Eulerian studies of homogeneous shear (Pumir and Shraiman, 1995; Pumir, 1996; Garg and Warhaft,

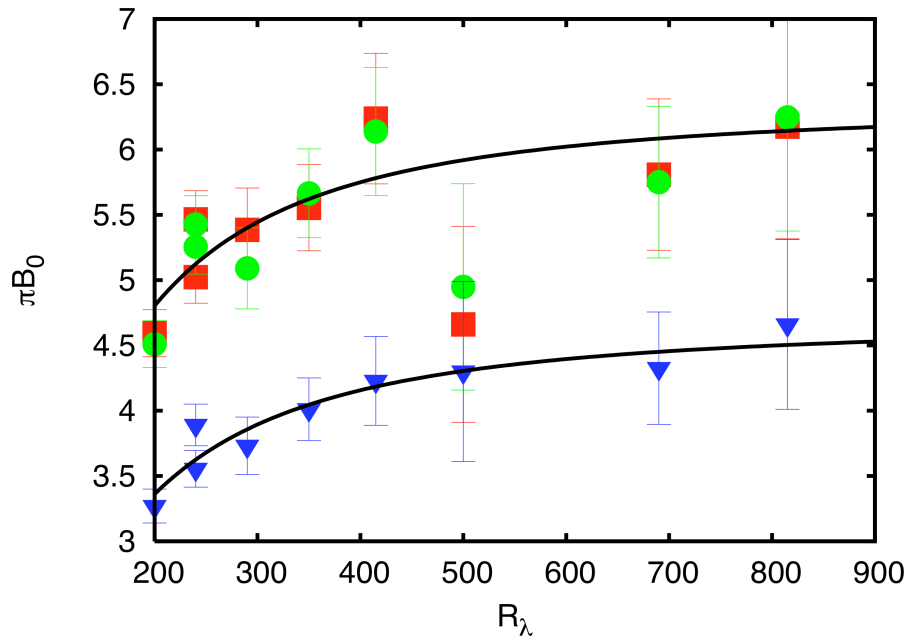


Figure 4.16: Measurements from the Lagrangian spectra for the x direction (\blacksquare), y direction (\bullet), and z direction (\blacktriangledown). The solid lines are again fits of eq. (4.14). Despite the larger degree of scatter in the data, we find good agreement with C_0 as calculated directly from the structure functions. Again, we have not included the $R_\lambda = 500$ data point in the fits.

1998; Shen and Warhaft, 2000) and Lagrangian studies of fluid element acceleration (La Porta *et al.*, 2001; Voth *et al.*, 2002). This anisotropy has not, however, been observed in previous studies of C_0 . Indeed, only a few measurements of C_0 have previously been made, as mentioned above. The experimental studies suffered both from large uncertainties and from overly large Lagrangian tracers that may have averaged out the smallest turbulence scales. Hanna (1981) measured the Lagrangian spectra in the atmospheric boundary layer by tracking large, neutrally buoyant balloons using radio triangulation, but acknowledged significant uncertainty in the measurements. He reported a value of 4 ± 2 for πB_0 . Though he measured all three diagonal components of the Lagrangian spectrum tensor, his uncertainties were too large to find any anisotropy. Lien *et al.* (1998) measured one-dimensional Lagrangian spectra using large floaters, approximately 1 m in scale, in the oceanic boundary layer. Due to the considerable noise in their measurements, they were only able to estimate that the value of πB_0 lies somewhere between 3.1 and 6.2. Since they measured only a single component of the spectrum, they were also unable to address questions of isotropy. Mordant *et al.* (2001) measured the radial Lagrangian structure function and spectrum in a one-dimensional laboratory acoustic particle tracking experiment in a von Kármán swirling flow similar to ours. While their Lagrangian tracers were significantly smaller than those of Hanna (1981) and Lien *et al.* (1998), they were still at least an order of magnitude larger than the Kolmogorov scale. Mordant *et al.* (2001) measured a maximum value of 4 for C_0 , though this result may be depressed by the filtering effect of their large tracers. Lien and D'Asaro (2002) have estimated a value of 5.5 for πB_0 from the spectral data of Mordant *et al.* (2001); since the inertial range of the spectrum is influenced by longer particle tracks than the structure function,

the filtering effects may be less of an issue. Again, since Mordant *et al.* (2001) measured only one component of both the structure function and the spectrum, they were unable to address the question of isotropy.

Both the structure function and the spectrum have also been studied in DNS (see, for example, Yeung (2001)). Since the Reynolds number must be high, however, to determine an accurate value for C_0 , DNS results are not conclusive. A recent 2048^3 DNS study at higher Reynolds number, however, has found results close to our measured radial values of C_0 (Yeung *et al.*, 2005). DNS, however, though it resolves the full structure function and spectrum tensors, is usually performed assuming homogeneity and isotropy, and so cannot address the persistence of large-scale anisotropy.

The anisotropy we see in C_0 and πB_0 persists for all Reynolds numbers measured. Figure 4.17 shows the ratio of the radial values of C_0 and πB_0 to the axial values as a function of Reynolds number. The anisotropy quantified in this way decreases weakly with Reynolds number, but is still strongly present even at the highest Reynolds numbers measured. This result is in contrast with measurements of the anisotropy in the acceleration variance made in this same experiment (La Porta *et al.*, 2001; Voth *et al.*, 2002), where the anisotropy was found to decrease much faster with Reynolds number. The current results show that any return of C_0 to isotropy is very slow and would require exceedingly high Reynolds numbers to observe. This persistent anisotropy has serious implications for the connection of isotropic theory, models, and simulations to real-world turbulent flows. The question of how to relate such isotropic results to anisotropic flows will be a very important topic of future research in turbulence.

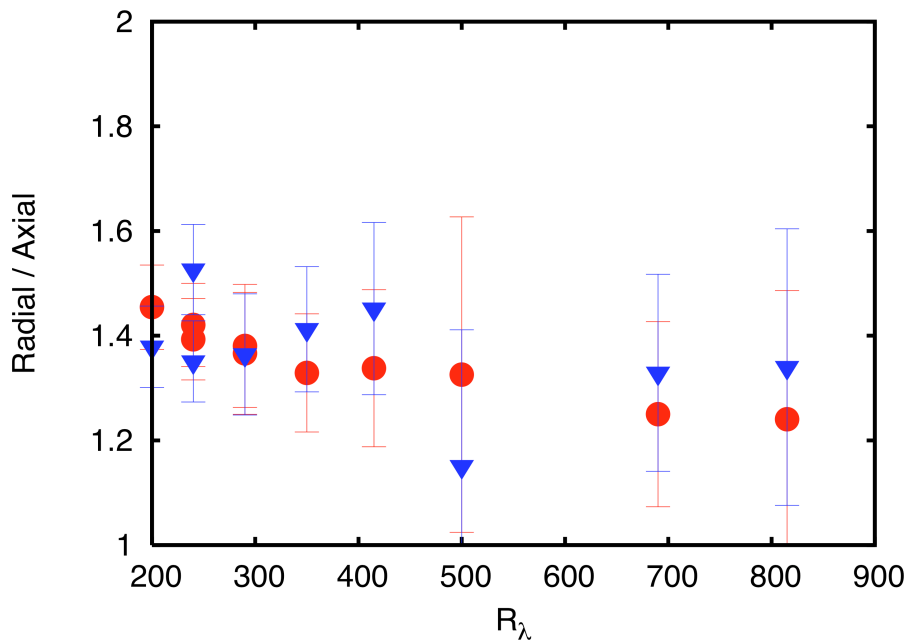


Figure 4.17: Ratio of the C_0 values measured in the radial direction and the C_0 values measured in the axial direction for both the structure function (●) and the spectrum (▼). While the anisotropy decreases weakly with increasing Reynolds number, the measurements remain far from isotropic even at the highest Reynolds numbers measured.

4.3.2 Higher-Order Structure Functions

While the second-order Lagrangian structure function is of great interest since the value of C_0 is a basic parameter in many models, precise measurements of the scaling of the higher-order Lagrangian structure functions can lead to a better understanding of intermittency. Recall that, according to K41, the Lagrangian structure function of order p scales in the inertial range as

$$D_p^L(\tau) \equiv \langle |\delta u(\tau)|^p \rangle \sim (\epsilon \tau)^{\zeta_p^L}, \quad (4.19)$$

where we have now taken the absolute value of the velocity increment in order to define the odd-order moments. K41 predicts that $\zeta_p^L = p/2$. But, as discussed above, since the mean rate of energy dissipation ϵ is insufficient to characterize turbulence, we expect deviations from the K41 prediction. This anomalous scaling is well-studied in the Eulerian framework (Anselmet *et al.*, 1984; Frisch, 1995; Chen *et al.*, 2005), but, as is usual, is not well-characterized in the Lagrangian framework. Mordant *et al.* (2001) measured the ζ_p^L for the first- through sixth-order Lagrangian structure functions. No other experimental measurements have been made, due in a large part to the inherent difficulties involved in directly recording Lagrangian information. Simulations can measure Lagrangian statistics more easily, but are limited by their low Reynolds numbers, especially since Lagrangian statistics require higher Reynolds numbers than their Eulerian counterparts for accurate measurement (Yeung, 2002). Nevertheless, a few such numerical studies have been performed. Biferale *et al.* (2004, 2005c) have studied the high-order Lagrangian structure functions in the context of the multifractal formalism. Mazzitelli and Lohse (2004) have studied the Lagrangian statistics of both fluid elements and bubbles in simulation. We here use our Lagrangian data to investigate the

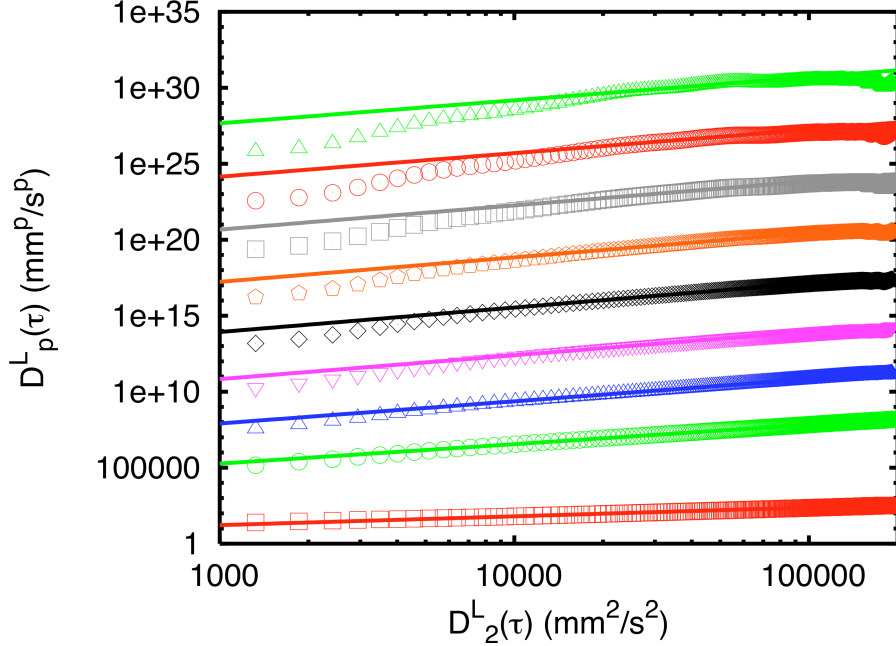


Figure 4.18: Extended self-similarity plot of the high-order Lagrangian structure functions at $R_\lambda = 815$. From top to bottom, the symbols correspond to the tenth-order structure function to the first-order structure function, with the second-order structure function omitted. The straight lines are fits to the data through which we extracted the scaling exponents. The power laws were fit only to values of $D_2^L(\tau)$ corresponding to times between $3\tau_\eta$ and $6\tau_\eta$, where $D_2^L(\tau)$ displayed a K41 scaling range with $\zeta_2^L \approx 1$.

scaling behavior of the high-order Lagrangian structure functions. These results were previously reported by Xu, Bourgoin, Ouellette, and Bodenschatz (2006a).

It has now become common in studies of the Eulerian structure function scaling exponents ζ_p^E to use the extended self-similarity (ESS) ansatz first proposed by Benzi *et al.* (1993). The foundation of ESS lies in Kolmogorov's (1941*b*) 4/5 law. Since Kolmogorov was able to show rigorously from the Navier-Stokes equations that $\zeta_3^E = 1$, we can write that

$$\langle |\delta u(r)|^p \rangle \sim r^{\zeta_p^E} \sim \langle |\delta u(r)|^3 \rangle^{\zeta_p^E} \quad (4.20)$$

exactly, for arbitrary order p . Plotting the structure function of order p versus the third-order structure function should therefore allow the measurement of ζ_p^E . Let us note that, strictly speaking, the Kolmogorov 4/5 law only applies to $\langle \delta u(r)^3 \rangle$ with no absolute value; Sreenivasan *et al.* (1996) have found small differences in the scaling of $\langle \delta u(r)^3 \rangle$ and $\langle |\delta u(r)|^3 \rangle$. The difference is slight, however, and is very difficult to observe experimentally.

The usefulness of ESS comes in the observation that imperfections in the power law scaling of the structure functions appear to be correlated between structure functions of different orders (Frisch, 1995). It has been suggested that this correlation of the small-scale imperfections of the structure functions may be evidence of new universal functions with the same scaling behavior in the near-dissipation range (Sreenivasan and Bershadskii, 2005). In any case, plotting the structure functions relative to one another often shows cleaner scaling behavior than plotting the raw structure functions.

Because of its utility in the Eulerian framework, researchers have extended the ESS technique to the Lagrangian case (Mordant *et al.*, 2001; Biferale *et al.*, 2004, 2005c). K41 predicts that $\zeta_2^L = 1$; though this has not been proved rigorously from the Navier-Stokes equations, deviation due to intermittency is not expected since K41 also predicts that the second-order Lagrangian structure function is linear in the dissipation rate (Boffetta *et al.*, 2002). In Fig. 4.18, we plot the Lagrangian structure functions of orders 1 through 10 measured at $R_\lambda = 815$ in the small measurement volume experiment using ESS.

Strictly speaking, ESS can only be used to measure relative scaling exponents. Since $\zeta_3^E = 1$ exactly, in the Eulerian case the relative exponents may be simply related to the true scaling exponents. This is not rigorously the case in the La-

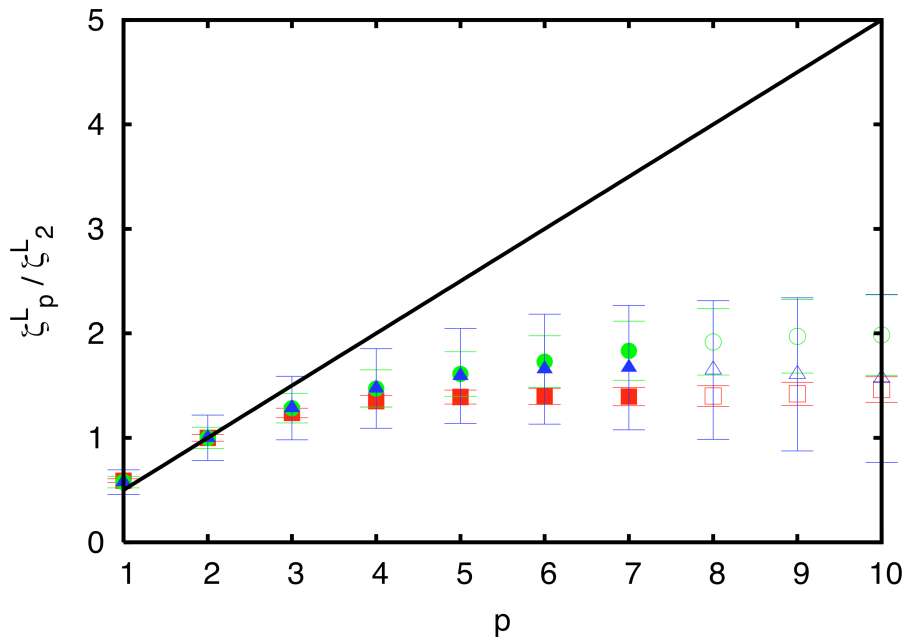


Figure 4.19: Anomalous scaling of the structure function relative scaling exponents ζ_p^L / ζ_2^L measured using ESS as a function of order. The solid line shows the K41 prediction for the scaling exponents, with $\zeta_2^L = 1$. Different symbols denote different Reynolds numbers: the \blacksquare are for $R_\lambda = 200$, the \bullet are for $R_\lambda = 690$, and the \blacktriangle are for $R_\lambda = 815$. Strong departure from the K41 prediction is clear for all Reynolds numbers investigated. Equivalent results are found without using ESS (not shown). Moments of orders higher than 7 are not as well-converged statistically as the lower-order moments, as suggested by their larger error bars. These high-order moments are plotted with open symbols.

grangian framework. To attempt to measure exponents as close to the true values as possible, we have fit power laws to the Lagrangian structure functions only in the region where the second-order structure function $D_2^L(\tau)$ showed a K41 inertial range so that $\zeta_2^L \approx 1$. For $R_\lambda = 690$ and $R_\lambda = 815$, we fit the structure functions between $3\tau_\eta$ and $6\tau_\eta$, and for $R_\lambda = 200$, we fit the structure functions between $2\tau_\eta$ and $4\tau_\eta$. These power law fits are shown in Fig. 4.18. The resulting relative exponents ζ_p^L/ζ_2^L are shown in Fig. 4.19 and are compared with the K41 prediction. The exponents measured without using ESS are very similar. We find that the ζ_p^L deviate more from the K41 prediction than their Eulerian counterparts, suggesting that intermittency is stronger in the Lagrangian framework. Interestingly, we see no anisotropy in the measured scaling exponents. Though we show only the radial values in Fig. 4.19, the axial exponents are the same to within the experimental accuracy.

There is some concern that the highest-order structure functions shown are not fully converged statistically. To investigate the convergence, we have computed the PDFs of the Lagrangian velocity increments for various times, as shown in Fig. 4.20 for $R_\lambda = 690$. The p^{th} moment of the velocity increment is converged if the tails of $\delta u^p P(\delta u)$ decrease, where $P(\delta u)$ is the PDF of the velocity increments. We show these moment PDFs in Fig. 4.21. For $p > 7$, the tails are noisy and do not return to zero, and so these moments may not be fully converged. For this reason, we plot their exponents with open symbols in Fig. 4.19.

Values of both the relative exponents are shown in Table 4.1, where they are compared with the DNS results of Biferale *et al.* (2005c) and the experimental measurements of Mordant *et al.* (2001). The absolute exponents are shown in Table 4.2. Our results agree within the uncertainty with those of Mordant *et al.* (2001);

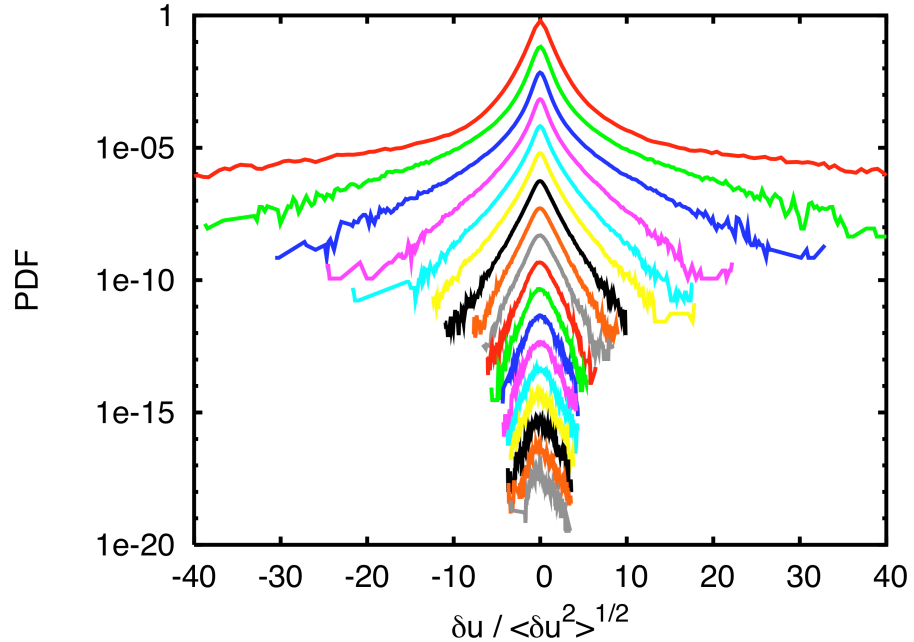


Figure 4.20: PDFs of the Lagrangian velocity increments $\delta u(\tau)$ at $R_\lambda = 690$. The PDFs have been offset for clarity. From top to bottom, the PDFs have been calculated for $\tau = \tau_\eta/5, 3\tau_\eta/5, \tau_\eta, 2\tau_\eta, 3\tau_\eta, 4\tau_\eta, 8\tau_\eta$, and then increasing by $4\tau_\eta$ each up to $52\tau_\eta \approx T_L/3$. For short times, the PDFs have very wide tails reminiscent of the acceleration PDF and are highly intermittent. The PDFs become more Gaussian as the time lag between the two velocities is increased.

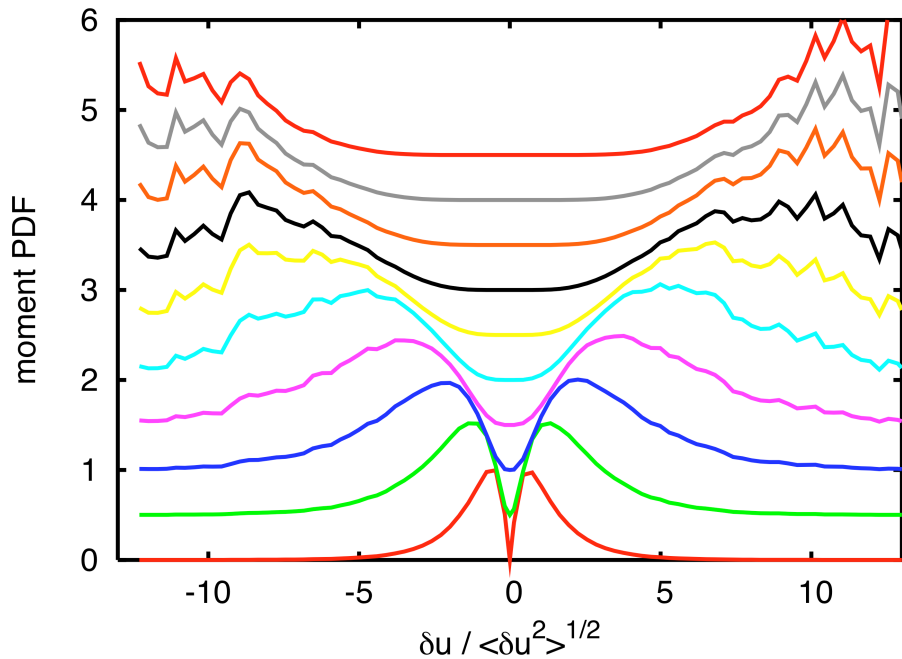


Figure 4.21: PDFs of the moments of the Lagrangian differences at $\tau = 4\tau_\eta$. Again, the curves are offset for clarity. From top to bottom, the curves correspond to the moment PDFs of orders 10 through 1. For orders higher than 7, the tails are very noisy, and there may be some problems with statistical convergence of the highest-order structure functions.

Table 4.1: Values of the relative scaling exponents measured in our experiment using ESS. The ESS curves were fit only in the range of times where the second order structure function displayed a K41 scaling range with exponent $\zeta_2^L \approx 1$. For comparison, we included the values measured from the DNS of Biferale *et al.* (2005c) at $R_\lambda = 284$ and the experiment of Mordant *et al.* (2001) at $R_\lambda = 740$.

R_λ	200	690	185	284	740
ζ_1^L/ζ_2^L	0.59 ± 0.02	0.58 ± 0.05	0.58 ± 0.12		0.56 ± 0.01
ζ_3^L/ζ_2^L	1.24 ± 0.04	1.28 ± 0.14	1.28 ± 0.30		1.34 ± 0.02
ζ_4^L/ζ_2^L	1.35 ± 0.06	1.47 ± 0.18	1.47 ± 0.38	1.7 ± 0.05	1.56 ± 0.06
ζ_5^L/ζ_2^L	1.39 ± 0.07	1.61 ± 0.21	1.59 ± 0.46	2.0 ± 0.05	1.73 ± 0.1
ζ_6^L/ζ_2^L	1.40 ± 0.08	1.73 ± 0.25	1.66 ± 0.53	2.2 ± 0.07	1.8 ± 0.2
ζ_7^L/ζ_2^L	1.39 ± 0.09	1.83 ± 0.28	1.67 ± 0.60		
ζ_8^L/ζ_2^L	1.40 ± 0.10	1.92 ± 0.32	1.65 ± 0.66		
ζ_9^L/ζ_2^L	1.42 ± 0.11	1.97 ± 0.35	1.61 ± 0.73		
ζ_{10}^L/ζ_2^L	1.46 ± 0.12	1.98 ± 0.38	1.57 ± 0.80		

Table 4.2: Values of the absolute scaling exponents measured in our experiment. The fits were performed over the same time ranges they were for the ESS method.

R_λ	200	690	815
ζ_1^L	0.58 ± 0.01	0.59 ± 0.04	0.58 ± 0.77
ζ_2^L	0.98 ± 0.02	1.03 ± 0.07	1.01 ± 0.15
ζ_3^L	1.21 ± 0.04	1.32 ± 0.11	1.30 ± 0.23
ζ_4^L	1.32 ± 0.05	1.51 ± 0.15	1.49 ± 0.31
ζ_5^L	1.36 ± 0.06	1.66 ± 0.18	1.61 ± 0.39
ζ_6^L	1.37 ± 0.07	1.78 ± 0.22	1.68 ± 0.46
ζ_7^L	1.37 ± 0.08	1.88 ± 0.26	1.69 ± 0.54
ζ_8^L	1.38 ± 0.09	1.97 ± 0.29	1.67 ± 0.62
ζ_9^L	1.40 ± 0.10	2.02 ± 0.33	1.62 ± 0.70
ζ_{10}^L	1.44 ± 0.11	2.03 ± 0.37	1.58 ± 0.77

all of the experimental results, however, are significantly lower than the simulation findings of Biferale *et al.* (2005c). Two parts of the analysis of Biferale *et al.* (2005c) stand out as unusual. First, they fit power laws to their structure functions between $10\tau_\eta$ and $50\tau_\eta$. Not only are these times significantly longer than those we fit to, but $50\tau_\eta$ is longer than their reported integral time scale. The exponents they have measured may therefore be contaminated by the large-scale forcing used in their DNS. They report that fitting their structure functions for times shorter than $10\tau_\eta$ produced scaling exponents that clustered near 2 as the order of the structure functions was increased, just as we see. In addition, Biferale *et al.* (2005c) removed all particle tracks that experienced accelerations greater than 7 times the RMS acceleration, attributing these high intensity acceleration events to particle trapping inside intense vortical structures. By filtering out these tracks, they find excellent agreement between their DNS and their multifractal model for the ζ_p^L , which we will discuss further in the next section. We, however, believe that these small-scale intense vortices are a fundamental part of the Lagrangian description of turbulence and cannot be removed without drastically altering the Lagrangian phenomenology.

We have seen from Figs. 4.18 and 4.19 that the scaling properties of the Lagrangian structure functions are anomalous when measured for time ranges where the second-order structure function shows a K41 scaling range, which we have defined to be the Lagrangian inertial range. If we blindly compensate the structure functions by their K41 scaling laws, however, a different picture emerges. As shown in Fig. 4.22, the structure functions do indeed show a K41 scaling range at every order, albeit at times that become shorter as the structure function order increases. The open circles in Fig. 4.22 show the centers of these K41 scaling ranges, which

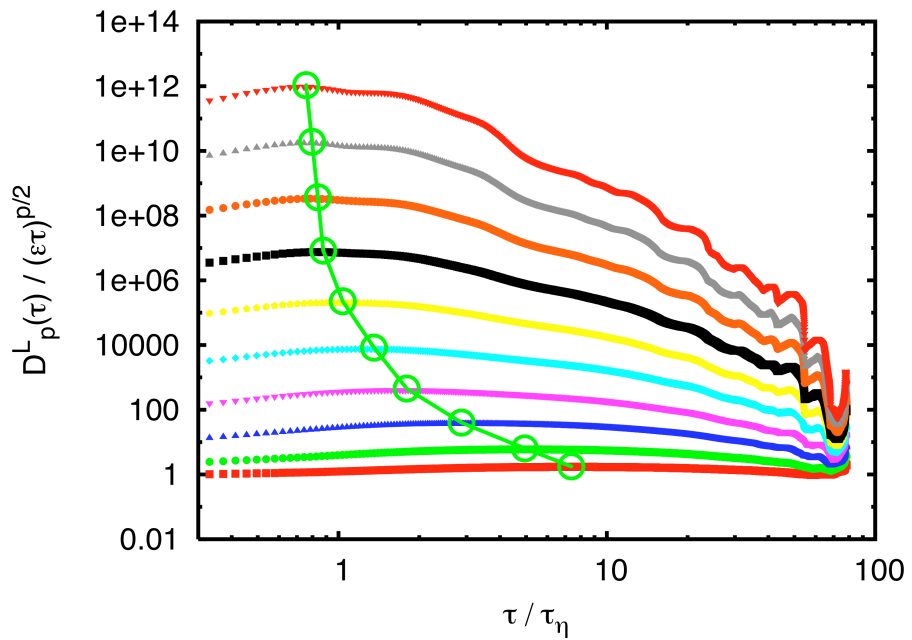


Figure 4.22: High order Lagrangian structure functions at $R_\lambda = 690$ compensated by the K41 predictions. The order of the structure function increases from 1 to 10 from the bottom curve to the top curve. A K41 scaling region is seen at all orders, but this plateau shifts to shorter times as the order of the structure function increases, as shown by the open circles.

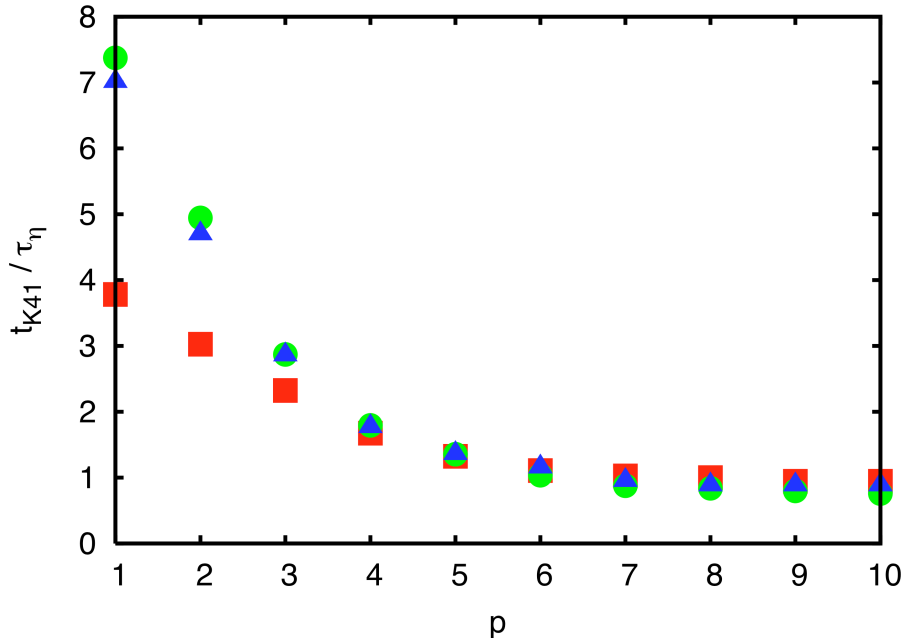


Figure 4.23: Shift of the effective inertial range as a function of structure function order p . Different symbols denote different Reynolds numbers: the ■ are for $R_\lambda = 200$, the ● are for $R_\lambda = 690$, and the ▲ are for $R_\lambda = 815$. For higher-order structure functions, the K41 inertial range scaling region appears at the same multiple of τ_η for all Reynolds numbers investigated.

occur at times we denote by t_{K41} .

Figure 4.22 suggests that t_{K41} decreases and saturates at a value smaller than τ_η as the structure function order increases. We have observed this effect for all three Reynolds numbers investigated. t_{K41} is shown as a function of structure function order in Fig. 4.23. While t_{K41} is smaller for the low-order structure functions at $R_\lambda = 200$ than at the higher Reynolds numbers, the $R_\lambda = 200$ values collapse with the higher Reynolds number data at high structure function orders. For all three Reynolds numbers measured, t_{K41} saturates at high structure function at times smaller than τ_η . This shift of the K41 inertial range towards the dissipation range may also be present in the Eulerian framework (Sreenivasan, 2005).

4.4 Single Particle Dispersion

Having now discussed the statistics of the velocity of a single fluid element in some detail, let us turn to position statistics. The motion of individual fluid elements in turbulence is much more complex than what would be expected from typical Brownian molecular diffusion. This dispersion of single fluid elements in a turbulent flow is common to many applied problems outside of typical homogeneous, isotropic turbulence studies; examples include the dispersal of marine larvae in the ocean (Siegel *et al.*, 2003) and the spread of plant pathogens in the atmosphere (Brown and Hovmøller, 2002). The relative motion of fluid elements is also of great relevance to these problems; we discuss turbulent relative dispersion in detail in the next chapter.

Just as with the velocity statistics discussed above, we consider here not the absolute position of a fluid particle but rather the position differences. Unfortunately, however, the raw position difference $\mathbf{x}(t + \tau) - \mathbf{x}(t)$ is not universal, and a Kolmogorov scaling law cannot be written for it (Monin and Yaglom, 1975). Instead, we consider the quantity

$$\delta y_i(\tau) = x_i(t + \tau) - [x_i(t) + u_i(t)\tau], \quad (4.21)$$

which measures the deviation of a fluid element trajectory from a straight track with constant velocity $\mathbf{u}(t)$. The usefulness of this quantity stems from the relation (Monin and Yaglom, 1975)

$$\delta y_i(\tau) = \int_0^\tau \delta u_i(t') dt'. \quad (4.22)$$

Let us consider the correlation of $\delta y_i(\tau)$ with the Lagrangian velocity increment.

Using eq. (4.22), we can write that

$$\begin{aligned}\langle \delta y_i(\tau) \delta u_j(\tau) \rangle &= \left\langle \left[\int_0^\tau \delta u_i(t') dt' \right] \delta u_j(\tau) \right\rangle \\ &= \int_0^\tau \langle \delta u_i(t') \delta u_j(\tau) \rangle dt'.\end{aligned}\quad (4.23)$$

The quantity inside the integral is nearly the Lagrangian structure function discussed above, except that the two velocity increments are taken over different times. We can now make use of an identity proved by Monin and Yaglom (1975) for isotropic turbulence, namely that

$$\langle \delta u_i(t') \delta u_j(t'') \rangle = \frac{1}{2} \delta_{ij} [D^L(t') + D^L(t'') - D^L(|t' - t''|)], \quad (4.24)$$

where $D^L(t)$ are the diagonal components of the second-order Lagrangian structure function tensor. We can then write the correlation of interest as

$$\begin{aligned}\langle \delta y_i(\tau) \delta u_j(\tau) \rangle &= \frac{1}{2} C_0 \epsilon \delta_{ij} \int_0^\tau (t' + \tau - |t' - \tau|) dt' \\ &= \frac{1}{2} C_0 \epsilon \tau^2 \delta_{ij}\end{aligned}\quad (4.25)$$

in the inertial range, where the last equality follows since $t' \leq \tau$ from the limits of integration. This correlation thus gives us yet another way to measure the Lagrangian structure function constant C_0 .

The autocorrelation of $\delta \mathbf{y}(\tau)$ gives us a fourth way to measure C_0 . In a similar manner as above, we can write

$$\begin{aligned}\langle \delta y_i(\tau) \delta y_j(\tau) \rangle &= \int_0^\tau dt' \int_0^\tau dt'' \langle \delta u_i(t') \delta u_j(t'') \rangle \\ &= \frac{1}{2} C_0 \epsilon \delta_{ij} \int_0^\tau dt' \int_0^\tau dt'' (t' + t'' - |t' - t''|).\end{aligned}\quad (4.26)$$

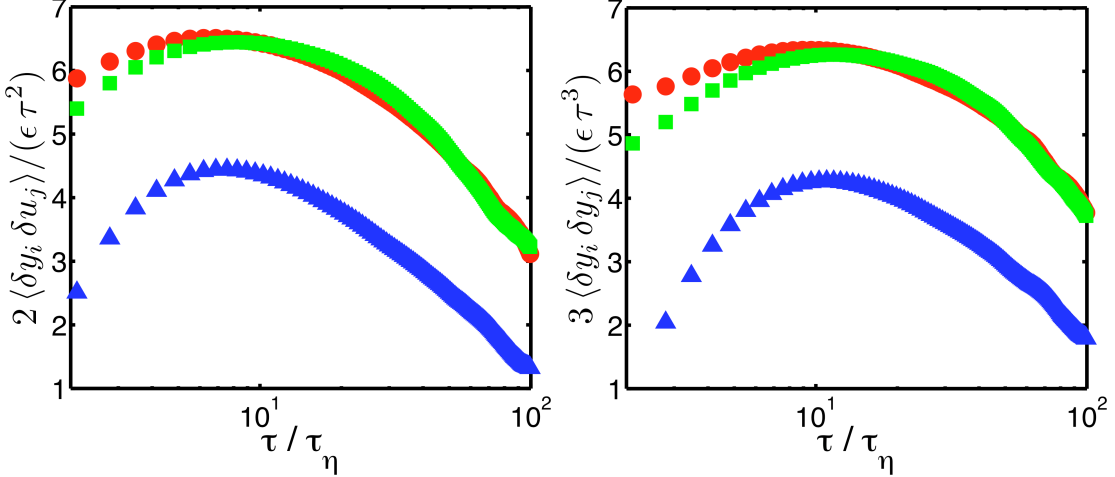


Figure 4.24: Compensated position correlations at $R_\lambda = 815$. The left plot shows $\langle \delta y_i(\tau) \delta u_j(\tau) \rangle$, while the right shows $\langle \delta y_i(\tau) \delta y_j(\tau) \rangle$. As with the structure functions, the scaling range is very short. We have estimated C_0 values from the peaks of these compensated plots. The symbols are the same as those in the similar compensated structure function plots shown earlier.

Breaking the inner integral into two parts, we have

$$\begin{aligned}
 \langle \delta y_i(\tau) \delta y_j(\tau) \rangle &= \frac{1}{2} C_0 \epsilon \delta_{ij} \int_0^\tau dt' \left[\int_0^{t'} (t' + t'' - (t' - t'')) dt'' \right. \\
 &\quad \left. + \int_{t'}^\tau (t' + t'' - (t'' - t')) dt'' \right] \\
 &= \frac{1}{2} C_0 \epsilon \delta_{ij} \int_0^\tau dt' [t'^2 + 2t'(\tau - t')] \\
 &= \frac{1}{3} C_0 \epsilon \tau^3 \delta_{ij}.
 \end{aligned} \tag{4.27}$$

Thus, in a sense, single particle dispersion is governed by exactly the same physics as the second-order Lagrangian structure function.

We have measured these two position correlations in our experiment, as reported by Chang, Xu, Ouellette, and Bodenschatz (2006). It is possible that measurements of single particle dispersion may be strongly affected by the complex mean flow in our experiment. To account for this possibility, we first differentiated the particle tracks using the Gaussian filter to obtain the velocity. We then

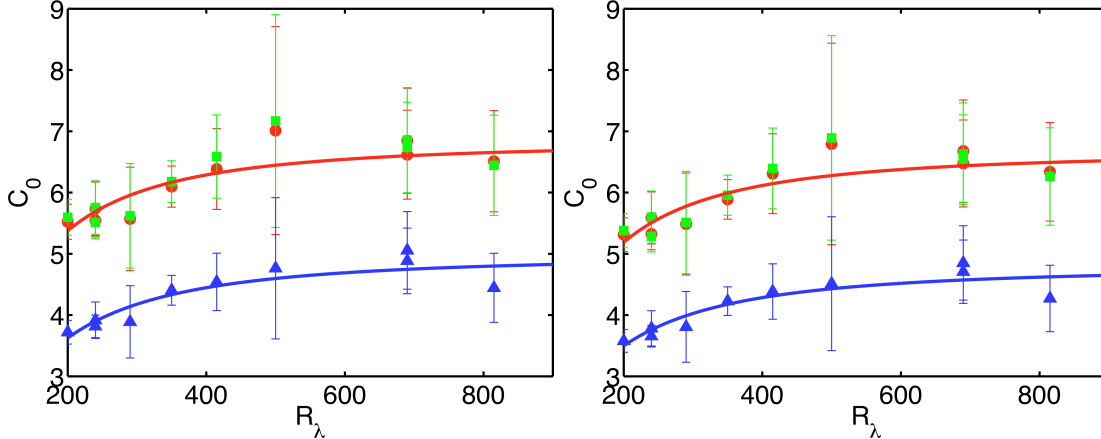


Figure 4.25: C_0 measured from the position correlations as a function of Reynolds number. On the left, we show C_0 determined from $\langle \delta y_i(\tau) \delta u_j(\tau) \rangle$, while on the right we show the C_0 values from $\langle \delta y_i(\tau) \delta y_j(\tau) \rangle$. The solid lines are again fits of Sawford's (1991) model.

subtracted the mean velocity field, just as we did for the velocity statistics presented above. The tracks were then integrated numerically to recover the tracer positions with the mean flow contribution removed. In Fig. 4.24, we show both $\langle \delta y_i(\tau) \delta u_j(\tau) \rangle$ and $\langle \delta y_i(\tau) \delta y_j(\tau) \rangle$ at $R_\lambda = 815$, compensated so that the peak value will be C_0 . The same striking anisotropy observed in the second-order structure function is also clearly present in the single particle dispersion data. Also, just as with the structure function, the scaling range is very short, and so we are forced to estimate C_0 simply by taking the peak values of the compensated correlation functions.

The measured C_0 values again show a Reynolds number dependence that appears to be well-captured by Sawford's (1991) model, as shown in Fig. 4.25. The extrapolated values for C_0 at infinite Reynolds number are consistent with the values we found earlier for the structure function and the Lagrangian velocity spectrum. The four measurements of C_0 are summarized in Table 4.3.

Table 4.3: Values of C_0 extrapolated to infinite Reynolds number from each of the four independent measurements. All four measurements are consistent.

Method	Radial C_0^∞	Axial C_0^∞
Structure function	6.2 ± 0.3	5.0 ± 0.4
Lagrangian spectrum	6.3 ± 0.4	4.7 ± 0.4
$\langle \delta y_i(\tau) \delta u_j(\tau) \rangle$	6.8 ± 0.3	5.0 ± 0.4
$\langle \delta y_i(\tau) \delta y_j(\tau) \rangle$	6.7 ± 0.3	4.8 ± 0.3

4.5 Multifractals

In addition to measuring traditional turbulence statistics, we have also investigated the multifractal turbulence model, discussed in Section 2.3. While experimental measurements cannot of course confirm the model, we have found excellent agreement with some of its predictions.

Central to the multifractal description of turbulence is the spectrum of allowed fractal dimensions $D(h)$, which is assumed to be universal. Meneveau and Sreenivasan (1987) and Chhabra *et al.* (1989) have measured the Eulerian multifractal dimension spectrum for a one-dimensional surrogate of the dissipation rate ϵ , though no other experimental measurements have been made. In particular, there are no measurements of the Lagrangian multifractal dimension spectrum, which is necessarily different from its Eulerian counterpart (Borgas, 1993). The two multifractal dimension spectra should be, however, related, offering a tantalizing connection between the Eulerian and Lagrangian descriptions of turbulence.

We present here measurements of the Lagrangian multifractal dimension spectrum $D^L(h)$. While this quantity has not been measured previously, several models have been proposed (Boffetta *et al.*, 2002; Chevillard *et al.*, 2003; Biferale *et al.*,

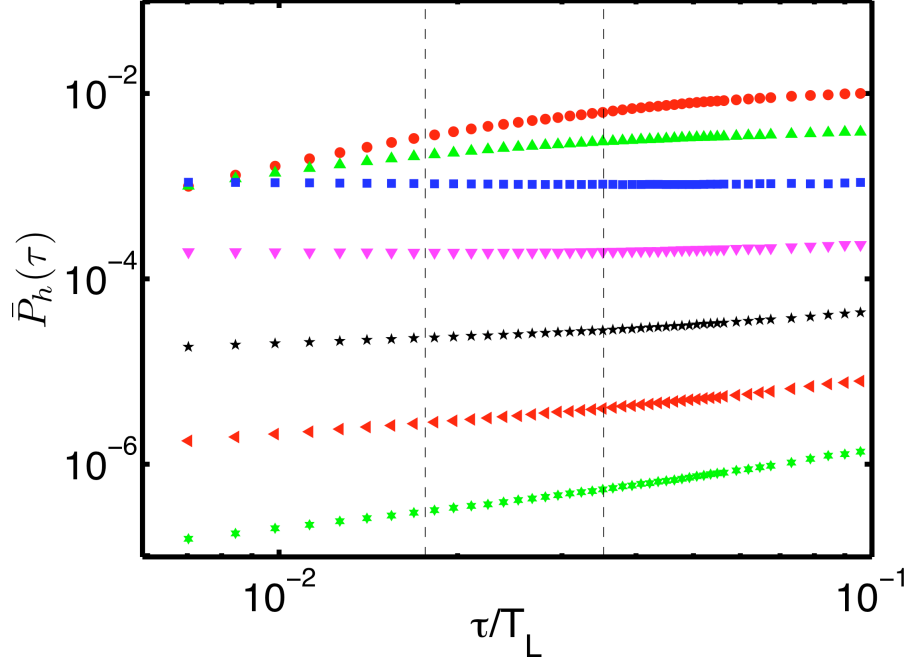


Figure 4.26: Probabilities $\bar{P}_h(\tau)$ plotted as a function of τ/T_L for seven values of h in logarithmic coordinates. The curves have been offset for clarity. From top to bottom, the data correspond to h values of 0.12, 0.25, 0.50, 0.75, 1.00, 1.25, and 1.50. The vertical lines show the region in which we fit power laws to the data. The exponents of these power laws are given by $1 - D^L(h)$.

2004). Without experimental measurements, however, there has been no way to differentiate between these models. The experimental results presented here were reported previously by Xu, Ouellette, and Bodenschatz (2006b).

To measure $D^L(h)$, we have used a modified form of the probabilistic formulation of the multifractal model given by Frisch (1995). Translating Frisch's (1995) work into the Lagrangian framework, recall that the probability $\bar{P}_h(\tau)$ that a velocity increment $\delta u(\tau)$ taken over a time τ scales as $(\tau/T_L)^h$ is proportional to $(\tau/T_L)^{1-D^L(h)}$. Following Frisch (1995), we define

$$\bar{P}_h(\tau) = \int_{u' \left(\frac{\tau}{T_L} \right)^h - \Delta}^{u' \left(\frac{\tau}{T_L} \right)^h + \Delta} P_\tau(\delta u(\tau)) d[\delta u(\tau)], \quad (4.28)$$

where P_τ is the PDF of $\delta u(\tau)$, u' is the large-scale RMS velocity, and Δ defines a small integration region. Formally, in the limit of infinite Reynolds number where $\tau_\eta \rightarrow 0$, we have that

$$\lim_{\tau \rightarrow 0} \frac{\ln \bar{P}_h(\tau)}{\ln \tau} = 1 - D^L(h), \quad (4.29)$$

In any experiment, however, the Reynolds number is finite, and we cannot take this limit. We have therefore fit power laws to $\bar{P}_h(\tau)$ in the inertial range as shown in Fig. 4.26. The exponents from these power laws are given by $1 - D^L(h)$, the codimension of the Lagrangian cascade. We note that the scaling behavior of $\bar{P}_h(\tau)$ is insensitive to the integration width Δ for $\Delta \in [0.1u'(\tau/T_L)^h, u'(\tau/T_L)^h]$.

Our measurements of $D^L(h)$ are shown in Fig. 4.27 for three different Reynolds numbers. The measurements agree well for all three Reynolds numbers, suggesting that $D^L(h)$ is independent of R_λ . In addition, though we show the dimension spectrum calculated from only a single component of $\delta u(\tau)$, the spectra calculated from the other two components are identical despite the large-scale anisotropy in our flow. Figure 4.27 also shows the predictions of several models. The left side of our measured fractal dimension curve agrees very well with all three models, to within the experimental accuracy. The right side of the experimental curve, however, is very different from the model predictions, and is linear with slope -1 . We will discuss this discrepancy below, after first describing the three models shown in Fig. 4.27 in detail.

Starting from completely Lagrangian arguments, Chevillard *et al.* (2003) have proposed a simple parabolic form for the dimension spectrum, namely

$$D_C^L(h) = 1 - \frac{(h - c_1)^2}{2c_2}, \quad (4.30)$$

where $c_1 = 0.579$ and $c_2 = 0.079$ were determined from experimental measurements of the PDF of the velocity increments. The relationship between c_1 and c_2 is fixed

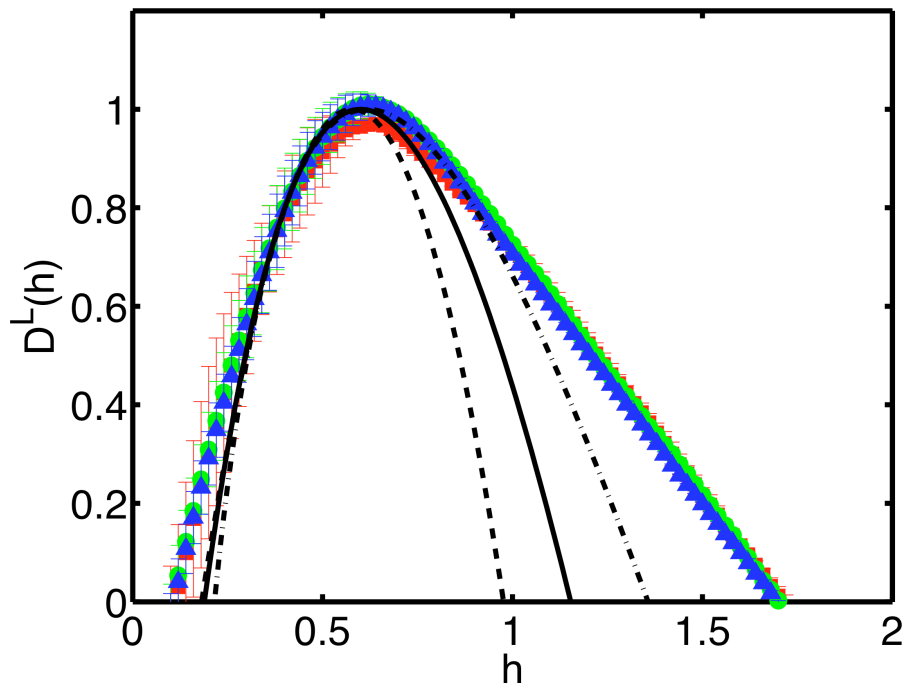


Figure 4.27: Direct measurement of the Lagrangian multifractal dimension spectrum. The symbols denote our experimental measurements at three different Reynolds numbers: the \blacksquare correspond to $R_\lambda = 200$, the \bullet to $R_\lambda = 690$, and the \blacktriangle to $R_\lambda = 815$. The measured multifractal dimension spectra agree well for all three Reynolds numbers, suggesting that $D^L(h)$ has no Reynolds number dependence. The three curves correspond to models: the dashed line is the model due to Chevillard *et al.* (2003), the solid line is the K62 log-normal model, and the dot-dashed line is the log-Poisson model of She and Lévéque (1994).

to be $c_1 = 1/2 + c_2$ in order to force ζ_2^L , the scaling exponent of the second order structure function, to be unity.

The other two models shown are Eulerian models translated into the Lagrangian framework. In the spirit of the work done by Borgas (1993), who made a connection between the Eulerian and Lagrangian multifractal dimension spectra of the dissipation rate by assuming that the turbulence is ergodic, Chevillard *et al.* (2003) proposed that

$$D^L(h) = -h + (1+h) \left(D^E \left(\frac{h}{1+h} \right) - 2 \right), \quad (4.31)$$

regardless of the form of $D^E(h)$. This equation follows from assuming a variation of the K62 Refined Similarity Hypothesis in addition to ergodicity (Chevillard, 2004). We here have subtracted two from D^E in order to account for the difference in the embedding dimension between 3D spatial Eulerian statistics and 1D temporal Lagrangian statistics.

Using eq. (4.31), we have translated both the K62 log-normal model and the She and Lévéque (1994) log-Poisson model into the Lagrangian framework. While K62 was not intended to be a multifractal model (indeed, the theory of multifractals had not yet been developed), we can use the Legendre transform relationship between the scaling exponents of the structure functions and the multifractal dimension spectrum in order to extract a multifractal prediction. K62 predicts that the Eulerian structure functions scale as

$$\langle \delta u_r^p \rangle \sim r^{\zeta_p^E} \sim r^{\frac{p}{3} - \frac{1}{2}\mu \frac{p}{3}(\frac{p}{3}-1)}. \quad (4.32)$$

Since

$$D^E(h) = \inf_h [hp + 3 - \zeta_p^E], \quad (4.33)$$

we find that

$$D_{K62}^E(h) = 3 - \frac{9}{2\mu} \left[h - \left(\frac{1}{3} + \frac{\mu}{6} \right) \right]^2. \quad (4.34)$$

Using eq. (4.31), we then have

$$D_{K62}^L = -h + (1+h) \left\{ 1 - \frac{9}{2\mu} \left[\frac{h}{1+h} - \left(\frac{1}{3} + \frac{\mu}{6} \right) \right]^2 \right\}. \quad (4.35)$$

In Fig. 4.27, we have taken $\mu = 1/4$, a value found in experiments (Pope, 2000).

In contrast to both K62 and the Chevillard *et al.* (2003) model, She and Lévéque (1994) have proposed a model of the Eulerian multifractal dimension spectrum with no free parameters. In this model, the dimension spectrum is given by

$$D_{SL}^E(h) = 1 + b_1 \left(h - \frac{1}{9} \right) - b_2 \left(h - \frac{1}{9} \right) \ln \left(h - \frac{1}{9} \right), \quad (4.36)$$

where

$$b_1 = 3 \left(\frac{1 + \ln \ln \frac{3}{2}}{\ln \frac{3}{2}} - 1 \right) \quad (4.37)$$

and

$$b_2 = \frac{3}{\ln \frac{3}{2}}. \quad (4.38)$$

Again using eq. (4.31), we can translate this form into the Lagrangian framework, obtaining

$$D_{SL}^L(h) = -h + (1+h) \left\{ -1 + b_1 \left(\frac{h}{1+h} - \frac{1}{9} \right) - b_2 \left(\frac{h}{1+h} - \frac{1}{9} \right) \ln \left(\frac{h}{1+h} - \frac{1}{9} \right) \right\}. \quad (4.39)$$

By comparing the structure function scaling exponents predicted by our multifractal measurements using the Legendre transform relationship

$$\zeta_p^L = \inf_h [hp + 1 - D^L(h)] \quad (4.40)$$

with directly measured scaling exponents, we can check for consistency in our measurements. Such a comparison is shown in Fig. 4.28. Included are the same three

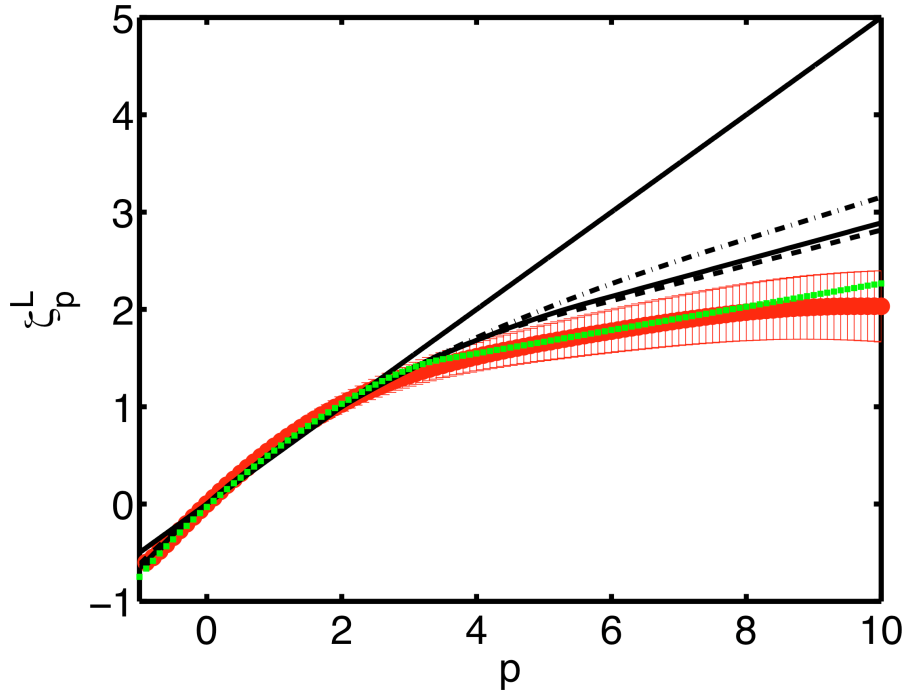


Figure 4.28: Scaling exponents ζ_p^L of the Lagrangian structure functions as a function of order. The \bullet denote direct measurements of the $\zeta^L(p)$ at $R_\lambda = 690$. The \blacksquare show the exponents extracted from our measured $D^L(h)$ data via eq. (4.40). The two experimental measurements agree very well with each other. The curves are models: the dashed line is again the model of Chevillard *et al.* (2003), the solid curved line is the K62 log-normal model, and the dot-dashed line is the model of She and Lévéque (1994). The solid straight line shows the K41 prediction for the ζ_p^L .

models as well as the K41 prediction. Clearly, the scaling exponents computed by taking the Legendre transform of the experimentally measured multifractal dimension spectrum agree very well with the directly measured Lagrangian structure function scaling exponents. The three models agree well with our experimental results for low structure function orders, but start to deviate significantly for orders greater than 5. This discrepancy is in part due to small differences in the value of h_{min} between our measurements and the three models. Due to the finite domain of h , eq. (4.40) implies that ζ_p^L will change from a curved function of p to a linear law at some p^* where h_{min} minimizes the right hand side of eq. (4.40). For $p > p^*$, the multifractal model predicts that $\zeta_p^L = h_{min}p + 1$. Small changes in h_{min} can therefore have a large impact in the predicted form of the ζ_p^L at high orders.

Before discussing the right side of the multifractal dimension spectrum in more detail, let us briefly discuss the proposed multifractal model of Boffetta *et al.* (2002). This model, giving an expression for the ζ_p^L based on the $D^E(h)$ of She and Lévéque (1994), is superficially different from the Lagrangian translation of the She and Lévéque (1994) model we have presented here. Boffetta *et al.* (2002) begin by assuming that, to leading order,

$$\delta u(\tau) \sim \delta u(r), \quad (4.41)$$

where $\delta u(r)$ is the Eulerian velocity increment. They also assume that the characteristic flow time scale at a length scale r is given by

$$\tau_r \sim \frac{r}{u_r}, \quad (4.42)$$

where u_r is the velocity at the scale r . Using the Eulerian multifractal formalism as presented in Section 2.3, we then have

$$\tau_r \sim \frac{r}{u_r} \sim \frac{r}{u'} \left(\frac{r}{L} \right)^{-h} \sim \frac{L}{u' L} \left(\frac{r}{L} \right)^{-h} \sim T_L \left(\frac{r}{L} \right)^{1-h}, \quad (4.43)$$

so that

$$\frac{r}{L} \sim \left(\frac{\tau_r}{T_L} \right)^{1/(1-h)}. \quad (4.44)$$

The velocity increment then scales as

$$\delta u(\tau) \sim \delta u(r) \sim u_r \left(\frac{r}{L} \right)^{3-D^E(h)} \sim u_r \left(\frac{\tau_r}{T_L} \right)^{\frac{3-D^E(h)}{1-h}}. \quad (4.45)$$

We can then construct the structure function as

$$\begin{aligned} \langle \delta u(\tau)^p \rangle &\sim \int_{h \in [h_{min}, h_{max}]} d[\mu(h)] u'^p \left(\frac{r}{L} \right)^{hp} \left(\frac{\tau_r}{T_L} \right)^{\frac{3-D^E(h)}{1-h}} \\ &\sim \int_{h \in [h_{min}, h_{max}]} d[\mu(h)] u'^p \left(\frac{\tau_r}{T_L} \right)^{\frac{hp+3-D^E(h)}{1-h}} \end{aligned} \quad (4.46)$$

Since in the inertial range the smallest exponent will dominate the integral, we finally have

$$\zeta_p^L = \inf_h \left[\frac{hp + 3 - D^E(h)}{1 - h} \right]. \quad (4.47)$$

Though this form looks significantly different from eq. (4.40), let us consider combining eq. (4.40) with eq. (4.31). We then have

$$\begin{aligned} \inf_h [hp + 1 - D^L(h)] &= \inf_h \left[hp + 1 + h - (1+h) \left(D^E \left(\frac{h}{1+h} \right) - 2 \right) \right] \\ &= \inf_\chi \left[\left(\frac{\chi}{1-\chi} \right) p + 1 + \left(\frac{\chi}{1-\chi} \right) - \left(1 + \frac{\chi}{1-\chi} \right) (D^E(\chi) - 2) \right] \quad (4.48) \\ &= \inf_\chi \left[\frac{\chi p + 3 - D^E(\chi)}{1-\chi} \right], \end{aligned}$$

where we have made the change of variables $\chi = h/(1+h)$. We therefore recover the prediction of Boffetta *et al.* (2002) using the translation equation of Chevillard *et al.* (2003). We prefer to treat the mapping of Chevillard *et al.* (2003) as more fundamental, since it makes fewer assumptions (Chevillard, 2004; Chevillard *et al.*, 2005).

Let us now return to the right side of $D^L(h)$ where our experimental measurements differ strongly from the three models. Just as the finite domain of h implies

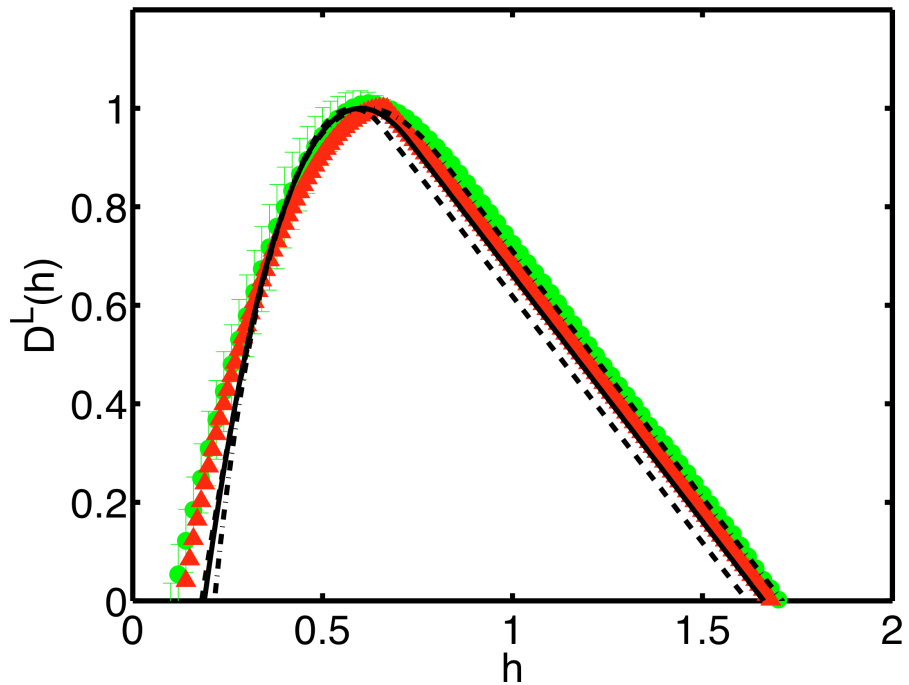


Figure 4.29: Comparison of the direct and indirect measurements of the multifractal dimension spectrum. The \bullet show again the direct measurement of the multifractal dimension spectrum at $R_\lambda = 690$, while the \blacktriangle show the inverse Legendre transform of the measured ζ_p^L data. The two experimental curves are consistent with each other. The solid lines are the same three models shown in Fig. 4.27 but modified to take into the non-existence of the moments of the velocity increments for orders less than -1 . The agreement between the model spectra and our measured spectra is excellent.

a transition to a linear law for the ζ_p^L , any minimum or maximum values of p would imply a linear portion of the multifractal dimension spectrum. It is well-known that the moments of the velocity increments do not converge for orders less than or equal to -1 (Frisch, 1995). Therefore, $p_{min} = -1$, and $D^L(h) = 1 + \zeta_{-1}^L - h$ for $p < p_{min}$. The right side of our $D^L(h)$ is therefore explained, since it is linear with a slope of -1 . We can also take p_{min} into account in the three models by using the Legendre transform relationship; these “corrected” models are shown in Fig. 4.29. The agreement with the experimental results is remarkable. We have also included in Fig. 4.29 the inverse Legendre transform of our directly-measured ζ_p^L for completeness. It too agrees very well with the directly measured multifractal dimension spectrum.

It remains unclear how the multifractal dimension spectrum computed from the velocity increments is related to that of the energy dissipation rate. The moments of ϵ are thought to be finite at all orders, so that there will be no linear region for the dimension spectrum computed from it. It is possible that the multifractal dimension spectrum simply cannot be fully measured from the velocity increments. Indeed, some researchers have claimed that wavelet transforms are needed instead (Muzy *et al.*, 1993). It is also possible, however, that the multifractal dimension spectra computed from different quantities are in fact themselves different.

Chapter 5

Multiparticle Statistics

5.1 Turbulent Relative Dispersion

In the previous chapter, we have discussed the statistics of single particles in turbulence. Since turbulent flows are replete with long-range correlations, however, a full understanding of the problem cannot be gained without also investigating the statistics of groups of particles. The simplest multiparticle problem is that of the rate of separation of a pair of fluid elements, termed turbulent relative dispersion.

In a quiescent fluid, the spreading of two fluid elements is dominated by diffusion. The fluid elements will undergo Brownian motion, and the mean-square separation between them will grow linearly in time. Two fluid elements in a turbulent flow will also experience this linear Taylor diffusion (Taylor, 1922), provided that they are separated by a distance larger than the integral length scale. For smaller, inertial range separations, however, the two fluid elements will separate faster. Since this relative dispersion is closely tied to turbulent mixing (Kraichnan, 1966; Nelkin and Kerr, 1981; Sawford, 2001), the superdiffusive separation of fluid element pairs explains why turbulent flows are so much more effective at mixing than their laminar counterparts.

Such turbulent mixing is ubiquitous in nature (Shraiman and Siggia, 2000): it is the basis of nearly all industrial fluid mixing processes, and it determines the spread of pollutants or bioagents in the atmosphere (Huber *et al.*, 2001) and oceans (Berloff *et al.*, 2002). Marine predator-prey systems exploit the properties of turbulent dispersion (Jørgensen *et al.*, 2005), and many animals use the structure of turbulent odor plumes to locate food, predators, and mates (Balkovsky and

Shraiman, 2002; Wolf *et al.*, 2004; Moore and Crimaldi, 2004). As with most aspects of turbulence, passively advected scalar fields like odors, heat, or pollutants are characterized by intense fluctuations in the local concentration relative to the mean concentration field. These fluctuations often largely determine the dynamics of these scalar fields. The rate of destruction of atmospheric ozone, for example, is heavily influenced by the local concentration of the various chemical species involved (Edouard *et al.*, 1996), just as in many other slow chemical reactions. It is natural to relate these concentration fluctuations to turbulent relative dispersion (Kraichnan, 1966; Nelkin and Kerr, 1981; Sawford, 2001).

In the following sections, we discuss some of the theoretical predictions for the scaling of turbulent relative dispersion as well as our experimental measurements. The results of Section 5.1.3 were previously reported in Bourgoin, Ouellette, Xu, Berg, and Bodenschatz (2006), and the results of Sections 5.1.4, 5.1.5, and 5.1.6 were reported in Ouellette, Xu, Bourgoin, and Bodenschatz (2006b).

5.1.1 The Richardson-Obukhov Law

In a turbulent flow, at scales smaller than the integral scales, pairs of fluid elements separate faster than pure Brownian motion would suggest. Once a pair of fluid elements has separated to the integral scale, the separation will again grow linearly. Based on physical arguments and measurements of pair separation over a wide range of scales, Richardson (1926) suggested that the mean-square separation between two fluid elements should grow not linearly in time but rather as t^3 . Subsequently, Obukhov (1941) used K41 theory to write that

$$\langle r^2 \rangle = g\epsilon t^3, \quad (5.1)$$

where r is the relative distance between two fluid elements. Equation (5.1) is known as the Richardson-Obukhov law, and g is termed the Richardson constant. Researchers have attempted to find Richardson-Obukhov scaling in experiments (Huber *et al.*, 2001; Ott and Mann, 2000), simulations (Yeung, 1994; Boffetta and Sokolov, 2002a; Ishihara and Kaneda, 2002; Yeung and Borgas, 2004; Gioia *et al.*, 2004; Biferale *et al.*, 2005a), and models (Sawford, 2001; Nicolleau and Yu, 2004) for decades. No convincing evidence of the Richardson-Obukhov law, however, has been found, and estimates of the Richardson constant span a full order of magnitude (Sawford, 2001).

5.1.2 Batchelor's Extension

While the Richardson-Obukhov law is the only choice consistent with K41 when the only relevant parameter is the time of separation, Batchelor (1950) realized that a different scaling law is possible if the initial separation r_0 of the two fluid elements remains a relevant parameter in their subsequent spreading. Let us consider the time derivative of the mean-square separation. Using the chain rule, we can write

$$\frac{d}{dt} \langle r^2(t) \rangle = 2 \langle r(t) \delta u(t) \rangle, \quad (5.2)$$

where $\delta u(t)$ is the relative velocity of the two fluid elements. Using the fundamental theorem of calculus, we can then write

$$\begin{aligned} \frac{d}{dt} \langle r^2(t) \rangle &= 2 \left\langle \left[r_0 + \int_0^t \delta u(t') dt' \right] \delta u(t) \right\rangle \\ &= 2 \left\{ \langle r_0 \delta u(t) \rangle + \int_0^t \langle \delta u(t) \delta u(t') \rangle dt' \right\}. \end{aligned} \quad (5.3)$$

In his original work, Batchelor set the term $\langle r_0 \delta u(t) \rangle$ to zero, reasoning that there should be no correlation between the initial pair separation and the relative ve-

locity. We, however, find that this assumption does not hold, as will be discussed below. We therefore keep this correlation in our calculations.

We now assume that the relative velocity changes slowly in time, so that

$$\langle \delta u(t) \delta u(t') \rangle \approx \langle \delta u(0)^2 \rangle. \quad (5.4)$$

This quantity in turn is exactly the same as $\langle \delta u(r_0)^2 \rangle$, the trace of the second-order Eulerian structure function. We therefore have that

$$\begin{aligned} \frac{d}{dt} \langle r^2(t) \rangle &= 2 \{ \langle r_0 \delta u(t) \rangle + [D_{LL}(r_0) + 2D_{NN}(r_0)] t \} \\ &= 2 \left\{ \langle r_0 \delta u(t) \rangle + \frac{11}{3} C_2 (\epsilon r_0)^{2/3} t \right\}. \end{aligned} \quad (5.5)$$

Therefore, when the initial separation is relevant, the relative dispersion is given by

$$\langle [r_i(t) - r_{0i}]^2 \rangle = \frac{11}{3} C_2 (\epsilon r_0)^{2/3} t^2. \quad (5.6)$$

This law, which we term Batchelor scaling, should hold for times of the order of the correlation time t_0 of an eddy of characteristic size r_0 . This time is given by K41 as

$$t_0 = \left(\frac{r_0^2}{\epsilon} \right)^{1/3}. \quad (5.7)$$

When $t \gg t_0$, the initial separation will no longer be a relevant parameter, and a particle pair is expected to obey the Richardson-Obukhov law. Finally, therefore, in turbulent relative dispersion, the mean-square separation between a pair of fluid elements should scale as

$$\langle [r_i(t) - r_{0i}]^2 \rangle = \begin{cases} \frac{11}{3} C_2 (\epsilon r_0)^{2/3} t^2, & t \ll t_0 \\ g \epsilon t^3, & t_0 \ll t \ll T_L \end{cases} \quad (5.8)$$

Both the Batchelor t^2 law and the Richardson-Obukhov t^3 law should be found in the inertial range. To distinguish these two scaling laws clearly, then, the inertial

range must be very large. The size of the inertial range is roughly given by the ratio of the eddy turnover time T_L to τ_η . Since $R_\lambda \sim (T_L/\tau_\eta)$, a large Reynolds number is required to see both the Batchelor and the Richardson-Obukhov laws. Previous experimental and numerical studies of relative dispersion have been conducted only at low Reynolds numbers ($R_\lambda < 300$) (Yeung, 1994; Ott and Mann, 2000; Boffetta and Sokolov, 2002a; Ishihara and Kaneda, 2002; Yeung and Borgas, 2004; Biferale *et al.*, 2005a) and cannot therefore be conclusive (Sawford, 2001). High Reynolds numbers are obtained in kinematic simulations (Nicolleau and Yu, 2004), but Thomson and Devenish (2005) have recently suggested that such models may be ill-suited to the pair dispersion problem.

5.1.3 Experimental Results

We have measured relative dispersion from the tracer particle trajectories in the $5 \times 5 \times 5 \text{ cm}^3$ volume over a range of Reynolds numbers (Bourgoin *et al.*, 2006). One such pair of trajectories is shown in Fig. 5.1, measured at $R_\lambda = 690$. The two particles enter the measurement volume at the same time with an initial separation r_0 of 0.9 mm. The particles are advected by the turbulence, and have separated to a distance of 6.3 mm by the time they leave the measurement volume. In Fig. 5.1, the small spheres mark every other measured position of the particles and are separated by $0.074 \text{ ms} = \tau_\eta/13$, while the large spheres mark every 30th position of the particles. The color of the spheres indicates the velocity of the particle.

By recording the relative separation of many such particle pairs, we have measured the relative dispersion. In Fig. 5.2, we show our measurements of $\langle [r_i(t) - r_{0i}]^2 \rangle$ at $R_\lambda = 815$ with both axes normalized by the Kolmogorov scales. Figure 5.2 shows the dispersion for fifty different bins of initial separations, 1 mm

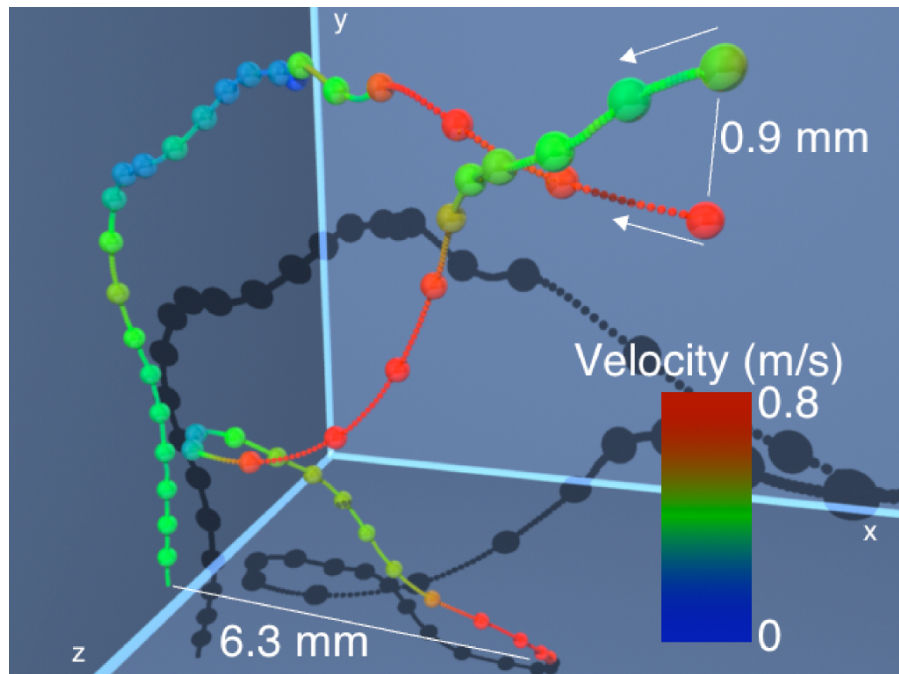


Figure 5.1: A pair of measured particle trajectories at $R_\lambda = 690$. The two particles enter the measurement volume as indicated and separate superdiffusively under the influence of the turbulence. The small spheres mark every other measured position of the particles, while the large spheres mark every 30th position. The color of each sphere indicates its absolute velocity in units of m/s.

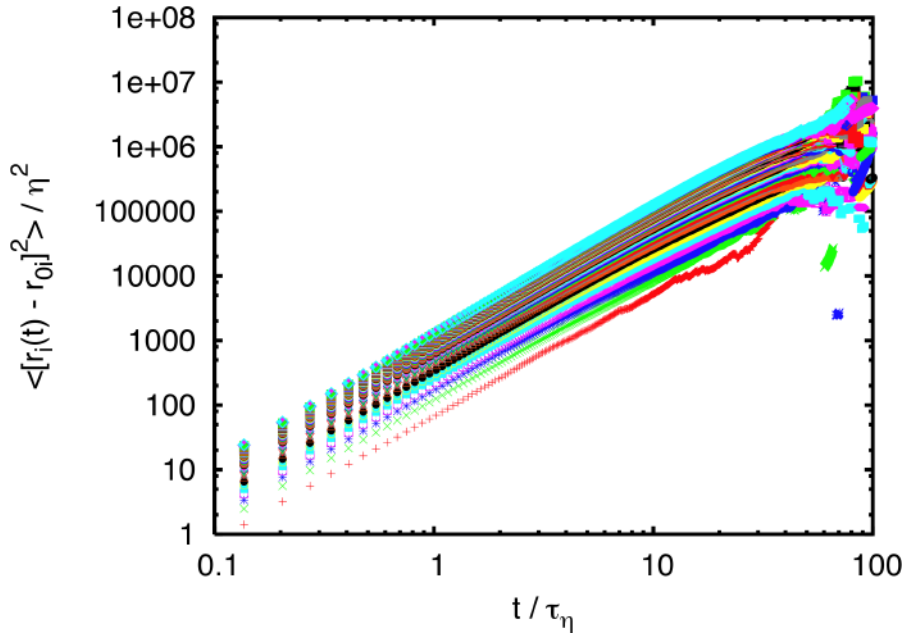


Figure 5.2: Evolution of the mean-square particle separation at $R_\lambda = 815$. Each set of symbols represents a bin of initial separations 1 mm ($\approx 43\eta$) wide, ranging from 0-1 mm to 49-50 mm. With both axes normalized by the Kolmogorov scales, each data curve follows a power law for over two decades in time.

wide ($\approx 43\eta$) and ranging from 0-1 mm to 49-50 mm. It is clear that for each of these initial separations, even though the largest is approximately 70% of the integral scale L , the data follows a power law for more than two decades in time. The data, however, do not collapse for the different initial separations, suggesting that the initial separation remains a relevant parameter and that therefore the data cannot be following the Richardson-Obukhov law. Recalling Batchelor's prediction for the short-time behavior of the relative dispersion, in Fig. 5.3 we scale the same data by $(11/3)C_2(\epsilon r_0)^{2/3}$ and observe a nearly perfect collapse of the data for the various initial separations. We emphasize that the dark line drawn in Fig. 5.3 is not a fit but is rather Batchelor's predicted power law.

If we now look closer at the agreement of our data with Batchelor's prediction by

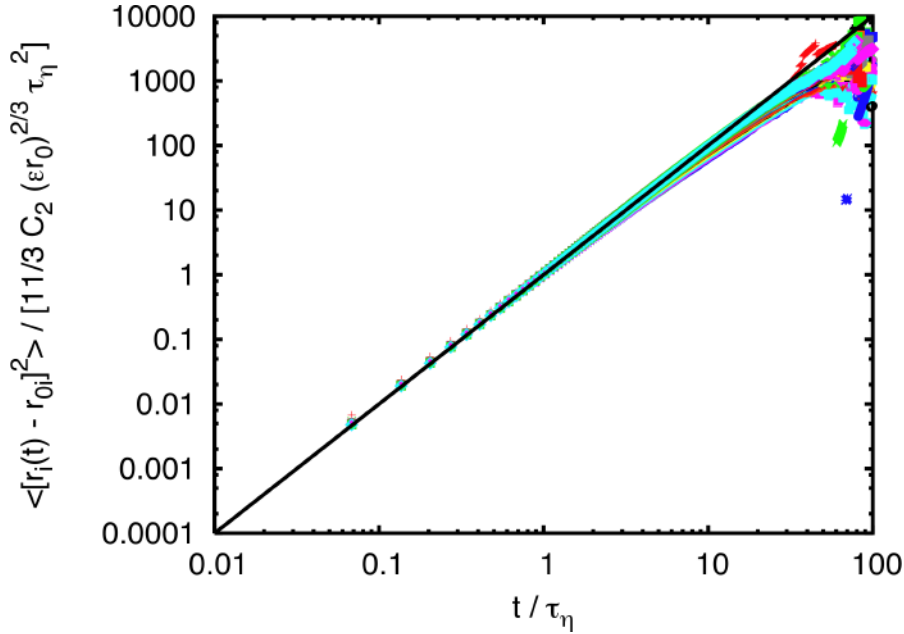


Figure 5.3: Scale collapse of the mean-square particle separation. The same data as in Fig. 5.2 is scaled by Batchelor's constant $(11/3)C_2(\epsilon r_0)^{2/3}$ and an almost perfect collapse of the data is seen for all fifty initial separations.

compensating our experimental results by $(11/3)C_2(\epsilon r_0)^{2/3}t^2$, as shown in Fig. 5.4, we observe that the data deviate from the Batchelor prediction at times that vary with the initial separation. In order to correct for this effect, we scaled time by Batchelor's $t_0 = (r_0^2/\epsilon)^{1/3}$, as shown in Fig. 5.5. This new scaling clearly collapses the data for the various initial separations much better, with each curve deviating from Batchelor's prediction at essentially the same value of (t/t_0) . Our data therefore confirm both Batchelor's scaling argument and the time for which he predicted it would hold. Moreover, the value t^* for which the data deviate from Batchelor's prediction appears to be independent of Reynolds number. In Fig. 5.6, we define t^* as the time when the data deviate by 5% from Batchelor's prediction. For the entire range of Reynolds numbers tested, $t^* \approx 0.075t_0$.

As we mentioned above, in Batchelor's (1950) original paper, he predicted a t^2

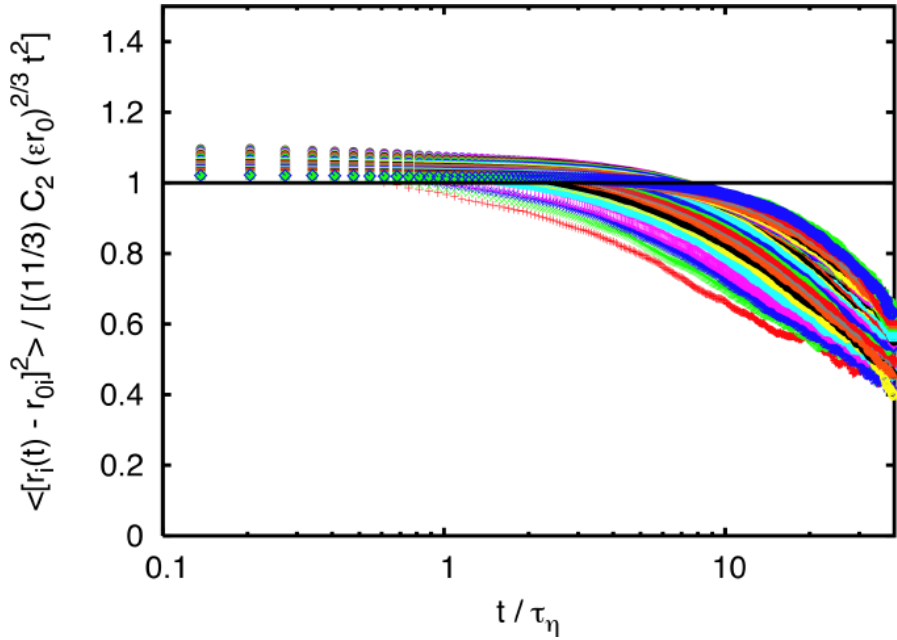


Figure 5.4: Compensated mean-square particle separation. The time axis is scaled by τ_η . The data for different initial separations deviate from the Batchelor prediction at different times.

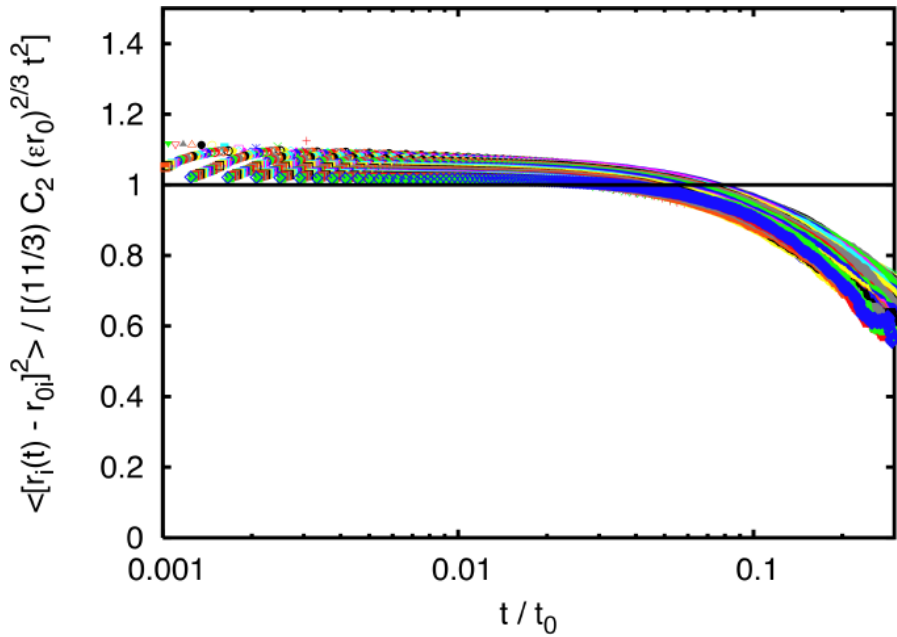


Figure 5.5: Compensated mean-square particle separation with time scaled by t_0 . Plotted in this way, there is a scale collapse in both space and time.

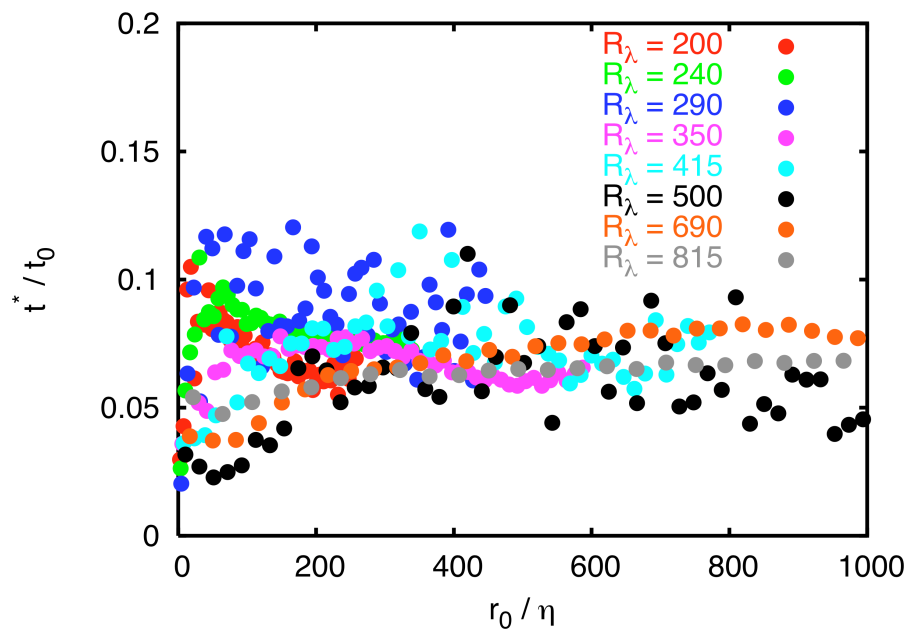


Figure 5.6: Deviation from Batchelor's prediction. t^* measures the time when the relative dispersion data deviate by more than 5% from Batchelor's prediction. t^* is plotted against the initial separation for eight different Reynolds numbers. Irrespective of Reynolds number, $t^* \approx 0.075t_0$.

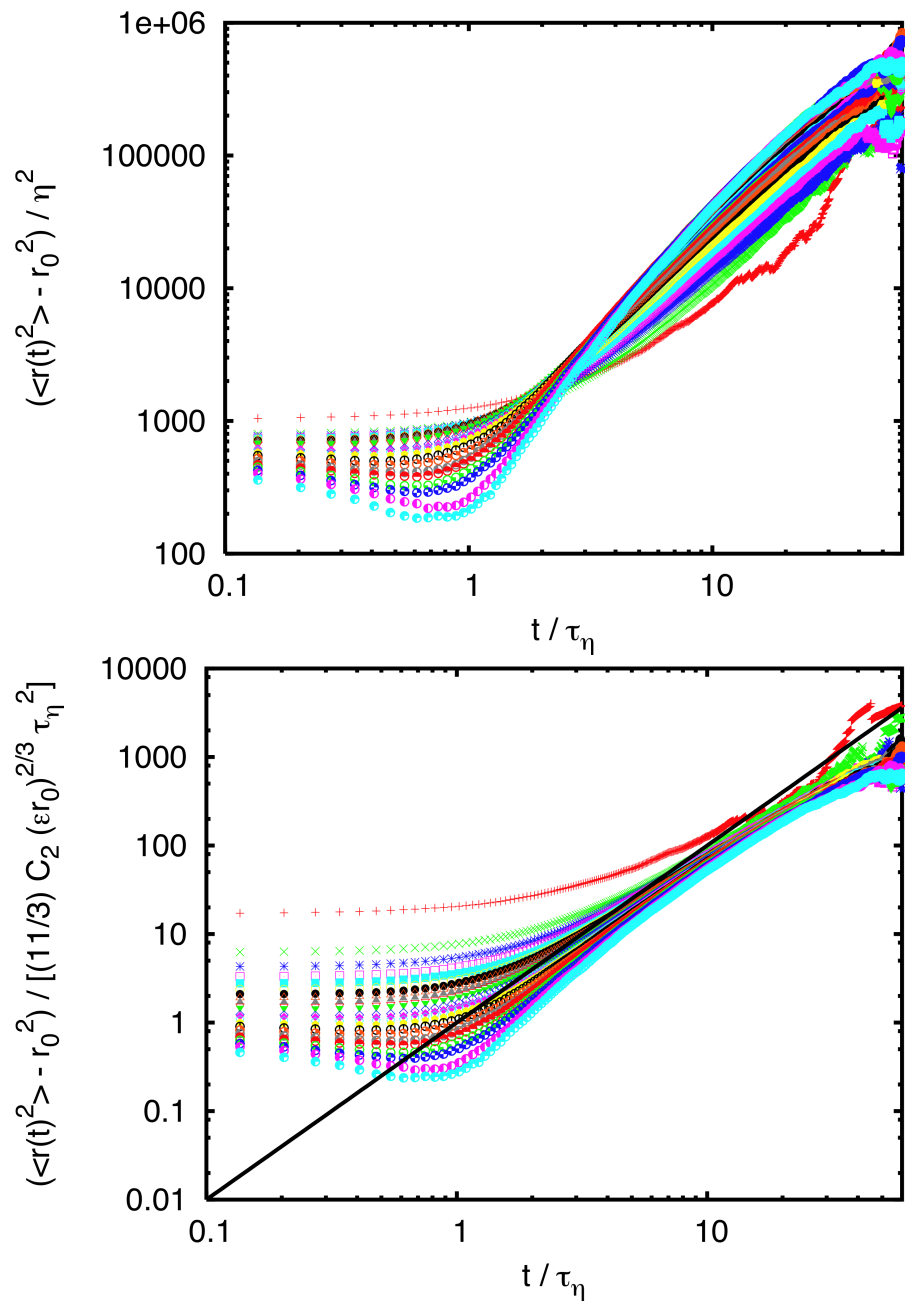


Figure 5.7: Batchelor's original measure of relative dispersion at $R_\lambda = 815$. No universal behavior is seen for different initial separations. The top plot shows the raw data, while the bottom shows an attempt to collapse the data with Batchelor's scaling prediction.

law for short times for the quantity $[\langle r(t)^2 \rangle - r_0^2]$ rather than for $\langle [r_i(t) - r_{0i}]^2 \rangle$, shown above. When we plot this quantity, we see no universal behavior, as shown in Fig. 5.7. This suggests that the difference between $[\langle r(t)^2 \rangle - r_0^2]$ and $\langle [r_i(t) - r_{0i}]^2 \rangle$, namely the correlation between the initial separation and the relative velocity, is not negligible. This non-universal behavior has also been seen in DNS studies of relative dispersion (Biferale *et al.*, 2005a).

As shown in Figs. 5.2-5.5, we see no Richardson-Obukhov t^3 scaling for $\langle [r_i(t) - r_{0i}]^2 \rangle$, nor do we see it for $[\langle r^2(t) \rangle - r_0^2]$ or $\langle r^2(t) \rangle$. It has been suggested by some researchers, however, that $\langle [r_i(t) - r_{0i}]^2 \rangle$ is contaminated by the effects of larger and smaller scales, and that different statistics are needed to observe the Richardson-Obukhov law (Boffetta and Celani, 2000; Boffetta and Sokolov, 2002a,b; Biferale *et al.*, 2005a). One proposed way to search for the Richardson-Obukhov law is to use so-called fixed scale statistics, we discuss in detail below. We have also investigated the quantity $(\langle r(t)^{2/3} \rangle - r_0^{2/3})$, which should dimensionally have the same scaling behavior as $\langle [r_i(t) - r_{0i}]^2 \rangle$ (Falkovich, 2005). This new measure of dispersion, nondimensionalized by $r_0^{2/3}$ and compensated by t/t_0 , is shown in Fig. 5.8. For small initial separations for which T_L/t_0 is of order 10, there is a transition to a regime consistent with t^3 scaling at times of the order of t_0 . For larger initial separations for which T_L/t_0 is smaller, however, no such transition is seen.

It is tempting to interpret this hint of t^3 scaling seen in $(\langle r(t)^{2/3} \rangle - r_0^{2/3})$ as evidence of the Richardson-Obukhov law. This, however, cannot be the case. If we do not include the initial separation r_0 by either subtracting it from $\langle r(t)^{2/3} \rangle$ or by scaling time by t_0 , we see no clear transition. The classical Richardson-Obukhov law requires that the initial separation not be a relevant parameter. In addition, the t^3 power law the data appears to be approaching in Fig. 5.8 is different for

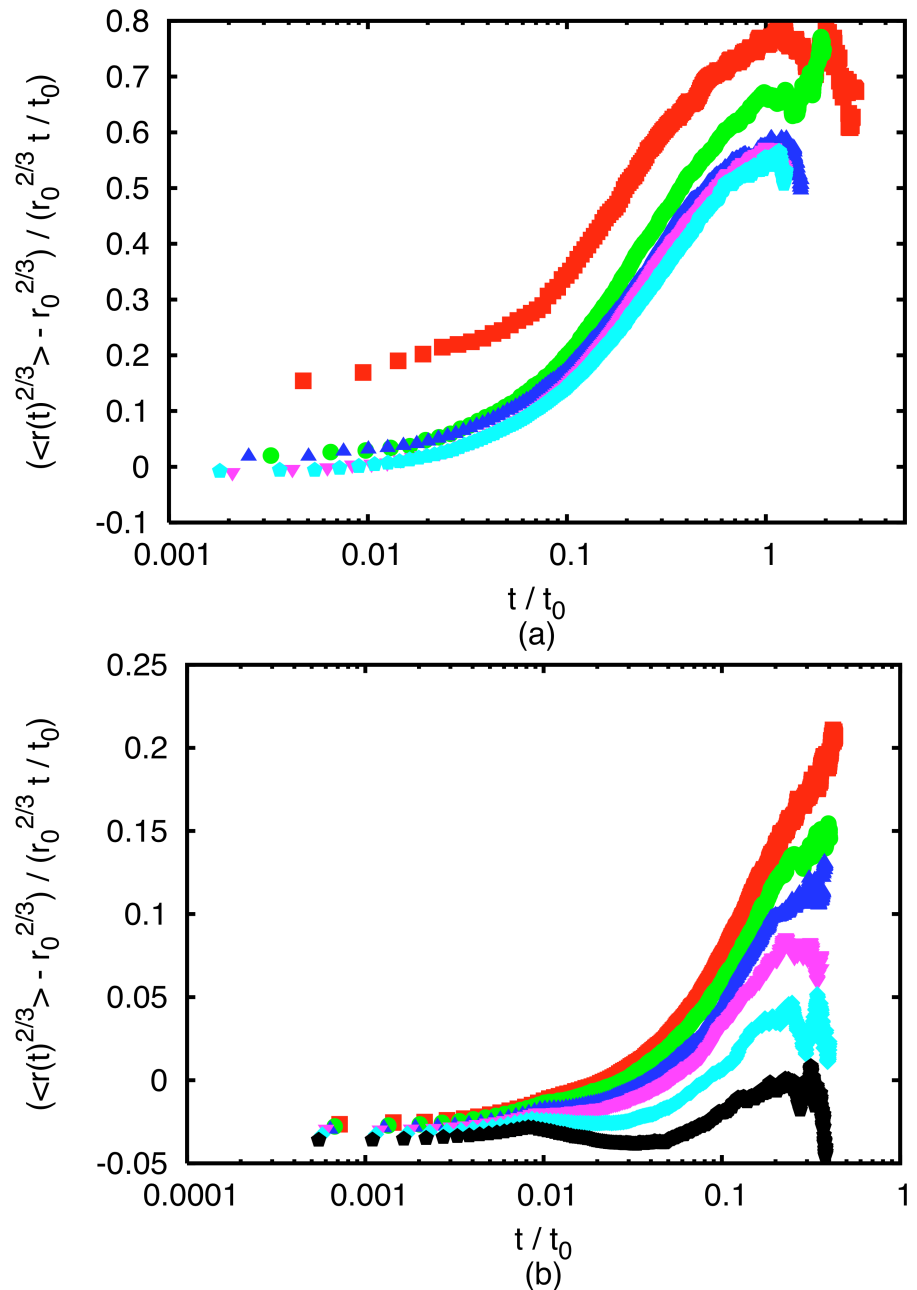


Figure 5.8: Alternative measure of relative dispersion at $R_\lambda = 815$. $(\langle r(t)^{2/3} \rangle - r_0^{2/3})$ is plotted, nondimensionalized by $r_0^{2/3}$ and compensated by t/t_0 . For initial separations for which T_L/t_0 is of order 10 (a), a transition is seen to a non-universal t^3 law at times of the order of t_0 , while for larger initial separations (b) no such transition is seen.

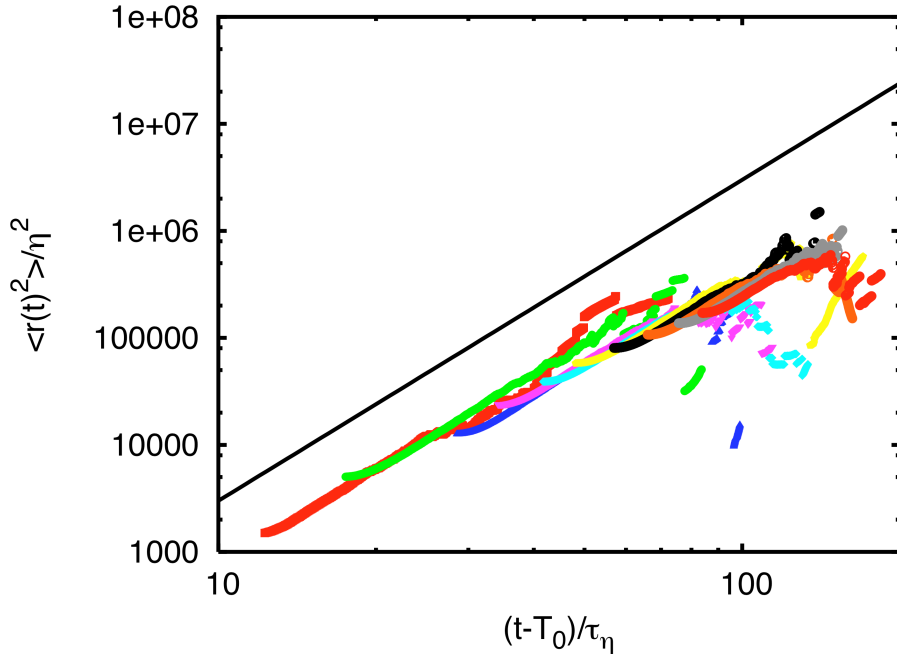


Figure 5.9: Applying the time shift of Mann *et al.* (1999) to our relative dispersion data at $R_\lambda = 815$. These time-shifted data show a non-universal t^3 law. From left to right, the curves represent 1 mm wide bins ranging from 0-1 mm to 9-10 mm. The solid line is a t^3 power law for reference.

different initial separations. Again, the classical Richardson-Obukhov law requires that data for any initial separation collapse onto a single power law.

Mann *et al.* (1999) proposed yet another way to try to find evidence of t^3 scaling. They found, like us, that $\langle r(t)^2 \rangle$ does not show Richardson-Obukhov behavior. They reasoned that this must be due to the finite initial separation of the pair, since Richardson's original argument assumed that the pair came from a point source. Mann *et al.* (1999) therefore suggested that an appropriate r_0 -dependent time shift is needed to see a t^3 law. To find this shift, they assumed that

$$\langle r(t)^2 \rangle^{1/3} = (g\epsilon)^{1/3}(t - T_0), \quad (5.9)$$

which follows from the Richardson-Obukhov law. They then fit straight lines to

their $\langle r(t)^2 \rangle^{1/3}$ data to extract the slope and intercept, finding that T_0 is, in general, negative. This result supported their implicit assumption that $r(t = T_0) = 0$. By subsequently shifting their data in time by T_0 , Mann *et al.* (1999) found a t^3 power law that they identified as the Richardson-Obukhov law. When we apply their method to our data, we also find a t^3 power law, as shown in Fig. 5.9, though the power law is not universal and is different for each initial separation. Mann *et al.* (1999) were only able to look at a very small range of initial separations, and so were not able to see the non-universality of the power law.

This method, however, has serious flaws. We can vary the process used to find the time shift to find other power laws in the data. To find a t^n power law, we simple fit a straight line to $\langle r^2(t) \rangle^{1/n}$ and fine the slope and intercept to calculate a time shift T_0 . We then shift the data by T_0 and obtain the desired t^n law. In Fig. 5.10, we show t^4 and t^5 laws obtained in this way. While they are not perfect, they are no worse than the t^3 law shown in Fig. 5.9. The reason for this behavior is the point source assumption implicit in this method. By assuming that at some time each particle was at the same point in space and further assuming that the pair subsequently separated according to a t^n law, the data must show a continuation of this t^n law.

Finally, we remark that since we have shown that t_0 accurately characterizes the duration of the Batchelor t^2 scaling regime, observation of a true Richardson-Obukhov scaling regime requires not only a large inertial range but also a large scale separation between T_L and t_0 . For the initial separations accessible in our experiment, the maximum value of the ratio T_L/t_0 was of order 10, with no observed Richardson-Obukhov scaling. To see a decade of Richardson-Obukhov scaling, which would unambiguously confirm the prediction, one must therefore at mini-

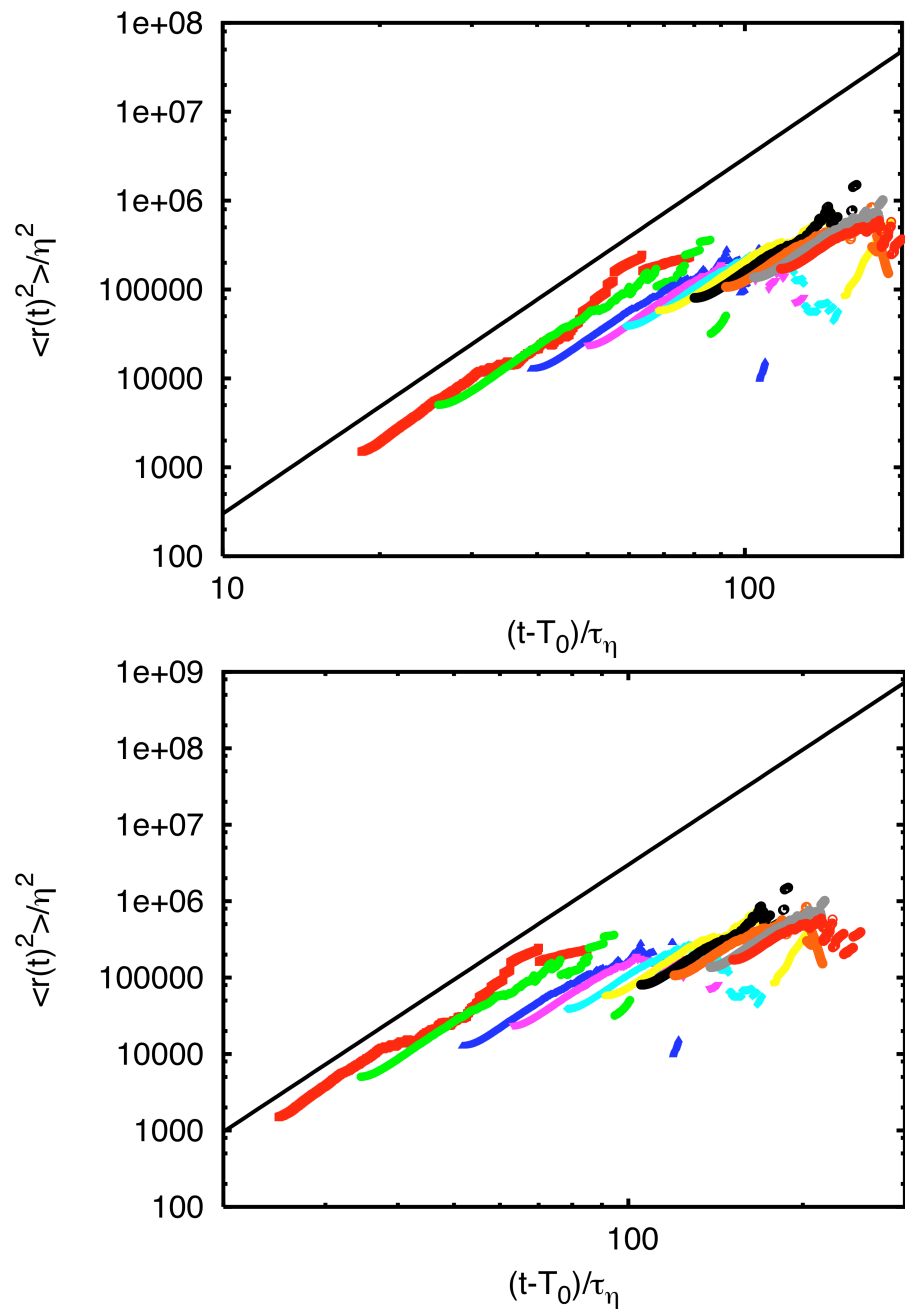


Figure 5.10: Variations of the time shifting procedure of Mann *et al.* (1999) that show a t^4 power law (top) and a t^5 power law (bottom) when applied to our data. The data are the same as those shown in Fig. 5.9; the solid lines show t^4 and t^5 power laws for reference.

mum have $T_L/t_0 \sim 100$. Using the definition of R_λ , we can write

$$R_\lambda = \sqrt{15} \left(\frac{T_L}{\tau_\eta} \right) = \sqrt{15} \left(\frac{T_L}{t_0} \right) \left(\frac{r_0}{\eta} \right)^{2/3}. \quad (5.10)$$

The classical Richardson-Obukhov prediction is an inertial range theory. The initial separation r_0 must therefore lie in the inertial range. Following Pope (2000), we use the common Eulerian definition of the approximate bottom of the inertial range as about 60η . With $T_L/t_0 \sim 100$ and $r_0/\eta \sim 60$, we can therefore estimate that a Reynolds number of at least $R_\lambda \approx 6000$ is required before a decade of Richardson-Obukhov scaling can be observed.

For most flows on Earth, the Reynolds numbers are small, with R_λ typically lower than 1000. Very turbulent atmospheric flows, such as warm clouds or the atmospheric boundary layer (Kurien and Sreenivasan, 2001), have $R_\lambda \sim 10^4$. Even the most violent flows on Earth, such as plinian volcanic eruptions, have similar Reynolds numbers. If we consider a pair of particles with an initial separation of 1 m in a flow with $R_\lambda \sim 10^4$, such as might be found in the smokestack of an industrial power plant, T_L/t_0 is only about 30, assuming typical atmospheric flow parameters (Shaw, 2003). Even for this high-Reynolds situation, therefore, we cannot expect the separation of the particles to be heavily influenced by Richardson-Obukhov scaling.

5.1.4 Higher-Order Statistics

As we have shown above in Figs. 5.5 and 5.6, the mean-square pair separation deviates from the Batchelor prediction at a universal time of roughly $0.075t_0$. The dispersion slows, and as we have shown this cannot be evidence of classical Richardson-Obukhov scaling. We are then left with only a few plausible explanations for the deviation. It could be due to the influence of the large scales,

representing a transition to the Taylor diffusion regime, or to finite volume effects. It is also possible that the deviation is due to higher-order corrections to the Batchelor scaling law.

Let us consider the Taylor expansion of $\langle [r_i(t) - r_{0i}]^2 \rangle$ about $t = 0$. To third order, we have

$$\begin{aligned} \langle [r_i(t) - r_{0i}]^2 \rangle &\approx \left[\langle r(t)^2 \rangle - 2\langle r_i(t) \rangle r_{0i} + r_0^2 \right] \Big|_{t=0} \\ &+ t [2\langle r_i(t) \delta u_i(t) \rangle - 2r_{0i} \langle \delta u_i(t) \rangle] \Big|_{t=0} \\ &+ \frac{1}{2} t^2 [2\langle \delta u_i(t) \delta u_i(t) \rangle + 2\langle r_i(t) \delta a_i(t) \rangle - 2r_{0i} \langle \delta a_i(t) \rangle] \Big|_{t=0} \\ &+ \frac{1}{6} t^3 \left[6\langle \delta u_i(t) \delta a_i(t) \rangle + 2 \left\langle r_i(t) \frac{\partial \delta a_i(t)}{\partial t} \right\rangle - 2r_{0i} \left\langle \frac{\partial \delta a_i(t)}{\partial t} \right\rangle \right] \Big|_{t=0}, \end{aligned} \quad (5.11)$$

where δu and δa are the relative velocity and acceleration of the particles, respectively. The first two terms of this expansion drop out, leaving us with

$$\langle [r_i(t) - r_{0i}]^2 \rangle \approx \langle \delta u_i(r_0) \delta u_i(r_0) \rangle t^2 + \langle \delta u_i(r_0) \delta a_i(r_0) \rangle t^3, \quad (5.12)$$

where we have made use of the relation $\delta u(t = 0) = \delta u(r_0)$. The t^2 term is exactly the Batchelor prediction we derived above. The t^3 term, however, involves the trace of the Eulerian mixed velocity-acceleration structure function. This structure function has the same units as the energy dissipation rate ϵ ; K41, therefore, predicts that it should depend only on ϵ , with no r_0 dependence. On the surface, this cubic term appears to be equivalent to the Richardson-Obukhov prediction: it scales as t^3 and has no dependence on the initial separation. Hill (2005), however, building on a result of Mann *et al.* (1999), has recently shown directly from the Navier-Stokes equations that $\langle \delta u_i(r) \delta a_i(r) \rangle$ is in fact strictly negative, and given by

$$\langle \delta u_i(r) \delta a_i(r) \rangle = -2\epsilon. \quad (5.13)$$

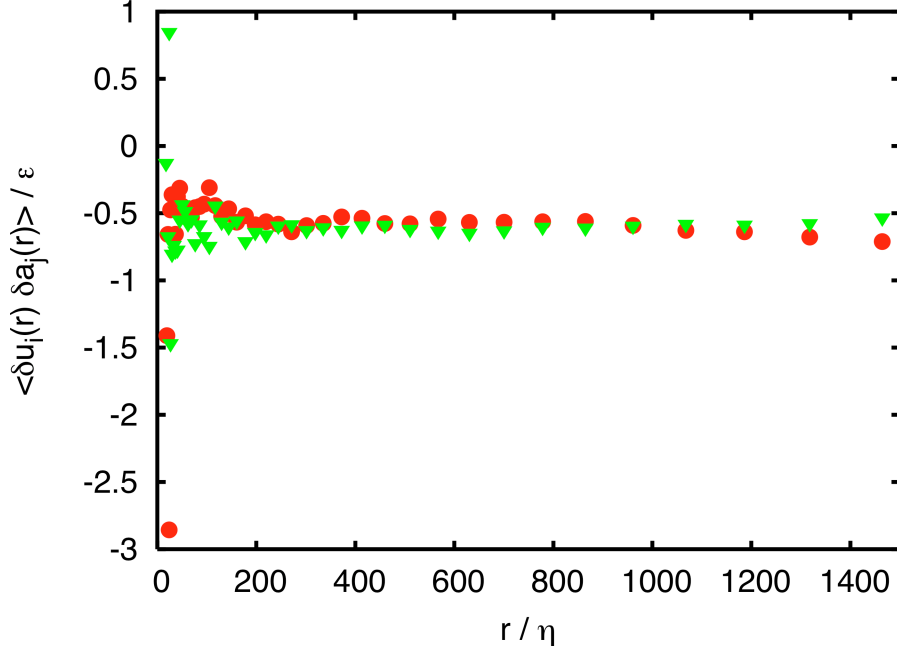


Figure 5.11: The Eulerian mixed velocity-acceleration structure function at $R_\lambda = 815$. Both the longitudinal (●) and transverse (▼) components are shown. As expected, the structure function is constant in the inertial range.

This term will therefore slow the dispersion rather than enhance it, in direct opposition to the Richardson-Obukhov prediction where g is a positive constant but potentially in agreement with our observations.

Our measurements of $\langle \delta u_i(r) \delta a_j(r) \rangle$ are shown in Fig. 5.11 for $R_\lambda = 815$. Following the same procedure as for the Eulerian second-order velocity structure functions, we split $\langle \delta u_i(r) \delta a_j(r) \rangle$ into a longitudinal component measured along the separation vector and a transverse component measured orthogonal to \mathbf{r} . We find these quantities to be constant in the inertial range, as expected. We have measured the longitudinal and transverse scaling constants over a range of Reynolds numbers, as shown in Fig. 5.12. The longitudinal scaling constant appears not to vary with R_λ , while the magnitude of the transverse scaling constant shrinks for $R_\lambda > 500$. This is most likely an effect of poor resolution of the acceleration at

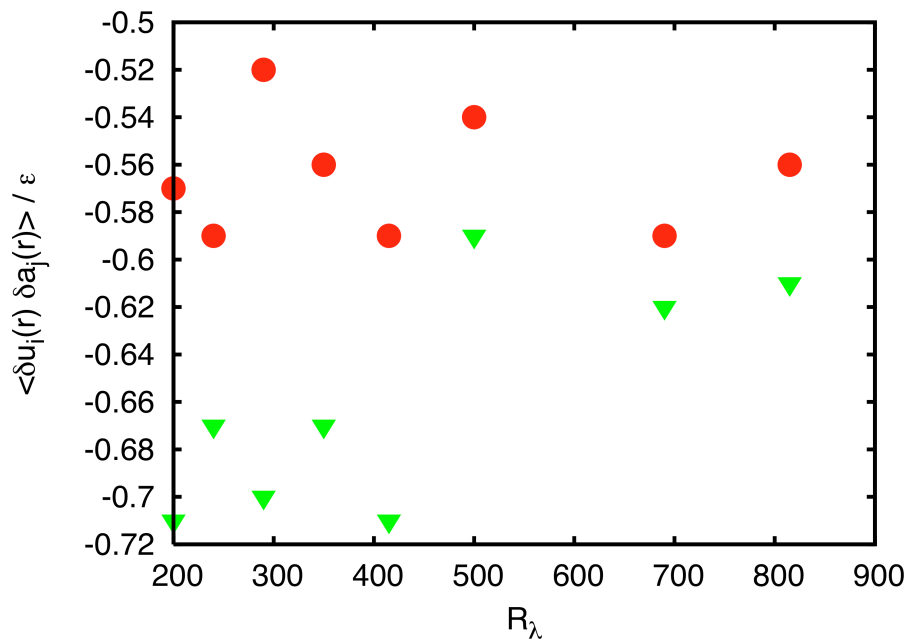


Figure 5.12: Longitudinal (\bullet) and transverse (\blacktriangledown) scaling constants for the Eulerian mixed velocity-acceleration structure function as a function of Reynolds number. The magnitude of the transverse scaling constant shrinks for $R_\lambda > 500$, possibly due to poor resolution of the accelerations.

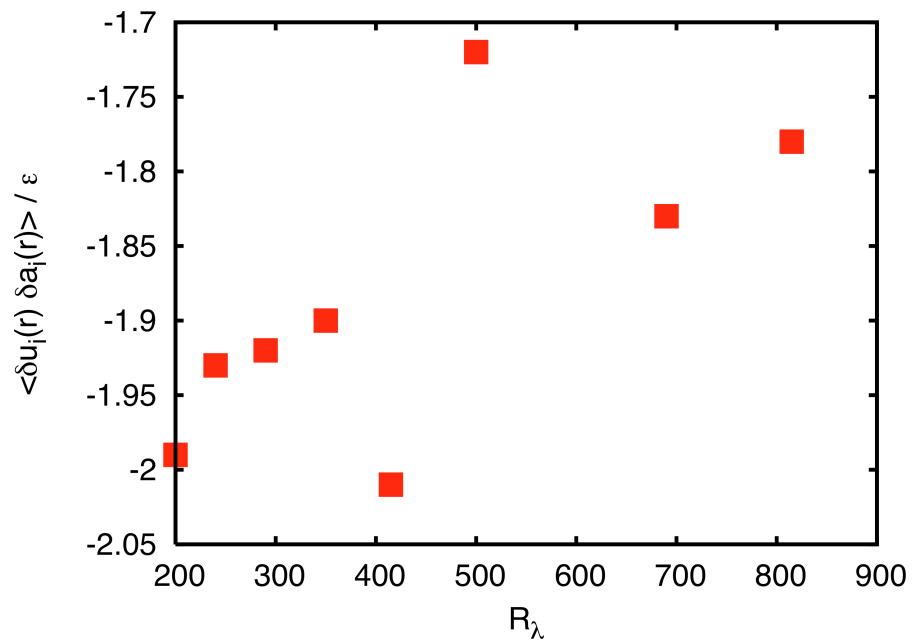


Figure 5.13: Trace of the Eulerian mixed velocity-acceleration structure function as a function of Reynolds number. At low Reynolds number, the trace is clustered near -2 , while for higher Reynolds number it is closer to -1.8 . The change is primarily due to the decrease of the transverse scaling constant.

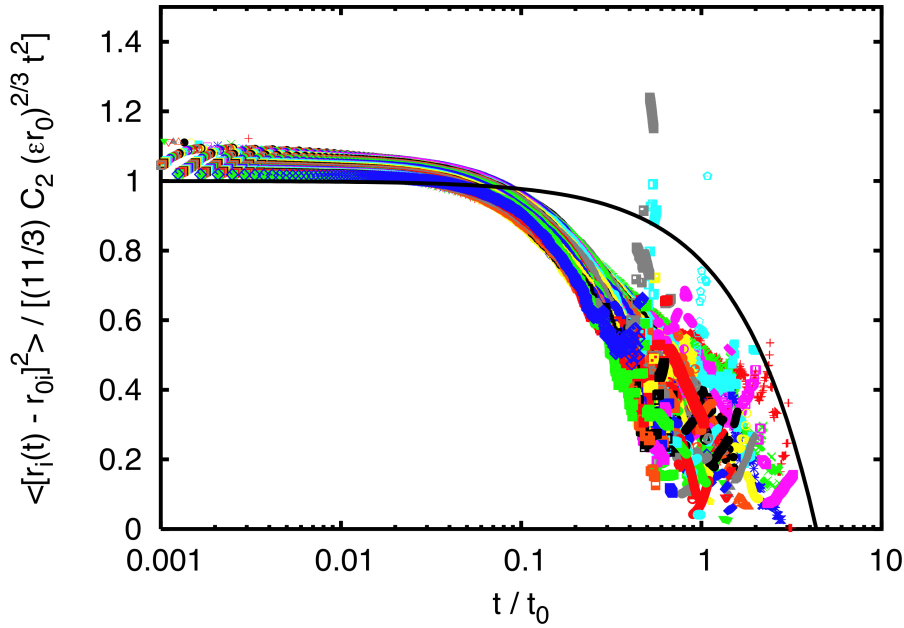


Figure 5.14: The same data from Fig. 5.5 shown with the Batchelor prediction augmented with the third-order correction (solid line). The new model captures the trend of the deviation, but is not quantitatively correct. It is therefore likely that the deviation of the data from Batchelor's law is due either to the influence of the large scales or to finite volume effects.

high Reynolds number. The trace of the structure function, shown in Fig. 5.13, is clustered near -2 for the low Reynolds number data, and is closer to -1.8 for higher Reynolds numbers. Most of this change is due to the smaller transverse scaling constant.

We have attempted to use this correction term to account for the deviation of the data from Batchelor's prediction shown in Fig. 5.5, as shown in Fig. 5.14. The new model does capture the trend of the data, but deviates from the original Batchelor prediction at a later time. It is therefore likely that the deviation is due either to interaction with the large scales or to finite volume effects rather than to higher-order corrections to Batchelor's law.

5.1.5 Distance Neighbor Function

In Richardson's (1926) seminal paper, he suggested that turbulent relative dispersion can be described by a diffusion-like equation. If we additionally assume that the flow is isotropic, we reduce the differential equation to one dimension, given by

$$\frac{\partial}{\partial t}q(r,t) = \frac{1}{r^2}\frac{\partial}{\partial r}\left[r^2K(r,t)\frac{\partial q(r,t)}{\partial r}\right]. \quad (5.14)$$

The function $q(r,t)$ is known as the distance neighbor function, and represents the spherically averaged PDF of the relative dispersion. Measuring the PDF gives us another way to characterize turbulent relative dispersion aside from simply considering the growth of the mean-square separation.

Equation (5.14) differs from a typical diffusion equation since the diffusion constant $K(r,t)$ is a function of space and time. Let us suppose that $K(r,t)$ has a power law dependence on r and t , so that

$$K(r,t) = Ar^\alpha t^\beta, \quad (5.15)$$

where A has the necessary dimensions. To solve this equation, we will look for a self-similar solution of the form

$$q(r,t) = Bt^{-m}f(\xi), \quad (5.16)$$

where $\xi = rt^{-n}$ is the self-similar variable. By making this ansatz, the partial differential equation for q may be written as an ordinary differential equation in f . After some manipulation, this equation reduces to

$$-mf - n\xi f' = A\xi^\alpha t^{\beta-2n+1-n\alpha} f'' + (\alpha+2)A\xi^{\alpha-1} t^{\beta-2n+1+n\alpha} f', \quad (5.17)$$

where the primes denote differentiation with respect to ξ . For the self-similarity condition to be fulfilled, this equation must be a function only of ξ and not of r or

t . We therefore fix n to be

$$n = -\frac{\beta + 1}{\alpha - 2} \quad (5.18)$$

so that the t dependence drops out, reducing eq. (5.17) to

$$A\xi^{\alpha+2}f'' + (\alpha + 2)A\xi^{\alpha+1}f' - \left(\frac{\beta + 1}{\alpha - 2}\right)\xi^3f' + m\xi^2f = 0. \quad (5.19)$$

We are free to choose a value for the parameter m , since there is no condition that sets it. Let us choose $m = 3n$; in this case, eq. (5.19) simplifies further to

$$\frac{d}{d\xi} \left\{ A\xi^{\alpha+2}f' - \left(\frac{\beta + 1}{\alpha - 2}\right)\xi^3f \right\} = 0. \quad (5.20)$$

We now use Richardson's initial condition that $q(r, 0) = \delta(r)$, meaning that the two fluid elements initially came from a point source. This condition leads to

$$\frac{1}{f}f' = \frac{1}{A} \left(\frac{\beta + 1}{\alpha - 2}\right)\xi^{1-\alpha}, \quad (5.21)$$

which is solved by

$$f(\xi) = C \exp \left[-\frac{1}{A} \left(\frac{\beta + 1}{(\alpha - 2)^2}\right)\xi^{2-\alpha} \right]. \quad (5.22)$$

Therefore,

$$q(r, t) = Bt^{3(\frac{\beta+1}{\alpha-2})} \exp \left[-\frac{1}{A} \left(\frac{\beta + 1}{(\alpha - 2)^2}\right)r^{2-\alpha}t^{-(\beta+1)} \right]. \quad (5.23)$$

We can now fix the constant B by requiring that the distance neighbor function be normalized, since it is a PDF. Therefore,

$$\int_0^\infty 4\pi r^2 q(r, t) dr = 1. \quad (5.24)$$

Inserting the solution for $q(r, t)$ given by eq. (5.23) and making the change of variables

$$\rho = \frac{1}{A} \frac{\beta + 1}{(\alpha - 2)^2} r^{2-\alpha} t^{-(\beta+1)}, \quad (5.25)$$

this integral may be written as

$$\frac{4\pi B}{A(2-\alpha)} \left(\frac{(\alpha-2)^2}{\beta+1} \right)^{\frac{3}{2-\alpha}} \int_0^\infty \rho^{\frac{1+\alpha}{2-\alpha}} e^{-\rho} d\rho = 1. \quad (5.26)$$

Solving this equation we have

$$B = \left(\frac{2-\alpha}{4\pi} \right) \left(A \frac{(\alpha-2)^2}{\beta+1} \right)^{-\frac{3}{2-\alpha}} \frac{1}{\Gamma\left(\frac{3}{2-\alpha}\right)}. \quad (5.27)$$

The relative dispersion $\langle r^2 \rangle$ may now be calculated from the distance neighbor function, since

$$\langle r^2 \rangle = \int_0^\infty 4\pi r^4 q(r, t) dr. \quad (5.28)$$

Making the same change of variables as in eq. (5.25), we find that

$$\langle r^2 \rangle = \left(A \frac{(\alpha-2)^2}{\beta+1} \right)^{\frac{2}{2-\alpha}} t^{2\left(\frac{\beta+1}{2-\alpha}\right)} \frac{\Gamma\left(\frac{5}{2-\alpha}\right)}{\Gamma\left(\frac{3}{2-\alpha}\right)}. \quad (5.29)$$

In terms of $\langle r^2 \rangle$, we can write the distance neighbor function as

$$q(r, t) = \left(\frac{2-\alpha}{4\pi} \right) \frac{\left[\Gamma\left(\frac{5}{2-\alpha}\right) \right]^{3/2}}{\left[\Gamma\left(\frac{3}{2-\alpha}\right) \right]^{5/2} \langle r^2 \rangle^{3/2}} \exp \left[- \left(\frac{\Gamma\left(\frac{5}{2-\alpha}\right)}{\Gamma\left(\frac{3}{2-\alpha}\right)} \frac{r^2}{\langle r^2 \rangle} \right)^{\frac{2-\alpha}{2}} \right]. \quad (5.30)$$

In the inertial range, K41 requires that the constant A can depend only on the dissipation rate ϵ . Suppose that $A = \kappa\epsilon^\gamma$, so that

$$K \sim \epsilon^\gamma r^\alpha t^\beta. \quad (5.31)$$

As K must have units of diffusivity, eq. (5.31) requires that

$$\alpha = 2(1 - \gamma) \quad (5.32)$$

and

$$\beta = 3\gamma - 1. \quad (5.33)$$

From eq. (5.29), it is then clear that *any* choice of α and β consistent both dimensionally and with K41 leads to $\langle r^2 \rangle \sim t^3$ (Klafter *et al.*, 1987). Comparing with the Richardson-Obukhov law, the Richardson constant is therefore given by

$$g = \left(\frac{4}{3} \kappa \gamma \right)^{1/\gamma} \frac{\Gamma\left(\frac{5}{2\gamma}\right)}{\Gamma\left(\frac{3}{2\gamma}\right)}. \quad (5.34)$$

Sawford (2001) shows that the Richardson constant is related to the Lagrangian structure function constant as $g = 2C_0$. This relation further gives

$$\kappa = \frac{3}{4\gamma} \left[2C_0 \frac{\Gamma\left(\frac{3}{2\gamma}\right)}{\Gamma\left(\frac{5}{2\gamma}\right)} \right]^\gamma. \quad (5.35)$$

In his initial work, Richardson (1926) suggested that $K(r, t) \sim r^{4/3}$ based on diffusion constants measured in systems ranging from molecular diffusion to volcanoes and cyclones. With this choice,

$$q_R(r, t) = \frac{429}{70} \sqrt{\frac{143}{2}} \pi^{-3/2} (g\epsilon t^3)^{-3/2} \exp \left[- \left(\frac{1287r^2}{8g\epsilon t^3} \right)^{1/3} \right], \quad (5.36)$$

where g is again the Richardson constant. Subsequently, Batchelor (1952) proposed instead that $K(r, t) \sim t^2$, which leads to

$$q_B(r, t) = \left(\frac{2\pi}{3} \right)^{-3/2} (g\epsilon t^3)^{-3/2} \exp \left[- \frac{3}{2} \frac{r^2}{g\epsilon t^3} \right]. \quad (5.37)$$

It is important to recognize that this prediction of Batchelor's is for the PDF of the relative dispersion at long times when a Richardson-Obukhov scaling regime is expected, and is distinct from the t^2 Batchelor scaling regime discussed above.

As described above, the solution to the distance neighbor function requires the initial condition that at $t = 0$, the two fluid elements were in the same location. We cannot replicate this condition in the laboratory. By subtracting off the initial separation of the fluid element pair componentwise, however, we can approximate

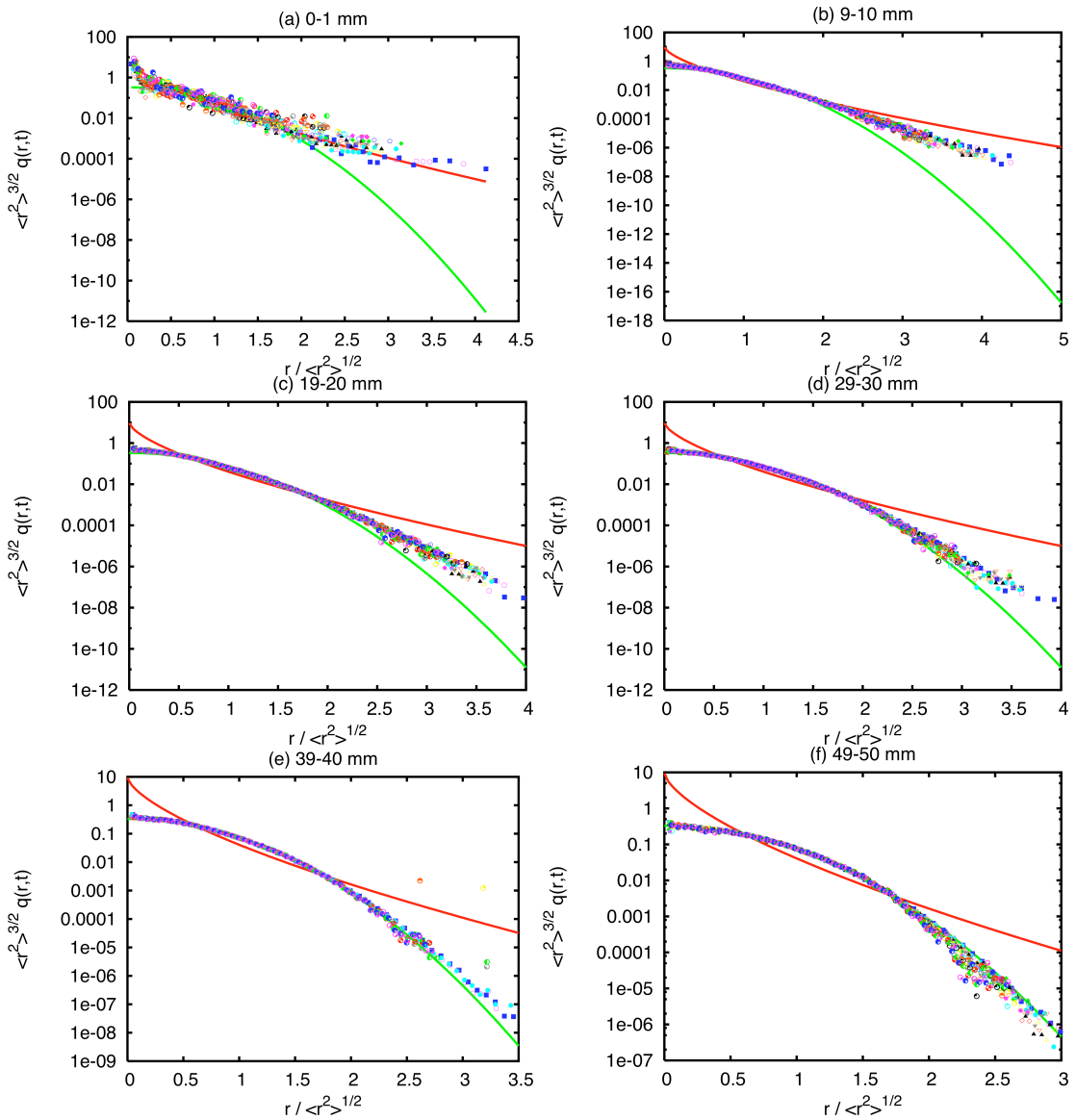


Figure 5.15: Plots of the distance neighbor function for different initial separations at $R_\lambda = 815$. The red line is Richardson's predicted PDF, while the green line is Batchelor's. The symbols show experimental measurements. Each plot shows a different initial separation. For each initial separation, PDFs from twenty times are shown ranging from τ_η to $20\tau_\eta$. At $R_\lambda = 815$, $1 \text{ mm} \sim 43\eta$.

this condition. We note, however, that not all fluid element pairs separate; some pairs will first move closer together before later spreading apart. This approach of subtracting the initial separation from each subsequent pair separation and then taking the length of this vector will treat both separating and approaching fluid element pairs in the same fashion.

Our measurements of the distance neighbor function, defined as above, are shown in Fig. 5.15 for six different initial separations at $R_\lambda = 815$. For each separation, $q(r, t)$ is shown for twenty different times ranging from τ_η to $20\tau_\eta$. We find that for small initial separations, the measured distance neighbor function agrees well with Richardson's predicted form, while for large initial separations, the data agree well with Batchelor's form. For intermediate initial separations, there is a transition region between the Richardson PDF and the Batchelor PDF.

We see the same qualitative trend in lower Reynolds number data. The distance neighbor function is shown in Fig. 5.16 for $R_\lambda = 200$. Again, as the initial separation increases, the data make a transition from Richardson's PDF to Batchelor's.

If we calculate the distance neighbor function without first subtracting the initial separation, different behavior is seen, as shown in Fig. 5.17. For short times, the distance neighbor function is strongly peaked around the RMS separation. In the ideal case where the initial separation r_0 is exact and not binned, the distance neighbor function at $t = 0$ would be a delta function at the RMS separation. As time increases, the distance neighbor function spreads out, appearing to approach the Batchelor prediction regardless of the initial separation. It remains unclear whether this approach is more justified for calculating the distance neighbor function or whether we should subtract the initial separation, as shown above, when

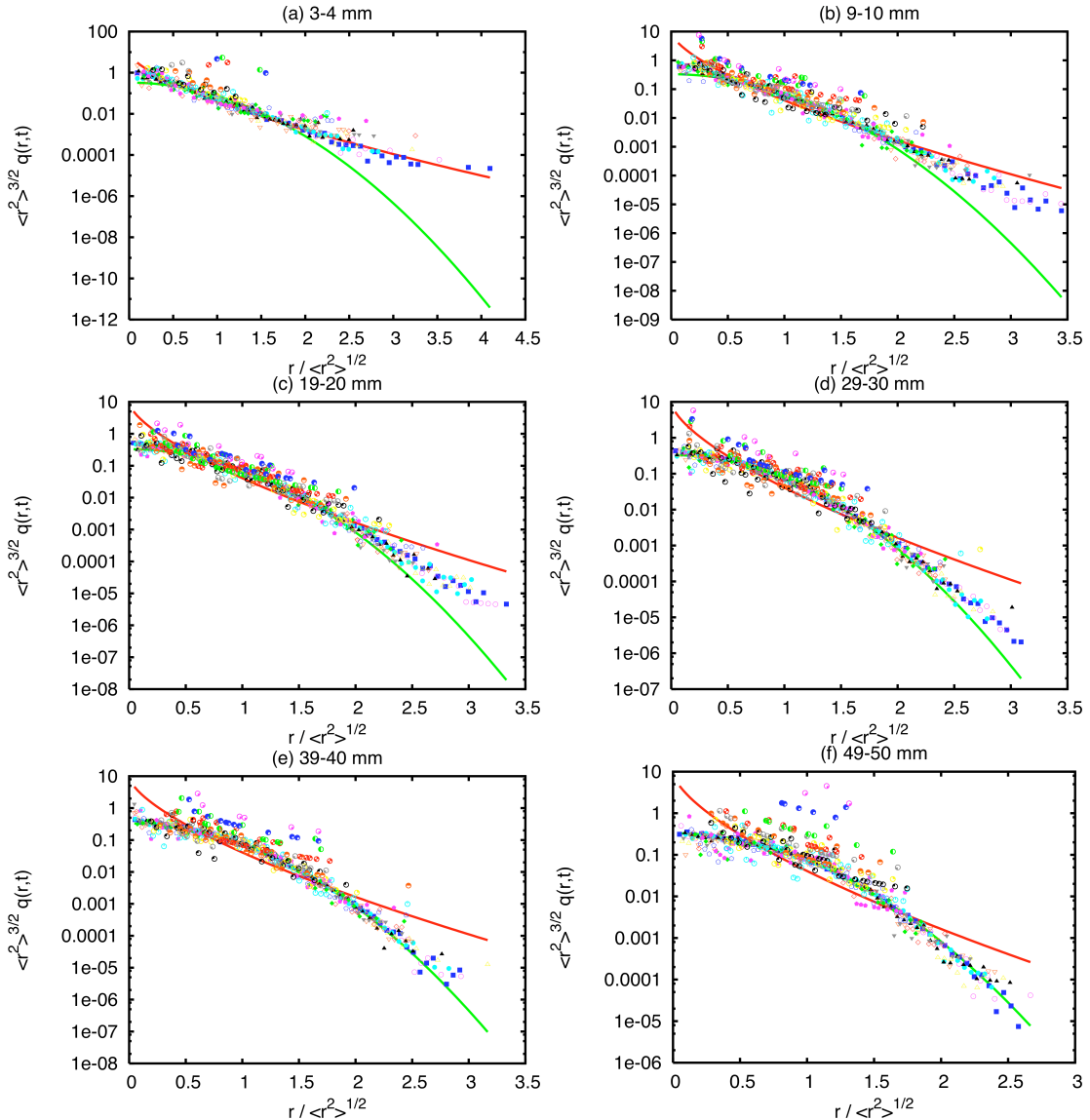


Figure 5.16: Plots of the distance neighbor function for different initial separations at $R_\lambda = 200$. The red line is again Richardson's PDF, while the green line is Batchelor's. The symbols show the experimental measurements. While the data is much noisier, the same qualitative trend towards Batchelor's PDF for large initial separations is apparent. Here, $1 \text{ mm} \sim 5\eta$.

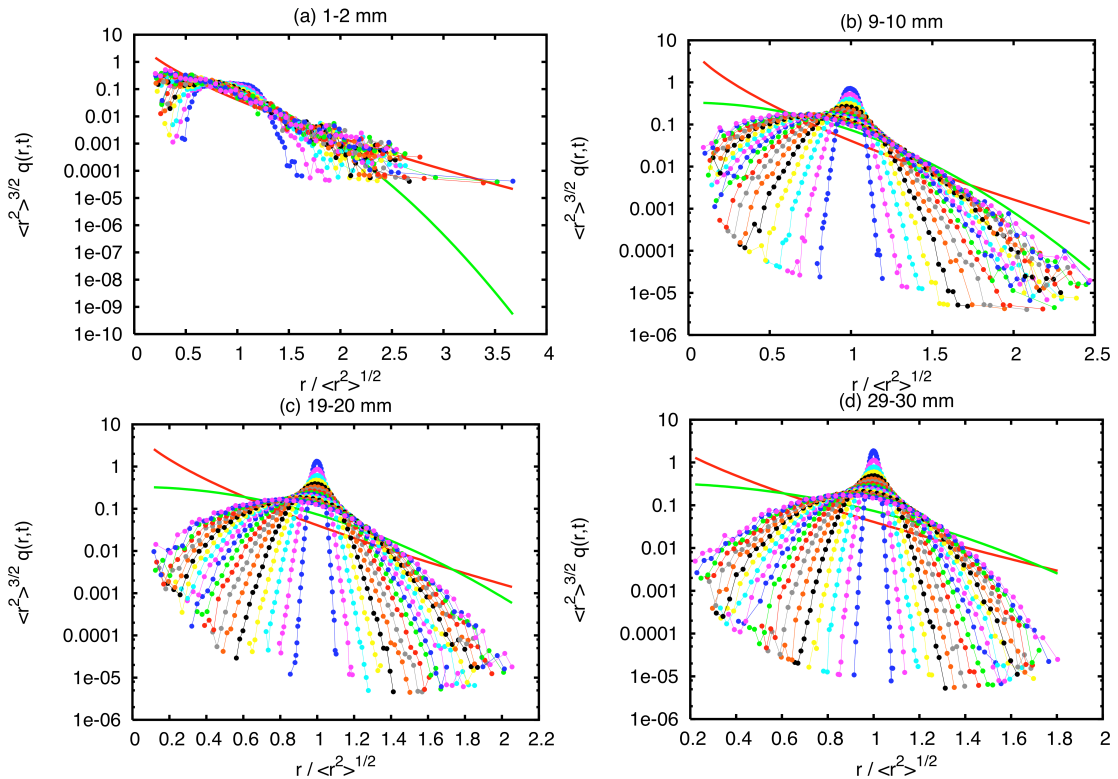


Figure 5.17: Plots of the distance neighbor function at $R_\lambda = 815$ calculated without subtracting the initial separation. The red heavy line is again Richardson's PDF, while the green heavy line is Batchelor's. The short-time data is peaked near unity, as it must be. The measured PDFs spread as time increases, approaching Batchelor's PDF.

faced with a realistic, physical situation where the fluid elements are not dispersing from a point source.

5.1.6 Fixed Scale Statistics

In our experiments at Reynolds numbers up to $R_\lambda = 815$ we have not observed the Richardson-Obukhov law in its original form; instead, we observed a regime consistent with Batchelor's predictions through most of our inertial range. As we have shown above, this behavior suggests that a much higher Reynolds number is required before the Richardson-Obukhov regime can be unambiguously observed. Because of the appeal of the Richardson-Obukhov prediction, however, researchers have introduced new statistics in the hope that behavior consistent with it can be found at the moderate Reynolds numbers reached in experiments and simulations. We have discussed one such quantity above when we considered $\langle r(t)^{2/3} \rangle$ instead of $\langle [r_i(t) - r_{0i}]^2 \rangle$. Instead of studying different averages of the relative particle separation as a function of time, however, one can also study averages of the time it takes for the relative separation to grow to a particular threshold. Such averages of time rather than of space are known as fixed scale statistics since the averaging is performed over an ensemble at a fixed spatial scale rather than at a fixed temporal scale as in the traditional Richardson-Obukhov or Batchelor description of turbulent relative dispersion (Boffetta and Celani, 2000). Dimensionally, a scaling law such as

$$\langle t \rangle = G\epsilon^{-1}r^{2/3} \quad (5.38)$$

is equivalent to the Richardson-Obukhov law.

A particular type of fixed scale statistics that has become well-known is the so-called exit time or doubling time statistics introduced by Artale *et al.* (1997).

An exit time analysis defines a set of thresholds r_n for every particle pair such that $r_n = \rho^n r_0$, where ρ is a scale factor. The exit time $t_\rho(r_n)$ is then defined to be the time it takes for the particle pair to grow from r_n to r_{n+1} . For $\rho = 2$, $t_2(r_n)$ is the time it takes for the pair separation to double in size. Exit time statistics have recently been touted as a powerful alternative to the traditional analysis of turbulent relative dispersion that should show “true” inertial range scaling behavior even at moderate Reynolds numbers (Artale *et al.*, 1997; Boffetta and Celani, 2000; Boffetta and Sokolov, 2002a; Biferale *et al.*, 2005a).

Dimensionally, the ensemble average of the exit times should scale as $\langle t_\rho(r_n) \rangle \sim r_n^{2/3}$. Without some assumptions, however, the exit time analysis cannot be directly compared with more traditional analyses. In particular, a measurement of the scaling of the exit times cannot give the value of the Richardson constant g without assumptions. By assuming the Richardson form for the distance neighbor function, Boffetta and Sokolov (2002a) have found that

$$\langle t_\rho(r_n) \rangle = \left(\frac{143}{81} (g\epsilon)^{-1} \right)^{1/3} \frac{\rho^{2/3} - 1}{\rho^{2/3}} r_n^{2/3}, \quad (5.39)$$

which in turn gives

$$g = \frac{143}{81} \frac{(\rho^{2/3} - 1)^3}{\rho^2} \frac{r_n^2}{\epsilon \langle t_\rho(r_n) \rangle^3}. \quad (5.40)$$

Our measurement of the average exit times at $R_\lambda = 815$ with $\rho = 1.05$ is shown in Fig. 5.18. There is no collapse for data with different initial separations, though at larger scales the data may be approaching an $r_n^{2/3}$ power law as predicted by Boffetta and Sokolov (2002a). In Fig. 5.19, we show a modified version of the exit time statistics where we have subtracted the initial pair separation r_0 componentwise. With the initial separation subtracted, our results appear more similar the simulations of Biferale *et al.* (2005a). Though Biferale *et al.* (2005a)

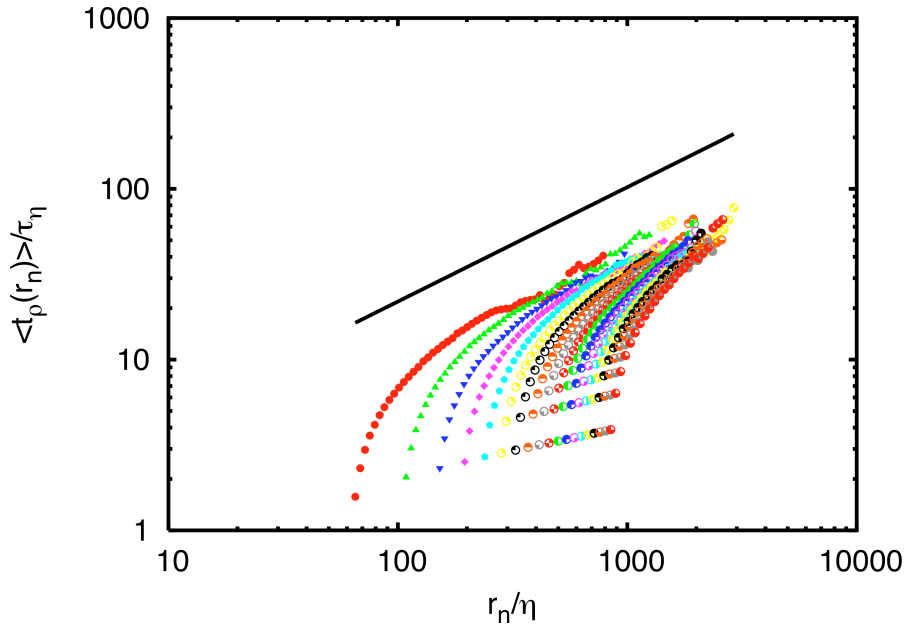


Figure 5.18: Average exit times at $R_\lambda = 815$. The solid line is an $r_n^{2/3}$ power law for reference. From left to right, the symbols correspond to 1 mm wide bins of initial separations ranging from 1–2 mm to 19–20 mm.

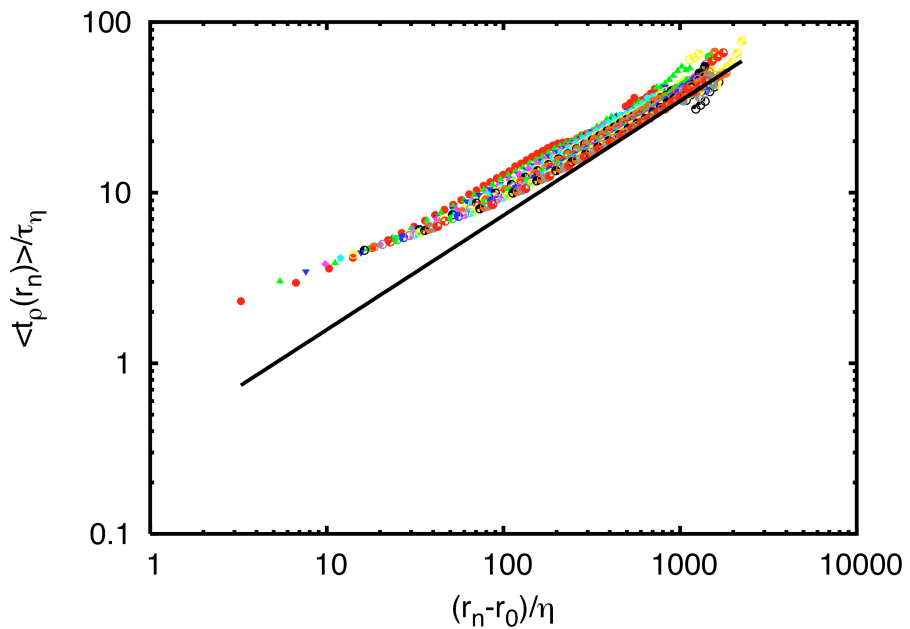


Figure 5.19: Average exit times with the initial separation subtracted at $R_\lambda = 815$. The solid line is again an $r_n^{2/3}$ power law for reference. The symbols are the same as those shown in Fig. 5.18.

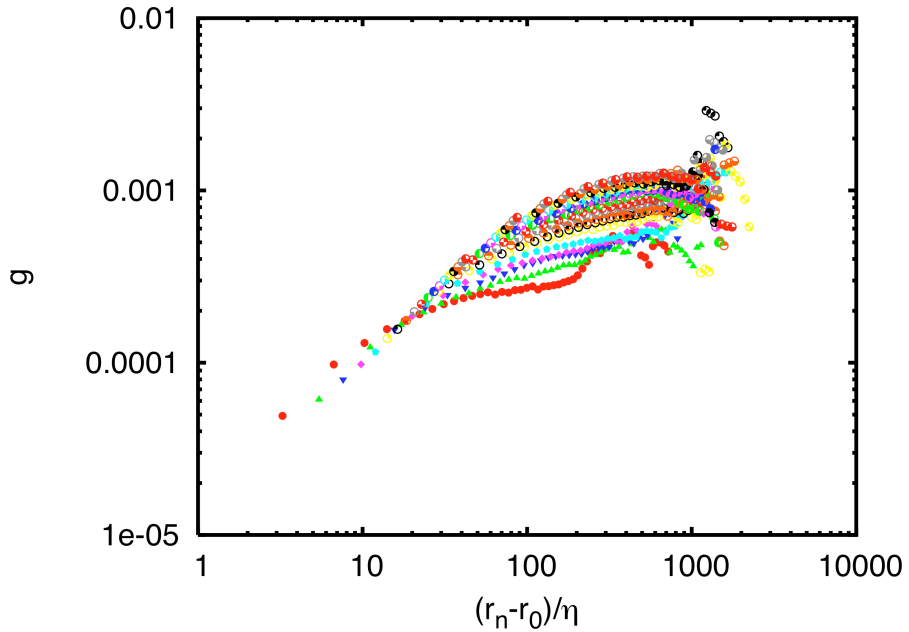


Figure 5.20: The Richardson constant computed from the exit times with the initial separation subtracted at $R_\lambda = 815$. If the exit time statistics were truly universal and independent of initial separation, the data plotted in this way should show a plateau with the same value for each initial separation. This does not appear to be the case.

did not subtract the initial pair separation, they considered only initial separations of less than 20η . With r_0 that small, initial separation effects may be negligible. We, however, do not have enough data at initial separations of that scale with which to test this hypothesis.

As shown above, eq. (5.40) can be used to extract the Richardson constant from exit time statistics, subject to several assumptions. We show this mapping in Fig. 5.20 for the exit time statistics with the initial separation subtracted. Biferale *et al.* (2005a) claim that this type of plot shows a plateau with $\sigma \approx 0.5$, irrespective of the initial separation. We, however, see different behavior. While the data does flatten, there is no universal value observed. In addition, the putative Richardson constant is two orders of magnitude smaller than that reported

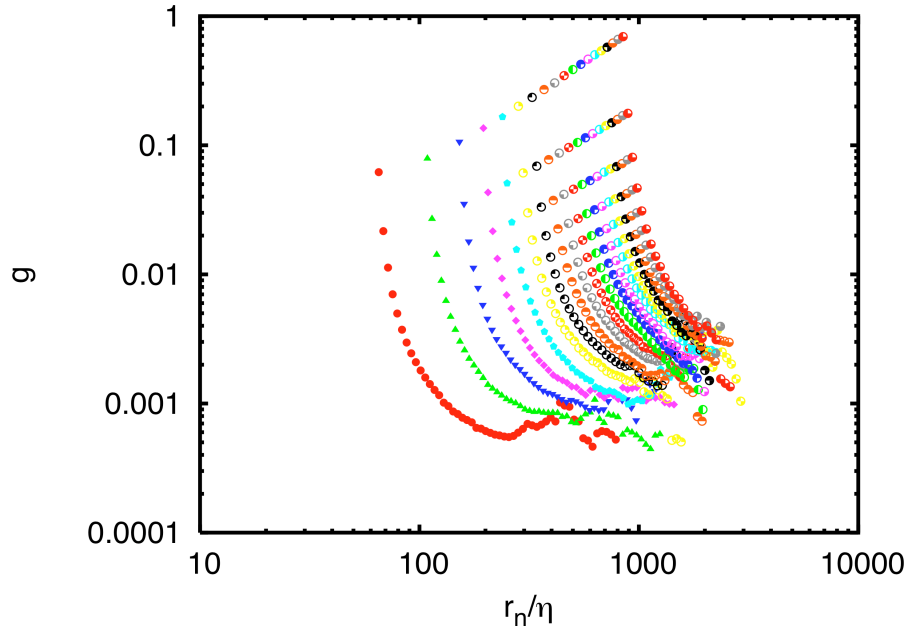


Figure 5.21: The Richardson constant computed from the exit times without subtracting the initial separation at $R_\lambda = 815$. No plateau is seen.

by Biferale *et al.* (2005a). If we instead plot the Richardson constant without subtracting the initial separation, no plateau is seen, as shown in Fig. 5.21.

The data reported by Biferale *et al.* (2005a) was simulated at a lower Reynolds number than the experimental results we have shown above. In order to make sure that our observations are not Reynolds number dependent, we have also computed the same quantities at $R_\lambda = 200$, as shown in Figs. 5.22 and 5.23. The data is both qualitatively and quantitatively similar to the $R_\lambda = 815$ data shown above.

It remains unclear why Biferale *et al.* (2005a) see good scaling for their simulation results while we do not for our experimental measurements. From our results, we can conclude that the exit time statistics do not show clear scaling behavior in our flow, and therefore cannot be universally applicable.

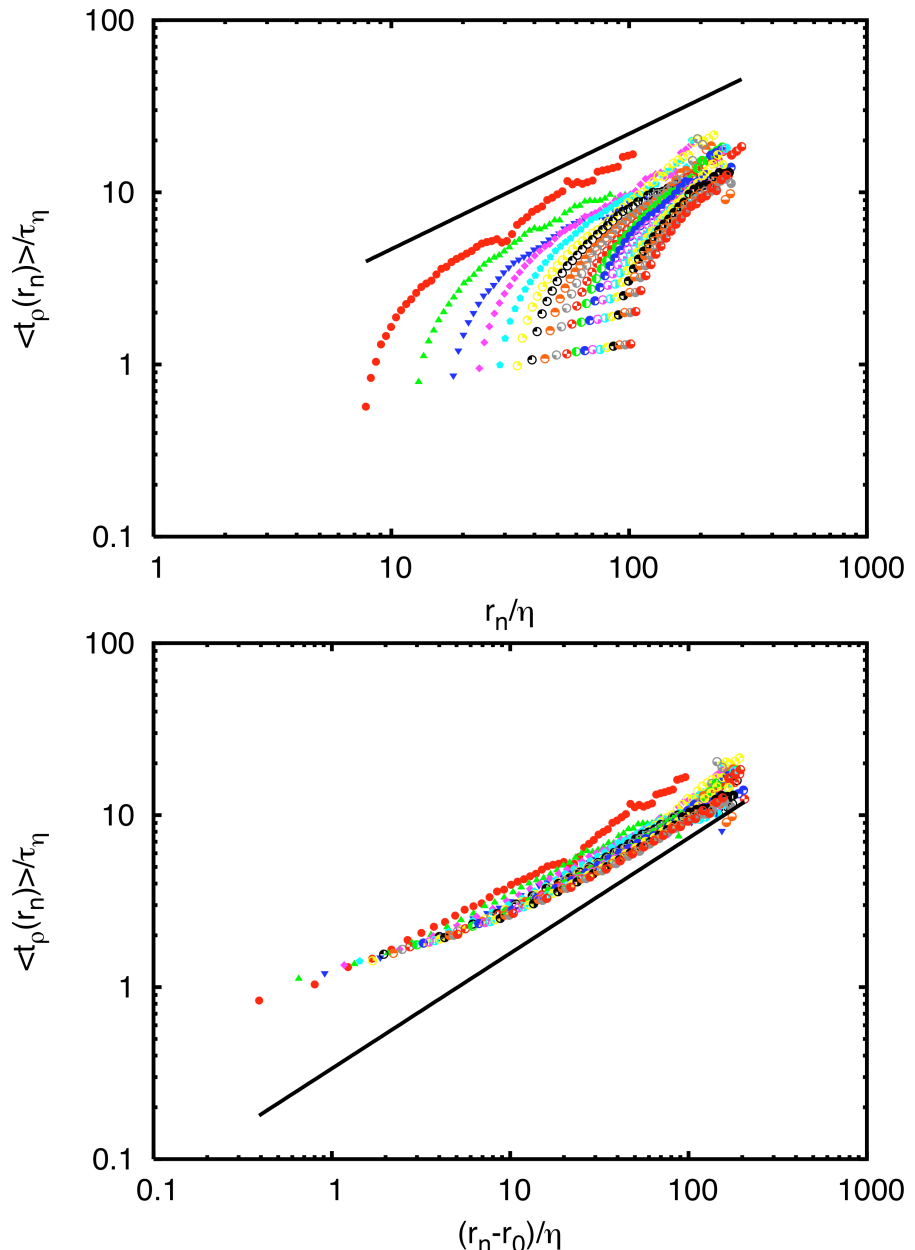


Figure 5.22: Average exit times at $R_\lambda = 200$. The solid line is an $r_n^{2/3}$ power law for reference. From left to right, the symbols again correspond to 1 mm wide bins of initial separations ranging from 1–2 mm to 19–20 mm. In the upper plot, we have not subtracted the initial separations, while in the lower plot we have.

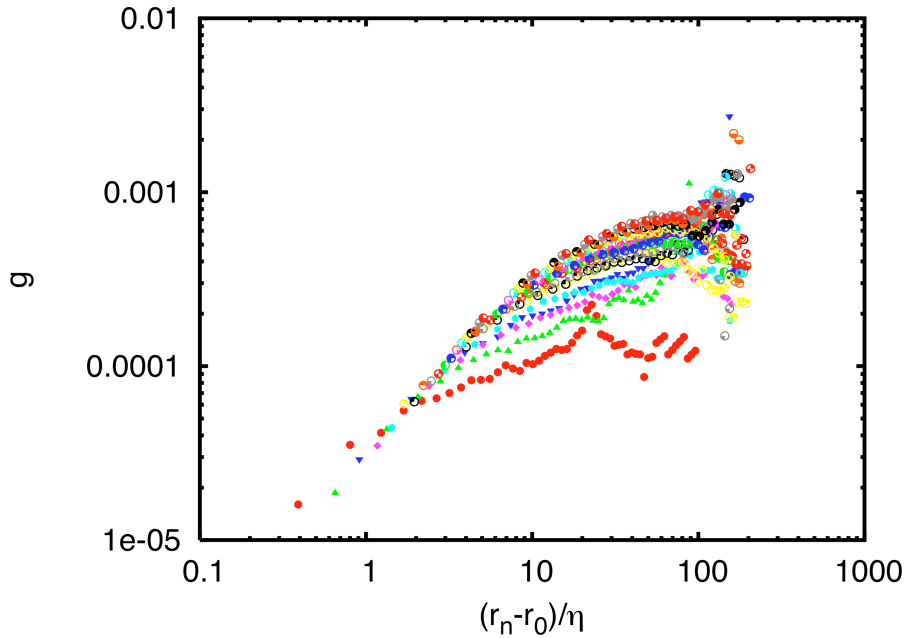


Figure 5.23: The Richardson constant computed from the exit times at $R_\lambda = 200$. Behavior similar to that of the $R_\lambda = 815$ case is observed.

5.2 Coarse-Grained Models

The Navier-Stokes equations are too complex to solve for realistic boundary conditions. In many situations of practical interest, such as solving for the flow field around a vehicle or in a turboengine, however, the boundary conditions are incredibly complex. Researchers are therefore turning increasingly to computer simulations to solve these difficult problems. Direct numerical simulation (DNS), where the Navier-Stokes equations are solved directly, is the most accurate simulation method known today. Due to limited computer power, however, DNS can only be used to simulate a relatively small range of scales, and is therefore restricted to low Reynolds numbers. The problem becomes worse when complex boundary conditions are included, and so in such cases DNS is not feasible.

Current commercial software packages generally use somewhat crude RANS-

level modeling, and the results of the simulation may be quantitatively poor, though such simulations can reach higher Reynolds numbers. A third technique, known as Large Eddy Simulation (LES), however, may be able to combine much of the accuracy of a DNS with the high Reynolds numbers achievable in RANS models.

Like in DNS, LES solves the Navier-Stokes equations directly on a grid. The primary difference between DNS and LES is the grid resolution. A DNS grid resolves the cascade all the way down to the Kolmogorov scale, while an LES grid is much more coarse. Because of the coarseness of the grid, an LES uses a subgrid-scale model for the small scales of turbulence, since these scales are presumed to be universal for all turbulent flows, regardless of how the turbulence is generated. The fixed computational resources are then free to be used to solve for the large scale flow directly, and the small scales are given by the model.

The fidelity of an LES to the real situation of interest is determined to a great degree by the quality of the subgrid-scale model. Many of the commonly used models have been surveyed by Meneveau and Katz (2000). A new model based on a coarse-graining of the velocity gradient tensor over a set of four points in the inertial range has recently been proposed (Chertkov *et al.*, 1999; Pumir *et al.*, 2000, 2001). We have attempted to address the validity of this model experimentally.

5.2.1 Tetrads Dynamics

The central quantity in the model of Chertkov *et al.* (1999) is a coarse-grained velocity gradient tensor. Before discussing the model, then, let us consider the dynamics of the true velocity gradient tensor. Let us define

$$\frac{\partial u_j}{\partial x_i} \equiv m_{ij} \quad (5.41)$$

for simplicity. In the limit of infinite Reynolds number and far away from any boundaries, the Navier-Stokes equations are well-approximated by the Euler equations, where the viscosity is set to zero. In that case, the momentum equation is

$$\frac{\partial u_j}{\partial t} + u_k \frac{\partial u_j}{\partial x_k} = - \frac{\partial p}{\partial x_j}. \quad (5.42)$$

Let us now take the gradient of this equation. Since the gradient commutes with the time differentiation, we have

$$\frac{\partial}{\partial t} \frac{\partial u_j}{\partial x_i} + \frac{\partial}{\partial x_i} \left(u_k \frac{\partial u_j}{\partial x_k} \right) = - \frac{\partial^2 p}{\partial x_i \partial x_j}, \quad (5.43)$$

which leads to

$$\frac{Dm_{ij}}{Dt} + m_{ik}m_{kj} = - \frac{\partial^2 p}{\partial x_i \partial x_j}. \quad (5.44)$$

Let us now consider the trace of this expression. Due to incompressibility, $\text{Tr } \mathbf{m} \equiv m_{ii} = 0$, and so

$$\text{Tr } \mathbf{m}^2 = -\nabla^2 p. \quad (5.45)$$

We can therefore model the pressure Hessian as

$$-\frac{\partial^2 p}{\partial x_i \partial x_j} = a_{ij} \text{Tr } \mathbf{m}^2 + z_{ij} \quad (5.46)$$

as long as

$$\text{Tr } \mathbf{a} = 1 \quad (5.47)$$

and

$$\text{Tr } \mathbf{z} = 0. \quad (5.48)$$

We identify $a_{ij} \text{Tr } \mathbf{m}^2$ with the local effect of the pressure of the fluid element on itself and z_{ij} with the nonlocal contribution of the pressure due to the rest of the

fluid (Vieillefosse, 1984; Cantwell, 1992; Chertkov *et al.*, 1999). We can therefore write the equation of motion of the velocity gradient as

$$\frac{Dm_{ij}}{Dt} + m_{ik}m_{kj} - a_{ij} \text{Tr } \mathbf{m}^2 = z_{ij}. \quad (5.49)$$

If we set $a_{ij} \equiv \delta_{ij}$ and $z_{ij} \equiv 0$, we recover the “restricted Euler dynamics” introduced by Vieillefosse (1984) and solved analytically by Cantwell (1992).

In LES, as discussed above, the true velocity gradient tensor cannot be determined. This is also the case in most experimental situations due the difficulty in measuring spatial gradients. Chertkov *et al.* (1999) have therefore introduced a coarse-graining of the velocity gradient tensor defined to be

$$M_{ij} \equiv \int_{\Gamma} \frac{\partial u_j}{\partial x_i} d\Gamma, \quad (5.50)$$

where Γ is a time-dependent volume of fluid with a characteristic length scale R lying in the inertial range. To simplify matters further, Chertkov *et al.* (1999) consider the minimal parameterization of such a volume by four fluid elements, which we label as \mathbf{x}_1 , \mathbf{x}_2 , \mathbf{x}_3 , and \mathbf{x}_4 . This collection of four points is termed a “tetrad.” In homogeneous, isotropic turbulence, the motion of the center of mass of the tetrad is irrelevant, and we define three vectors that parameterize the relative positions of the four points defining the tetrad:

$$\begin{aligned} \mathbf{X}_1 &= \frac{1}{\sqrt{2}}(\mathbf{x}_2 - \mathbf{x}_1) \\ \mathbf{X}_2 &= \frac{1}{\sqrt{6}}[(\mathbf{x}_3 - \mathbf{x}_2) + (\mathbf{x}_3 - \mathbf{x}_1)] \\ \mathbf{X}_3 &= \frac{1}{\sqrt{12}}[(\mathbf{x}_4 - \mathbf{x}_3) + (\mathbf{x}_4 - \mathbf{x}_2) + (\mathbf{x}_4 - \mathbf{x}_1)] \end{aligned} \quad (5.51)$$

These three vectors may be interpreted as the columns of a matrix \mathbf{X} . In the same ways, we define \mathbf{V} to be the matrix of the relative velocities of the four tetrad

points by simply replacing the tetrad point positions in eq. (5.51) by the tetrad point velocities.

Defining $\mathbf{K} \equiv \mathbf{X}^{-1}$, we can write the coarse-grained velocity gradient tensor as

$$M_{ij} = K_{ik}V_{kj} - \frac{1}{3}\delta_{ij}\text{Tr}(\mathbf{KV}), \quad (5.52)$$

where the term proportional to the Kronecker delta enforces $\text{Tr } \mathbf{M} = 0$, as required by incompressibility. Chertkov *et al.* (1999) then proceed to assume that this coarse-grained tensor evolves according to the same equation of motion as the true velocity gradient tensor, namely by

$$\frac{DM_{ij}}{Dt} + M_{ik}M_{kj} - A_{ij}\text{Tr } \mathbf{M}^2 = Z_{ij}, \quad (5.53)$$

where now

$$A_{ij} \equiv \frac{K_{ik}K_{kj}}{\text{Tr } \mathbf{K}^2}. \quad (5.54)$$

\mathbf{A} is a measure of the anisotropy of the tetrad. Chertkov *et al.* (1999) model \mathbf{Z} as a random variable.

The restricted Euler dynamics lie in the phase space spanned by

$$Q \equiv -\frac{1}{2}\text{Tr } \mathbf{M}^2 \quad (5.55)$$

and

$$R \equiv -\frac{1}{3}\text{Tr } \mathbf{M}^3, \quad (5.56)$$

two of the invariants implied the Cayley-Hamilton theorem (Vieillefosse, 1984; Cantwell, 1992). The third invariant of \mathbf{M} is (Vieillefosse, 1984)

$$D = 3[\text{Tr } \mathbf{M}^3]^2 - \frac{1}{2}[\text{Tr } \mathbf{M}^2]^3 = 27R^2 + 4Q^3. \quad (5.57)$$

When $D = 0$, \mathbf{M} has degenerate eigenvalues. For $D > 0$, the eigenvalues of \mathbf{M} are complex and the flow is dominated by vorticity. When $D < 0$, the eigenvalues are real and strain dominates the flow (Cantwell, 1992).

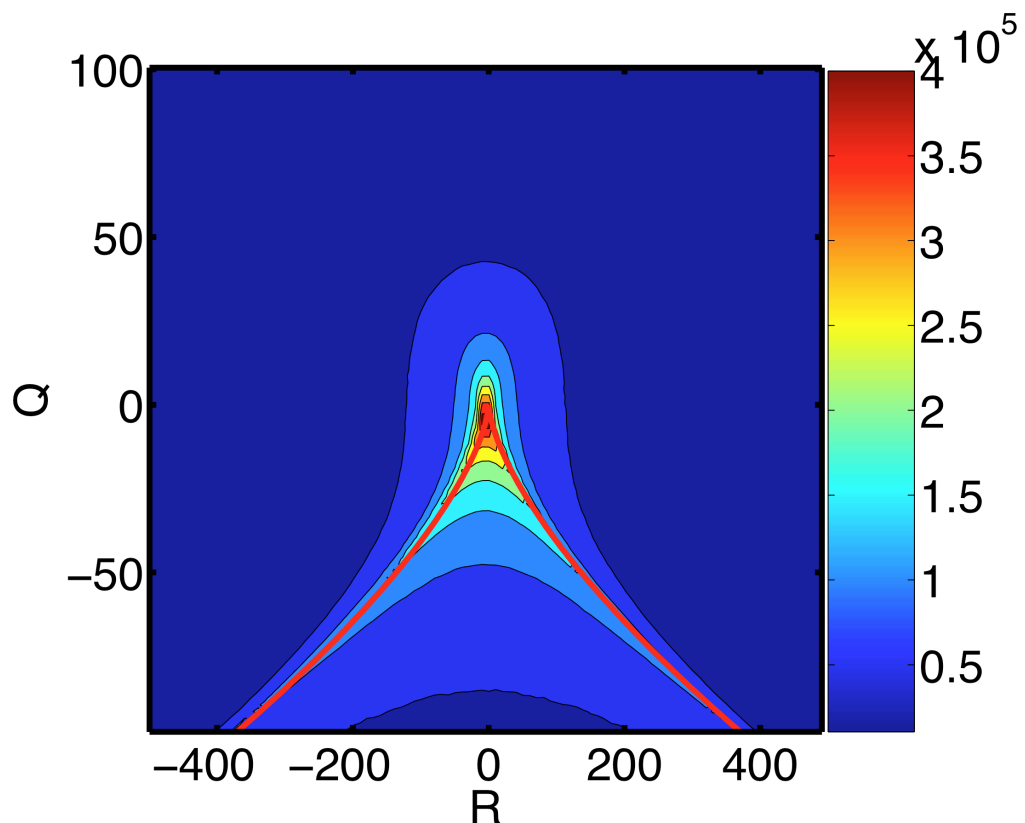


Figure 5.24: PDF of all tetrads in the phase space spanned by Q and R at $R_\lambda = 815$. The initial radius of gyration of the tetrads was fixed to lie between 18 and 21 mm. The heavy solid line shows the $D = 0$ separatrix.

In studying the dynamics of the true velocity gradient tensor, it is common to investigate the PDFs of \mathbf{m} in the $Q - R$ phase space. These PDFs, as shown in Borue and Orszag (1998) and Chertkov *et al.* (1999), for example, show an asymmetry characterized by a pronounced stretching in the positive R , negative Q quadrant. Chertkov *et al.* (1999) have seen similar stretching in their tetrad model for tetrads that initially have a radius of gyration larger than the dissipation scale but still very small compared to the integral scale. We have measured these PDFs in our flow; an example is shown in Fig. 5.24 at $R_\lambda = 815$. For this PDF, we have considered all the tetrads with initial radii of gyration that lie between 18 and 21 mm, corresponding to 775–900 Kolmogorov lengths. While we do see stretching of the PDF along the $D = 0$ separatrix, as expected, we see no extra stretching in the positive R , negative Q quadrant. It is possible that this lack of stretching is due to the large initial size of the tetrads (Pumir, 2005); Chertkov *et al.* (1999) considered only much smaller tetrads. We, however, do not see enough tetrads with small initial sizes to resolve their PDF.

Chertkov *et al.* (1999) also only considered tetrads that were initially isotropic. We have attempted to mimic this initial condition by constructing the $Q - R$ PDF only for tetrads that were initially within 10% of isotropy, defined by the relative magnitude of the three eigenvalues of the coarse-grained velocity gradient tensor. The PDF of these initially nearly isotropic tetrads is shown in Fig. 5.25 for the same conditions as the previous PDF. The statistics are much poorer, but it seems that there may be some stretching in the positive R , negative Q quadrant, as predicted by the model.

More data will have to be taken in order to confirm the tetrad model fully. The PDFs we have measured here are essentially Eulerian quantities. Since our

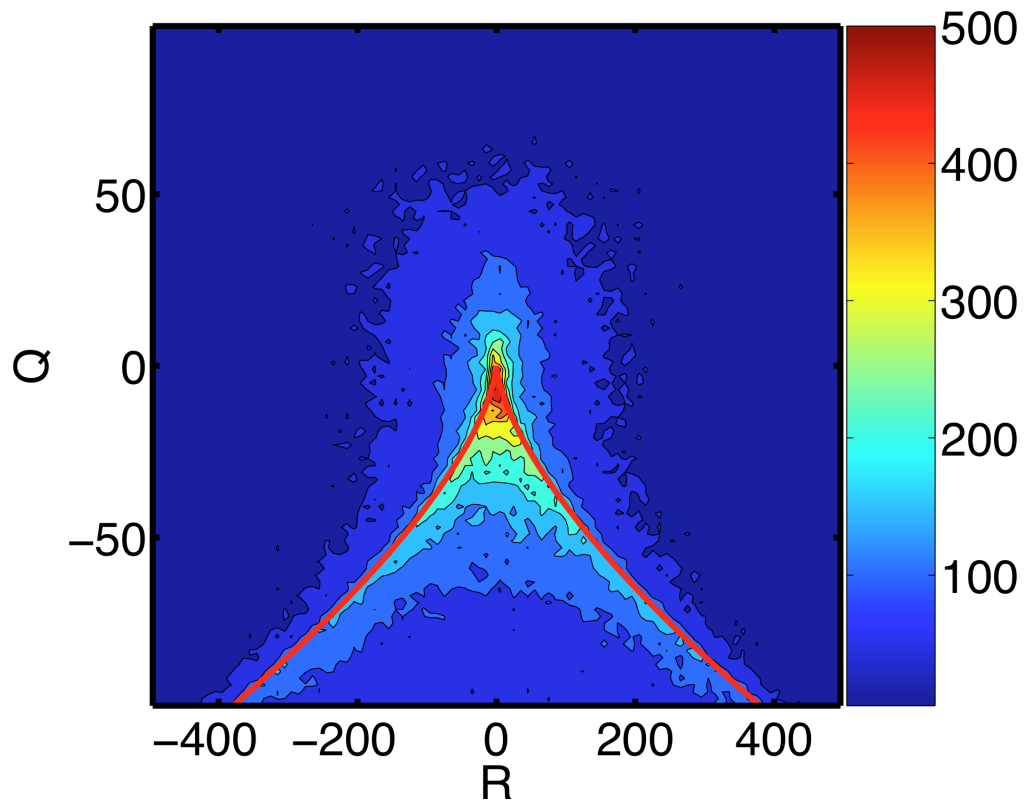


Figure 5.25: PDF of initially nearly isotropic tetrads at $R_\lambda = 815$. Again, the initial radius of gyration was fixed to lie between 18 and 21 mm. The heavy solid line shows the $D = 0$ separatrix. A small amount of stretching in the positive R , negative Q quadrant is evident for these tetrads.

experiment is inefficient for measuring such quantities, we expect more traditional Eulerian measurement techniques, particularly multiprobe hot-wire anemometry, will be more effective for confirming or contradicting the tetrad model.

5.2.2 The Geometry of Turbulence

Pumir *et al.* (2000) have also investigated the statistical geometry implicit in their tetrad model. Let us define a tensor

$$g_{ij} \equiv X_{ik}X_{kj} \quad (5.58)$$

analogous to the inertia tensor of a collection of point masses. The radius of gyration R of the tetrad, defined as $R^2 \equiv \text{Tr } \mathbf{g}$, provides a convenient linear measure of the tetrad size.

Let us consider the eigenvalues of \mathbf{g} , which we denote as g_1 , g_2 , and g_3 where

$$g_1 > g_2 > g_3. \quad (5.59)$$

Note that, by definition, $g_1 + g_2 + g_3 = R^2$. We can therefore normalize the eigenvalues by R^2 to force them to lie between zero and one; we denote these scaled eigenvalues by $g_i/R^2 \equiv I_i$. The evolution of the three eigenvalues gives information on the shape changes of the tetrad. When the three eigenvalues are equal, the tetrad is a regular tetrahedron. If the eigenvalues are not equal, however, the tetrad will be anisotropic. If $g_1 \approx g_2$ and $g_1 \gg g_3$, the tetrad will be nearly planar, while if $g_1 \gg g_2$ and $g_2 \approx g_3$, the tetrad will be needle-like. The evolution of the tetrad shapes has recently been considered in simulation (Biferale *et al.*, 2005b), but there have been no experimental studies to date.

We begin by considering the nearly isotropic tetrads introduced above in the context of the $Q-R$ PDFs for the coarse-grained velocity gradient tensor. The evo-

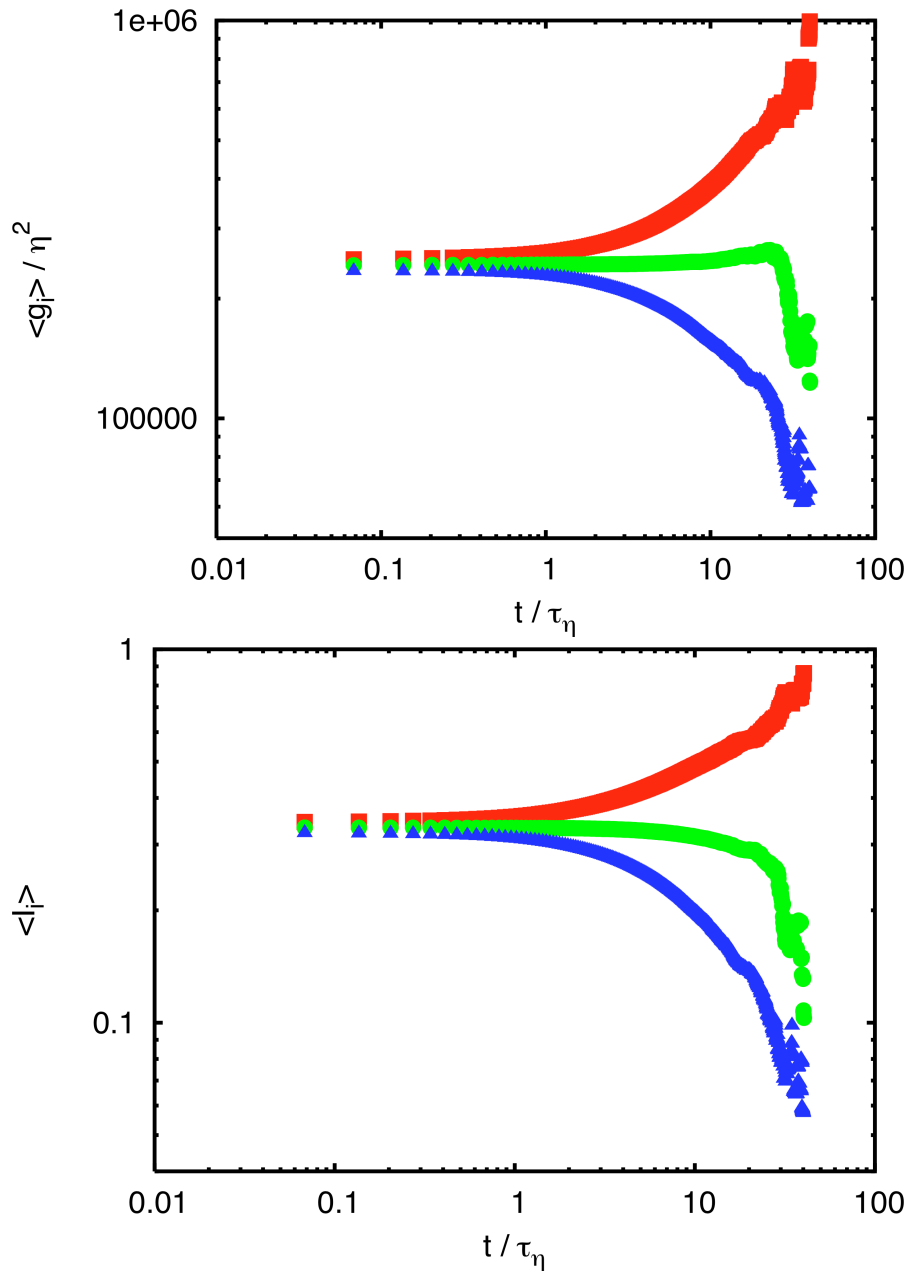


Figure 5.26: The shape evolution of the initially nearly isotropic tetrads at $R_\lambda = 815$, as characterized by the eigenvalues of \mathbf{g} . As above, the initial radius of gyration was fixed to lie between 18 and 21 mm.

lution of the ensemble averages of the tetrad eigenvalues for these nearly isotropic tetrads is shown in Fig. 5.26. By construction, the three eigenvalues begin almost equal to each other. In a very short amount of time, however, the eigenvalues start to diverge and the shape of the tetrads begins to change. The tetrads flatten from their initially regular tetrahedral shapes to asymmetric flat, elongated structures as the largest eigenvalue grows rapidly while the smallest eigenvalue decreases. Since the three eigenvalues retain different values, however, the tetrads become effectively two-dimensional as time increases. Unfortunately, it is highly unlikely that four tracer particles will remain together in our measurement volume for long times, and so the time range of the eigenvalue evolution we can investigate is very short; indeed, the sharp drop in g_2 in Fig. 5.26 is a manifestation of this problem. We cannot, therefore, effectively investigate the true scaling behavior of the tetrad shapes. We also have not considered the removal of the initial size of the tetrads; in analogy with the two-particle case, the initial size may play an important role in the tetrad dynamics at short times. It is unclear, however, how to account for the initial separations of the four particles that make up the the tetrads. Considering the $\langle I_i \rangle$ instead of the $\langle g_i \rangle$ can account for some of the initial size effect, but other statistics may be needed as well.

The evolution of the eigenvalues of the full ensemble of tetrads is shown in Fig. 5.27. The initial ratio of the three eigenvalues effectively shows the steady-state situation, and compares well with the longer-time behavior we saw for the eigenvalues in the nearly isotropic case. As seen from the $\langle g_i \rangle$, the size of all the tetrads increases with time. When the radius of gyration is scaled out, as shown in the plot of $\langle I_i \rangle$, very little shape change occurs, supporting the interpretation of the full ensemble of tetrads as representative of the steady-state situation.

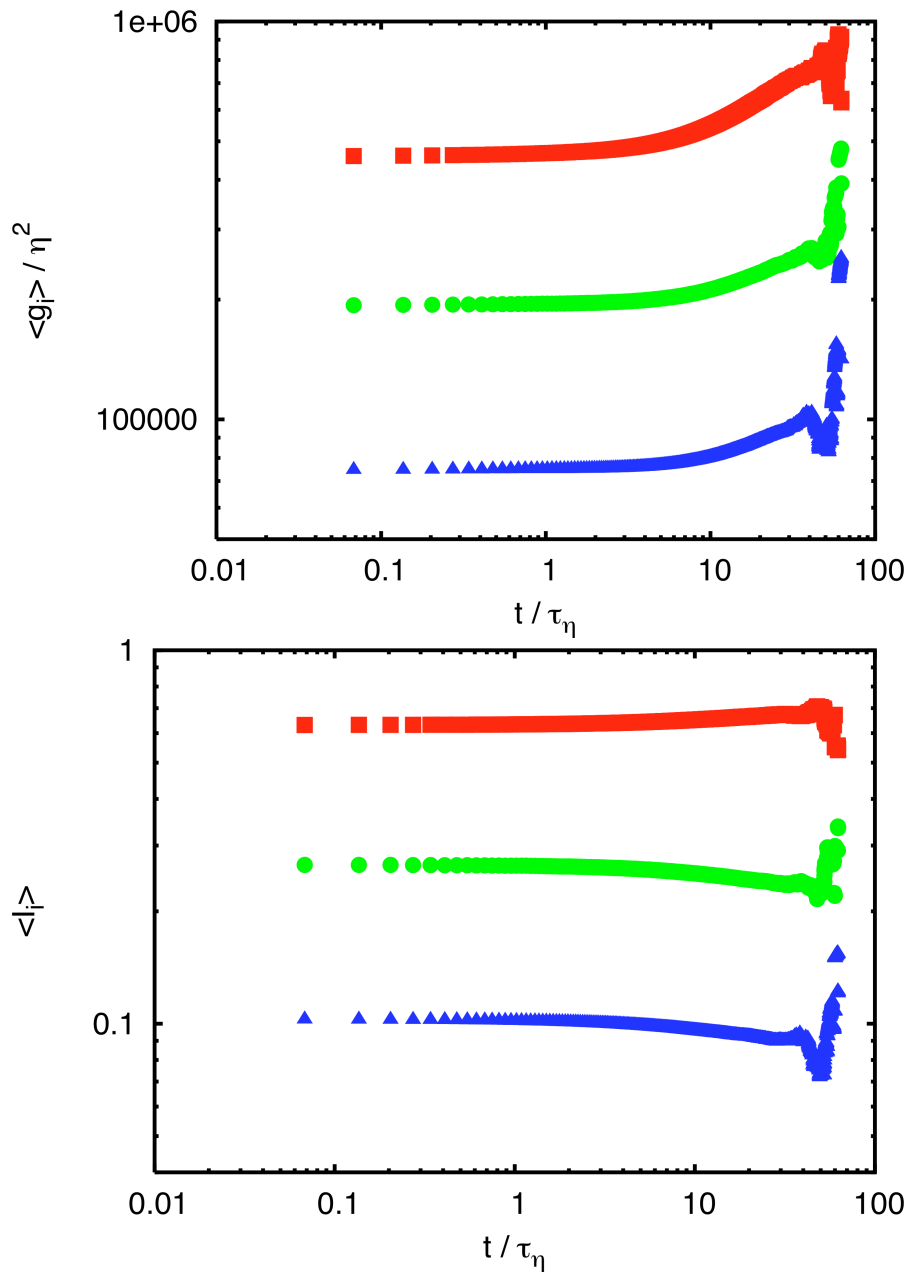


Figure 5.27: The shape evolution of the full ensemble of tetrads at $R_\lambda = 815$, as characterized by the eigenvalues of \mathbf{g} . The initial radius of gyration was fixed to lie between 18 and 21 mm.

Chapter 6

Conclusions and Outlook

In the preceding chapters, we have presented experimental measurements of the Lagrangian velocity and position statistics of both single passive tracer particles and clusters of tracers. We have measured the anomalous scaling of the Lagrangian structure functions, as well as the scaling constant for the second-order structure function. We have investigated turbulent relative dispersion in many forms, and have performed some preliminary experimental tests of the higher-order tetrad models. We have also made the first experimental measurements of the multi-fractal dimension spectrum of Lagrangian turbulence. In order to make these measurements, we have developed a versatile Lagrangian particle tracking system, and have made a study of tracking algorithms.

And yet, despite the data presented here, experimental studies of Lagrangian turbulence are in a large part still in their infancy. Only recently have digital cameras become fast enough to track particles accurately at high Reynolds numbers, and camera speed is still the primary factor that limits the maximum measurable Reynolds number. The fastest cameras on the market today also suffer from small sensor sizes at their maximum imaging speeds. The experimental turbulence community is therefore eagerly awaiting new advances in imaging technology.

The Lagrangian particle tracking techniques we have described in this thesis are very powerful for measuring the trajectories of individual tracers and their time derivatives. But, except for very low Reynolds numbers where the Kolmogorov scale is relatively large, the measurement of spatial derivatives along particle trajectories is not yet possible (Lüthi, 2002). In particular, measurements of the La-

grangian velocity gradients at high Reynolds number would be of great importance since the energy dissipation rate ϵ is so fundamental to the statistical description of turbulence as we know it. Equivalent information, however, is contained in the *enstrophy* dissipation rate. The enstrophy, defined as $\omega^2/2$ where ω is the vorticity, is related to the antisymmetric part of the velocity gradient tensor just as the energy is related to the symmetric part. The primary difference between the two is experimental: while the local energy dissipation rate cannot be determined without measuring the full velocity gradient tensor, the local vorticity and therefore the local enstrophy dissipation can in principle be determined by the Vorticity Optical Probe (VOP) technique developed by Frish and Webb (1981). VOP replaces the simple transparent tracer particles used in typical LPT experiments with crystals of lead carbonate encased in spherical polymer shells. Lead carbonate forms a planar hexagonal crystal that reflects visible light. Every VOP tracer therefore behaves as a small, Kolmogorov-scale planar mirror. As the tracers feel the local vorticity field and spin, they will blink on and off. The frequency of this blinking directly gives the rotation rate and therefore the local flow vorticity without the need for any numerical differentiation. While there are significant technical challenges that must be overcome to implement the VOP technique in a high Reynolds number turbulent flow, VOP has the potential to provide tremendously important information about Lagrangian turbulence.

Lagrangian particle tracking can also be used to investigate the behavior of heavy particles in turbulence, that is, particles that are not passive tracers. Many problems of practical interest are fundamentally problems of the transport of particulate matter in turbulent flows, including fuel sprays, the formation and growth of rain droplets in warm clouds (Shaw, 2003), or the transport of pollutants or

pathogens in the atmosphere (Brown and Hovmöller, 2002). For all of these examples, the transported particles have non-negligible inertia compared to the flow, and their Stokes numbers will be close to or larger than unity. Unlike our passive tracers, then, these inertial particles will not perfectly follow the flow, and we therefore expect that their velocities and accelerations will be depressed when compared with a fluid element of the carrier flow. These effects have indeed been seen in simulation (Bec *et al.*, 2006) and in preliminary experimental work (Ayyalaso-mayajula *et al.*, 2005), but significant work must still be done to characterize the Stokes number dependence of turbulence statistics fully.

Irrespective of measurement technique, there are still fundamental issues to be resolved in the study of turbulence. The most fundamental assumption we have about turbulence, and the quality of turbulence that makes it such an interesting problem, is its universality. According to K41, the statistics of turbulence at small scales are independent of the large-scale flow geometry or forcing. Our results on the scaling of the Lagrangian structure functions and the dispersion of single tracer particles call this universality into question, as do previous results from many other researchers. It is therefore imperative that turbulence statistics be investigated with the same measurement and analysis techniques in a wide variety of turbulent flows in order to investigate the extent to which universality holds. Here, we have used only our von Kármán swirling flow, and have found results that, in some cases, differ from measurements made in wind tunnels, the workhorse of laboratory flows. Many other types of laboratory flows have also been developed, including flow between oscillating grids (Mann *et al.*, 1999), in arrays of turbulent jets (Variano *et al.*, 2004), or in boxes driven by fans or speakers (Hwang and Eaton, 2004). In addition, natural flows in the atmosphere and oceans provide high

Reynolds numbers due to their large scales, though they are less well-controlled.

The questions raised above will soon be under investigation at the Max Planck Institute for Dynamics and Self-Organization. In addition to the von Kármán water flow used in the experiments reported here, there are plans to build a von Kármán flow with sulfur hexafluoride (SF_6), an inert gas heavier than air, as the working fluid. Construction has already begun on a large-scale wind tunnel using SF_6 pressurized to 15 atmospheres that should be able to reach Reynolds numbers of order $R_\lambda \sim 10^4$. In addition, a large “wind box” with dimensions of $5 \times 5 \times 5$ m³ is also planned. The Lagrangian particle tracking system used here will also be used for each of these flows, in addition to traditional hot wire anemometry and laser doppler anemometry. There are also plans to develop a working VOP system for use with these high-Reynolds number flows. The outlook in general for experimental studies of turbulence is therefore bright, and it is an exciting time to be working in the field.

REFERENCES

- R. J. Adrian. Particle-imaging techniques for experimental fluid mechanics. *Annu. Rev. Fluid Mech.*, **23**:261–304, 1991.
- F. Anselmet, Y. Gagne, E. J. Hopfinger, and R. A. Antonia. High-order velocity structure functions in turbulent shear flow. *J. Fluid Mech.*, **140**:63–89, 1984.
- V. Artale, G. Boffetta, A. Celani, M. Cencini, and A. Vulpiani. Dispersion of passive tracers in closed basins: Beyond the diffusion coefficient. *Phys. Fluids*, **9**:3162–3171, 1997.
- S. Ayyalasomayajula, A. Gylfason, and Z. Warhaft. Lagrangian measurements of inertial particles in wind tunnel turbulence. *Bull. Am. Phys. Soc.*, **50**:65, 2005.
- E. Balkovsky and B. I. Shraiman. Olfactory search at high Reynolds number. *Proc. Natl. Acad. Sci. USA*, **99**:12589–12593, 2002.
- G. K. Batchelor. The theory of axisymmetric turbulence. *Proc. R. Soc. Lond. A*, **186**:480–502, 1946.
- G. K. Batchelor. The application of the similarity theory of turbulence to atmospheric diffusion. *Q. J. R. Meteorol. Soc.*, **76**:133–146, 1950.
- G. K. Batchelor. Diffusion in a field of homogeneous turbulence II. The relative motion of particles. *Proc. Camb. Phil. Soc.*, **48**:345–362, 1952.
- G. K. Batchelor. *An Introduction to Fluid Dynamics*. Cambridge University Press, Cambridge, England, 1967.
- J. Bec, L. Biferale, G. Boffetta, A. Celani, M. Cencini, A. Lanotte, S. Musacchio, and F. Toschi. Acceleration statistics of heavy particles in turbulence. *J. Fluid Mech.*, **550**:349–358, 2006.
- R. Benzi, S. Ciliberto, R. Tripiccione, C. Baudet, F. Massaioli, and S. Succi. Extended self-similarity in turbulent flows. *Phys. Rev. E*, **48**:R29–R32, 1993.
- P. S. Berloff, J. C. McWilliams, and A. Bracco. Material transport in oceanic gyres. Part I: Phenomenology. *J. Phys. Oceanogr.*, **32**:764–796, 2002.

- L. Biferale, G. Boffetta, A. Celani, B. J. Devenish, A. Lanotte, and F. Toschi. Multifractal statistics of Lagrangian velocity and acceleration in turbulence. *Phys. Rev. Lett.*, **93**:064502, 2004.
- L. Biferale, G. Boffetta, A. Celani, B. J. Devenish, A. Lanotte, and F. Toschi. Lagrangian statistics of particle pairs in homogeneous isotropic turbulence. *Phys. Fluids*, **17**:115101, 2005a.
- L. Biferale, G. Boffetta, A. Celani, B. J. Devenish, A. Lanotte, and F. Toschi. Multiparticle dispersion in fully developed turbulence. *Phys. Fluids*, **17**:111701, 2005b.
- L. Biferale, G. Boffetta, A. Celani, A. Lanotte, and F. Toschi. Particle trapping in three-dimensional fully developed turbulence. *Phys. Fluids*, **17**:021701, 2005c.
- G. Boffetta and A. Celani. Pair dispersion in turbulence. *Physica A*, **280**:1–9, 2000.
- G. Boffetta, F. De Lillo, and S. Musacchio. Lagrangian statistics and temporal intermittency in a shell model of turbulence. *Phys. Rev. E*, **66**:066307, 2002.
- G. Boffetta and I. M. Sokolov. Relative dispersion in fully developed turbulence: the Richardson's law and intermittency corrections. *Phys. Rev. Lett.*, **88**:094501, 2002a.
- G. Boffetta and I. M. Sokolov. Statistics of two-particle dispersion in two-dimensional turbulence. *Phys. Fluids*, **14**:3224–3232, 2002b.
- M. S. Borgas. The multifractal Lagrangian nature of turbulence. *Phil. Trans. R. Soc. Lond. A*, **342**:379–411, 1993.
- V. Borue and S. A. Orszag. Local energy flux and subgrid-scale statistics in three-dimensional turbulence. *J. Fluid Mech.*, **366**:1–31, 1998.
- F. Bourgeois and J.-C. Lasalle. An extension of the Munkres algorithm for the assignment problem to rectangular matrices. *Commun. ACM*, **14**:802–804, 1971.
- M. Bourgoin, N. T. Ouellette, H. Xu, J. Berg, and E. Bodenschatz. The role of pair dispersion in turbulent flow. *Science*, **311**:835–838, 2006.

- J. K. M. Brown and M. S. Hovmöller. Aerial dispersal of pathogens on the global and continental scales and its impact on plant disease. *Science*, **297**:537–541, 2002.
- B. J. Cantwell. Exact solution of a restricted Euler equation for the velocity gradient tensor. *Phys. Fluids A*, **4**:782–793, 1992.
- F. Carosone, A. Cenedese, and G. Querzoli. Recognition of partially overlapped particle images using the Kohonen neural network. *Exp. Fluids*, **19**:225–232, 1995.
- S. Chandrasekhar. The theory of axisymmetric turbulence. *Phil. Trans. R. Soc. Lond. A*, **242**:557–577, 1950.
- K. Chang, H. Xu, N. T. Ouellette, and E. Bodenschatz. Experimental measurements of the Lagrangian Kolmogorov constant. *In preparation*, 2006.
- S. Y. Chen, B. Dhruva, S. Kurien, K. R. Sreenivasan, and M. A. Taylor. Anomalous scaling of low-order structure functions of turbulent velocity. *J. Fluid Mech.*, **533**:183–192, 2005.
- Y. Chen and A. T. Chwang. Particle image velocimetry system with self-organized feature map algorithm. *J. Eng. Mech.—ASCE*, **129**:1156–1163, 2003.
- M. Chertkov, A. Pumir, and B. I. Shraiman. Lagrangian tetrad dynamics and the phenomenology of turbulence. *Phys. Fluids*, **11**:2394–2410, 1999.
- D. Chetverikov and J. Verestóy. Feature point tracking for incomplete trajectories. *Computing*, **62**:321–338, 1999.
- L. Chevillard. *Description multifractale unifiée du phénomène d'intermittence en turbulence Eulérienne et Lagrangienne*. PhD thesis, Université Bordeaux I, 2004.
- L. Chevillard, A. Arnéodo, B. Castaing, E. Lévêque, J.-F. Pinton, and S. G. Roux. Unified multifractal description of Eulerian and Lagrangian velocity increments in turbulence. *Bull. Am. Phys. Soc.*, **50**:53, 2005.
- L. Chevillard, S. G. Roux, E. Lévêque, N. Mordant, J.-F. Pinton, and A. Arneodo. Lagrangian velocity statistics in turbulent flows: effects of dissipation. *Phys. Rev. Lett.*, **91**:214502, 2003.

- A. B. Chhabra, C. Meneveau, R. V. Jensen, and K. R. Sreenivasan. Direct determination of the $f(\alpha)$ singularity spectrum and its application to fully developed turbulence. *Phys. Rev. A*, **40**:5284–5294, 1989.
- W.-C. Chiu and L. N. Rib. The rate of dissipation of energy and the energy spectrum in a low-speed turbulent jet. *T. Am. Geophys. Union*, **37**:13–26, 1956.
- L. Collins, 2003. Personal communication.
- E. A. Cowen and S. G. Monismith. A hybrid digital particle tracking velocimetry technique. *Exp. Fluids*, **22**:199–211, 1997.
- A. M. Crawford. *Particle tracking measurements in fully developed turbulence: water and dilute polymer solutions*. PhD thesis, Cornell University, 2004.
- D.-H. Doh, D.-H. Kim, S.-H. Choi, S.-D. Hong, T. Saga, and T. Kobayashi. Single-frame (two-field image) 3-D PTV for high speed flows. *Exp. Fluids*, **29**:S85–S98, 2000.
- T. Dracos. Particle tracking in three-dimensional space. In T. Dracos, editor, *Three-Dimensional Velocity and Vorticity Measuring and Image Analysis Techniques*, pages 129–152. Kluwer Academic Publishers, Dordrecht, the Netherlands, 1996.
- S. Edouard, B. Legras, F. Lefèvre, and R. Eymard. The effect of small-scale inhomogeneities on ozone depletion in the arctic. *Nature*, **384**:444–447, 1996.
- G. Falkovich, 2005. Personal communication.
- R. P. Feynman, R. B. Leighton, and M. L. Sands. *The Feynman Lectures on Physics*, volume 1. Addison-Wesley, Reading, MA, 1963.
- U. Frisch. *Turbulence: The Legacy of A. N. Kolmogorov*. Cambridge University Press, Cambridge, England, 1995.
- M. B. Frish and W. W. Webb. Direct measurement of vorticity by optical probe. *J. Fluid Mech.*, **107**:173–200, 1981.
- S. Garg and Z. Warhaft. On the small scale structure of simple shear flow. *Phys. Fluids*, **10**:662–673, 1998.

- G. Gioia, G. Lacorata, E. P. Marques Filho, A. Mazzino, and U. Rizza. Richardson's law in large-eddy simulations of boundary-layer flows. *Boundary-Layer Meteorol.*, **113**:187–199, 2004.
- I. Grant and X. Pan. The use of neural techniques in PIV and PTV. *Meas. Sci. Tech.*, **8**:1399–1405, 1997.
- I. Grant, X. Pan, F. Romano, and X. Wang. Neural-network method applied to the stereo image correspondence problem in three-component particle image velocimetry. *Appl. Optics*, **37**:3656–3663, 1998.
- Y. G. Guezennec, R. S. Brodkey, N. Trigui, and J. C. Kent. Algorithms for fully automated three-dimensional particle tracking velocimetry. *Exp. Fluids*, **17**:209–219, 1994.
- S. R. Hanna. Lagrangian and Eulerian time-scale relations in the daytime boundary layer. *J. Appl. Meteorol.*, **20**:242–249, 1981.
- R. J. Hill. Opportunities for use of exact statistical equations. Accepted for publication in *J. Turbul.*; also preprint physics/0512038 at <http://www.arxiv.org>, 2005.
- K. D. Hinsch and H. Hinrichs. Three-dimensional particle velocimetry. In T. Dracos, editor, *Three-Dimensional Velocity and Vorticity Measuring and Image Analysis Techniques*, pages 129–152. Kluwer Academic Publishers, Dordrecht, the Netherlands, 1996.
- M. Huber, J. C. McWilliams, and M. Ghil. A climatology of turbulent dispersion in the troposphere. *J. Atmos. Sci.*, **58**:2377–2394, 2001.
- W. Hwang and J. K. Eaton. Creating homogeneous and isotropic turbulence without a mean flow. *Exp. Fluids*, **36**:444–454, 2004.
- T. Ishihara and Y. Kaneda. Relative diffusion of a pair of fluid particles in the inertial subrange of turbulence. *Phys. Fluids*, **14**:L69–L72, 2002.
- J. B. Jørgensen, J. Mann, S. Ott, H. L. Pécseli, and J. Trulsen. Experimental studies of occupation and transit times in turbulent flows. *Phys. Fluids*, **17**:035111, 2005.

- L. V. King. On the convection of heat from small cylinders in a stream of fluid. Determination of convective constants of small platinum wires with application to hot-wire anemometry. *Phil. Trans. R. Soc. Lond. A*, **214**:373–432, 1914.
- J. Klafter, A. Blumen, and M. F. Shlesinger. Stochastic pathway to anomalous diffusion. *Phys. Rev. A*, **35**:3081–3085, 1987.
- A. N. Kolmogorov. The local structure of turbulence in incompressible viscous fluid for very large Reynolds numbers. *Dokl. Akad. Nauk SSSR*, **30**:301–305, 1941a.
- A. N. Kolmogorov. Dissipation of energy in the locally isotropic turbulence. *Dokl. Akad. Nauk SSSR*, **32**:16–18, 1941b.
- A. N. Kolmogorov. On the representation of continuous functions of many variables by superpositions of continuous functions of one variable and addition. *Dokl. Akad. Nauk SSSR*, **114**:953–956, 1957.
- A. N. Kolmogorov. A refinement of previous hypotheses concerning the local structure of turbulence in a viscous incompressible fluid at high Reynolds number. *J. Fluid Mech.*, **13**:82–85, 1962.
- R. H. Kraichnan. Dispersion of particle pairs in homogeneous turbulence. *Phys. Fluids*, **9**:1937–1943, 1966.
- S. Kurien and K. R. Sreenivasan. Dynamical equations for high-order structure functions, and a comparison of a mean-field theory with experiments in three-dimensional turbulence. *Phys. Rev. E*, **64**:056302, 2001.
- A. La Porta, G. A. Voth, A. M. Crawford, J. Alexander, and E. Bodenschatz. Fluid particle accelerations in fully developed turbulence. *Nature*, **409**:1017–1019, 2001.
- G. Labonté. A new neural network for particle-tracking velocimetry. *Exp. Fluids*, **26**:340–346, 1999.
- G. Labonté. Neural network reconstruction of fluid flows from tracer-particle displacements. *Exp. Fluids*, **30**:399–409, 2001.
- R.-C. Lien and E. A. D'Asaro. The Kolmogorov constant for the Lagrangian velocity spectrum and structure function. *Phys. Fluids*, **14**:4456–4459, 2002.

- R.-C. Lien, E. A. D'Asaro, and G. T. Dairiki. Lagrangian frequency spectra of vertical velocity and vorticity in high-Reynolds-number oceanic turbulence. *J. Fluid Mech.*, **362**:177–198, 1998.
- B. Lüthi. *Some aspects of strain, vorticity and material element dynamics as measured with 3D particle tracking velocimetry in a turbulent flow*. PhD thesis, Swiss Federal Institute of Technology, Zürich, 2002.
- H.-G. Maas. Contributions of digital photogrammetry to 3-D PTV. In T. Dracos, editor, *Three-Dimensional Velocity and Vorticity Measuring and Image Analysis Techniques*, pages 191–207. Kluwer Academic Publishers, Dordrecht, the Netherlands, 1996.
- H.-G. Maas, A. Gruen, and D. Papantoniou. Particle tracking velocimetry in three-dimensional flows—Part 1. Photogrammetric determination of particle coordinates. *Exp. Fluids*, **15**:133–146, 1993.
- N. A. Malik, T. Dracos, and D. A. Papantoniou. Particle tracking velocimetry in three-dimensional flows—Part 2. Particle tracking. *Exp. Fluids*, **15**:279–294, 1993.
- B. B. Mandelbrot. Intermittent turbulence in self-similar cascades: divergence of high moments and dimension of the carrier. *J. Fluid Mech.*, **62**:331–358, 1974.
- J. Mann, S. Ott, and J. S. Andersen. Experimental study of relative, turbulent diffusion. Technical Report Risø-R-1036(EN), Risø National Laboratory, 1999.
- I. M. Mazzitelli and D. Lohse. Lagrangian statistics for fluid particles and bubbles in turbulence. *New J. Phys.*, **6**:203, 2004.
- C. Meneveau and J. Katz. Scale-invariance and turbulence models for large-eddy simulation. *Annu. Rev. Fluid Mech.*, **32**:1–32, 2000.
- C. Meneveau and K. R. Sreenivasan. The multifractal spectrum of the dissipation field in turbulent flows. *Nucl. Phys. B Proc. Suppl.*, **2**:49–76, 1987.
- T. M. Mitchell. *Machine Learning*. McGraw-Hill, Boston, MA, 1997.
- A. S. Monin and A. M. Yaglom. *Statistical Fluid Mechanics*, volume 2. MIT Press, Cambridge, MA, 1975.

- P. Moore and J. Crimaldi. Odor landscapes and animal behavior: tracking odor plumes in different physical worlds. *J. Marine Syst.*, **49**:55–64, 2004.
- N. Mordant. *Mesure lagrangienne en turbulence: mise en œuvre et analyse*. PhD thesis, École Normale Supérieure de Lyon, 2001.
- N. Mordant, A. M. Crawford, and E. Bodenschatz. Experimental Lagrangian acceleration probability density function measurement. *Physica D*, **193**:245–251, 2004a.
- N. Mordant, E. Lévéque, and J.-F. Pinton. Experimental and numerical study of the Lagrangian dynamics of high Reynolds turbulence. *New J. Phys.*, **6**:116, 2004b.
- N. Mordant, P. Metz, O. Michel, and J.-F. Pinton. Measurement of Lagrangian velocity in fully developed turbulence. *Phys. Rev. Lett.*, **87**:214501, 2001.
- J. F. Muzy, E. Bacry, and A. Arnéodo. Multifractal formalism for fractal signals: the structure-function approach versus the wavelet-transform modulus-maxima method. *Phys. Rev. E*, **47**:875–884, 1993.
- M. Nelkin and R. M. Kerr. Decay of scalar variance in terms of a modified Richardson law for pair dispersion. *Phys. Fluids*, **24**:1754–1756, 1981.
- F. Nicolleau and G. Yu. Two-particle diffusion and locality assumption. *Phys. Fluids*, **16**:2309–2321, 2004.
- A. M. Obukhov. Spectral energy distribution in turbulent flow. *Izv. Akad. Nauk SSSR*, **5**:453–566, 1941.
- K. Ohmi and H.-Y. Li. Particle-tracking velocimetry with new algorithms. *Meas. Sci. Tech.*, **11**:603–616, 2000.
- S. Ott and J. Mann. An experimental investigation of the relative diffusion of particle pairs in three-dimensional turbulent flow. *J. Fluid Mech.*, **422**:207–223, 2000.
- N. T. Ouellette, H. Xu, and E. Bodenschatz. A quantitative study of three-dimensional Lagrangian particle tracking algorithms. *Exp. Fluids*, **40**:301–313, 2006a.

- N. T. Ouellette, H. Xu, M. Bourgoin, and E. Bodenschatz. An experimental study of turbulent relative dispersion models. *In preparation*, 2006b.
- N. T. Ouellette, H. Xu, M. Bourgoin, and E. Bodenschatz. Small-scale anisotropy in Lagrangian turbulence. *In review*, 2006c.
- M. Ould-Rouiss. The axisymmetric equivalent of Kolmogorov's equation. *Eur. Phys. J. B*, **23**:107–120, 2001.
- G. Parisi and U. Frisch. On the singularity structure of fully developed turbulence. In M. Ghil, R. Benzi, and G. Parisi, editors, *Turbulence and Predictability in Geophysical Fluid Dynamics and Climate Dynamics*, pages 84–88. North-Holland, Amsterdam, the Netherlands, 1985.
- M. Pashtrapanshka and W. van de Water. The dispersion of microscopic molecular clouds in turbulence. *Bull. Am. Phys. Soc.*, **50**:153–154, 2005.
- S. B. Pope. *Turbulent Flows*. Cambridge University Press, Cambridge, England, 2000.
- C. Poulain, N. Mazellier, P. Gervais, Y. Gagne, and C. Baudet. Spectral vorticity and Lagrangian velocity measurements in turbulent jets. *Flow Turbul. Combust.*, **72**:245–271, 2004.
- W. H. Press, S. A. Teukolsky, W. T. Vetterling, and B. P. Flannery. *Numerical Recipes in C: The Art of Scientific Computing*. Cambridge University Press, Cambridge, England, 1992.
- A. Pumir. Turbulence in homogeneous shear flows. *Phys. Fluids*, **8**:3112–3127, 1996.
- A. Pumir, 2005. Personal communication.
- A. Pumir and B. I. Shraiman. Persistent small scale anisotropy in homogeneous shear flows. *Phys. Rev. Lett.*, **75**:3114–3117, 1995.
- A. Pumir, B. I. Shraiman, and M. Chertkov. Geometry of Lagrangian dispersion in turbulence. *Phys. Rev. Lett.*, **85**:5324–5327, 2000.
- A. Pumir, B. I. Shraiman, and M. Chertkov. The Lagrangian view of energy transfer in turbulent flow. *Europhys. Lett.*, **56**:379–385, 2001.

- L. F. Richardson. *Weather Prediction by Numerical Process*. Cambridge University Press, Cambridge, England, 1922.
- L. F. Richardson. Atmospheric diffusion shown on a distance-neighbour graph. *Proc. R. Soc. Lond. A*, **110**:709–737, 1926.
- H. C. Rodean. The universal constant for the Lagrangian structure function. *Phys. Fluids A*, **3**:1479–1480, 1991.
- D. F. Rogers and J. A. Adams. *Mathematical Elements for Computer Graphics*. McGraw-Hill, Boston, 1990.
- B. L. Sawford. Reynolds number effects in Lagrangian stochastic models of turbulent dispersion. *Phys. Fluids A*, **3**:1577–1586, 1991.
- B. L. Sawford. Turbulent relative dispersion. *Annu. Rev. Fluid Mech.*, **33**:289–317, 2001.
- I. K. Sethi and R. Jain. Finding trajectories of feature points in a monocular image sequence. *IEEE T. Pattern Anal.*, **9**:56–73, 1987.
- R. A. Shaw. Particle-turbulence interactions in atmospheric clouds. *Annu. Rev. Fluid Mech.*, **35**:183–227, 2003.
- Z.-S. She and E. Lévéque. Universal scaling laws in fully developed turbulence. *Phys. Rev. Lett.*, **72**:336–339, 1994.
- X. Shen and Z. Warhaft. The anisotropy of the small scale structure in high Reynolds number ($r_\lambda \sim 1000$) turbulent shear flow. *Phys. Fluids*, **12**:2976–2989, 2000.
- B. I. Shraiman and E. D. Siggia. Scalar turbulence. *Nature*, **405**:639–646, 2000.
- D. A. Siegel, B. P. Kinlan, B. Gaylord, and S. D. Gaines. Lagrangian descriptions of marine larval dispersion. *Mar. Ecol. Prog. Ser.*, **260**:83–96, 2003.
- K. R. Sreenivasan. On the universality of the Kolmogorov constant. *Phys. Fluids*, **7**:2778–2784, 1995.
- K. R. Sreenivasan. Anomalous scaling in 3D turbulence. LANL Center for Non-linear Studies Workshop on Multi-Scale Interactions in Turbulent Flows, 2005.

- K. R. Sreenivasan and A. Bershadskii. Logarithmic scaling in the near-dissipation range of turbulence. *Pramana–J. Phys.*, **64**:315–321, 2005.
- K. R. Sreenivasan, S. I. Vainshtein, R. Bhiladvala, I. San Gil, S. Chen, and N. Cao. Asymmetry of velocity increments in fully developed turbulence and the scaling of low-order moments. *Phys. Rev. Lett.*, **77**:1488–1491, 1996.
- G. I. Taylor. Diffusion by continuous movements. *Proc. Lond. Math. Soc.*, **20**:196–212, 1922.
- D. J. Thomson and B. J. Devenish. Particle pair separation in kinematic simulations. *J. Fluid Mech.*, **526**:277–302, 2005.
- R. Y. Tsai. A versatile camera calibration technique for high-accuracy 3D machine vision metrology using off-the-shelf TV cameras and lenses. *IEEE T. Robotic. Autom.*, **RA-3**:323–344, 1987.
- E. A. Variano, E. Bodenschatz, and E. A. Cowen. A random synthetic jet array driven turbulence tank. *Exp. Fluids*, **37**:613–615, 2004.
- C. J. Veenman, M. J. T. Reinders, and E. Backer. Resolving motion correspondence for densely moving points. *IEEE T. Pattern Anal.*, **23**:54–72, 2001.
- C. J. Veenman, M. J. T. Reinders, and E. Backer. Establishing motion correspondence using extended temporal scope. *Artif. Intell.*, **145**:227–243, 2003.
- P. Vieillefosse. Internal motion of a small element of fluid in an inviscid flow. *Physica A*, **125**:150–162, 1984.
- T. von Kármán and L. Howarth. On the statistical theory of isotropic turbulence. *Proc. R. Soc. Lond. A*, **164**:192–215, 1938.
- G. A. Voth. *Lagrangian acceleration measurements in turbulence at large Reynolds numbers*. PhD thesis, Cornell University, 2000.
- G. A. Voth, A. La Porta, A. M. Crawford, J. Alexander, and E. Bodenschatz. Measurement of particle accelerations in fully developed turbulence. *J. Fluid Mech.*, **469**:121–160, 2002.

- G. A. Voth, A. La Porta, A. M. Crawford, C. Ward, E. Bodenschatz, and J. Alexander. A silicon strip detector system for high resolution particle tracking in turbulence. *Rev. Sci. Instr.*, **12**:4348–4353, 2001.
- Z. Warhaft. Turbulence in nature and in the laboratory. *Proc. Natl. Acad. Sci. USA*, **99**:2481–2486, 2002.
- K. A. Weinman and A. Y. Klimenko. Estimation of the Kolmogorov constant c_0 by direct numerical simulation of a continuous scalar. *Phys. Fluids*, **12**:3205–3220, 2000.
- J. Westerweel. *Digital particle image velocimetry—theory and applications*. PhD thesis, Delft University, 1993.
- M. C. Wolf, R. Voigt, and P. A. Moore. Spatial arrangement of odor sources modifies the temporal aspects of crayfish search strategies. *J. Chem. Ecol.*, **30**:501–517, 2004.
- H. Xu, M. Bourgoin, N. T. Ouellette, and E. Bodenschatz. High order Lagrangian velocity statistics in turbulence. *Phys. Rev. Lett.*, **96**:024503, 2006a.
- H. Xu, N. T. Ouellette, and E. Bodenschatz. The multifractal dimension of Lagrangian turbulence. *Accepted for publication in Phys. Rev. Lett.*, 2006b.
- P. K. Yeung. Direct numerical simulation of two-particle relative diffusion in isotropic turbulence. *Phys. Fluids*, **6**:3416–3428, 1994.
- P. K. Yeung. Lagrangian characteristics of turbulence and scalar transport in direct numerical simulations. *J. Fluid Mech.*, **427**:241–247, 2001.
- P. K. Yeung. Lagrangian investigations of turbulence. *Annu. Rev. Fluid Mech.*, **34**:115–142, 2002.
- P. K. Yeung and M. S. Borgas. Relative dispersion in isotropic turbulence. Part 1. Direct numerical simulations and Reynolds-number dependence. *J. Fluid Mech.*, **503**:93–124, 2004.
- P. K. Yeung, D. A. Donzis, E. A. Kurth, and S. B. Pope. Reynolds number dependence of Lagrangian velocity, acceleration, and dissipation statistics in large numerical simulations of isotropic turbulence. *Bull. Am. Phys. Soc.*, **50**:76, 2005.

P. J. Zandbergen and D. Dijkstra. Von Kármán swirling flows. *Annu. Rev. Fluid Mech.*, **19**:465–491, 1987.